INFORMATION TO USERS

This manuscript has been reproduced from the microfilm master. UMI films the text directly from the original or copy submitted. Thus, some thesis and dissertation copies are in typewriter face, while others may be from any type of computer printer.

The quality of this reproduction is dependent upon the quality of the copy submitted. Broken or indistinct print, colored or poor quality illustrations and photographs, print bleedthrough, substandard margins, and improper alignment can adversely affect reproduction.

In the unlikely event that the author did not send UMI a complete manuscript and there are missing pages, these will be noted. Also, if unauthorized copyright material had to be removed, a note will indicate the deletion.

Oversize materials (e.g., maps, drawings, charts) are reproduced by sectioning the original, beginning at the upper left-hand corner and continuing from left to right in equal sections with small overlaps.

Photographs included in the original manuscript have been reproduced xerographically in this copy. Higher quality 6" x 9" black and white photographic prints are available for any photographs or illustrations appearing in this copy for an additional charge. Contact UMI directly to order.

ProQuest Information and Learning
300 North Zeeb Road, Ann Arbor, MI 48106-1346 USA
800-521-0600

DISSERTATION

FORMULATION AND SENSITIVITY ANALYSIS OF A NONHYDROSTATIC, AXISYMMETRIC TROPICAL CYCLONE MODEL

Submitted by

Scott A. Hausman

Department of Atmospheric Science

In partial fulfillment of the requirements

for the degree of Doctor of Philosophy

Colorado State University

Fort Collins, Colorado

Spring 2001

UMI Number: 3013841

UMI Microform 3013841

Bell & Howell Information and Learning Company
300 North Zeeb Road
P.O. Box 1346
Ann Arbor, MI 48106-1346

COLORADO STATE UNIVERSITY

February 23, 2001

WE HEREBY RECOMMEND THAT THE DISSERTATION PREPARED UNDER OUR SUPERVISION BY SCOTT A. HAUSMAN ENTITLED FORMULATION AND SENSITIVITY ANALYSIS OF A NONHYDROSTATIC, AXISYMMETRIC TROPICAL CYCLONE MODEL BE ACCEPTED AS FULFILLING IN PART REQUIREMENTS FOR THE DEGREE OF DOCTOR OF PHILOSOPHY.

Committee on Graduate Work

Michael T. Montgomery

Joe M. Prusa

William M. Gray

Gerald D. Taylor

Richard H. Johnson

Wayne Schubert

Adviser Steven A. Rutledge

Department Head

ABSTRACT OF DISSERTATION

FORMULATION AND SENSITIVITY ANALYSIS OF A NONHYDROSTATIC, AXISYMMETRIC TROPICAL CYCLONE MODEL

To better understand the processes limiting tropical cyclone intensity, we simulate a symmetric tropical cyclone-like vortex using a two-dimensional model of a precipitating atmosphere. The model physics is derived from the unique equilibrium thermodynamics and nonhydrostatic primitive dynamics formulated by Ooyama. In addition, we generalize Ertel's potential vorticity (PV) principle to a precipitating atmosphere, expressing the resulting moist PV in terms of a virtual potential temperature that is a function of the total pressure and total density, including condensate. The distribution of moist PV is exactly invertible and similar to the dry PV distribution. Control and sensitivity experiments reveal that the simulated tropical cyclone is sensitive to the horizontal grid resolution, the ice and precipitation microphysics, and the horizontal diffusion. Most importantly, we reproduce the frontal collapse of the eyewall theorized by Emanuel and demonstrate indirectly that the moist PV structure is barotropically unstable. In addition, we find that the mesoscale downdraft outside the primary eyewall inhibits the inflow of entropy and absolute angular momentum into the storm core, weakening the tropical cyclone. Finally, we speculate that the intensity is indirectly linked to radiation, which drives the subsident drying necessary to maintain the moisture budget of the boundary layer against surface evaporation.

Scott A. Hausman
Department of Atmospheric Science
Colorado State University
Fort Collins, Colorado 80523
Spring 2001

ACKNOWLEDGEMENTS

Clearly, a work of this magnitude is not accomplished by the author alone, but with the helpful support of many friends and colleagues. To express my appreciation, I would like to acknowledge those individuals who have made an outstanding contribution to this work.

Most importantly, I would like to thank my advisor, Dr. Wayne Schubert, for his accessibility, guidance, and mentorship. I would also like to thank Dr. Michael Montgomery, who served as a co-advisor, and the remaining members of my committee: Dr. William Cotton, Dr. Richard Johnson, Dr. John McGinley, and Dr. Gerald Taylor. Special thanks are extended to Dr. Katsuyuki "Vic" Ooyama for allowing me to use his model and for being the epitome of a pure scientist. Vic's uncompromising quest for the perfect hurricane model has taught me the meaning of excellence. In addition, I want to thank Dr. James Kossin for our lengthy technical discussions; Maj Rob Fleishauer, Matthew Garcia, and Jason Knievel for carefully reviewing this manuscript; and Paul Ciesielski, Rick Taft, and Gail Cordova for their expert support and friendship.

Finally, I would like to thank my wife, Marianne, and daughters, Christina and Allison, for their sacrifice, patience, and moral support during these challenging years. This work could not have been completed without them.

This research was funded by the National Science Foundation under grants ATM–9729970 and ATM–0087072. Salary and tuition were provided by the Air Force Institute of Technology under the Civilian Institution Program. Computer resources were supplied by the National Center for Atmospheric Research, which is sponsored by the National Science Foundation.

DEDICATION

Solo Deo Gloria

CONTENTS

LIST OF FIGURES

LIST OF TABLES

LIST OF SYMBOLS

Mass Densities $\left(\text{kg m}^{-3}\right)$

ρ_a	dry air
ρ_v	water vapor
ρ_c	cloud (water droplets and/or ice crystals)
ρ_r	precipitation (water drops and/or snow flakes)
$\rho_m = \rho_v + \rho_c$	airborne water (vapor and cloud)
$\rho_w = \rho_m + \rho_r$	total water
$\rho = \rho_a + \rho_w$	moist air
$\xi = \ln(\rho_a/\rho_{a0})$	nondimensional dry-air density

Mixing Ratios

$\mu_m = \rho_m/\rho_a$	airborne water
$\mu_r = \rho_r/\rho_a$	precipitation
$\mu = \rho_w/\rho_a$	total water
μ_0	bias used in transform
ν_r	transformed precipitation
ν	transformed total water

Velocities $\left(\text{m s}^{-1}\right)$

$\mathbf{u} = (u, v, w)$	parcel (dry air and airborne water)
$\mathbf{U} = (0, 0, W)$	precipitation terminal (relative to parcel)
$\mathbf{u}_r = \mathbf{u} + \mathbf{U}$	precipitation (relative to ground)
$\bar{\mathbf{u}} = \mathbf{u} + \frac{\rho_r}{\rho}\mathbf{U}$	mass weighted mean
u	radial component
v	tangential component
w	vertical component
W	settling speed of precipitation relative to parcel

Specific Entropies $\left(\text{J kg}^{-1}\ \text{K}^{-1}\right)$

s_a	dry air
$s_m^{(1)}$	water - state 1 (no condensate)
$s_m^{(2)}$	water - state 2 (saturated at wet bulb temperature)
$s = s_a + \mu_m s_m + \mu_r s_r$	moist air per unit mass of dry air

Entropy Densities $\left(\text{J m}^{-3}\ \text{K}^{-1}\right)$

$\sigma_a = \rho_a s_a$	dry air
$\sigma_m = \rho_m s_m$	airborne water
$\sigma_v = \rho_v s_m$	vapor
$\sigma_c = \rho_c C(T)$	cloud
$\sigma_r = \rho_r C(T)$	precipitation
$\sigma = \sigma_a + \sigma_m + \sigma_r$	moist air
$S_1(\rho_a, \rho_m, T_1)$	state 1 (no condensate)
$S_2(\rho_a, \rho_w, T_2)$	state 2 (saturated at wet bulb temperature)

Pressure (hPa) and Temperature (K)

p_a	partial pressure of dry air
p_v	partial pressure of water vapor
$p = p_a + p_v$	total pressure
T	temperature
T_1	state 1 temperature
T_2	state 2 temperature
T_ρ	virtual temperature
θ	potential temperature
θ_e	equivalent potential temperature
θ_ρ	virtual potential temperature
θ_m	moist potential temperature

Thermodynamic Functions of Temperature

$E(T)$	saturation vapor pressure over a plane surface of synthesized condensate
$E_w(T)$	saturation vapor pressure over a plane surface of liquid water
$E_{w_0} = E_w(T_0)$	reference saturation vapor pressure over a plane surface of liquid water
$E_i(T)$	saturation vapor pressure over a plane surface of solid water
$E_{i_0} = E_i(T_0)$	reference saturation vapor pressure over a plane surface of solid water
$\rho_v^*(T) = E(T)/R_v T$	saturation vapor mass density
$\Lambda(T) = R_v T d\ln E(T)/dT$	specific entropy gained by evaporating a unit mass of condensate at T
$C(T)$	specific entropy of a unit mass of condensate at T
$c_c(T)$	specific heat of a unit mass of the combined condensate at T
$L(T)$	latent heat at T

Constants

$f = 2\lvert\boldsymbol{\Omega}\rvert \sin\phi$	Coriolis parameter
$\boldsymbol{\Omega} = 7.292 \times 10^{-5}\ \mathrm{s}^{-1}$	Earth's angular velocity
$\phi = 20°\mathrm{N}$	latitude
$g = 9.80665\ \mathrm{ms}^{-1}$	Earth's gravitational acceleration
Φ	potential of gravitation and centrifugal forces

$R_a = 287.05$ J kg^{-1} K^{-1}	gas constant for dry air
$R_v = 461.51$ J kg^{-1} K^{-1}	gas constant for water vapor
$R = \frac{\rho_a R_a + \rho_v R_v}{\rho_a + \rho_v}$	mass-weighted-mean gas constant of moist air
$c_{pa} = 1004.675$ J kg^{-1} K^{-1}	specific heat of dry air at constant pressure
$c_{pv} = 1850.0$ J kg^{-1} K^{-1}	specific heat of water vapor at constant pressure
$c_p = \frac{\rho_a c_{pa} + \rho_v c_{pv}}{\rho_a + \rho_v}$	mass-weighted-mean specific heat of moist air at constant pressure
$c_{va} = c_{pa} - R_a$	specific heat of dry air at constant volume
$c_{vv} = c_{pv} - R_v$	specific heat of water vapor at constant volume
$c_v = c_p - R$	mass-weighted-mean specific heat of moist air at constant volume
$p_{a0} = 1000$ hPa	reference dry air pressure
$T_0 = 273.15$ K	reference temperature
$\rho_{a0} = p_{a0}/R_a T_0$	reference dry air mass density
$E_0 = E(T_0)$	reference saturation water vapor pressure
$\rho^*_{v0} = \rho^*_v(T_0)$	reference saturation water vapor mass density
$\Lambda_0 = \Lambda(T_0)$	reference specific entropy (i.e., the entropy gained by evaporating a unit mass of water at T_0)

Microphysical Parameterization

$Q_r = Q_{auto} + Q_{col} - Q_{evap}$	precipitation generation rate
Q_{auto}	autoconversion of cloud to precipitation
Q_{col}	collection of cloud by precipitation
Q_{evap}	evaporation of precipitation
Q_σ	total entropy generation rate
T_f	center of the freezing zone
ΔT_f	width of the freezing zone
$\Omega(T)$	structure function of freezing zone
D_χ	turbulent diffusion
F_χ	turbulent vertical flux profile in the atmospheric boundary layer
C_χ	exchange coefficient
C_D	drag coefficient
U	magnitude of horizontal velocity at anemometer level
α_s	maximum damping in sponge layer
$\phi_s(z)$	vertical structure function of damping in sponge layer
z_t	height of the domain top
z_s	height of the sponge layer base
z_b	height of the boundary layer top
z_a	height of the surface layer top (anemometer level)
z_0	roughness length

Numerics

$\Psi(\xi)$	cubic B-spline basis function
ξ	nondimensional coordinate
$\phi_m(x)$	open form of the basis function
$\psi_m(x)$	closed form of the basis function
$a_m(t)$	basis function amplitudes
$\epsilon(x,t)$	truncation error
J	continuity limit of the basis function
j	order of the derivative constraint
l_c	cutoff wavelength of the derivative constraint
$\mathcal{R}^1$	one dimensional physical space
$\mathcal{S}^J$	spectral space
$\mathcal{D} = [x_0, x_M]$	domain in physical space
x_0	location of first grid point
x_M	location of final grid point
M	number of grid intervals
$\Delta x = (x_M - x_0)/M$	grid interval

Chapter 1

INTRODUCTION

> Isaac Cline's concern was tempered by his belief that no storm could do serious damage to Galveston. He had concluded this on the basis of his own analysis of the unique geography of the Gulf and how it shaped the region's weather. In 1891, in the wake of a tropical storm that Galveston weathered handily, the editors of the Galveston *News* invited Isaac to appraise the city's vulnerability to extreme weather. Isaac ... wrote: "The opinion held by some who are unacquainted with the actual conditions of things, that Galveston will at some time be seriously damaged by some such disturbance, is simply an absurd delusion."
>
> From Erik Larson's
> *Isaac's Storm: A Man, a Time, and the Deadliest Hurricane in History*

With the arrogance and hubris characteristic of those living in the late nineteenth and early twentieth centuries, Dr. Isaac Cline, chief of the local Weather Bureau, confidently predicted that intense hurricanes were not a plausible threat to the residents of Galveston, Texas. Within a decade, however, his confidence and that of Galveston's citizens was shattered as an intense hurricane swept across the city, destroying it and killing over 8000 of its unprepared residents. Since this tragedy, we have actively observed and painstakingly studied the development and intensification of tropical cyclones, with the ultimate intent of avoiding what happened in Galveston over a century ago. Despite our best efforts, however, there are still many unanswered questions. One of the most intriguing and predominant questions is: What regulates the intensity of tropical cyclones?

1.1 A Brief History of Tropical Cyclone Intensity Theory

As the coverage and frequency of tropical observations increased during and after World War II, so did our understanding of the fundamental atmospheric and oceanic conditions

that limit tropical cyclone intensity[1]. For instance, Palmén (1948) discovered that if the sea surface temperature is less than 26–27°C, the latent and sensible energy inputs from the ocean surface will not support tropical cyclone development or intensification. Others found that the interaction of a tropical cyclone with its surrounding environment also affects intensity. Specifically, Riehl (1948) observed that the interaction with the divergent flow of an upper-level ridge increases the intensity of the tropical cyclone by enhancing the low-level convergence and the development of deep convection. However, as shown by Gray (1968), if the vertical shear between the low-level vortex and upper-level flow is excessive, the tropical cyclone will not develop or intensify. Under these conditions, the deep convection is well ventilated, and is unable to sustain the temperature and moisture anomalies that support the thermal balance of the vortex and the undilute ascent of moist convection, respectively. If we understand the conditions that limit intensity, can we then predict the maximum possible intensity for a given set of conditions?

Inspired by the observation that tropical cyclones do not intensify without bound but attain some maximum intensity prior to dissipation, several attempts were made to predict, or quantify, the maximum intensity using fundamental physical principles. For instance, Kuo (1958) and Malkus and Riehl (1960) computed the maximum tangential wind speed by solving the axisymmetric dynamical equations of momentum and energy conservation along a steady state trajectory within the boundary layer inflow. Neglecting the dynamics and focusing instead on the thermodynamics, Miller (1958) calculated the minimum central surface pressure resulting from moist adiabatic ascent within the eyewall and dry adiabatic descent within the eye, assuming hydrostatic balance and mixing between the eye and eyewall. Using the complete set of dynamic and thermodynamic equations, Kleinschmidt (1951) developed a two-layer model with shallow frictional inflow beneath deep moist-neutral outflow in gradient and hydrostatic balance. Unfortunately, all three approaches

---

[1]Typically, tropical cyclone intensity is measured in terms of the maximum tangential wind speed or the minimum surface pressure.

were limited by their assumptions and were never used routinely to predict tropical cyclone intensity.[2]

Physical approaches were used instead to predict the track of tropical cyclones, while empirical (Dvorak, 1975; Hebert and Jarvinen, 1977) and statistical (Elsberry et al., 1975; Merrill, 1988; Jarvinen and Neumann, 1979; Pike, 1985) methods were used to analyze or predict intensity. Gentry (1950) points out that, by 1950, "objective techniques [had] been developed for forecasting the position of the tropical cyclone for periods up to 72 hours in advance, but relatively little success [had] been achieved in developing objective techniques for forecasting storm intensity other than those techniques which use persistence and climatology as the primary predictors." Even these techniques, however, were not improving our basic understanding of maximum intensity. Failing to predict extreme events and lacking any physical foundation, intensity forecast errors remained steady as track forecast errors declined (Keenan, 1982).

To overcome this apparent empirical and statistical impasse, a renewed interest in the physical approach has emerged during the past two decades. Applying the lessons learned from Kleinschmidt (1951), Miller (1958) and others, a new set of maximum intensity theories have arisen (Emanuel, 1986, 1988, 1989, 1995a,b, 1997; Holland, 1997; Gray, 1998). Of these theories, Camp (1999) shows that the most physically consistent and widely accepted is that of Emanuel.

While developing a theory to understand the instability leading to tropical cyclone development, Emanuel (1986) formulated an axisymmetric steady state model of the maximum intensity. Rather than tapping available energy from the ambient environment through moist convection, Emanuel theorized that the tropical cyclone extracts energy from the thermodynamic disequilibrium between the atmosphere and warm ocean surface. Moist convection then simply transports this energy reversibly to the cold upper troposphere, assuming that the tropical atmosphere is neutral to slantwise moist convection and the

---

[2]For an excellent review of tropical cyclone maximum intensity theory, read the thesis of Camp (1999).

additional latent effects due to ice microphysics are negligible. In this way, the tropical cyclone functions as a Carnot heat engine, transferring energy between warm and cold reservoirs and performing work during the process. Using an axisymmetric steady-state two-layer model similar to Kleinschmidt's (1951), Emanuel derived relationships for the radius and magnitude of the maximum tangential wind speed, and the minimum surface pressure. Both observations (Emanuel, 1986), and axisymmetric nonhydrostatic (Rotunno and Emanuel, 1987) and balanced (Emanuel, 1995a) numerical simulations appear to support the theory, despite later modifications (Emanuel, 1995b; Bister and Emanuel, 1998; Schade and Emanuel, 1999). Nevertheless, some of the theory's assumptions may lead to an overprediction of maximum intensity. For instance, several studies indicate that the intensity of a tropical cyclone decreases when ice or horizontal mixing by asymmetries is included.

1.2 The Influence of Ice on Tropical Cyclone Intensity

Surprisingly, few observational and numerical studies have investigated the influence of ice microphysics on the evolution of tropical cyclones. The first numerical studies were performed by Willoughby et al. (1984), Lord et al. (1984), and Lord and Lord (1988). Using an axisymmetric nonhydrostatic model with relatively sophisticated precipitation microphysics (Lin et al., 1983), Willoughby et al. compared tropical cyclone simulations that included and excluded ice. Their results are presented in figure 1.1 as experiments W and I. When ice was included, the tropical cyclone intensified more slowly and attained a maximum tangential wind speed that was slightly less than the no-ice simulation. Furthermore, the evolution of the maximum tangential wind speed in the ice simulation was more erratic than the no-ice simulation; but, the evolution of the minimum pressure was relatively steady in both. The reduced intensity and variability of the tangential wind in the ice simulation resulted from the formation and contraction of numerous secondary rings of convection. Each convective ring was collocated with a maximum in the tangential wind profile and apparently formed due to symmetric instability in regions where the potential vorticity was negative.

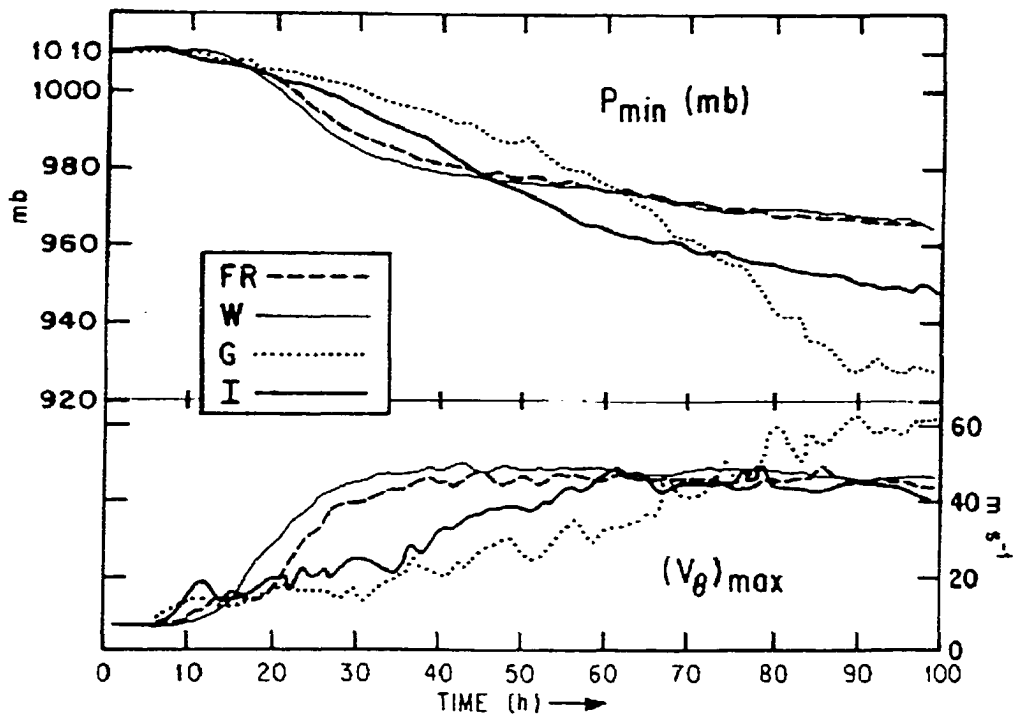

Figure 1.1: W, I, FR, and G Experiments — Evolution of the maximum tangential wind speed $[(v_\theta)_{max}]$ and minimum surface pressure (p_{min}) for Lord and Lord's (1988) frozen rain (FR), water only (W), ice (I), and graupel but no cloud ice or snow (G) experiments. Note that the W and I experiments are identical to the W5A and I7A experiments of Willoughby et al. (1984) [reproduced from Lord and Lord (1988)].

In a companion paper to Willoughby et al. (1984), Lord et al. (1984) examined in more detail the influence of the ice microphysics on the tropical cyclone intensity. Their results show that the decreased terminal velocity of ice particles, combined with rapid outflow in the upper troposphere, result in the advection of ice far from the tropical cyclone core and the formation of a broad region of stratiform precipitation. The resulting thermodynamic and kinematic structure is then very similar to that observed in other tropical (Leary and Houze, 1979; Houze, 1977; Gamache and Houze, 1985) and mid-latitude (Leary and Rappaport, 1987) mesoscale convective systems. Their results further show that, within the convective updraft of the eyewall, ascending condensate rapidly freezes above the 0°C isotherm, generating additional buoyancy and accelerating the updraft through the release of latent heat. The larger particles of frozen condensate, or graupel, quickly fall from the sloping updraft while the smaller particles, or ice crystals, are cast into the outflow where they continue to grow by deposition. Eventually, the growing ice crystals become graupel and snow aggregates, which settle below the 0°C isotherm and melt. The vertical dipole of freezing and melting produce a weak mesoscale updraft above the 0°C isotherm and a weak mesoscale downdraft below. It is possible that the mesoscale downdraft disturbs the low-level inflow and alters the tropical cyclone intensity (Willoughby et al., 1982; Samsury and Zipser, 1995).

In an effort to quantify some of the qualitative conclusions of Lord et al. (1984), Lord and Lord (1988) performed additional experiments, similar to those of Willoughby et al. (1984), using two idealized ice microphysics parameterizations. Figure 1.1 compares Lord and Lord's "frozen rain" and "graupel" experiments (FR and G, respectively) to the experiments of Willoughby et al (W and I). Experiment FR is identical to W except that the latent effects of ice are included. In other words, condensate may freeze through thermodynamic processes, whereas it settles, as if composed of liquid drops only, when only dynamic processes are considered. The results of experiment FR are nearly identical to W. Considering the differences between FR and I, Lord and Lord conclude that the influence of the ice phase "by itself" on tropical cyclone development is a "secondary effect." In contrast, the G experiment assumes that graupel is the only form of ice. Initially, G

develops more slowly than the other experiments; however, it eventually becomes significantly more intense. Since the graupel falls more rapidly than cloud ice or snow, the drag on the eyewall updraft is reduced such that the tropical cyclone becomes more intense. Furthermore, due to the rapid settling of the graupel, there are no mesoscale downdrafts identified in experiment G. Overall, these results confirm the observation of Lord et al. (1984) that tropical cyclone intensity is modulated by mesoscale downdrafts, which are driven by melting ice outside of the eyewall.

It is important to note that the structures and physical processes simulated by Willoughby et al. (1984) and Lord et al. (1984) had not yet been observed. According to Black and Hallett (1996), observations collected during flights through Hurricanes Ella (1978), Allen (1980), and Irene (1981) show that ascending liquid water inside the eyewall is almost completely converted to ice within 5°C of the 0°C isotherm. Supercooled water was only detected at lower temperatures within the most intense updrafts of the eyewall. Using Doppler-derived winds from hurricane Alicia (1983), Marks and Houze (1987) found that buoyant accelerations resulting from this freezing produce a vertical velocity maximum above 5 km. They further observed weak convective downdrafts just outside the eyewall, in the region of heaviest precipitation, and a broad mesoscale downdraft beneath the stratiform precipitation. Houze et al. (1992) observed similar features in Hurricane Norbert (1984). Most importantly, Marks and Houze (1987) showed that the mesoscale downdraft does disturb the boundary layer inflow, which may ultimately weaken the tropical cyclone by preventing the transport of entropy and absolute angular momentum into the storm core.

The observations also reveal that the concentric rings of convection, or secondary eyewalls, simulated by Willoughby et al. (1982) modulate tropical cyclone intensity (Willoughby et al., 1982; Willoughby, 1990; Black and Willoughby, 1992; Dodge et al., 1999). Analyzing flight-level data through Hurricanes Anita (1979), David (1979), and Allen (1980), Willoughby et al. (1982) observed the contraction and intensification of secondary maxima in the tangential wind profile. Each of these maxima was collocated with a ring of

moist convection. As the predominant secondary maximum contracted, the primary maximum weakened and was ultimately replaced by the secondary maximum. In addition, Willoughby et al. (1982) showed that the eyewall replacement cycle marked the climax or at least an interruption in the intensification of the tropical cyclone. Along with Samsury and Zipser (1995), they also argued that the outflow from the secondary rings of convection may interrupt the inflow of entropy and absolute angular momentum to the primary eyewall, further limiting intensification.

1.3 The Influence of Asymmetries on Tropical Cyclone Intensity

In addition to the ice microphysics, the neglect of asymmetries may also affect the prediction of maximum intensity. Numerous idealized numerical studies of tropical cyclone-like vortices suggest that asymmetries affect intensity (Enagonio and Montgomery, 1998; Montgomery and Enagonio, 1998; Möller and Montgomery, 1999; Schubert et al., 1999; Frank and Ritchie, 1999). For instance, Schubert et al. (1999) used an unforced barotropic nondivergent model to demonstrate that a two-dimensional symmetric vortex, which is initialized using a sufficiently narrow annulus of potential vorticity (PV), is barotropically unstable to small asymmetric perturbations. The ring corresponds to the relatively high PV generated by moist convective heating within the eyewall. Small asymmetric perturbations applied to the symmetric vortex produce a spectrum of counter-propagating vortex Rossby waves that exist within the PV gradient of the ring. The phase locking and mutual amplification of the Rossby waves (i.e., barotropic instability) results in the two-dimensional turbulent breakdown of the vortex. Schubert et al. (1999) showed that this turbulence preferentially mixes PV from the ring into the vortex center. Within a tropical cyclone, this mixing increases the PV in the eye but decreases the PV in the eyewall. In response to the PV changes, the tangential wind speed accelerates in the eye and decelerates in the eyewall. Furthermore, to maintain gradient balance inside the eye, the central pressure must also decrease. Both the observational data (Kossin and Eastin, 2000) and other numerical simulations (Montgomery et al., 2000; Kossin and Schubert, 2000) support this model of the

inner-core evolution. By definition, however, this mixing process and its effect on intensity are absent from maximum intensity theories that rely on the axisymmetric assumption.

Of course the highly idealized model of Schubert et al. (1999) neglects the complex vertical structure of the three-dimensional PV distribution, and the frictional and diabatic processes that lead to its generation and destruction. In their simulated vortex, the barotropically unstable distribution of PV is imposed initially and then is advected by the ensuing turbulent flow. In a tropical cyclone, however, convective heating continuously generates PV. In other words, the Schubert et al. (1999) model is unforced, whereas the natural atmosphere is forced. This limitation was recognized by Schubert et al. (1999) when they noted that "there remains the question of the relevance of the concepts presented here to the moist convective environment in real hurricanes... This difficult question might partially be answered through the use of PV diagnostics on the output of 'full-physics' models."

No full-physics model has yet been used to diagnose the fine-scale structure of the PV within a tropical cyclone; however, several theoretical models and observational studies have provided some initial insight. Theoretically, Schubert and Alworth (1987), and Möller and Smith (1994) investigated the PV evolution of a symmetric vortex using Eliassen's (1952) balanced vortex model with different prescribed heating functions. Applying a maximum heating rate of 27 K day^{-1} for 12 hours, Möller and Smith produced a 50–55 m s^{-1} vortex with a 50 km radius of maximum tangential wind. Assuming the vortex is at 20°N, the associated PV anomaly had a maximum of over 170 PVU[3] located at the surface. Observationally, several studies have diagnosed the horizontal PV distribution to investigate tropical cyclone motion (Shapiro and Franklin, 1995; Shapiro, 1996; Wu and Emanuel, 1995a,b); however, only recently has the vertical structure been examined (Shapiro and Franklin, 1995; Molinari et al., 1995, 1998). For example, Shapiro and Franklin (1995) diagnosed a maximum PV anomaly of 100 PVU inside the radius of maximum tangential wind of Hurricane Gloria (1985), using Omega dropwindsonde and airborne Doppler radar

[3]A potential vorticity unit, or PVU, is equal to 1×10^{-6} K m^2 kg^{-1} s^{-1}.

data. Given the "data deficiencies" inside the eye and the approximations required to diagnose the PV, however, it is clear that the fine-scale structure and magnitude of the PV in the eyewall has yet to be observed, although such an analysis of the observational data is in progress (Kossin, 2000, personal communication).

1.4 Overview

Given the limits of our understanding discussed above, we investigate the sensitivity of a numerically simulated tropical cyclone to variations of the physics and numerics, with the ultimate goal of better understanding the parameters limiting tropical cyclone intensity. We first develop an appropriate model based on the equilibrium moist thermodynamics and superior numerics formulated by Ooyama (1984, 1987, 1990, 1995, 1997, 1999, 2000) (chapter 2). Since scarce computer resources still prevent the three-dimensional modeling of tropical cyclones at resolutions fine enough to capture many observed processes [e.g., secondary eyewall cycles, see Liu et al. (1997)], we use the two-dimensional, or axisymmetric, version of the model. This choice also allows the easy comparison of the simulated steady state tropical cyclone with intensity theories that assume axisymmetry. To investigate the generation of PV as proposed by Schubert et al. (1999), we next derive a new expression for the PV of a moist precipitating atmosphere using the virtual potential temperature (chapter 3). This new form of moist PV reduces to the dry PV in the limit of zero moisture and is exactly invertible, unlike the moist PV derived using the equivalent potential temperature. With the model and moist PV diagnostics defined, we then perform a control experiment, or baseline simulation, to validate the model against observations, theory, and other axisymmetric tropical cyclone simulations (chapter 4). To explore the sensitivity of the steady state to variations of the model numerics and physics (e.g., grid resolution and cloud microphysics), we compare the control experiment to a series of sensitivity experiments (chapter 5). Finally, we discuss what we have learned from these experiments as it relates to tropical cyclone intensity (chapter 6).

Chapter 2

MODEL DERIVATION

> The scientist is a practical man and his are practical (i.e., practically attainable) aims. He does not seek the ultimate but the proximate. He does not speak of the last analysis but rather of the next approximation. His are not those beautiful structures so delicately designed that a single flaw may cause the collapse of the whole. The scientist builds slowly and with a gross but solid kind of masonry. If dissatisfied with any of his work, even if it be near the very foundations, he can replace that part without damage to the remainder. On the whole he is satisfied with his work, for while science may never be wholly right it certainly is never wholly wrong; and it seems to be improving from decade to decade.
>
> Gilbert Newton Lewis
> American Chemist (1875-1946)

In this chapter, we formulate an axisymmetric tropical cyclone model using the nonhydrostatic, primitive equations and numerical schemes developed by Ooyama (1984, 1987, 1990, 1995, 1997, 1999, 2001). We begin by reviewing the fundamental physics of a moist, precipitating atmosphere, as expressed through a closed system of prognostic and diagnostic equations (section 2.1). This review is followed by a discussion and evaluation of the numerical methods used to solve the predictive equations (section 2.2). Last, we combine the approximate physics and numerics to obtain the desired axisymmetric tropical cyclone model (section 2.3). For comparison, appendix A contains a tabular summary of the basic features and findings of past axisymmetric tropical cyclone models.

2.1 Physics: Formulation of Moist Atmospheric Dynamics

Following Ooyama (1990, 1995, 2001), we formulate a nonhydrostatic, primitive equation model, which contains the essential physics needed to simulate a moist, precipitating atmosphere. The model atmosphere is composed of moist air parcels similar to that symbolized in Figure 2.1. After defining the basic assumptions and conservative variables that describe the instantaneous state of this parcel, we present a system of hydrodynamic equations to predict the parcel's future state. To close this system of equations, we further derive a set of thermodynamic equations to diagnose the equilibrium state of the parcel.

2.1.1 Semantics: Basic Assumptions and Conservative Variables Defined

Basic Assumptions: Several basic assumptions are needed to simplify the model development. As with any model of a continuous fluid, we first assume that the parcel contains a sufficiently large number of molecules such that its state is represented by equilibrium thermodynamics, yet the number of molecules must also be sufficiently small such that the parcel's matter is distributed homogeneously. Second, we assume that the parcel's matter is in local thermodynamic equilibrium and that the equation of state for all gases is given by the ideal gas law. Third, we assume that the condensate volume is negligible in comparison to the parcel volume, so that the specific volume of the condensate may be neglected in the equation of state.

Mass: Given these assumptions, we next define the distribution of matter within the parcel. To maximize the simplicity of the model, we include only those constituents and phases of matter needed to simulate moist convection. In addition, we represent the matter in bulk form, using mass densities expressed in terms of subscripted ρ. To simulate moist convection, then, the total mass ($\rho = \rho_a + \rho_w$) must contain dry air (ρ_a) and water ($\rho_w = \rho_v + \rho_c + \rho_r$), which potentially exists in different phases, including vapor (ρ_v) and condensate. The condensate is further subdivided into cloud (ρ_c) and precipitation (ρ_r). The criteria that distinguish precipitating condensate from airborne condensate and the

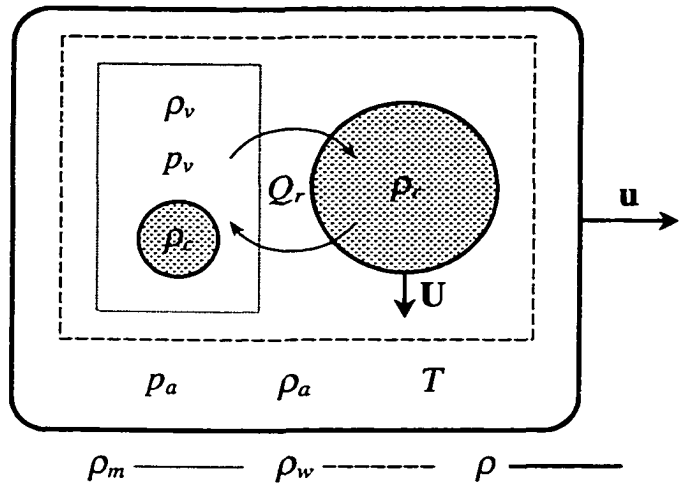

Figure 2.1: Parcel of moist air with total mass density $\rho = \rho_a + \rho_w$, which is composed of dry air and total water with mass densities ρ_a and ρ_w, respectively. The total water mass density, $\rho_w = \rho_v + \rho_c + \rho_r$, is further separated into the mass densities of water vapor (ρ_v) and of condensate (liquid and/or solid), which includes cloud (ρ_c) and precipitation (ρ_r). The dry air and airborne water, which has mass density $\rho_m = \rho_v + \rho_c$, move with velocity $\mathbf{u} = (u, v, w)$, while the precipitation falls relative to the volume with terminal velocity $\mathbf{U} = (0, 0, W)$ or relative to the Earth with velocity $\mathbf{u}_r = \mathbf{u} + \mathbf{U}$. Note that the lines of demarcation enclosing the different mass densities illustrate the partition of mass, but not its location; we assume that all mass is distributed uniformly over the parcel volume.

conditions that determine the formation of each are defined later. Keep in mind that the condensate densities represent the distribution of condensate mass over the parcel volume and not the density of the condensate itself. The further partitioning of condensate into solid and liquid phases will be introduced later.

Momentum: The mass of the parcel is in motion, so it has momentum. We assume that the gases move with the parcel, which has velocity (i.e., momentum per unit mass) $\mathbf{u} = (u, v, w)$, wherein u, v, and w are the three velocity components. Condensate, however, may move relative to the parcel, depending on the size of a given condensate particle. We assume that condensate particles instantaneously adjust to changes in the flow. In other words, the force balance is maintained between the downward pull of gravity and the upward drag produced by the frictional stress acting on the particle surface, which is a function of its terminal velocity $\mathbf{U} = (0, 0, W)$. As the particle size increases, the surface-to-volume ratio decreases; thus, $\mathbf{U}$ must increase so that the frictional stress acting on the particle surface increases to overcome the gravitational pull acting on the mass within the

much larger particle volume. Rather than represent all possible particle sizes, the implied condensate size distribution within the model is discretized into two modes: condensate that moves with the flow (i.e., airborne condensate or cloud with $W = 0$) and condensate that moves relative to the flow (i.e., precipitating condensate or rain/snow with $W \neq 0$). Thus, the dry air, water vapor, and cloud all move with the parcel, while precipitation moves relative to the parcel with settling velocity $\mathbf{U}$ or relative to the ground with velocity $\mathbf{u}_r = \mathbf{u} + \mathbf{U} = (u, v, w + W)$. Combining these definitions, we obtain an expression for the mass-weighted, mean velocity (i.e., total momentum per unit total mass),

$$\bar{\mathbf{u}} = \frac{(\rho_a + \rho_m)\,\mathbf{u} + \rho_r\,(\mathbf{u} + \mathbf{U})}{\rho} = \mathbf{u} + \frac{\rho_r}{\rho}\mathbf{U}, \tag{2.1}$$

wherein $\bar{\mathbf{u}} = (\bar{u}, \bar{v}, \bar{w}) = (u, v, w + \rho_r W/\rho)$. Since the water vapor and cloud move together, we combine them here to form the airborne water, which has mass density $\rho_m = \rho_v + \rho_c$.

Entropy: The mass of the parcel also has thermodynamic energy. Since most atmospheric motions are nearly adiabatic (i.e., isentropic) and in approximate thermodynamic equilibrium over short time scales, and since energy and entropy are related through the first law of thermodynamics, this energy is more conveniently expressed in terms of entropy. Specifically, we use the total entropy density, $\sigma = \sigma_a + \sigma_v + \sigma_c + \sigma_r$, which comprises the entropy densities of dry air (σ_a), water vapor (σ_v), cloud (σ_c), and precipitation (σ_r). We assume that the temperature of the cloud and precipitation is always the wet-bulb temperature (T_w), whether the atmosphere is saturated or unsaturated. This implies that the cloud and precipitation have the same specific entropy, $C\,(T)$, such that $\sigma_c = \rho_c C\,(T_w)$ and $\sigma_r = \rho_r C\,(T_w)$.

In addition to the entropy, there are several other thermodynamic state variables that must be defined. The air within the parcel is assumed to have temperature T and total pressure p. Using Dalton's law of partial pressures, $p = p_a + p_v$ is decomposed into the dry air (p_a) and water vapor (p_v) partial pressures, both of which are related to T through the ideal gas law. Variations in p_v due to particle geometry, surface contaminants, or ventilation

are neglected such that at saturation, $p_v = E(T)$, where $E(T)$ is the saturation vapor pressure over a plain surface of condensate. From this, we further define the mass density of saturated vapor, $\rho_v^*(T) = E(T)/R_v T$, wherein R_v is the gas constant for water vapor.

2.1.2 Hydrodynamics: Prognostic Equations of Conservation Principles

With the variables symbolizing the current state of the parcel defined, we next discuss the conservation relationships, or prognostic equations, that predict the future state of the parcel. The five (seven scalar) prognostic equations, in conservative flux form, for the densities of dry air mass (ρ_a), airborne water mass (ρ_m), precipitation mass (ρ_r), total momentum ($\rho\bar{\mathbf{u}}$), and total entropy (σ) are given by

$$\frac{\partial \rho_a}{\partial t} + \nabla \cdot (\rho_a \mathbf{u}) = D_{\rho_a}, \tag{2.2}$$

$$\frac{\partial \rho_m}{\partial t} + \nabla \cdot (\rho_m \mathbf{u}) = -Q_r + D_{\rho_m}, \tag{2.3}$$

$$\frac{\partial \rho_r}{\partial t} + \nabla \cdot (\rho_r \mathbf{u}) = -\nabla \cdot (\rho_r \mathbf{U}) + Q_r + D_{\rho_r}, \tag{2.4}$$

$$\frac{\partial (\rho\bar{\mathbf{u}})}{\partial t} + \nabla \cdot (\rho\bar{\mathbf{u}}\mathbf{u}) + 2\boldsymbol{\Omega} \times (\rho\bar{\mathbf{u}}) + \nabla p + \rho\nabla\Phi = -\nabla \cdot [\rho_r (\mathbf{u} + \mathbf{U})\mathbf{U}] + Q_r \mathbf{U} + D_{\rho\bar{\mathbf{u}}}, \tag{2.5}$$

$$\frac{\partial \sigma}{\partial t} + \nabla \cdot (\sigma \mathbf{u}) = -\nabla \cdot (\sigma_r \mathbf{U}) + Q_\sigma + D_\sigma, \tag{2.6}$$

wherein $\boldsymbol{\Omega}$ is the Earth's angular velocity, and Φ is the potential of the Earth's gravity. The terms on the left of the equality represent the explicit physics, while the terms on the right represcent implicit physics, which must be parameterized. Specifically, the Q-terms

symbolize internal sources or sinks of mass, momentum, and entropy due to precipitation (Q_r) and entropy (Q_σ) generation. Similarly, the D-terms and terms involving $\mathbf{U}$ (i.e., W) represent external sources or sinks due to turbulent diffusive and precipitation fluxes, respectively, of mass, momentum, and entropy across the parcel's boundary. While the explicit terms are well understood, some additional explanation is needed to understand the physics of the implicit terms as applied to this model.

Internal Sources (Q-terms): The Q_r-term in (2.3) and (2.4) symbolizes the conversion of water mass from airborne water to precipitation. For example, positive Q_r may represent the conversion of cloud to precipitation by autoconversion or accretion, or vapor to precipitation by condensation or deposition. Likewise, negative Q_r may represent the conversion of precipitation to cloud by particle breakup, or precipitation to vapor by evaporation or sublimation. Conversions between vapor and cloud are internal to the airborne water and implicitly included in (2.3).

A Q_r-term also appears in (2.5). This term results from the velocity discontinuity between airborne and precipitating condensate. Inside a real cloud, gravity accelerates growing precipitation particles, gradually increasing the precipitation momentum. Inside a model cloud, however, this same process occurs instantaneously as cloud with $W = 0$ is converted to precipitation with $W \neq 0$. This instantaneous acceleration increases the precipitation momentum at the rate $Q_r W$. To fully understand the origin of this term, see the detailed derivation of (2.5) presented in appendix B.

Interestingly, no term involving the conversion of water vapor to cloud appears in (2.6). In contrast, models that use the potential temperature (θ) to represent the dry air entropy (e.g., Klemp and Wilhelmson, 1978) must include such a term to represent the transfer of entropy as condensation releases latent energy and warms the dry air. When the total entropy is used, this energy transfer is an internal process; thus, no additional heating term is needed. The only other form of heating is that due to nonconservative entropy sources or sinks such as radiation, which are symbolized by Q_σ, and diffusive mixing, which is discussed below.

External Sources (D-terms and W-terms): The D-terms symbolize macroscale changes of the parcel's mass, momentum, and entropy due to microscale turbulent variations within the parcel. Previously, we assumed that the parcel is relatively small such that its internal structure is nearly homogeneous; however, when the parcel size approaches that of a typical grid cell in a numerical model, variability of this structure can lead to exchanges of mass, momentum, and entropy between parcels. To account for this effect, we assume that the average structure represents the macroscale state of the parcel, while the variations from this structure represent microscale turbulence. Equations (2.2)–(2.6) should thus be regarded as Reynolds-averaged versions of the continuous equations, with the D-terms representing the divergence of the turbulent fluxes.

Equations (2.4)–(2.6) also include a term involving external fluxes by precipitation, which are unique to this model. As precipitation falls from the parcel, it transports not only mass, but momentum and entropy as well. Most other models neglect these fluxes by assuming that the precipitation process is pseudoadiabatc. Furthermore, along the lower boundary, $W \neq 0$; thus, precipitation transports mass, momentum, and entropy from the domain.

One last comment is needed regarding the precipitation. Since the precipitation moves relative to the parcel, a separate conservation equation is required to track its mass. By this reasoning, there should also be separate conservation equations for the precipitation momentum and entropy. However, cloud chamber experiments reveal that precipitation particles rapidly (i.e., within 5–10 s) adjust to mechanical (Pruppacher and Klett, 1996) and thermodynamic (Kinzer and Gunn, 1951) equilibrium. Mechanically, the particles have negligible inertia; therefore, their motion rapidly adjusts to changes in the parcel motion and to gravitational accelerations. Likewise, thermodynamically, the energy required to change the temperature of water is much less than that required to change its phase; therefore, the particle temperature rapidly adjusts to that of its environment, while the precipitation mass changes at a finite rate (i.e., Q_r). Assuming that these adjustments are instantaneous, we may diagnose, rather than predict, both the precipitation momentum

per unit mass relative to the parcel (W) and the entropy density [$\sigma_r(T_w) = \rho_r C(T_w)$], including them as part of the totals in (2.5) and (2.6).

In summary, (2.2)–(2.6) represent a system of 7 scalar prognostic equations involving the 23 dependent variables: ρ_a, ρ_m, ρ_r, ρ, Q_r, $\rho\bar{u}$, $\rho\bar{v}$, $\rho\bar{w}$, u, v, w, W, p, σ, σ_r, Q_σ, D_{ρ_a}, D_{ρ_m}, D_{ρ_r}, $D_{\rho\bar{u}}$, $D_{\rho\bar{v}}$, $D_{\rho\bar{w}}$, and D_σ. Clearly this system is not closed and cannot be solved until additional diagnostic equations are found for u, v, w, W, ρ, p, σ_r, Q_r, Q_σ, and the D-terms. Given $\rho = \rho_a + \rho_m + \rho_r$, W, and the prognostic variables, we simply diagnose u, v, and w using (2.1). This leaves p, σ_r, W, Q_r, Q_σ, and the D-terms unknown. We define these variables in the next section using equilibrium thermodynamics and microphysical parameterizations.

2.1.3 Thermodynamics: Diagnostic Equations Representing Fluid State

Although all processes in the atmosphere are irreversible, some are approximately reversible. For example, condensation of water vapor to cloud is a nearly reversible process. Contrast this with precipitation falling from a saturated to an unsaturated parcel, which is far from reversible. Considering the reversible processes first, we diagnose the equilibrium state of the parcel using Ooyama's (1990) equilibrium moist thermodynamics. Next, we formulate the irreversible, or nonequilibrium, processes using empirically-derived microphysical parameterizations.

2.1.3.1 Reversible Processes: Equilibrium Phase Changes of Water

Ooyama (1990) proposed that the fundamental role of hydrodynamics is to predict the evolution of the conservative, or extensive, properties of a fluid, such as its mass, momentum, and entropy, while the role of thermodynamics is to diagnose the intensive properties, or the state, of the fluid. Since p and T are not conservative quantities, they should not be predicted directly but diagnosed from the predicted values of the conservative quantities ρ_a, ρ_m, ρ_r, and σ.

The needed diagnostic equations are derived using the classical reversible, or equilibrium, thermodynamics. Close inspection of the predictive variables reveals that we lack sufficient information to determine the thermodynamic state of the parcel. For instance, neglecting precipitation for the moment, we know the predicted ρ_m, but we do not know the fraction of ρ_v or ρ_c. However, if we know that the air is unsaturated and in equilibrium, then $\rho_v = \rho_m$ and $\rho_c = 0$. Likewise, if we know that the air is saturated and in equilibrium, then $\rho_v = \rho_v^*(T)$ and $\rho_c = \rho_m - \rho_v$. Using this information, and the predicted values of ρ_a, ρ_m, ρ_r, and σ, Ooyama (1990) developed a systematic method for determining the equilibrium moist thermodynamic state of the parcel.

Neglecting precipitation for the moment, we define two functions of entropy, representing two hypothetical states of water within a parcel for the same σ. In state 1, represented by entropy S_1, we assume that there is no condensate. The water is entirely vapor, even if supersaturated. In state 2, represented by entropy S_2, we assume that the water is always saturated at the wet bulb temperature, T_2. Using σ as the predicted entropy of the parcel, the entropy functions of the two states are then given by

$$\begin{aligned} S_1(\rho_a, \rho_m, T_1) &= \sigma, \\ S_2(\rho_a, \rho_m, T_2) &= \sigma. \end{aligned} \tag{2.7}$$

Since ρ_a, ρ_m, and σ are known, the two states are distinguished by their respective temperatures, T_1 and T_2.

If precipitation is present, we must extend the reversible thermodynamics to include irreversible processes. Since state 1 excludes condensate, we subtract the precipitation entropy, $\sigma_r(T_2) = \rho_r C(T_2)$, from σ. In contrast, since state 2 includes condensate, we simply add ρ_r to ρ_m. With these two changes, (2.7) becomes

$$\begin{aligned} S_1(\rho_a, \rho_m, T_1) + \rho_r C(T_2) &= \sigma, \\ S_2(\rho_a, \rho_m + \rho_r, T_2) &= \sigma. \end{aligned} \tag{2.8}$$

wherein σ now includes σ_r. Integrating the entropy equation from a predefined zero-entropy reference state (denoted by subscript zero), Ooyama (1990, 1995) derived the following expressions for the entropy functions:

$$\begin{aligned} S_1(\rho_a, \rho_m, T_1) &= \rho_a \left[c_{p_a} \ln\left(\frac{T_1}{T_0}\right) - R_a \ln\left(\frac{p_a}{p_{a0}}\right) \right] \\ &+ \rho_m \left[c_{p_v} \ln\left(\frac{T_1}{T_0}\right) - R_v \ln\left(\frac{p_v}{E_0}\right) + \Lambda_0 \right], \end{aligned} \tag{2.9}$$

$$\begin{aligned} S_2(\rho_a, \rho_w, T_2) &= \rho_a \left[c_{p_a} \ln\left(\frac{T_2}{T_0}\right) - R_a \ln\left(\frac{p_a}{p_{a0}}\right) \right] \\ &+ \rho_w \left[C(T_2) + \frac{\rho_v^*(T_2)}{\rho_w} \Lambda(T_2) \right], \end{aligned} \tag{2.10}$$

wherein

$$C(T) = c_{p_v} \ln\left(\frac{T}{T_0}\right) - R_v \ln\left(\frac{E(T)}{E_0}\right) - \Lambda(T) + \Lambda_0 \tag{2.11}$$

is the specific entropy of condensate at T, $\Lambda(T) = L(T)/T$ is the specific entropy gained per unit mass of condensate vaporized at T, and $L(T)$ is the specific latent heat of vaporization of condensate at T. The remaining parameters are defined in the List of Symbols. Since σ is a function of T_1 and T_2 for state 1 in (2.7), the temperature T_2 must be obtained from S_2 before T_1 may be diagnosed from S_1.

Figure 2.2 illustrates hypothetical curves of S_1 and S_2 as a function of T and ρ_m for a given ρ_a and, for simplicity, $\rho_r = 0$. The marginal saturation point (MSP) represents the boundary between unsaturated and saturated air for state 1. To the left of the MSP, T_1 and T_2 are the temperatures of unsaturated and saturated moist air, respectively. To convert moist air from state 1 to state 2, water must be "borrowed" from ρ_c and evaporated until the moist air becomes saturated at the wet bulb temperature T_2. In this case, state 1 is clearly the equilibrium state and $T_1 > T_2$, due to evaporative cooling. To the right of

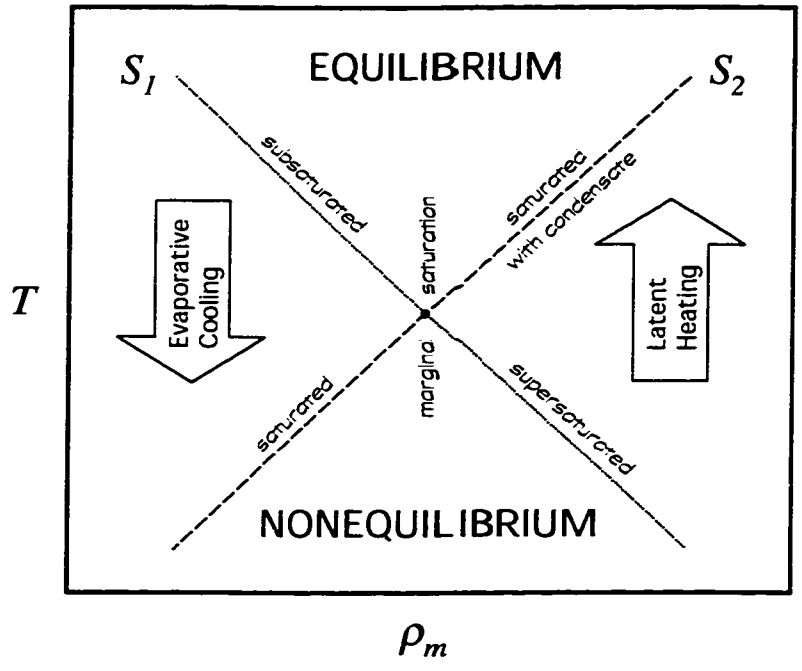

Figure 2.2: Relationship of S_1 and S_2 to T and ρ_m for a given ρ_a, neglecting precipitation. Function S_1 applies when there is no condensate ($\rho_c = 0$), while S_2 applies when the water vapor is always saturated $[\rho_v = \rho_v^*(T)]$. The function occupying an equilibrium state determines the temperature of the system. Function S_1 is bisected by the marginal saturation, which is the point where $\rho_v = \rho_v^*(T)$. To the left of this point, the atmosphere is unsaturated. To satisfy the saturation condition on S_2, condensate is added to the system and evaporated until the wet bulb temperature is reached. Since this addition is physically impossible, S_1 is chosen as the equilibrium state. To the right of the marginal saturation point, the atmosphere is either saturated with condensate or is supersaturated. Since supersaturation typically represents a state of nonequilibrium, S_2 is chosen as the equilibrium state.

the MSP, T_1 is the temperature of supersaturated moist air while T_2 is the temperature of saturated moist air with condensate. To convert moist air from state 2 to state 1, water must be condensed until the moist air is saturated at temperature T_1. In this case, state 2 is the equilibrium state and $T_2 > T_1$, due to latent warming. As a result, for the system to be in equilibrium, the temperature must satisfy

$$T = \mathrm{MAX}(T_1, T_2), \tag{2.12}$$

from which ρ_v, ρ_c, ρ, p_a, p_v, and p are obtained from

$$\begin{cases} \rho_v = \rho_m, & \rho_c = 0, & p_v = \rho_v R_v T, & \text{if } T = T_1 > T_2, \\ \rho_v = \rho_v^*(T), & \rho_c = \rho_m - \rho_v, & p_v = E(T), & \text{if } T = T_2 > T_1, \end{cases} \tag{2.13}$$

$$\rho = \rho_a + \rho_m + \rho_r, \tag{2.14}$$

$$p_a = \rho_a R_a T, \tag{2.15}$$

$$p = p_a + p_v. \tag{2.16}$$

2.1.3.2 Irreversible Processes: Microphysical Parameterizations

Ultimately, the least understood terms in (2.2)–(2.6) are arguably the most important. The irreversible processes symbolized by W, Q_r, Q_σ, and the D-terms are the driving forces of our atmosphere; however, the physics from which these terms are derived are extremely complex and not fully understood. Incorporating much of these complex physics is theoretically possible; but as a first step in the development of this model, we choose instead to use simpler, empirically-derived parameterizations. These parameterizations are believed to capture the essential microphysics, yet are computationally inexpensive, and include the precipitation, ice, radiation, and turbulence microphysics.

Precipitation: Since moist convection drives tropical cyclones, probably the most important microphysical parameterization is that representing the precipitation process. This parameterization may be either implicit (Kuo, 1965; Yamasaki, 1968a,b; Rosenthal, 1969, 1970a,b; Sundqvist, 1970a; Anthes, 1971b, 1972; Jones, 1977), in which case the precipitation microphysics are parameterized indirectly through a convective parameterization, or explicit (Yamasaki, 1977a,b; Willoughby et al., 1984; Rotunno and Emanuel, 1987). To avoid the inherent problems with implicit parameterizations as applied to tropical cyclones models (Rosenthal, 1978, 1979; Nguyen et al., 2000), we choose an explicit approach.

In choosing an explicit approach, however, we must carefully avoid unnecessary complexity. The more complex precipitation parameterizations (e.g., Orville and Kopp, 1977; Lin et al., 1983; Schoenberg Ferrier et al., 1995; Walko et al., 1995) involve many additional predictive and diagnostic equations than already presented here. However, lacking the necessary data, we have thus far been unable to verify that such parameterizations accurately reproduce the microphysical structure of clouds within a tropical cyclone. As a result, it is difficult to interpret changes in tropical cyclone structure or evolution in terms of these additional microphysical details.

To gain further insight into the basic dynamics of axisymmetric tropical cyclones, we choose to avoid complex microphysical schemes and apply a simple bulk approach. Specifically, we use a modified form of Kessler's parameterization, proposed by Klemp and Wilhelmson (1978) and further modified by Ooyama (1995), to compute $Q_r = Q_{auto} + Q_{accr} - Q_{evap}$ and W. This parameterization includes the autoconversion of cloud to precipitation (Q_{auto}) and the accretion of cloud by precipitation (Q_{accr}). In addition, if the parcel is unsaturated, precipitation is permitted to evaporate (Q_{evap}). The details of the parameterization are presented in appendix C.

Ice: To this point, we have neglected the explicit partitioning of condensate into its liquid and solid phases. This is not surprising, considering the additional complexity that the inclusion of ice introduces into the model. When including ice, we must consider the nonequilibrium phase changes of water to ice in mixed-phase clouds. Also, we must consider the different species of ice, as defined by their complex geometry (e.g., ice crystals, snow aggregates, graupel, etc.), and how best to predict their evolution.

Because of this complexity, virtually all of the early tropical cyclone models neglected the ice phase, assuming that water remains liquid at all temperatures. Willoughby et al. (1984) and Lord et al. (1984) were the first to include a detailed microphysical representation of ice in an axisymmetric tropical cyclone model. Their model contained five species of condensate (i.e., cloud water, rain, cloud ice, snow, and graupel) with thirty different conversion processes among the species. Due to the complexity of the ice microphysics,

however, we believe it is difficult to determine the cause-and-effect relationships among the changes in the storm structure and the various ice species (Lord et al., 1984).

As a compromise between the extremes of including ice with all of its complexity or neglecting ice, Ooyama (1990) chose instead to represent the liquid and solid phases in terms of a single, synthesized condensate. This single phase, or combined condensate, has the properties of water for temperatures above a specified *freezing zone* and the properties of ice for temperatures below this zone. Within the freezing zone, the properties of the liquid and solid phases are interpolated. Specifically, Ooyama interpolates the specific entropies of water, $C_w(T)$, and ice, $C_i(T)$, i.e.,

$$C(T) = \Omega(T)\, C_w(T) + [1 - \Omega(T)]\, C_i(T)\,, \tag{2.17}$$

to obtain the specific entropy of the combined condensate, $C(T)$, wherein

$$\Omega(T) = \frac{1}{2}\left[1 + \tanh\left(\frac{T - T_f}{\Delta T_f}\right)\right] \tag{2.18}$$

is the interpolation function, with T_f and ΔT_f being the center temperature and width of the freezing zone, respectively. The expressions for C_w and C_i are found in Ooyama's paper.

The result of this interpolation is a large positive anomaly in the specific heat of the combined condensate, $c_c(T)$, centered at T_f (see Ooyama, 1990, fig. 3). To understand the physical implications of this anomaly, consider a small drop of water that is being cooled. Due to the near constant $c_c(T)$ for $T \gg T_f$, the drop gradually releases energy as it is cooled until its temperature nears the freezing zone. Here, $c_c(T)$ increases dramatically such that any further cooling of the drop produces a large release of energy. This, of course, simulates the release of latent heat due to the phase change of liquid water to ice as the

drop freezes. Any nonequilibrium phase changes due to the Bergeron-Findeisen process are assumed to be included in this parameterization.

In addition to $C(T)$, we also require an expression for $E(T)$, since this term is yet undefined in the thermodynamic diagnosis presented above. To obtain $E(T)$, Ooyama (1990) used an integrated form of Kirchoff's equation, with the Clausius-Clapeyron equation inserted for the latent heat $L(T)$, to obtain the first-order differential equation

$$\begin{aligned} \frac{d}{dT}\left\{T\ln\left[\frac{E(T)}{E_{w_0}}\right]\right\} &= \Omega(T)\frac{d}{dT}\left\{T\ln\left[\frac{E_w(T)}{E_{w_0}}\right]\right\} \\ &+ [1-\Omega(T)]\frac{d}{dT}\left\{T\ln\left[\frac{E_i(T)}{E_{i_0}}\right]\right\}, \end{aligned} \tag{2.19}$$

wherein $E_w(T)$ and $E_i(T)$ are the saturation vapor pressures over a plane surface of liquid water and ice, respectively, and E_{w_0} and E_{i_0} are their reference values at T_0. Note that E_{w_0} is used as the reference state for the combined condensate. Integrating (2.19), with the boundary condition $E(T) \to E_w(T)$ for $T \gg T_f$, we obtain $E(T)$. To complete this parameterization, we have used the Goff-Gratch formulae (List, 1949) for $E_w(T)$ and $E_i(T)$.

Not only does the ice phase affect the thermodynamics but also the hydrodynamics as it alters the settling velocity (W) of the precipitation. Due to its complex geometry, the drag on an ice particle is much greater than that on a water drop. Typically, the average fall speed of particles accelerates from $1-2$ m s^{-1} above the melting level to about 8 m s^{-1} below (Pruppacher and Klett, 1996; Black and Hallett, 1996; Böhm, 1992)[1]. To account for this acceleration, Ooyama (1995) added an ice modification factor to the diagnostic equation for W, as shown in (C.7). Since changes in W also affect the accretion rate and the ventilation of condensate particles, (Ooyama, 2001) added the ice factor to expressions (C.3) and (C.5).

---

[1] In the stratiform region, the terminal velocity of snow aggregates is 1–2 m s^{-1}; whereas, in the convective region, the terminal velocity of graupel is 4–6 m s^{-1}.

Radiation: Since tropical cyclones persist for many days, we naturally wonder if the slow net cooling by outgoing longwave radiation significantly alters their structure and evolution. Diabatic warming near the storm core due to convective heating, and adiabatic warming in the surrounding environment due to compensating subsidence, gradually increase the mean temperature of the atmosphere (Kuo, 1965; Yamasaki, 1968a). Assuming that the excess internal energy is not exported as rapidly as it is generated, the surface pressure will slowly decrease, which increases the saturation equivalent potential temperature. According to Rotunno and Emanuel (1987), this increases the tropical cyclone intensity by increasing the surface energy flux away from the storm core. Kasahara (1961) estimated that a uniform cooling of 1.0°C day^{-1} would balance the net warming, leaving the tropical cyclone in a steady state.

Past axisymmetric tropical cyclone simulations showed that including radiative cooling is of secondary importance and therefore negligible. Representing the radiative cooling as a diabatic mass flux in his three-layer model, Ooyama (1969) found that uniform cooling has little effect on the storm behavior. However, he did note that nonuniform cooling due to the presence of clouds could alter this result, which was later verified by Sundqvist (1970b). Using a prescribed vertical profile of radiative cooling in the cloud-free regions, Sundqvist (1970b, see fig. 2) found that the tropical cyclone intensified about 20 hours earlier than without the cooling, but that the overall intensity was about the same. In a similar experiment, using a more sophisticated radiation parameterization (Sasamori, 1968), Anthes (1971a, see fig. 10) verified that tropical cyclone intensity remains approximately unchanged. Neglecting radiative cooling, Willoughby et al. (1984, see fig. 3) showed a decrease of only 0.5 mb day^{-1} of the central surface pressure during the steady-state period of their simulation. These results suggest that including radiative cooling has only a slight modifying effect; therefore, rather than parameterize it in a costly or *ad hoc* fashion, we instead neglect radiative cooling (i.e., $Q_\sigma = 0$) at this stage of the model development.

Turbulent Diffusion: Recall that the D-terms represent resolved, macroscale forcing due to unresolved, microscale turbulent fluctuations. In general, these terms are assumed to have two parts, i.e.,

$$D_\chi = D_\chi^{FA} + D_\chi^{ABL}, \tag{2.20}$$

wherein D_χ^{FA} and D_χ^{ABL} are the turbulent flux divergences in the free atmosphere (FA) and the atmospheric boundary layer (ABL), respectively, for $\chi = \rho_a, \rho_m, \rho_r, \rho\bar{u}, \rho\bar{v}, \rho w,$ or σ.

Although D_χ^{FA} is a physical term representing unresolved turbulent mixing, historically it has become a numerical term used to control computational instability. In a three-dimensional turbulent fluid, nonlinear interactions produce a cascade of kinetic energy to smaller scales. Physically, this cascade extends to the dissipation scale, where kinetic energy is converted to thermodynamic energy [another process generally neglected (Bister and Emanuel, 1998)]. Numerically, the cascade is arrested at the smallest resolved scale of the model, where the kinetic energy accumulates. Almost all atmospheric models control this accumulation, or instability, using a form of turbulent diffusion parameterized through D_χ^{FA}. Physically, we argue that in a cloud-resolving model the mixing due to unresolved eddies is negligible compared to that of the resolved eddies; however, numerically, we must control the instability. Rather than solve a numerical problem by altering the physics, we assume that

$$D_\chi^{FA} = 0, \tag{2.21}$$

and control the instability by spectrally filtering the smallest resolved signal using the numerics (see section 2.2).

In earlier axisymmetric tropical cyclone models (Anthes, 1971a; Rosenthal, 1978; Rotunno and Emanuel, 1987), D_χ^{FA} has also been used to represent mixing by horizontal processes. For example, Anthes used Smagorinsky's (1963) equation for horizontal diffusion,

$$D_\chi^{FA} = (k_s \Delta x)^2 |\mathbf{D}| \nabla^2 \chi, \tag{2.22}$$

wherein $k_s \approx 0.2$, Δx is the grid spacing, and $|\mathbf{D}|$ is the deformation. However, it has been demonstrated that asymmetric mixing, if due primarily to barotropic instability, does not mix uniformly, as with diffusion, but preferentially toward the tropical cyclone core (Schubert et al., 1999; Kossin, 2000a; Kossin and Schubert, 2000; Nolan and Montgomery, 2000b,a). Thus, rather than crudely parameterize this mixing, since it is not well understood observationally, we instead neglect it and consider the implications of this assumption when interpreting the results.

Near the surface, we cannot assume that mixing by small-scale eddies is negligible in comparison to the resolved eddies as above, since these small-scale eddies are essential to the vertical advection of mass, momentum, and entropy to and from the surface. Although there are a wide range of approaches to simulate the ABL, with varying degrees of complexity, we again choose a very simple approach.

To begin, we let

$$D_{\chi}^{ABL} = \frac{\partial F_{\chi}}{\partial z}, \tag{2.23}$$

wherein $F_{\chi}(z)$ is the vertical turbulent flux of $\chi = \rho_m, \rho u, \rho v$, and σ. Here, we assumed that the dry air mass is materially conserved (i.e., $F_{\rho_a} = 0$), that the precipitation rapidly falls through turbulent eddies (i.e., $F_{\rho_r} = 0$), and that there is no turbulent transport of vertical momentum (i.e., $F_{\rho w} = 0$). While sophisticated ABL parameterizations predict the complex vertical structure of the retained fluxes, we simply assume that they have a known structure:

$$F_{\chi}(z) = F_{\chi}(z_a)\,\phi_a(z), \tag{2.24}$$

wherein $F_{\chi}(z_a)$ is the flux at the top of the constant flux surface layer, z_a is the prescribed surface layer depth, and $\phi_a(z)$ is the vertical structure function. This structure function

may vary depending on the problem. As a first step to parameterizing the tropical cyclone ABL, we use a linear relationship of the form

$$\phi_a(z) = \begin{cases} \frac{z_b - z}{z_b - z_a}, & \text{if} \quad z_a \leq z \leq z_b, \\ 0, & \text{if} \quad z_b \leq z, \end{cases} \tag{2.25}$$

wherein z_b is the fixed top of the ABL. Ooyama (1999) demonstrated that, although this flux does not produce an Ekman-like spiral nor a typical ABL sounding, it does provide the essential ABL dynamics needed to simulate tropical cyclones (i.e., the frictional inflow of mass toward low pressure and the flux of mass, momentum, and energy to and from the surface).

Just above the surface, the molecular flux in the viscous sublayer is typically assumed to represent a continuous extension of the turbulent flux in the surface layer (Haltiner and Williams, 1980). As a result, the flux at the top of the surface layer is given by the surface flux, which we represent using the bulk aerodynamic formula,

$$F_\chi(z_a) = F_\chi(0) = -C_\chi U(\chi_a - \chi_0), \tag{2.26}$$

wherein $U = (u^2 + v^2)^{\frac{1}{2}}$, C_χ are the exchange coefficients, and subscripts a and 0 denote the values of χ at the anemometer level and at the surface, respectively.

2.2 Numerics: Discretization of Space and Time

In the previous section, we developed a mathematical model of a moist, precipitating atmosphere. Each of the model predictive equations, (2.2)–(2.6), may be written in the succinct form

$$\frac{\partial u}{\partial t} = F(u, u_x, u_{xx}, ...), \tag{2.27}$$

wherein u now represents any one of the predictive variables and F is the forcing provided by the primitive equations. In this section, we derive and evaluate numerical techniques to solve this equation. First, to solve the right side, we review Ooyama's (1984, 1987; DeMaria et al., 1992) spatial discretization scheme, the Spectral Application of Finite Element Representation (SAFER) method, including a discussion of the method's advantages and disadvantages. Second, to solve the left side, we discuss the temporal discretization scheme, which is based on the semi-implicit method (Ooyama, 1997) with leapfrog time differencing.

2.2.1 Spatial Discretization: The SAFER Method

One physically fascinating, yet numerically frustrating, aspect of tropical cyclone dynamics is the wide range of dynamically interacting spatial scales. As pointed out by Ooyama (1984), the radius of deformation may vary by several orders of magnitude from the storm center ($\sim$ 5–10 km) to the surrounding environment ($\sim$ 1000 km). Consequently, near the storm center, gravity-inertia waves with wavelengths similar to the local radius of deformation affect the quasi-balanced dynamics, whereas in the surrounding environment, these same waves would be dynamically invisible. Furthermore, the tropical cyclone itself is relatively small compared to the large-scale environment through which it moves. Thus, to accurately yet efficiently simulate the essential dynamics of tropical cyclones, we need a spatial discretization scheme with flexible boundary conditions that permits grid nesting and limited area domains.

In response to this need, Ooyama developed a unique spatial discretization scheme, the SAFER method, for objective analysis (Ooyama, 1987) and hurricane prediction (Ooyama, 1984; DeMaria et al., 1992). The approach has benefits inherent in both finite (grid point) and continuous (spectral) spatial discretization schemes. The SAFER method is similar to a harmonic spectral method in that the finite elements are differentiable; thus, the dispersion errors are much smaller than those produced by finite-difference approximations. Likewise, the SAFER method is similar to a grid-point method in that the finite elements are defined locally; thus, many different boundary conditions are possible, unlike

pure harmonic spectral methods, which require periodic boundary conditions. In this section, we derive the basic concepts of the SAFER method, and discuss its advantages and disadvantages.

2.2.1.1 General Spectral Representation and Transforms

Transform from Spectral to Physical Space $\left(\mathcal{S}^J \rightarrow \mathcal{R}^1\right)$*:* To understand the basic concepts of the SAFER method, we first discuss spectral methods in general, as applied to a scalar field in one dimension, $\mathcal{R}^1$. Consider an arbitrary, continuous function $\bar{u}(x,t)$ defined within the closed domain $\mathcal{D} \subset \mathcal{R}^1$ with $x \in \mathcal{D}$. An approximate, continuous representation of $\bar{u}$ is given by the truncated series expansion

$$\bar{u}(x,t) = u(x,t) + \varepsilon(x,t) = \sum_{m=0}^{M} a_m(t)\,\phi_m(x) + \varepsilon(x,t), \tag{2.28}$$

wherein M is the truncation limit, or the degrees of representational freedom, and $\varepsilon(x,t)$ is the truncation error. The functions $\phi_m(x) \in C_J, m = 0, 1, \ldots, M$ in (2.28) form a set of linearly independent basis functions that have time-dependent amplitudes $a_m(t)$ and are continuously differentiable to the continuity limit J. If we neglect ε, (2.28) reduces to the transformation from spectral space $\mathcal{S}^J$ to physical space $\mathcal{R}^1$,

$$u(x,t) = \sum_{m=0}^{M} a_m(t)\,\phi_m(x), \tag{2.29}$$

wherein u is an approximate representation of $\bar{u}$ when $\varepsilon \neq 0$. We may think of u as the projection of $\bar{u}$ into $\mathcal{S}^J$. Only when $\bar{u}$ is a member of the family of functions represented in $\mathcal{S}^J$ will $u = \bar{u}$. To represent u using (2.29) requires knowing each a_m, which are obtained using a reverse transformation from physical to spectral space.

Transform from Physical to Spectral Space $\left(\mathcal{R}^1 \rightarrow \mathcal{S}^J\right)$*:* The transformation from physical to spectral space is found by minimizing the error between $\bar{u}$ and u using the least-squares

approximation. Following DeMaria et al. (1992), we let $\|f(x)\| \equiv (f,f)^{\frac{1}{2}}$ be the norm of $f(x)$ and

$$(f,g) \equiv \int_{\mathcal{D}} f(x)\, g(x)\, dx, \tag{2.30}$$

be the definition of the inner product between two arbitrary, well-behaved functions $f(x)$ and $g(x)$. The error between $\bar{u}$ and u is then given by

$$E = \|u - \bar{u}\|. \tag{2.31}$$

Before minimizing the error, we must make a simple yet extremely useful modification to (2.31). Up to this point in the derivation, we have assumed that $\bar{u}$ is a continuous function of x. In most numerical models, however, we do not know $\bar{u}$ analytically for all x but only discretely at individual grid points x_i. Under these conditions, the minimization of (2.31) yields zero errors at $x = x_i$ and unacceptably large errors for $x \neq x_i$. To both minimize the error and smooth the solution (i.e., minimize the error between the points), a penalty term or derivative constraint,

$$E_p = \left\| \sqrt{\alpha(x)} \frac{d^j u}{dx^j} \right\|, \tag{2.32}$$

is added to (2.31), yielding the total error

$$E_t = \left(E^2 + E_p^2\right)^{\frac{1}{2}}, \tag{2.33}$$

wherein $j = 1, 2$, or 3 is the order of the derivative constraint, $\alpha(x) \equiv (l_c(x)/2\pi)^{2j}$, and $l_c(x)$ is the cutoff wavelength. If short-wavelength (relative to l_c), large-amplitude oscillations are present, the penalty term is large; thus, these oscillations will be removed,

or filtered, to minimize E_t. The derivative constraint thus acts as a low-pass filter, with the filter characteristics controlled by careful selection of j and l_c. A detailed analysis of the spectral characteristics of the derivative constraint is presented in appendix F.

Using (2.33) instead of (2.31) for the error, we seek a_m such that E_t is minimized. Substituting (2.29) into (2.31) and (2.32) for u, we find the minimum E_t for each a_m by solving $\partial E_t/\partial a_m = 0$ for $m = 0, 1, 2, \ldots, M$. This minimization yields the desired reverse transform from $\mathcal{R}^1$ to $\mathcal{S}^J$,

$$\mathbf{a} = \left(\mathbf{P} + \mathbf{Q}^{(j)}\right)^{-1} \mathbf{b}, \tag{2.34}$$

wherein $\mathbf{a} = \{a_m : \ m = 0, 1, \ldots, M\}^T$,

$$\mathbf{b} = \left\{b_m = \left(\bar{u}\left(x\right), \phi_m\left(x\right)\right) : \ m = 0, 1, \ldots, M\right\}^T, \tag{2.35}$$

$$\mathbf{P} = \left\{p_{mm'} = \left(\phi_m\left(x\right), \phi_{m'}\left(x\right)\right) : \ m, m' = 0, 1, \ldots, M\right\}, \tag{2.36}$$

$$\mathbf{Q}^{(j)} = \left\{q^{(j)}_{mm'} = \left(\alpha\left(x\right)\phi^{(j)}_m\left(x\right), \phi^{(j)}_{m'}\left(x\right)\right) : \ m, m' = 0, 1, \ldots, M\right\}, \tag{2.37}$$

and $\phi^{(j)}_m\left(x\right) = d^j\phi_m/dx^j$.

Equation (2.34) represents a linear system of equations we solve for a_m. Notice that, in general, this solution takes two steps. First, the function $\bar{u}\left(x\right)$ is transformed into $\mathcal{S}^J$ by solving (2.35) for $\mathbf{b}$. Second, if the basis functions are not orthogonal, we solve (2.34) for $\mathbf{a}$. If the basis functions are orthogonal, the solution takes one step, i.e., $\mathbf{a} = \mathbf{b}$, since $\mathbf{P} + \mathbf{Q}$ is equal to the identity matrix.

The approach outlined above is extendible to two and three dimensions. For example, using a two-dimensional, rectangular domain, $\mathcal{D} \subset \mathcal{R}^2$ with $x, y \in \mathcal{D}$, the transform equations (2.29) and (2.34) may be written in the following bilinear form:

$$u(x,y,t) = \sum_{m=0}^{M} \sum_{n=0}^{N} a_{mn}(t)\, \phi_m(x)\, \phi_n(y), \tag{2.38}$$

$$\mathbf{a} = \left\{ \left(\mathbf{P}_m + \mathbf{Q}_m^{(j)} \right) \otimes \left(\mathbf{P}_n + \mathbf{Q}_n^{(j)} \right) \right\}^{-1} \mathbf{b}, \tag{2.39}$$

wherein M and N are the degrees of representational freedom in the x and y directions, $\mathbf{a} = \{a_{mn} : \ m = 0, 1, \ldots, M; \ n = 0, 1, \ldots, N\}$ are the time dependent amplitudes for the basis functions $\phi_m(x)$, $m = 0, 1, \ldots, M$ and $\phi_n(y)$, $n = 0, 1, \ldots, N$, and

$$\mathbf{b} = \{b_{mn} = (\bar{u}(x), \phi_m(x)\, \phi_n(y)) : \ m = 0, 1, \ldots, M; \ n = 0, 1, \ldots, N\}^T. \tag{2.40}$$

$\mathbf{P}_i$ and $\mathbf{Q}_i^{(j)}$ are defined as in (2.36) and (2.37) for $i = m, n$.

2.2.1.2 Specific Spectral Representation and Transforms using the Cubic B-Spline

The specific choice of basis function depends on the problem being solved. For most atmospheric problems, Ooyama (1984) suggested that the basis function must 1) be second order differentiable (i.e., to the highest order of differentiability in the prognostic equations), 2) have spatially uniform resolution, 3) be computationally efficient, and 4) have flexible boundary conditions. Ooyama (1984) compared various basis functions (e.g., harmonic functions, nth-degree polynomials, Legendre orthogonal polynomials, Chebyshev polynomials, linear and cubic splines) against these requirements and chose the finite elements of C_2 continuity.

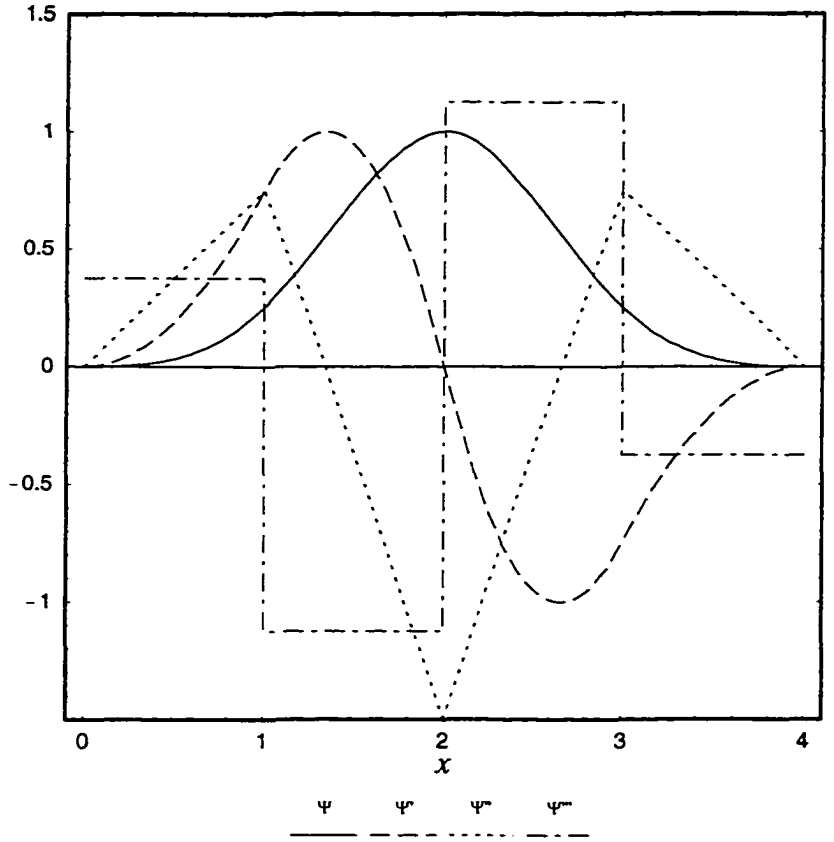

Figure 2.3: The cubic B-spline $\Psi(x)$ and its first three derivatives. Note that the second derivative has been scaled by 1/2 and the third derivative by 1/4.

Specifically, Ooyama (1984) chose the cubic B-spline (DeBoor, 1972; Lyche and Schumaker, 1973) (hereafter referred to as the spline) as the finite element. The spline is defined by

$$\Psi(\xi) \equiv \begin{cases} 0 & \text{if } 2 \le |\xi|, \\ \frac{1}{4}(2-|\xi|)^3 & \text{if } 1 \le |\xi| \le 2, \\ \frac{1}{4}(2-|\xi|)^3 - (1-|\xi|)^3 & \text{if } 0 \le |\xi| \le 1, \end{cases} \tag{2.41}$$

wherein ξ is a nondimensional coordinate. As illustrated in figure 2.3, the spline is symmetric about the origin (2,0) and is composed of four equal-width cubic-polynomial segments. Outside two intervals on either side of the origin, the spline vanishes. While the spline is not analytic, it is continuous through the second derivative and piecewise continuous for the third derivative.

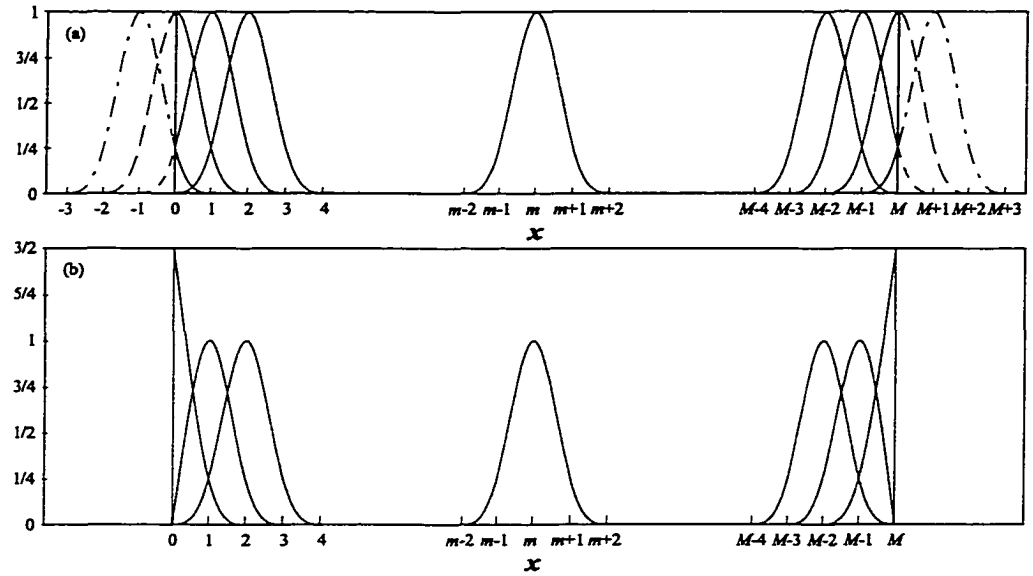

Figure 2.4: Distribution of the a) open bases $\psi_m(x)$ and b) closed bases $\phi_m(x)$ for the boundary condition R1T2 (see appendix D).

We now use the spline as a local basis function. At each node x_m we center a spline, letting $\xi = (x - x_m)/\Delta x$, such that

$$\psi_m(x) = \Psi\left(\frac{x - x_m}{\Delta x}\right), \tag{2.42}$$

wherein $x_m = x_0 + m\Delta x$, $m = -1, 0, \ldots, M+1$, m is the node number within and outside the closed domain $\mathcal{D} = [x_0, x_M]$, $\Delta x = (x_M - x_0)/M$ is the constant nodal spacing, and M is the number of nodal intervals. Using linear combinations of ψ_m, as in (2.29), $\bar{u}$ is then approximated by

$$u(x,t) = \sum_{m=-1}^{M+1} a_m(t)\,\psi_m(x), \tag{2.43}$$

wherein a_m is now the amplitude of the spline centered at x_m. Figure 2.4a illustrates the location of the splines at selected x_m.

Notice that additional splines are located at auxiliary nodes one interval outside the domain at x_{-1} and x_{M+1}. Since these auxiliary splines have nonzero contribution inside the domain, they are necessary to represent $\bar{u}$, as (2.43) demonstrates; however, any representation of $\bar{u}$ outside the domain by these splines is an artifact of the formulation, since $\bar{u}$ is not defined outside $\mathcal{D}$. Ooyama (1984) refers to this as the *open* form of the representation. Using this form, it is impossible to calculate a_m using (2.34), since b_m for $m = -1$ and $M + 1$ is undefined.

A *closed* form is needed to eliminate the auxiliary splines. Given appropriate lateral boundary conditions on u, we *fold*, or incorporate, the auxiliary splines into the definition of the overlapping splines located within the domain (see appendix D for details). An example of the folded splines, symbolized by $\phi_m(x)$, is shown in figure 2.4b. Using ϕ_m as the basis function, the transform pair for the SAFER method is now given by (2.29) and (2.34) in one dimension, or (2.38) and (2.39) in two dimensions.

2.2.1.3 Nesting using the SAFER Method

One of the principle advantages of the SAFER method is its simple yet extremely accurate two-way nesting capability. Ideally, we want the interface between grids to be transparent. The SAFER method accomplishes this through the flexibility of its boundary conditions and the filtering capability of the derivative constraint. For a more detailed discussion of this topic, see the papers by DeMaria et al. (1992) and Ooyama (1997).

Coarse-to-Fine: For coarse-to-fine grid communication, we simply assume that the physical space solution and its first two derivatives are continuous across the interface. Consider, for example, the left interface (denoted by subscript L) of the nest configuration illustrated in figure 2.5. The physical space solution is represented on the two grids by (2.43) with spectral amplitudes a and A for the fine and coarse grids, respectively. Assuming that the function and its first two derivatives are equal at the interface, we obtain the boundary amplitudes on the fine grid by solving a simple 3×3 matrix:

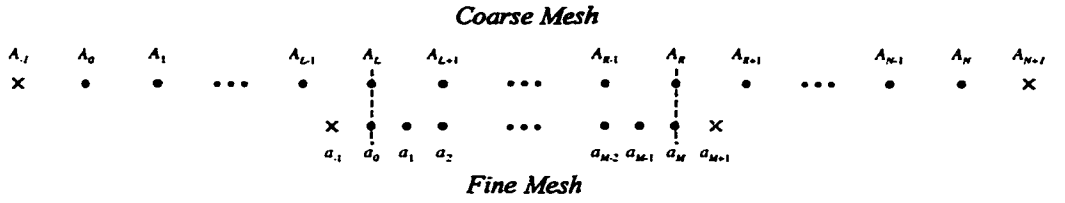

Figure 2.5: Nesting schema of two grids, a fine grid (a's) with M nodes and a coarse grid (A's) with N nodes, for which the nodal spacing differs by a factor of 2. Both interfaces are identified by the vertical dashed line. Subscripts L and R distinguish the left and right interfaces, respectively. The large filled circles denote the primary nodes and the ×'s the auxiliary nodes. The small filled circles denote gaps in the depiction of the grids [adapted from DeMaria et al. (1992)].

$$\begin{bmatrix} a_{-1} \\ a_0 \\ a_1 \end{bmatrix} = \begin{bmatrix} \frac{1}{2} & \frac{1}{2} & 0 \\ \frac{1}{8} & \frac{3}{4} & \frac{1}{8} \\ 0 & \frac{1}{2} & \frac{1}{2} \end{bmatrix} \begin{bmatrix} A_{L+1} \\ A_L \\ A_{L-1} \end{bmatrix}. \tag{2.44}$$

A similar expression is then solved for the right interface, with the remaining amplitudes on the fine grid calculated using the least-squares transform. See appendix D for a detailed derivation of this expression.

Fine-to-Coarse: Fine-to-coarse grid communication is more complicated, since the smallest resolved waves on the fine grid are unrepresentable on the coarse grid. Intuitively, one might consider simply projecting the solution from the fine grid onto the coarse grid; however, the spectral truncation of the unresolvable components of the fine grid solution results in undesirable Gibbs oscillations. Instead, we project only that portion of the solution needed for waves near the interface to propagate from the fine to the coarse grid. In practice, the coarse grid need only extend one coarse-grid nodal interval into the fine grid. Any unresolvable waves are filtered in the region of grid overlap using the derivative constraint. By increasing the cutoff wavelength of the derivative constraint from 2 to 4, we filter longer, non-transmissible waves, thus preventing them from reaching the interface.

2.2.1.4 Numerical Application of the SAFER Method

The first step in the transformation to spectral space involves the solution of (2.35), (2.36), and (2.37). We solve the inner product in each using Gaussian quadrature to approximate

the integrals. Experience has shown reasonable convergence with as few as two quadrature points per nodal interval. Clearly, the computation of $\mathbf{P}$ and $\mathbf{Q}^{(j)}$ is greater than that of $\mathbf{b}$ since the integral in (2.36) and (2.37) is solved for each m and m', while the integral in (2.35) is solved for each m only; however, if the grids are not changing with time, this cost is incurred only once at the start of the simulation.

In the next step of the transformation to spectral space, we solve (2.34). Note that, due to the local definition of the spline, both $\mathbf{P}$ and $\mathbf{Q}^j$ are banded matrices with three non-zero elements on either side of the diagonal. Thus, both are 7-banded symmetric matrices. We could solve the transformation for $\mathbf{a}$ by inverting $\left(\mathbf{P}+\mathbf{Q}^{(j)}\right)$ as shown in (2.34); however, by inverting this matrix, we would convert a sparse matrix to a full matrix. Taking advantage of the sparseness of the matrices, we instead solve the linear system of equations using Gaussian elimination. While the inversion would require $O\left(M^2\right)$ calculations, the elimination requires only $O\left(M\right)$.

In the reverse transformation to physical space, we solve (2.29). Again, due to the local definition of the spline, the solution of this transformation requires the sum of three to four overlapping basis functions. Compare this with a harmonic method, which requires the sum of all M basis functions.

2.2.1.5 Advantages and Disadvantages of the SAFER Method

Since the SAFER method is not widely used, it is essential that we discuss its advantages and disadvantages compared with more commonly used methods. We begin by discussing the representation and dispersion errors associated with the spline approximation. These errors are compared to the second-order, centered, finite-difference method to show the improved dispersion and nesting characteristics of the SAFER method. Finally, we address the criticism that such a method is computationally more expensive than other approaches.

Representation Errors: Generally, any finite representation of an arbitrary function, $\bar{u}\left(x\right)$, whether by grid-point or spectral methods, will be inexact due to representational errors.

In other words, the finite representation only approximates $\bar{u}(x)$. For example, consider a single harmonic mode,

$$\bar{u}(x) = \exp\left(i\frac{2\pi x}{l\Delta x}\right), \tag{2.45}$$

wherein $l\Delta x$ is the wavelength. Of course, a harmonic spectral method that includes this wavelength represents the function exactly. In contrast, grid-point methods represent the function approximately by

$$u(j\Delta x) = \exp\left(i\frac{2\pi j}{l}\right), \tag{2.46}$$

wherein Δx is now the grid spacing and j is the grid point. If l is large, the representation error will be small, because the wave is represented by many grid points. However, if $l = 2$, the representational error is a maximum. In this case, the sine wave is not represented at all, and the cosine wave is represented its extreme values only.

Similar representation errors occur with the SAFER method. If we again input a single harmonic mode of the form (2.45), transforming to and from $\mathcal{S}^J$ with no derivative constraint, we find that the output solution has the form

$$u(x) = r_o(l)\exp\left(i\frac{2\pi x}{l\Delta x}\right) + r_p(l')\exp\left(-i\frac{2\pi x}{l'\Delta x}\right), \tag{2.47}$$

wherein $r_o(l)$ is the reduced amplitude of the input wave and $r_p(l')$ is the amplitude of the representational error, which has wavelength $l'\Delta x$. From figure 2.6, we see that $l' = l/(l-1)$ or, more simply, $k' = 1 - k$, wherein k and k' are the wavenumbers of the input wave and representational error, respectively. Ooyama (personal notes) terms the representational error the "parasite" wave. As an example, figure 2.7 illustrates the spline

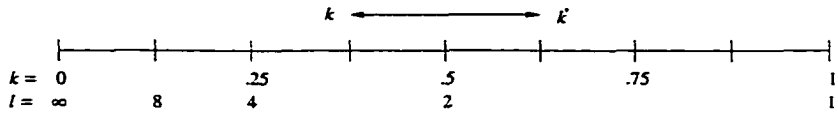

$$0 < k < \frac{1}{2} \quad \text{and} \quad k' = 1 - k$$
$$l = \frac{1}{k} \quad \text{and} \quad l' = \frac{1}{k'}$$

Figure 2.6: Graphical representation of the relationship between the wavenumbers k and k', or wavelengths l and l'. Notice that a wave with wavelength l is always resolved, whereas a wave with wavelength l' is never resolved. Both k and l are defined in units of Δx (adapted from Ooyama's personal notes).

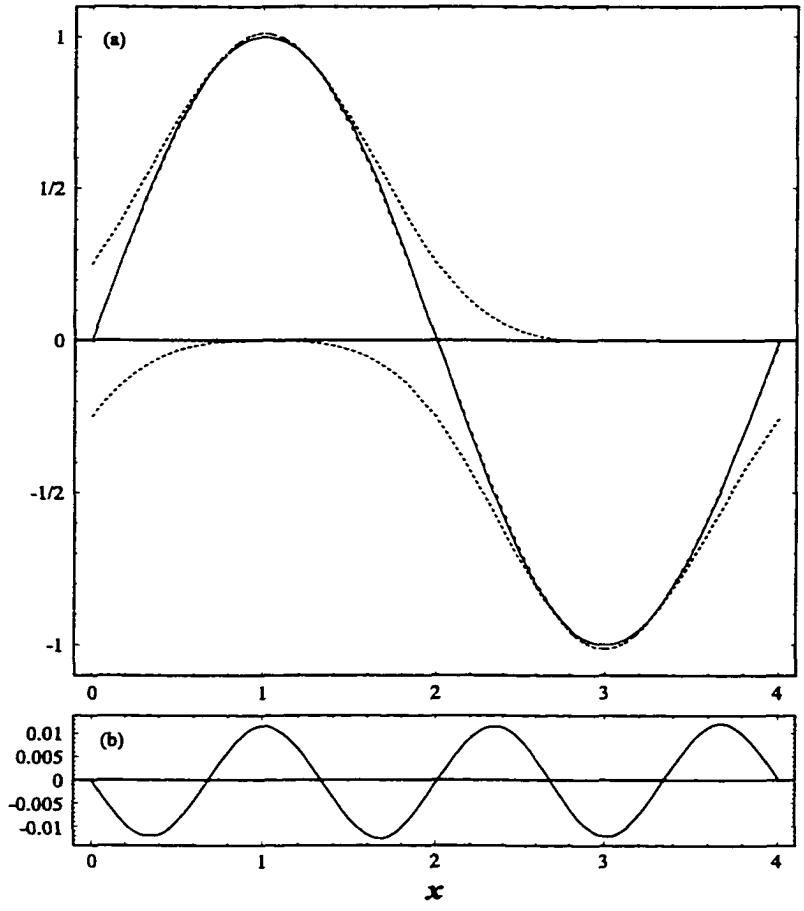

Figure 2.7: Plots of an a) input $4\Delta x$ sine wave (solid) and its spline representation (large dash), and b) the representational error or "parasite" wave. Included in a) are the individual splines (small dashed) used to obtain the spline representation (redrafted from Ooyama's personal notes).

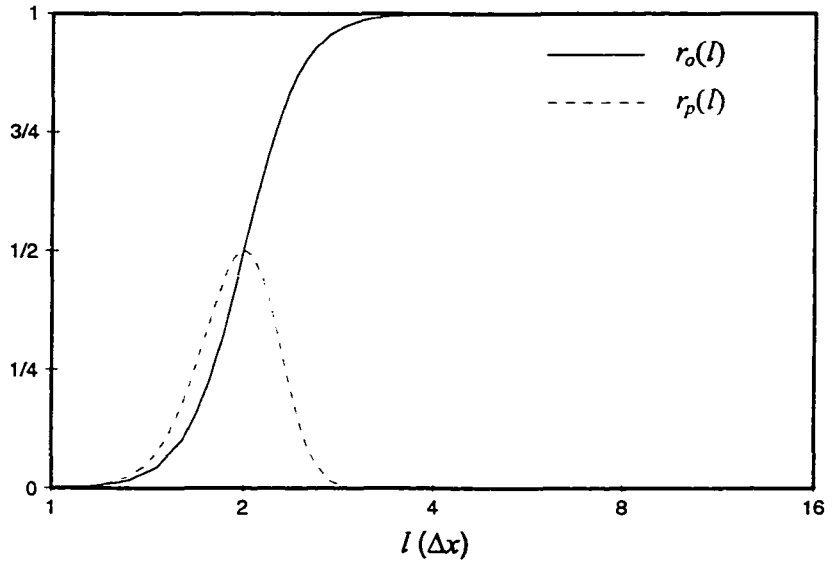

Figure 2.8: Reduced input, $r_o(l)$, and error, $r_p(l')$, amplitudes (curves fit to data in Ooyama's personal notes).

solution (dashed) for an input wave (solid) with $l = 4$. The resulting parasite wave with $l' = 4/3$ is also shown.

By performing the same analysis for all wavelengths, we obtain the amplitudes r_o and r_p for all l, as shown in figure 2.8. Similar to the grid-point method, we see that the representation error is small (i.e., $r_o \to 1$ and $r_p \to 0$) for large l; however, when $l = 2$, the representation error is a maximum (i.e., $r_o = r_p = 1/2$). Again, the sine wave is not represented at all, and the cosine wave is represented by its extreme values only.

Notice that for all input wavelengths, the parasite wave is not resolvable, as shown in figure 2.6; as a result, it is aliased onto the resolved waves. To prevent aliasing, the parasite wave must be filtered. Recall that the derivative constraint acts as a low-pass filter; thus, we may use it to filter the parasite wave. Including the derivative constraint in the transformation, the output solution now has the form

$$u(x) = r_\alpha(l)\, r_o(l) \exp\left(i\frac{2\pi x}{l\Delta x}\right) + r_\alpha(l')\, r_p(l') \exp\left(-i\frac{2\pi x}{l'\Delta x}\right), \tag{2.48}$$

wherein r_α is the response function of the derivative constraint, which is derived in appendix F. As illustrated in figure 2.9, for a given wavelength (l), the derivative constraint

(i.e., $j > 0$ and $l_c > 0$) damps the amplitude of the parasite wave (r_p), though not without cost, since it also damps the amplitude of the input wave (r_o). For the best results, we choose $j = 3$ and $l_c = 2$.

Dispersion Errors: Computational dispersion of advected waves has long been recognized as a significant source of error in any numerical model that approximates spatial derivatives using finite-differences (Browning et al., 1973). Less recognized are the dispersion errors associated with spatial derivatives approximated using the SAFER method. To better understand these errors, we compare the dispersion characteristics of the SAFER method with those of the more commonly used second-order, centered, finite-difference method as applied to the one-dimensional, linear advection equation

$$\frac{\partial u}{\partial t} + c_s \frac{\partial u}{\partial x} = 0, \tag{2.49}$$

with constant advective phase speed, c_s. The exact solution to this expression is given by (2.45) with dispersion relation $c = c_s$. In appendix E, we further derive the dispersion equations for the finite-difference and SAFER approximations to (2.49), with equations (2.46) and (2.47) as the respective input solutions.

This comparison reveals that use of the SAFER method significantly reduces the computational dispersion. To show this, the dispersion equations, (E.6) and (E.10), are compared figure 2.10 for the SAFER and finite-difference methods, respectively. For a Courant number $\mu = c_s \Delta t / \Delta x = 0.4$ and wavelengths $l = 4, 8,$ and 16, the computational phase speeds, c, of the finite-difference approximation are 0.65, 0.91, and 0.98, respectively, of the true phase speed, c_s. Thus, waves with $l < 8$ have dispersion errors of 10% or greater. Contrast this with the SAFER method, which does not attain similar errors until $l < 4$. In theory, the dispersion errors of the finite-difference approximation could be reduced by using higher-order methods; however, in practice, these methods are avoided due to their mathematical complexity and computational cost.

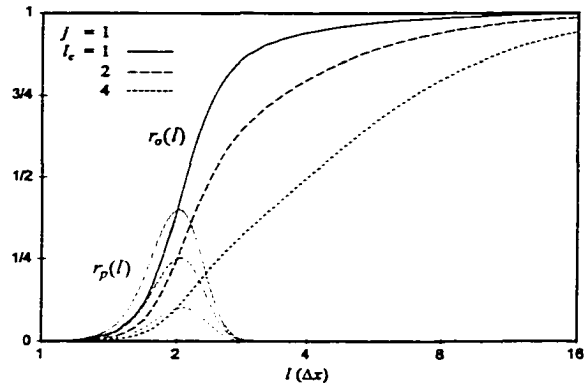

(a)

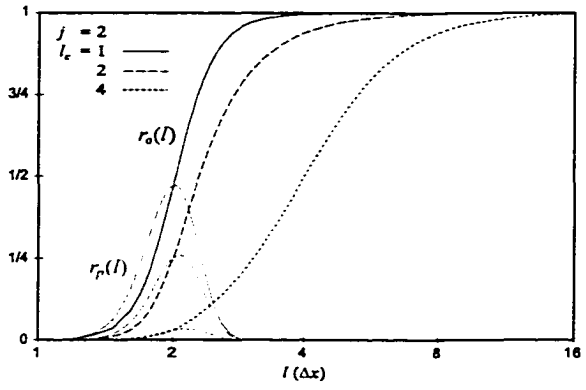

(b)

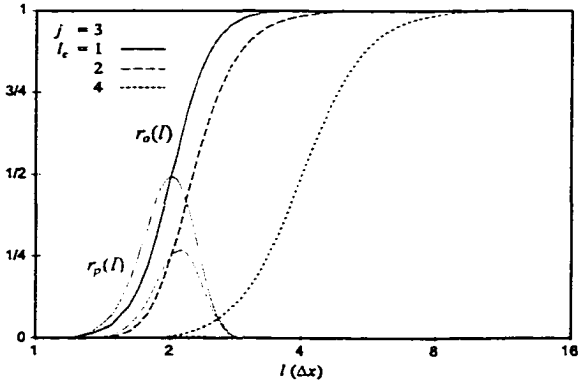

(c)

Figure 2.9: Filtering effect of the derivative constraint on the input wave amplitude, $r_o(l)$, and parasite wave amplitude, $r_p(l')$, for $l_c = 1, 2, 4$ and a) $j = 1$, b) $j = 2$, and c) $j = 3$.

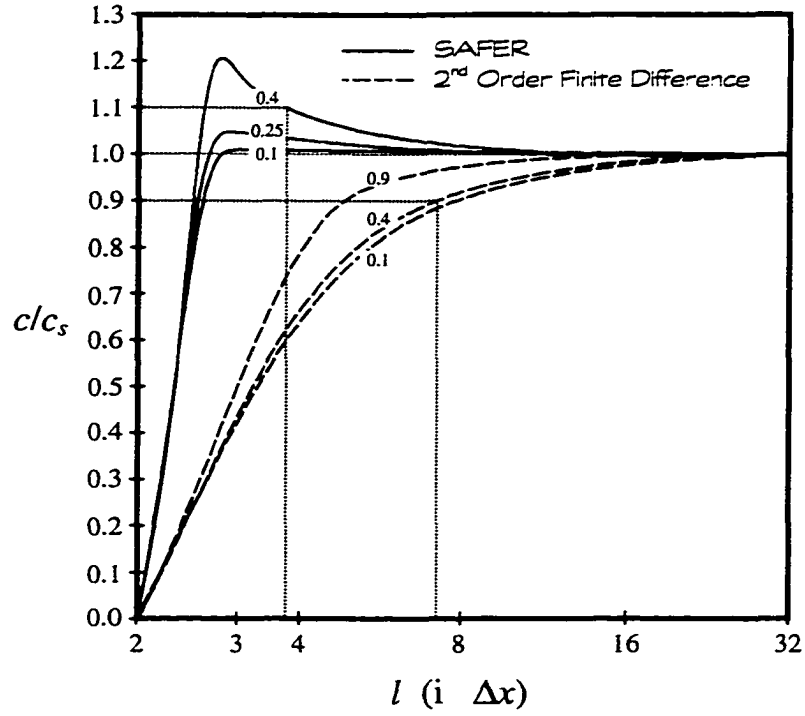

Figure 2.10: Normalized phase speed, c/c_s, as a function of wavelength, l (in units of Δx), for the SAFER (solid) and second-order, centered finite-difference (dashed) methods applied to the one-dimensional advection equation, with constant phase speed, c_s. The numbers along each curve represent the Courant number, $\mu = c_s \Delta t / \Delta x$. Finally, the dotted lines identify the wavelengths with 10% dispersion errors (redrafted from Ooyama's personal notes).

Improved Nesting: The decreased dispersion errors of the SAFER method also improve its nesting capabilities relative to the second-order, centered, finite-difference method. Ideally, an $8\Delta x_f$ ($l_f = 8$) wave on a fine grid with grid spacing Δx_f should become a $4\Delta x_c$ ($l_c = 4$) wave as it propagates into a coarse grid with grid spacing $\Delta x_c = 2\Delta x_f$; however, in reality, this may not occur due to dispersion errors. As the $8\Delta x_f$ wave crosses the interface, its phase speed decreases, i.e.,

$$c_c(l_c) < c_f(l_f). \tag{2.50}$$

Keep in mind that the frequency of a wave, $\omega = c/l\Delta x$, is set by the forcing and should be identical in both grids, i.e.,

$$\frac{c_c(l_c)}{l_c} = \frac{c_f(l_f)}{l_f}. \tag{2.51}$$

From (2.50) and (2.51), we find that the wavelength must also decrease as the wave crosses the interface. As a result, the wave is actually unresolvable (i.e., $l_c < 2$) and non-transmissible; thus, it reflects back into the fine grid.

This problem is much worse for the second-order, centered, finite-difference method than for the SAFER method. Figures 2.11a and b compare the dispersion equations, (E.7) and (E.12), expressed in terms of frequency, ω, for the SAFER and finite-difference methods, respectively. Also shown in each figure is the exact solution of (2.49), which has no dispersion (i.e., $\omega = c_s/l$ with $c_s = 1$). According to figure 2.11, using centered, finite-differences, waves smaller than $11.6\Delta x$ on the fine grid are not transmitted to the coarse grid. Using the SAFER method, in contrast, waves as small as $4.8\Delta x$ are transmitted.

Computational Efficiency: To be useful, any numerical technique must not only be accurate, but computationally efficient. Ooyama (1984) sacrificed orthogonality of basis functions for flexibility in choosing boundary conditions. Although this complicates the

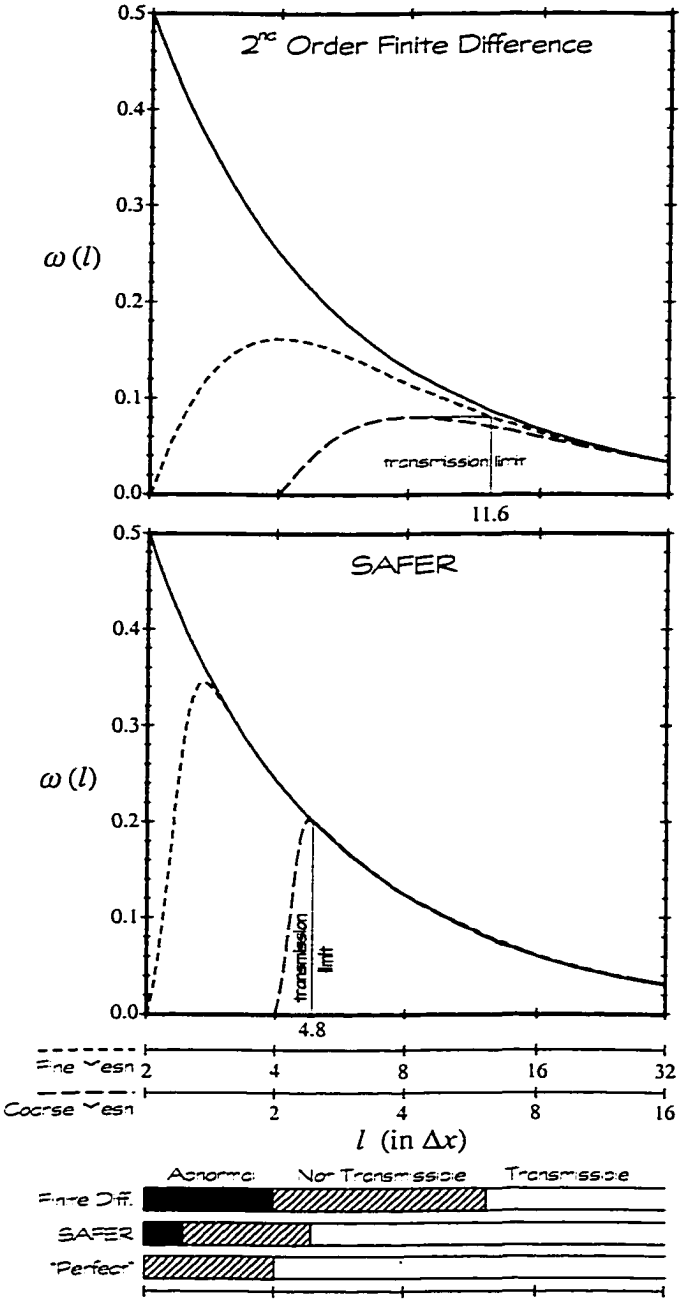

Figure 2.11: Frequency, ω, as a function of wavelength, l (in units of Δx), for the second-order, centered finite-difference (top) and SAFER (bottom) methods applied to the one-dimensional, linear advection equation, with constant phase speed, $c_s = 1$. The solid curve in each represents the exact or "perfect" solution, $\omega = c_s/l$, while the other curves represent the approximate solution on the fine (Δx_f, dashed) and coarse ($\Delta x_c = 2\Delta x_f$, dotted) grids (redrafted from Ooyama's personal notes).

transform from physical to spectral space by adding an additional step, the computational cost is mitigated by the local definition of the spline. According to Ooyama (1984), the calculation of (2.34) is relatively inexpensive in comparison to the calculation of (2.35) and (2.29), both of which are unavoidable in any spectral method, whether orthogonal or not. Furthermore, since the calculations of (2.35) and (2.29) require the sum over a limited domain in both physical and spectral space, respectively, we could argue that the transforms of the SAFER method are more efficient than a harmonic method, which requires the sum over the entire domain in both physical and spectral space. Finally, Ooyama (1984) stresses that a numerical technique should not only be judged by the computational cost per degree of freedom but also by the quality of information per degree of freedom. As demonstrated previously, the SAFER method produces a higher quality of information by decreasing the dispersion errors.

2.2.2 Temporal Discretization: Leapfrog and Semi-Implicit Methods

With the spatial discretization scheme defined, we next choose a temporal discretization scheme and apply it to (2.27). However, we do not discretize this equation directly; instead, we partially transform it by using (2.35) to obtain

$$\frac{\partial b_m}{\partial t} = \left(F\left(u, u_x, u_{xx}, ...\right), \phi_m\left(x\right)\right). \tag{2.52}$$

The time derivative is then approximated using a second-order centered or leapfrog time difference, i.e.,

$$b_m^{n+1} = b_m^{n-1} + 2\Delta t \left(F^n\left(u, u_x, u_{xx}, ...\right), \phi_m\left(x\right)\right), \tag{2.53}$$

wherein Δt is the time step and n is the number of time steps. In this case, a forward step must be used for the first time step. Using $\mathbf{b}^{n+1} = \{b_m^{n+1},\ m = 0, 1, \ldots, M\}$ obtained

from (2.53), the physical to spectral space transform is then completed by solving (2.34) for $\mathbf{a}^{n+1}$. Finally, the future state of the atmosphere is found by solving (2.29). See the paper by DeMaria et al. (1992) for a detailed discussion of the solution of (2.52) using the nested grids.

The time step used to solve (2.53) must be small enough to satisfy the numerical constraints on computational stability. The Courant-Freidrichs-Levy (CFL) condition for computational stability requires that

$$\frac{c\Delta t}{\Delta x}, \frac{c\Delta t}{\Delta z} \leq \frac{1}{\pi}, \tag{2.54}$$

wherein c is the phase speed of the fastest propagating wave contained in the model physics. For a compressible atmosphere, c is the speed of sound, $c_s = 331.4$ m s^{-1} at 0°C. Notice that this is a more restrictive constraint than the customary CFL condition of unity. The inverse π results from the spectral, rather than finite difference, approximation to the spatial derivatives. Using (2.54), we find that, for a grid spacing of 500 m, the time step must be 0.5 s or less. Given our current computational capabilities, this is unacceptably small.

There are essentially three ways to eliminate this problem: 1) we can filter the sound waves, either numerically or physically, by altering the predictive equations (e.g., the anelastic equations); 2) we can separate the sound wave dynamics and solve them explicitly using a smaller time step, as in the time-splitting method (Skamarock and Klemp, 1992); or 3) we can slow the sound waves down such that they become stable for longer time steps, as in the semi-implicit method (Robert, 1969). Of these three methods, the third is the most appealing. The first choice is unacceptable because it would involve unnecessary approximations to the physics. The second choice, while acceptable, is not as easily applied to the SAFER method as the third choice. Using the semi-implicit method, we gain a five-fold increase in the time step on the finest grid (i.e., $\Delta t = 2.5$ s). For more details on this approach, see Ooyama (1997, 2001).

Finally, an Asselin (1972) filter is applied during the centered time steps. According to Ooyama (2001), this filter is not used to damp the computational mode of the leapfrog scheme, but rather to control an instability in the moisture field. In this instability, which occurs in regions where the atmosphere is marginally saturated, water may condense at one time step and immediately evaporate at the next. Occasionally, the amplitude of this oscillation grows due to a dynamic feedback. Applying the Asselin filter with a coefficient of 0.3 eliminates this instability.

2.3 Pragmatics: Accommodation of Physics to Numerics

As the physics are merged with the numerics, we must make several changes to the model predictive equations, (2.2)–(2.6), in order to maintain the integrity of the physics and to maximize the model accuracy. In summary, the modified predictive equations in cylindrical coordinates are given by

$$\frac{\partial \xi'}{\partial t} = -u\frac{\partial \xi'}{\partial r} - w\frac{\partial \xi}{\partial z} - \left(\frac{\partial u}{\partial r} + \frac{\partial w}{\partial z} + \frac{u}{r}\right), \tag{2.55}$$

$$\begin{aligned}\frac{\partial \nu'}{\partial t} &= -u\frac{\partial \nu'}{\partial r} - w\frac{\partial \nu}{\partial z} - \frac{\partial}{\partial z}\left[\left(\frac{\mu-\nu}{\mu}\right)\mu_r W\right] \\ &\quad -\frac{1}{\mu}\left[1-\left(\frac{\nu}{\mu-\nu}\right)\right]\mu_r W\frac{\partial \nu}{\partial z} - \left(\frac{\mu-\nu}{\mu}\right)\mu_r W\frac{\partial \xi}{\partial z} \\ &\quad -F_\mu\left(\frac{\mu-\nu}{\mu}\right)\left(\frac{d\phi_a}{dz} + \phi_a\frac{\partial \xi}{\partial z}\right),\end{aligned} \tag{2.56}$$

$$\begin{aligned}\frac{\partial \nu_r}{\partial t} &= -u\frac{\partial \nu_r}{\partial r} - w\frac{\partial \nu_r}{\partial z} - \frac{\partial}{\partial z}\left[\left(\frac{\mu_r-\nu_r}{\mu_r}\right)\mu_r W\right] \\ &\quad -\mu_r W\left\{\frac{1}{\mu_r}\left[1-\left(\frac{\nu_r}{\mu_r-\nu_r}\right)\right]\frac{\partial \nu_r}{\partial z} + \left(\frac{\mu_r-\nu_r}{\mu_r}\right)\frac{\partial \xi}{\partial z}\right\} \\ &\quad +\left(\frac{\mu_r-\nu_r}{\mu_r}\right)\frac{Q_r}{\rho_a},\end{aligned} \tag{2.57}$$

$$\frac{\partial u}{\partial t} = -u\frac{\partial u}{\partial r} - \left(w + \frac{\mu_r}{1+\mu}W\right)\frac{\partial u}{\partial z} + \left(f + \frac{v}{r}\right)v - \frac{1}{1+\mu}\left(\frac{\partial \pi'}{\partial r} + \pi\frac{\partial \xi'}{\partial r}\right) - \frac{F_u}{1+\mu}\left(\frac{d\phi_a}{dz} + \phi_a\frac{\partial \xi}{\partial z}\right) + \alpha_s\phi_s u, \tag{2.58}$$

$$\frac{\partial v}{\partial t} = -u\frac{\partial v}{\partial r} - \left(w + \frac{\mu_r}{1+\mu}W\right)\frac{\partial v}{\partial z} - \left(f + \frac{v}{r}\right)u - \frac{F_v}{1+\mu}\left(\frac{d\phi_a}{dz} + \phi_a\frac{\partial \xi}{\partial z}\right) + \alpha_s\phi_s v, \tag{2.59}$$

$$\frac{\partial w}{\partial t} = -u\frac{\partial w}{\partial r} - \left(w + \frac{\mu_r}{1+\mu}W\right)\frac{\partial w}{\partial z} - \frac{1}{1+\mu}\left(\frac{\partial \pi'}{\partial z} + \pi'\frac{\partial \xi}{\partial z} + \bar{\pi}\frac{\partial \xi'}{\partial z} + g\mu'\right) + \alpha_s\phi_s w, \tag{2.60}$$

$$\frac{\partial s'}{\partial t} = -u\frac{\partial s'}{\partial r} - w\frac{\partial s}{\partial z} - \frac{\partial}{\partial z}\left(\mu_r s_r W\right) - \mu_r s_r W\frac{\partial \xi}{\partial z} + \frac{Q_\sigma}{\rho_a} - F_s\left(\frac{d\phi_a}{dz} + \phi_a\frac{\partial \xi}{\partial z}\right) + \alpha_s\phi_s s'. \tag{2.61}$$

We explain the modifications in detail below.

Axisymmetry: Most importantly, we reduce the model equations to their two-dimensional, axisymmetric form. Of course, we would prefer to solve the three-dimensional equations; however, the current SAFER numerics have only been developed for two-dimensions. As a result of this limitation, we first test the two-dimensional model by investigating the axisymmetric dynamics of tropical cyclones. In the future, when the three-dimensional SAFER numerics are complete, we will use the results of these investigations as a basis for comparison.

Derivatives of Transformed Variables: In addition, we write the equations from flux to advective form. For our numerical discretization, we chose a spectral technique to more accurately compute derivatives. These derivatives are calculated by differentiating (2.43). Since we only have spectral amplitudes for the predictive variables, we rewrite the equations in advective form. For the derivatives of pressure, we perform a separate spectral transform

to compute the necessary spectral amplitudes. For the remaining derivatives in (2.55)–(2.61), which do not involve predictive variables, we solve (2.35) by parts with a prescribed lower boundary condition.

Normalization and Perturbations: Most noticeably, we redefine our predictive variables to increase the numerical accuracy of the model. First, we normalize the mass and entropy variables by the dry air mass to obtain the normalized dry air mass [$\xi = \ln(\rho_a/\rho_{a_0})$], airborne water mixing ratio ($\mu_m = \rho_m/\rho_a$), precipitation mixing ratio ($\mu_r = \rho_r/\rho_a$), total water mixing ratio ($\mu = \rho_w/\rho_a$), and dry air specific total entropy ($s = \sigma/\rho_a$), with ρ_{a_0} being the reference value of the dry air density. We also normalize the pressure to obtain $\pi = p/\rho_a$. Second, we take the deviation of these normalized variables from a horizontally homogeneous, resting basic state (denoted by a caret), i.e., $\xi' = \ln(\rho_a/\rho_{a_0}) - \ln(\hat{\rho}_a(z)/\rho_{a_0}) = \xi - \hat{\xi}(z)$, $\mu_r' = \mu_r$, $\mu' = \mu - \hat{\mu}_m(z)$, and $s' = s - \hat{s}(z)$. Notice that there is no basic state for the precipitation mixing ratio. We further require that the basic state be hydrostatically balanced (i.e., $g\hat{\rho} + d\hat{p}/dz = 0$, wherein $\hat{\rho}(z) = \hat{\rho}_a + \hat{\rho}_m$ and $\hat{p}(z)$ are the basic state total mass density and total pressure, respectively). Finally, using equation (2.26), the surface fluxes for the modified variables are given by

$$F_u = -C_D U u, \tag{2.62}$$

$$F_v = -C_D U v, \tag{2.63}$$

$$F_\mu = -C_H U \left(\mu_{v_a} - \mu_{v_0}^*\right), \tag{2.64}$$

$$F_s = -C_H U \left[c_p \left(\frac{\theta_{m_a} - \theta_{m_0}}{\theta_{m_0}}\right) + s_{v_0}\left(\mu_{v_a} - \mu_{v_0}^*\right)\right], \tag{2.65}$$

wherein C_D and C_H are the drag and entropy/mass exchange coefficients, respectively; μ_v^* is the saturation water vapor mixing ratio; $\theta_m = T(p_0/p)^\kappa$ is the moist potential temperature; $\kappa = R/c_p$; c_p and R are the mass-weighted specific heat at constant pressure and gas constant, respectively; and s_v is the water vapor entropy.

Mass Conservation: Notice that we also have replaced the mass continuity equation for μ_m, (2.3), with the mass continuity equation for μ, (2.56). While we can write mass

conservation equations for ρ_a, ρ_m, ρ_r, ρ_w, and ρ, any three of these equations could be used to predict the entire mass distribution, keeping in mind that ρ_v and ρ_c are diagnosed. In practical application, however, we have found that the mass continuity equation for μ provides more realistic results.

Mixing Ratio Transform: An inevitable problem with any spectral model is the appearance of negative values associated with positive definite quantities. The truncation of critical spectral components produces Gibbs oscillations in the physical representation. For example, a limited set of basis functions is unable to represent the sharp gradient in liquid water at the edge of a cloud. As a result, Gibbs oscillations in the cloud water mixing ratio lead to negative values just outside the cloud edge.

There are four common approaches to partially correct this problem. First, we could redistribute water mass from adjacent regions; however, this is extremely arbitrary. Second, we could use a sign-preserving, finite-difference advection scheme (Smolarkiewicz, 1991), but this would require two different spatial-discretization schemes in one model, which is technically undesirable. Third, we could use the upstream difference scheme, which prevents the generation of negative values; however, this scheme is highly dispersive (Haltiner and Williams, 1980). Last, we could transform the water variable to a positive definite form. The last option is the best for our purposes, since it focuses directly on the problem without altering any other part of the numerics.

The transform proposed by Ooyama (2001) uses one branch of a hyperbola to transform μ to ν, the hyper-transformed mixing ratio. Specifically, the biased hyperbolic transform pair is given by

$$\nu = 0.5\left[(\mu+\mu_0) - \frac{\mu_0^2}{(\mu+\mu_0)}\right], \tag{2.66}$$

$$\mu = \begin{cases} (\nu^2+\mu_0^2)^{\frac{1}{2}} + \nu - \mu_0, & \text{if} \quad \nu \geq 0, \\ 0, & \text{if} \quad \nu \leq 0, \end{cases} \tag{2.67}$$

wherein μ_0 is a constant bias of 10^{-17}. The primary advantage of this approach is that the transform only alters the smallest values of μ (i.e., $\mu \sim \mu_0$), which are relatively insignificant. For large values of μ (i.e., $\mu \gg \mu_0$), the transform is nearly linear such that $\nu \sim 0.5\mu$. Thus, the transform ensures that μ is either zero or positive for extremely small values and essentially unaltered for larger values. Note that the additional terms appearing in (2.56) and (2.57) result from the transformation of the derivatives of μ and μ_r. Details of this transformation are explained by Ooyama (2001).

Homogeneous Lower Boundary Conditions: Since the SAFER numerics do not currently allow for inhomogeneous lateral boundary conditions, we must alter the vertical momentum equation to account for nonzero $\bar{w}$ at the surface. To prevent the accumulation of liquid water along the lower boundary, we must allow $W \neq 0$ at the surface so that precipitation passes through the lower boundary. According to (2.1), this indicates that $\bar{w} \neq 0$ at the surface. The easiest solution is simply to neglect the W contribution to $\bar{w}$, leaving w as the predictive variable. This is a reasonable approximation. If $\rho_r/\rho \approx 0.001$ and $W \sim w$, then from the definition of $\bar{w}$ we see that the term involving W is three orders of magnitude smaller than w. To be more physically consistent, however, we assume that the precipitation gradually accelerates such that $D_r W/Dt \approx 0$, which produces the same result (Ooyama, 2001). See appendix B for details. This approximation is reasonable except near the melting level, where slowly falling snow and graupel particles rapidly accelerate after melting.

Homogeneous Upper Boundary Condition: Similarly, the homogeneous boundary condition at the top boundary requires that w vanish (i.e., a rigid lid). To minimize the adverse effects of vertically propagating gravity waves that reflect off this lid, we add a *sponge* layer, or Rayleigh damping layer, of the form

$$D_\chi = \alpha_s \phi_s(z)\,(\chi - \bar{\chi}), \tag{2.68}$$

for $\chi = u, v, w,$ or s, wherein

$$\phi_s(z) = \begin{cases} \frac{z-z_s}{z_t-z_s}, & \text{if } z_s \leq z \leq z_t, \\ 0, & \text{if } z \leq z_s, \end{cases} \tag{2.69}$$

is a vertical structure function. The depth of the damping layer extends from z_s to the model top, z_t, and its strength is set by the coefficient α_s.

Chapter 3

MOIST POTENTIAL VORTICITY DERIVATION

> Every novel idea in science passes through three stages. First people say it isn't true. Then they say it's true, but not important. And finally they say it's true and important, but not new.
>
> Anonymous

In the previous chapter, we developed a mathematical model describing the evolution of a moist precipitating atmosphere, which included conservation equations for the mass, momentum, and entropy. Using these equations, we now derive the model's potential vorticity (PV) conservation equation. We begin this derivation by generalizing Ertel's (1942a) PV equation to a moist, precipitating atmosphere (section 3.1). As in Ertel's original formulation, our PV equation involves an arbitrary scalar field ψ. Next, we show that the generalized moist PV has an invertibility principle and satisfies the impermeability theorem. With the complete PV principle developed, we then choose a specific expression for ψ (section 3.2). Lastly, we present the PV equation in its axisymmetric form, including the approximation of section 2.3 (section 3.3).

3.1 Generalized Potential Vorticity Principle

3.1.1 Moist Potential Vorticity

Combining basic vector identities with the conservation equations for the total mass and momentum, we derive the generalized moist PV equation in terms of the arbitrary scalar

field ψ as follows. Taking the difference of the vector identities $\nabla \cdot [\nabla\psi \times (\partial\mathbf{u}/\partial t)] = (\partial\mathbf{u}/\partial t)\cdot(\nabla \times \nabla\psi) - \nabla\psi\cdot[\nabla \times (\partial\mathbf{u}/\partial t)]$ and $\nabla\cdot[(\partial\psi/\partial t)\,\boldsymbol{\zeta}] = \boldsymbol{\zeta}\cdot\nabla\,(\partial\psi/\partial t) + (\partial\psi/\partial t)\,\nabla\cdot\boldsymbol{\zeta}$, for which $\boldsymbol{\zeta} = 2\boldsymbol{\Omega} + \nabla \times \mathbf{u}$ is the absolute vorticity, and recognizing that $\nabla \times \nabla\psi \equiv 0$ and $\nabla \cdot \boldsymbol{\zeta} \equiv 0$, we obtain

$$\frac{\partial}{\partial t}(\boldsymbol{\zeta} \cdot \nabla\psi) + \nabla \cdot \left(\nabla\psi \times \frac{\partial \mathbf{u}}{\partial t} - \boldsymbol{\zeta}\frac{\partial \psi}{\partial t}\right) = 0. \tag{3.1}$$

Defining $\dot{\psi} \equiv D\psi/Dt$, where $D/Dt = \partial/\partial t + \mathbf{u} \cdot \nabla$ is the material derivative following $\mathbf{u}$, and using the vector identity $\boldsymbol{\zeta}\,(\mathbf{u} \cdot \nabla\psi) \equiv \mathbf{u}\,(\boldsymbol{\zeta} \cdot \nabla\psi) + \nabla\psi \times (\boldsymbol{\zeta} \times \mathbf{u})$, we rewrite (3.1) as

$$\frac{\partial}{\partial t}(\boldsymbol{\zeta} \cdot \nabla\psi) + \nabla \cdot \left[\mathbf{u}\,(\boldsymbol{\zeta} \cdot \nabla\psi) + \nabla\psi \times \left(\frac{\partial \mathbf{u}}{\partial t} + \boldsymbol{\zeta} \times \mathbf{u}\right)\right] = \boldsymbol{\zeta} \cdot \nabla\dot{\psi}, \tag{3.2}$$

which, after substituting the vector identity $\nabla\cdot[\mathbf{u}\,(\boldsymbol{\zeta} \cdot \nabla\psi)] = \mathbf{u}\cdot\nabla\,(\boldsymbol{\zeta} \cdot \nabla\psi) + (\boldsymbol{\zeta} \cdot \nabla\psi)\,\nabla\cdot\mathbf{u}$, expands to

$$\frac{D}{Dt}(\boldsymbol{\zeta} \cdot \nabla\psi) + (\boldsymbol{\zeta} \cdot \nabla\psi)\,\nabla \cdot \mathbf{u} + \nabla \cdot \left[\nabla\psi \times \left(\frac{\partial \mathbf{u}}{\partial t} + \boldsymbol{\zeta} \times \mathbf{u}\right)\right] = \boldsymbol{\zeta} \cdot \nabla\dot{\psi}. \tag{3.3}$$

Despite our use of symbols with implied meanings (i.e., $\mathbf{u}$ and $\boldsymbol{\zeta}$), this result was derived using very little physics; instead, purely mathematical arguments were used.

We introduce the physics by defining a particular $\mathbf{u}$, and then substituting an appropriate mass conservation equation for $\nabla\cdot\mathbf{u}$ and momentum conservation equation for $\partial\mathbf{u}/\partial t + \boldsymbol{\zeta}\times\mathbf{u}$. For example, letting $\mathbf{u}$ be the dry air velocity, we substitute the continuity equation for dry air (2.2) and the rotational form of the momentum equation (B.17) into (3.3) to obtain

$$\frac{D}{Dt}\left(\frac{1}{\rho_a}\boldsymbol{\zeta} \cdot \nabla\psi\right) = \frac{1}{\rho_a^3}(\nabla\rho_a \times \nabla p_a) \cdot \nabla\psi + \frac{1}{\rho_a}\boldsymbol{\zeta} \cdot \nabla\dot{\psi} + \frac{1}{\rho_a}(\nabla \times \mathbf{F}) \cdot \nabla\psi, \tag{3.4}$$

wherein $\mathbf{F}$ represents friction produced by the turbulent diffusion of momentum. If we let $\psi = \theta(\rho_a, p_a)$, where θ is the potential temperature, and assume that the flow is adiabatic (i.e., $\dot{\theta} = 0$) and frictionless (i.e., $\mathbf{F} = 0$), equation (3.4) reduces to the material conservation relation

$$\frac{DP}{Dt} = 0, \tag{3.5}$$

where

$$P = \frac{1}{\rho_a}\boldsymbol{\zeta} \cdot \nabla\theta, \tag{3.6}$$

is Ertel's PV for a dry atmosphere.

To derive a more general form of PV that is applicable to a moist atmosphere, we must include the additional physics associated with water. For instance, similar to the approach used to derive (3.4), we let $\mathbf{u}$ be the mass–weighted mean velocity (2.1), and substitute the continuity (B.12) and momentum (B.15) equations for the total mass into (3.3), to obtain the PV equation for a moist, precipitating atmosphere,

$$\frac{\bar{D}}{Dt}\left(\frac{1}{\rho}\bar{\boldsymbol{\zeta}} \cdot \nabla\psi\right) = \frac{1}{\rho^3}(\nabla\rho \times \nabla p) \cdot \nabla\psi + \frac{1}{\rho}\bar{\boldsymbol{\zeta}} \cdot \nabla\bar{\dot{\psi}} + \frac{1}{\rho}(\nabla \times \bar{\mathbf{F}}) \cdot \nabla\psi, \tag{3.7}$$

wherein $\bar{\mathbf{F}}$ now includes not only friction, but also sources and sinks of momentum due to changes in precipitation mass [see (B.16)]; $\bar{D}/Dt = \partial/\partial t + \bar{\mathbf{u}} \cdot \nabla$ is the material derivative following $\bar{\mathbf{u}}$; and $\bar{\dot{\psi}} \equiv \bar{D}\psi/Dt$. Comparing equations (3.4) and (3.7), we see that ρ_a, p_a, $\mathbf{u}$, $\boldsymbol{\zeta}$, $\dot{\psi}$, and D/Dt are replaced by ρ, p, $\bar{\mathbf{u}}$, $\bar{\boldsymbol{\zeta}}$, $\bar{\dot{\psi}}$, and $\bar{D}/Dt$, respectively. Clearly, the latter terms reduce to the former in the dry limit; thus, (3.7) reduces to (3.4). As a result, we can say that (3.7) represents a more general form of the PV conservation equation.

However, as with (3.5), we prefer that (3.7) be a material conservation relation. Unfortunately, in general, such a relation is not possible, since $\bar{\mathbf{F}} \neq 0$ even for frictionless flow due to precipitation. Furthermore, we may not be able to eliminate both $(\nabla\rho \times \nabla p) \cdot \nabla\psi$ and $\bar{\boldsymbol{\zeta}} \cdot \nabla\bar{\dot{\psi}}$ for a specific choice of ψ. The solenoidal term, $\nabla\psi \cdot (\nabla\rho \times \nabla p)$, in particular, can be eliminated by simply requiring that $\psi = \psi(\rho, p)$. When ψ is of this form, $\nabla\psi = (\partial\psi/\partial\rho)_p \nabla\rho + (\partial\psi/\partial p)_\rho \nabla p$, which implies that $\nabla\psi \cdot (\nabla\rho \times \nabla p) = 0$[1], since $\nabla p \cdot (\nabla\rho \times \nabla p) \equiv 0$ and $\nabla\rho \cdot (\nabla\rho \times \nabla p) \equiv 0$. Later, we consider the possibility of eliminating $\bar{\boldsymbol{\zeta}} \cdot \nabla\bar{\dot{\psi}}$ by choosing a particular $\psi(\rho, p)$ satisfying $\bar{\dot{\psi}} = 0$. With the solenoidal term removed, (3.7) reduces to

$$\frac{\bar{D}P_\psi}{Dt} = \frac{1}{\rho}\bar{\boldsymbol{\zeta}} \cdot \nabla\bar{\dot{\psi}} + \frac{1}{\rho}(\nabla \times \bar{\mathbf{F}}) \cdot \nabla\psi, \tag{3.8}$$

where

$$P_\psi = \frac{1}{\rho}\bar{\boldsymbol{\zeta}} \cdot \nabla\psi \tag{3.9}$$

is the generalized moist potential vorticity for the yet unspecified scalar field ψ.

3.1.2 Invertibility Principle

The power of PV as a dynamic tool is ultimately in its invertibility. If the PV of a quasi–static balanced flow is known, amazingly, we can diagnose the fluid's complete mass and momentum fields. The elliptic equation or system of balanced equations with boundary conditions used to perform this diagnosis is termed the invertibility principle (Hoskins et al., 1985).

---

[1] In a two–dimensional fluid, $\nabla\rho$, ∇p, and $\nabla\psi$ all lie in the same plane; therefore, $\nabla\psi$ is always perpendicular to $\nabla\rho \times \nabla p$ such that $\nabla\psi \cdot (\nabla\rho \times \nabla p) \equiv 0$, no matter what the choice of ψ.

As a specific example of an invertibility principle for (3.9), we consider an axisymmetric fluid that is in gradient and hydrostatic balance. From equations (3.9) and (2.5), the PV and balanced conditions, respectively, for this fluid are given by

$$P_\psi = \frac{1}{\rho}\left[-\frac{\partial \bar{v}}{\partial z}\frac{\partial \psi}{\partial r} + \left(f + \frac{\partial\left(r\bar{v}\right)}{r\partial r}\right)\frac{\partial \psi}{\partial z}\right], \tag{3.10}$$

$$\frac{\partial p}{\partial r} = \rho\left(f + \frac{\bar{v}}{r}\right)\bar{v}, \tag{3.11}$$

$$\frac{\partial p}{\partial z} = -\rho g. \tag{3.12}$$

Assuming that P_ψ is known, this system consists of three equations and four unknowns (i.e., ρ, p, $\bar{v}$, and ψ). Since the system is not closed, we need an additional equation for ψ as a function of ρ, p, $\bar{v}$, or some combination of the three. Considering the previous section, we see that

$$\psi = \psi\left(\rho, p\right) \tag{3.13}$$

not only eliminates the solenoidal term but closes the invertibility problem as well.

However, there is a more fundamental reason for choosing $\psi = \psi\left(\rho, p\right)$. Eliminating the solenoidal term is critical to separating the slow (i.e., balanced) and fast (i.e., inertia–gravity wave) manifold dynamics during inversion. To understand why, consider a dry barotropic atmosphere with frictionless adiabatic motions. According to Salmon (1992), this fluid has three material conservation equations for the PV. If the atmosphere is baroclinic, the solenoidal term appears in each equation and destroys the material conservation. However, by choosing ψ such that one of the solenoidal terms is eliminated, then one of

the material conservation relations is regained. The resulting relation is Ertel's PV equation. The slow manifold dynamics are contained in this equation, while the fast manifold dynamics are contained in the remaining two equations. Therefore, we choose $\psi = \psi(\rho, p)$ not out of convenience (i.e., simply to eliminate the solenoidal term and close the invertibility problem) but out of necessity (i.e., to guarantee invertibility of the slow manifold). If $\psi \neq \psi(\rho, p)$, the inverted solution represents neither the slow nor fast manifold independently, but some combination, which is ultimately of little use. With $\psi(\rho, p)$ defined, we can then solve the invertibility problem for the slow manifold, given the necessary boundary conditions.

Interestingly, this solution yields no information about the partition of mass into dry air and water in its various forms. For example, we are unable to partition ρ into ρ_a, ρ_v, ρ_c, or ρ_r; nor are we able to partition p into p_a or p_v. The additional detail is dynamically unnecessary to solve the invertibility problem. To obtain these details, we must include other prognostic equations in addition to (3.8).

3.1.3 Impermeability Theorem

We next prove that the generalized moist PV also satisfies Haynes and McIntyre's (1987; 1990) impermeability theorem, which states that while surfaces of constant ψ are permeable to mass, they are impermeable to "PV substance" (i.e., ρP). Since $\rho P = \bar{\boldsymbol{\zeta}} \cdot \nabla\psi$ and since $\bar{\boldsymbol{\zeta}} \cdot \nabla\bar{\dot{\psi}} = \nabla \cdot \left(\bar{\dot{\psi}}\bar{\boldsymbol{\zeta}}\right)$ and $\nabla\psi \cdot (\nabla \times \mathbf{F}) = \nabla \cdot (\mathbf{F} \times \nabla\psi)$, we begin this proof by rewriting (3.7) as

$$\frac{\partial(\rho P)}{\partial t} + \nabla \cdot \mathbf{J} = 0, \tag{3.14}$$

wherein $\mathbf{J} = \bar{\mathbf{u}}\rho P - \bar{\boldsymbol{\zeta}}\bar{\dot{\psi}} - \mathbf{F} \times \nabla\psi$ is the total flux, consisting of the advective flux ($\rho P\bar{\mathbf{u}}$) and the nonadvective flux ($-\bar{\boldsymbol{\zeta}}\bar{\dot{\psi}} - \mathbf{F} \times \nabla\psi$).

By determining the components of this flux that are perpendicular and parallel to ψ–surfaces, we show that there is no flux of ρP across these surfaces. To prove this, let

$\bar{\mathbf{u}}_\perp$ and $\bar{\boldsymbol{\zeta}}_\perp$ denote the components of $\bar{\mathbf{u}}$ and $\bar{\boldsymbol{\zeta}}$ that are perpendicular to the ψ–surface. The parallel components are then $\bar{\mathbf{u}}_{||} = \bar{\mathbf{u}} - \bar{\mathbf{u}}_\perp$ and $\bar{\boldsymbol{\zeta}}_{||} = \bar{\boldsymbol{\zeta}} - \bar{\boldsymbol{\zeta}}_\perp$. Since $\nabla\psi/|\nabla\psi|$ denotes a unit vector normal to the ψ–surface, the velocity and vorticity may be written as $\bar{\mathbf{u}} = \bar{\mathbf{u}}_{||} + |\nabla\psi|^{-2}(\bar{\mathbf{u}}\cdot\nabla\psi)\nabla\psi$ and $\bar{\boldsymbol{\zeta}} = \bar{\boldsymbol{\zeta}}_{||} + |\nabla\psi|^{-2}(\bar{\boldsymbol{\zeta}}\cdot\nabla\psi)\nabla\psi$. Using these last two relations, we rewrite $\mathbf{J}$ as

$$\mathbf{J} = \left(\bar{\mathbf{u}}_{||} + \frac{\bar{\mathbf{u}}\cdot\nabla\psi}{|\nabla\psi|^2}\nabla\psi\right)\rho P - \left(\bar{\boldsymbol{\zeta}}_{||} + \frac{\bar{\boldsymbol{\zeta}}\cdot\nabla\psi}{|\nabla\psi|^2}\nabla\psi\right)\bar{\dot{\psi}} - \mathbf{F}\times\nabla\psi. \tag{3.15}$$

Since the second term in the second parentheses involves $\bar{\boldsymbol{\zeta}}\cdot\nabla\psi$, we may rewrite it as ρP. This allows us to combine the second terms in the parentheses, so that (3.15) reduces to

$$\mathbf{J} = \bar{\mathbf{U}}_\perp\rho P + \bar{\mathbf{u}}_{||}\rho P - \bar{\boldsymbol{\zeta}}_{||}\bar{\dot{\psi}} - \mathbf{F}\times\nabla\psi, \tag{3.16}$$

where

$$\bar{\mathbf{U}}_\perp \equiv -\frac{\partial\psi/\partial t}{|\nabla\psi|^2}\nabla\psi. \tag{3.17}$$

Since the last three terms on the right hand side of (3.16) all represent vectors parallel to the local ψ–surface, any perpendicular component of $\mathbf{J}$ must be due to the first term. To illustrate how $\bar{\mathbf{U}}_\perp$ transports ρP relative to a ψ–surface, we take the scalar product of $\nabla\psi$ with (3.17) to show that $\bar{\mathbf{U}}_\perp$ satisfies

$$\frac{\partial\psi}{\partial t} + \bar{\mathbf{U}}_\perp\cdot\nabla\psi = 0. \tag{3.18}$$

Similarly, we assumed in section 3.1 that[2]

---

[2]Note that $\bar{\mathbf{u}}_\perp\cdot\nabla\psi = \left(\bar{\mathbf{u}}\cdot\frac{\nabla\psi}{|\nabla\psi|}\right)(\nabla\psi\cdot\nabla\psi) = \bar{\mathbf{u}}\cdot\nabla\psi$.

$$\frac{\partial \psi}{\partial t} + \bar{\mathbf{u}}_{\perp} \cdot \nabla \psi = \bar{\dot{\psi}}. \tag{3.19}$$

According to (3.18), if we are moving with velocity $\bar{\mathbf{U}}_{\perp}$, ψ does not change; thus, from (3.16) we see that ρP is moving with the ψ–surface. In contrast, from (3.19) we see that mass is moving through the surface, when $\bar{\dot{\psi}} \neq 0$. Although mass may pass through, PV substance may not; thus, ψ–surfaces are impermeable to ρP.

Interestingly, this result proves that impermeability is satisfied for any choice of ψ. In other words, as the definition of ψ changes, the definition of P_{ψ} also changes so that impermeability is always satisfied.

3.2 Specific Potential Vorticity Principles

The obvious question remaining is what expression do we use for the arbitrary scalar field ψ? Thus far, we elected not to specify ψ until the entire generalized moist PV principle was derived and the requirements on ψ were identified. In summary, these requirements are that:

i. $\psi = \psi(\rho, p)$ such that $(\nabla\rho \times \nabla p) \cdot \nabla\psi \equiv 0$,

ii. $\lim_{\mu \to 0} \psi(\rho, p) \to \psi(\rho_a, p_a)$,

iii. $\bar{\dot{\psi}} = 0$.

The requirements are listed in order of importance. Theoretically, (*i*) is the most important requirement, since the solenoidal term must be eliminated; otherwise, we cannot isolate the slow manifold dynamics when inverting the PV. Similarly, (*ii*), although less important, guarantees that (3.7) reduces to (3.4) in the dry limit; thus, the moist dynamics are a generalization of the dry dynamics. Even though it is unnecessary, (*iii*) is desirable since it provides for the material conservation of PV, assuming that the first requirement is met, the flow is frictionless, and there is no precipitation.

Historically, however, most variants of the moist PV equation were derived assuming that (*iii*) is the most important requirement. For example, consider the moist PV defined using the equivalent potential temperature[3]

$$\theta_e = \theta \exp\left(\frac{L_v \mu_v}{c_{p_a} T}\right). \tag{3.20}$$

Substituting (3.20) into (3.4), we obtain the PV conservation equation

$$\frac{DP_e}{Dt} = \frac{1}{\rho_a^3}(\nabla \rho_a \times \nabla p_a) \cdot \nabla \theta_e + \frac{1}{\rho_a} \boldsymbol{\zeta} \cdot \nabla \dot{\theta}_e + \frac{1}{\rho_a}(\nabla \times \mathbf{F}) \cdot \nabla \theta_e, \tag{3.21}$$

wherein

$$P_e = \frac{1}{\rho_a} \boldsymbol{\zeta} \cdot \nabla \theta_e, \tag{3.22}$$

is the moist-equivalent PV. Equations (3.20)–(3.22) have been used extensively to study hurricanes (Rotunno and Emanuel, 1987), mesoscale convective systems (Rotunno and Klemp, 1985), extratropical cyclones (Cao and Cho, 1995), fronts (Bénard et al., 1992; Persson, 1995), and moist-symmetric instability (Bennetts and Hoskins, 1979; Guoxiong et al., 1996). In all of these studies, θ_e is materially conserved.

However, in reality, θ_e is only approximately conserved (Wilhelmson, 1977). Fundamentally, conservation of θ_e expresses the conservation of moist entropy; therefore, we derive

---

[3]Note that θ_e defined by (3.20) is approximately conserved in a saturated atmosphere only (Hauf and Höller, 1987; Klemp and Wilhelmson, 1978; Rotunno and Emanuel, 1987). If we qualify this definition by requiring that T be the temperature at which a parcel of air is saturated, then θ_e is approximately conserved in both a saturated and unsaturated atmosphere (Bluestein, 1992).

(3.20) from the thermodynamic energy conservation equation for a moist atmosphere undergoing isentropic variations. During this derivation, however, we make several simplifying assumptions (Hauf and Höller, 1987; Dutton, 1995). As a result, conservation of θ_e only approximately expresses the conservation of moist entropy. Furthermore, θ_e is not conserved if there is appreciable radiative heating, mixing, evaporation of condensate into unsaturated air, or latent heating due to fusion and sublimation. As a result, we see that (*iii*) is only approximately satisfied.

In addition, the dynamics expressed in terms of the moist-equivalent PV are not comparable to those expressed in terms of the dry PV. Clearly, θ_e reduces to θ in the dry limit (i.e., $\mu_v = 0$) such that (*ii*) is satisfied; however, the distributions of dry and moist-equivalent PV within moist convection can be significantly different. Consider, for example, the generation of PV in the eyewall of a tropical cyclone. Since $\dot{\theta} \neq 0$ where condensational heating is present, dry PV is generated in the eyewall. In contrast, since $\dot{\theta}_e = 0$ when the atmosphere is saturated, no moist-equivalent PV is generated in the eyewall. The dry PV is a maximum and the moist-equivalent PV is zero. Because of this disparity, it is difficult to compare the theoretical understanding obtained from simple dry models that use the dry PV (Schubert and Alworth, 1987; Möller and Smith, 1994; Guinn and Schubert, 1993; Montgomery and Enagonio, 1998) to those of more complex full–physics models that use the moist-equivalent PV.

Most importantly, θ_e does not eliminate the solenoidal term everywhere; therefore, the inversion of the moist-equivalent PV is approximate. Since $\theta_e = \theta_e(\rho_a, p_a, \mu_v)$, the solenoidal term is not eliminated unless ρ and p are replaced by ρ_a and p_a, respectively, and the atmosphere is saturated such that $\mu_v = \mu_{vs}(\rho_a, p_a)$ and $\theta_e = \theta_e(\rho_a, p_a)$. One might argue that small errors introduced by the non-zero solenoidal term in unsaturated regions are negligible and do not affect the regions of interest within the moist convection (Rotunno and Klemp, 1985); however, recall that the invertibility problem is solved globally such that any small errors in one region are communicated to the entire domain.

Of course, none of this criticism of the moist-equivalent PV should suggest that it is not a useful tool for understanding moist dynamics. Instead, we simply show that it is

approximate and wonder if there is a more exact form of moist PV. To obtain such a form, we shift our focus from (*iii*) to (*i*) and (*ii*), assuming that, in general, $\bar{\tilde{\psi}} \neq 0$.

Let us derive the moist PV in terms of a virtual potential temperature. We first define a virtual temperature T_ρ in terms of the total pressure and density, using $p = \rho R_a T_\rho$ (Ooyama, 1990). From this expression, we further define the virtual potential temperature

$$\theta_\rho = T_\rho \left(\frac{p_0}{p}\right)^\kappa = \frac{p}{\rho R_a}\left(\frac{p_0}{p}\right)^\kappa. \tag{3.23}$$

Since $\theta_\rho = \theta_\rho(\rho, p)$, the solenoidal term in (3.7) is eliminated under all atmospheric conditions. Additionally, θ_ρ satisfies the dry limit as $(\rho, p) \to (\rho_a, p_a)$; however, in general, $\bar{\tilde{\theta}}_\rho \neq 0$ due to latent heating and the irreversible loss of precipitation. Substituting (3.23) into (3.7), we obtain

$$\frac{\bar{D}P_\rho}{Dt} = \frac{1}{\rho}\bar{\zeta}\cdot\nabla\bar{\tilde{\theta}}_\rho + \frac{1}{\rho}(\nabla\times\bar{\mathbf{F}})\cdot\nabla\theta_\rho, \tag{3.24}$$

where

$$P_\rho = \frac{1}{\rho}\bar{\zeta}\cdot\nabla\theta_\rho \tag{3.25}$$

is the moist PV.

3.3 Approximate Potential Vorticity Principle

In Chapter 2, due to a restriction on the lower boundary condition of $\bar{w}$, we approximated the momentum equation. This approximation alters the model PV equation as well. To derive the approximate PV equation, we follow a combination of the steps used to derive

(3.4) and (3.7). First, as in (3.7), we let $\bar{\mathbf{u}}$ be the mass–weighted mean velocity (2.1) in the divergence and material derivative terms of (3.3), and substitute the continuity equation for the total mass (B.12) to obtain

$$\frac{\bar{D}}{Dt}\left(\frac{\boldsymbol{\zeta}\cdot\nabla\theta_\rho}{\rho}\right)+\nabla\cdot\left[\nabla\theta_\rho\times\left(\frac{\partial\mathbf{u}}{\partial t}+\boldsymbol{\zeta}\times\mathbf{u}\right)\right]=\boldsymbol{\zeta}\cdot\nabla\bar{\dot{\theta}}_\rho, \tag{3.26}$$

where we have used $\psi=\theta_\rho$. Second, as in (3.4), we let $\mathbf{u}$ be the dry air velocity in the definition of $\boldsymbol{\zeta}$ and the bracketed term of (3.26), and substitute the approximate momentum equation (B.21) so that (3.26) simplifies to

$$\frac{\bar{D}\tilde{P}_\rho}{Dt}=\frac{1}{\rho}\boldsymbol{\zeta}\cdot\nabla\bar{\dot{\theta}}_\rho+\frac{1}{\rho}\left(\nabla\times\tilde{\mathbf{F}}\right)\cdot\nabla\theta_\rho, \tag{3.27}$$

wherein $\tilde{\mathbf{F}}$ is given by (B.22) and

$$\tilde{P}_\rho=\frac{1}{\rho}\boldsymbol{\zeta}\cdot\nabla\theta_\rho \tag{3.28}$$

is the approximate form of the moist PV. Equations (3.27) and (3.28) are formally identical to (3.24) and (3.25), except that $\bar{\boldsymbol{\zeta}}$ and $\bar{\mathbf{F}}$ are replaced by $\boldsymbol{\zeta}$ and $\tilde{\mathbf{F}}$, respectively.

Chapter 4

CONTROL EXPERIMENT

> Basic research is like shooting an arrow into the air and, where it lands, painting a target.
>
> Homer Adkins

In the last two chapters, we developed a set of conservation equations for a moist, precipitating atmosphere. Next, we present results from our control experiment, an axisymmetric tropical cyclone simulation, to validate the model against current observations and theory. To facilitate the comparison of this experiment with other tropical cyclone simulations, we setup the model using the fundamental physics and appropriate numerics (section 4.1) necessary to simulate a tropical cyclone, as applied in past axisymmetric models (see appendix A). The model setup is followed by a detailed analysis of the results from the control experiment (section 4.2), including a description of the evolution and steady state structure.

4.1 Model Setup

4.1.1 Physics

Background State: We begin the initialization with a conditionally unstable resting atmosphere as a background basic state. The vertical structure of this atmosphere is defined using Jordan's (1958) mean hurricane season sounding, as shown in figure 4.1. The sounding has approximately 1600 J kg^{-1} of ambient CAPE, which hastens the formation of

Table 4.1: Model parameters that define the control experiment.

Parameter	Value	Description
v_m	12 m s^{-1}	maximum tangential wind speed
r_m	100 km	radius of maximum tangential wind
z_t	24 km	height of domain top
z_s	18 km	height at which Rayleigh damping layer begins
z_m	15 km	height at which tangential winds vanish
z_b	1 km	height of atmospheric boundary layer
z_a	10 m	height of surface layer (anemometer level)
T_s	28°C	sea surface temperature
T_f	0°C	center of freezing zone
ΔT_f	1°C	width of freezing zone
f	5×10^{-5} s^{-1}	Coriolis parameter (20°N)
α_s	0.015 s^{-1}	maximum value of Rayleigh damping

the initial convection and secondary circulation, but is ultimately unnecessary for tropical cyclone development in an axisymmetric model given a sufficient finite amplitude initial disturbance (Rotunno and Emanuel, 1987). Along the lower boundary, we assume that the water vapor is saturated immediately above the ocean surface, with a sea surface temperature of 28°C. For a complete list of the model parameters, see table 4.1.

Vortex Perturbation: Superimposed on the basic state is a cyclonic vortex with vertical shear. We define this vortex analytically using the function

$$v(r,z) = \begin{cases} 0, & \text{if } z > z_m, \\ v_m \left(\frac{z_m - z}{z_m}\right) \left[\frac{2\left(\frac{r}{r_m}\right)}{1+\left(\frac{r}{r_m}\right)^2}\right], & \text{if } z \leq z_m, \end{cases} \tag{4.1}$$

where r_m and v_m are the radius and speed of the maximum tangential wind (Ooyama, 1969; Zeng, 1996). The vortex is a maximum at the surface, linearly decays with height, and vanishes above z_m. Most importantly, for any r_m and v_m, the initial vortex is inertially stable. For the control experiment, we choose $r_m = 100$ km, $z_m = 15$ km, and $v_m = 12$ m s^{-1}, yielding the vortex illustrated in figure 4.2a.

The initial vortex expedites the development of the tropical cyclone. First, it provides low-level frictional convergence and ascent. This convergent ascent is used instead of buoyant

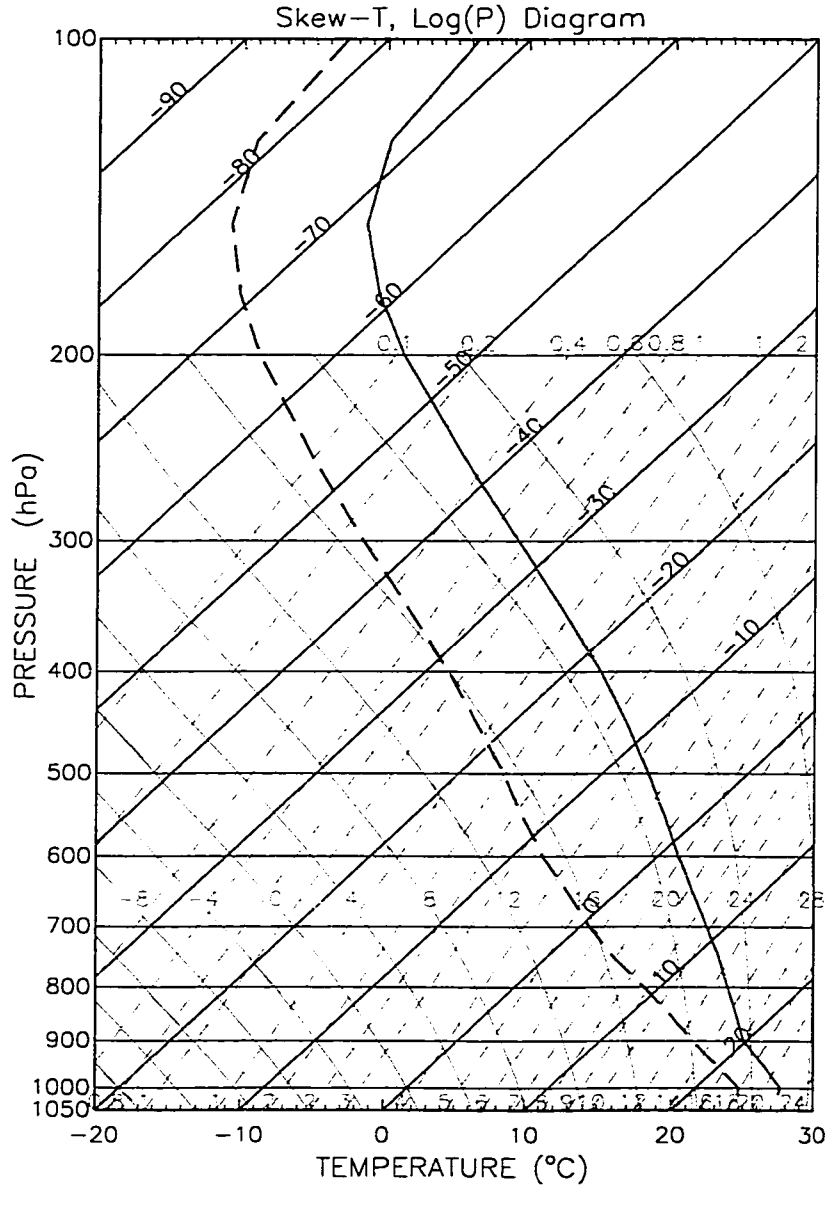

Figure 4.1: Jordan's (1958) mean hurricane season temperature (solid) and dew–point temperature (dashed) soundings.

ascent (i.e., a warm bubble) to produce the initial moist convection. Second, the vortex provides additional vorticity for tropical cyclone development above that provided by the planetary vorticity alone (Gray, 1968, 1979). In the control experiment, for instance, we place the vortex at 20°N such that $f = 5 \times 10^{-5}$ s^{-1}. By comparison, the central vorticity of the initial vortex is about 5×10^{-4} s^{-1} or $10f$.

Thermal Wind Balance: To complete the initialization, we iteratively adjust the basic state by solving the gradient and hydrostatic balance equations for the pressure until the vortex is in thermal wind balance. During the iteration, we assume that the relative humidity remains horizontally uniform. This assumption prevents unintended saturation as the central pressure decreases. Figures 4.2b and c illustrate the resulting pressure (p') and temperature (T') perturbations relative to the basic state. The iterative adjustment produces a maximum perturbation in both fields near the surface, with minimum $p' = -7.1$ hPa and maximum $T' = 1.1$ K. Since temperature can be related to the vertical derivative of pressure through the hydrostatic equation and since the derivative of a field is generally more variable than the field itself, there is some noise in the temperature field; however, it has no apparent adverse effect on the resulting thermal wind balance.

Ice Microphysics: Recall from section 2.1.3.2 that we parameterized the phase changes of water between solid and liquid by defining a synthesized condensate representing a solid and liquid mixture within a prescribed temperature zone. This zone is the same for both ascending (i.e., freezing) and descending (i.e., melting) condensate; however, for a given problem, the freezing and melting zones may be significantly different. For example, within intense mid–latitude mesoscale convective systems, the freezing zone may be very deep, as water drops are rapidly lofted above the 0°C isotherm; however, the melting zone is typically very shallow, as ice particles quickly melt while gradually falling below the 0°C isotherm. In contrast, the updrafts of a tropical cyclone are generally much weaker (Jorgensen et al., 1983; Black et al., 1994, 1996), thus the freezing and melting zones are relatively thin and nearly coincident (Black and Hallett, 1996; Pueschel et al., 1995). As a result, our assumption of a single zone is believed a reasonable one for at least some

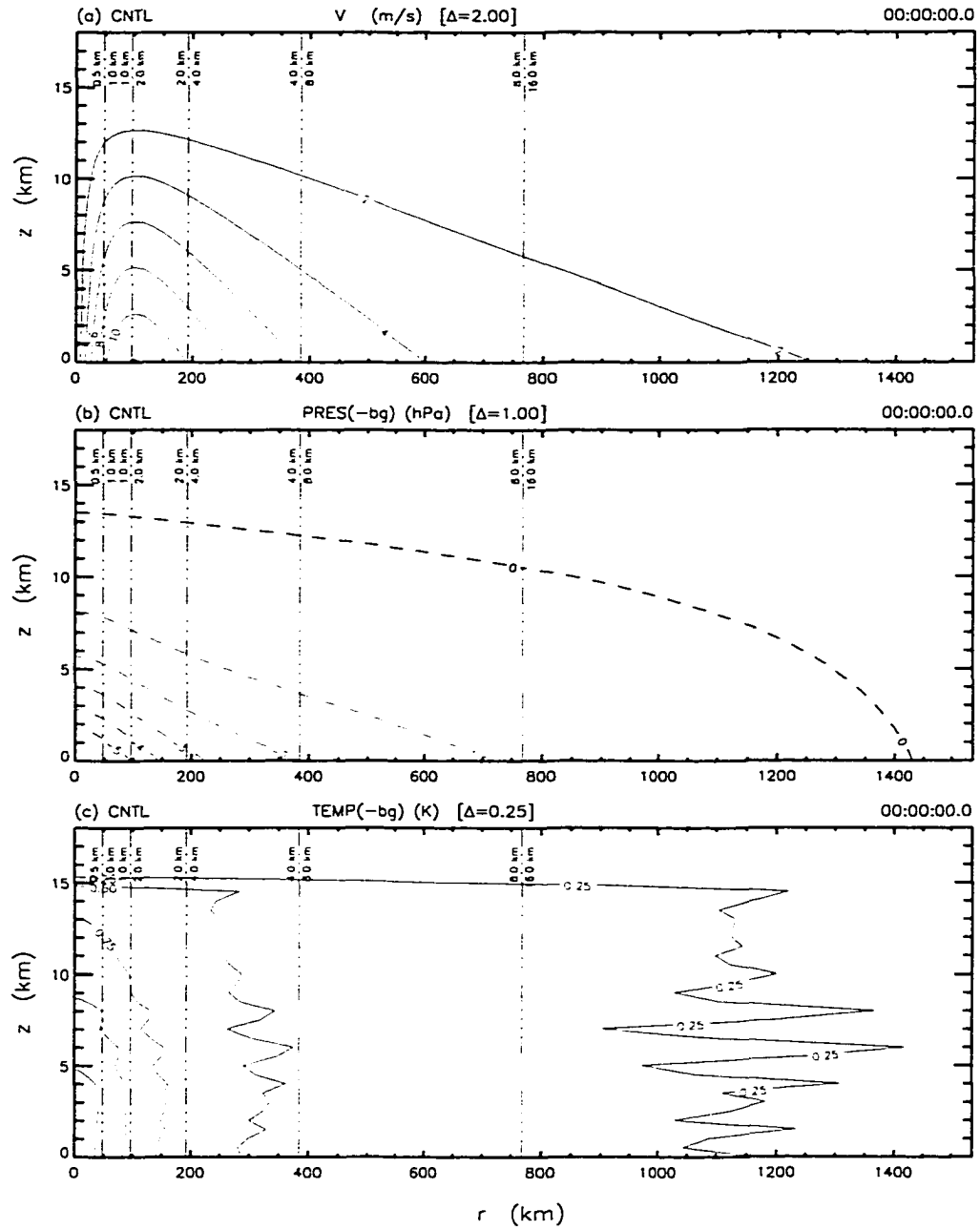

Figure 4.2: Initial vertical cross-sections (r, z) of the vortex a) tangential wind speed (v), b) pressure perturbation (p'), and temperature perturbation (T'). Headings above each figure indicate the experiment (left); the contoured variable, including units and contour interval (Δ) (center); and the time in units of hh:mm:ss.s (right). Perturbation variables are identified by the (-bg) to the right of the variable name. The vertically-oriented chained lines mark the interfaces between nested grids, while the distances straddling these lines indicate the grid spacing to either side.

tropical cyclones. For all of the experiments, we define the zone using $T_f = 273.15$ K and $\Delta T_f = 1.0$ K [see equation (2.18)].

Boundary Layer Microphysics: In section 2.1.3.2, we developed an atmospheric boundary layer parameterization. For all of the experiments, the depths of the surface and boundary layers are fixed at $z_a = 10$ m and $z_b = 1000$ m, respectively. In addition, we assume that all of the exchange coefficients are based on the drag coefficient (C_D), which is given by Deacon's formula (Rosenthal, 1971; Rotunno and Emanuel, 1987)

$$C_D = 1.1 \times 10^{-3} + \left(4.0 \times 10^{-5} \text{ s m}^{-1}\right) U, \tag{4.2}$$

wherein $U = (u^2 + v^2)^{\frac{1}{2}}$ is the speed of the horizontal wind at z_a.

4.1.2 Numerics

Domain and Boundary Conditions: The vortex and balanced-mass fields are initialized on a two-dimensional domain with cylindrical coordinates. The domain size is 24 km high by 1536 km wide. In the horizontal, the inner, or left, boundary is the axis of the cylindrical domain, and the outer, or right, boundary is open with an exponentially decaying solution. The *e*-folding distance of the decay is 1400 km (Ooyama, 1969). In the vertical, the top and bottom of the domain are bounded by rigid lids. To prevent the reflection of gravity waves off the top lid, a Rayleigh damping layer [see equation (2.68)] extends from $z_s = 18$ km to the domain top, with a maximum damping rate of $\alpha_s = 0.015$ s^{-1}.

Nested Grids: The domain is discretized into a series of nested grids. As illustrated in figure 4.2 and detailed in table 4.2, the horizontal domain consists of 6 nested grids, each having 96 grid intervals. The horizontal grid spacing (Δr) within each grid increases by a factor of two from the finest grid at 0.5 km to the coarsest grid at 16.0 km. The vertical domain, in contrast, consists of a single grid with 48 grid intervals each, with a grid spacing (Δz) of 0.5 km. To focus the finest resolution on the vortex core, we align the left boundary

Table 4.2: Horizontal grid setup, including the grid number, number of grid points, grid spacing (Δr), grid width, and time step (Δt).

Grid Number	No. of Points	Δr (km)	Width (km)	Δt (s)
1	96	0.5	48	2.5
2	96	1.0	96	5.0
3	96	2.0	192	5.0
4	96	4.0	384	10.0
5	96	8.0	768	10.0
6	96	16.0	1536	10.0

of each grid along the central axis of the domain. In addition, the time step on each grid is adjusted to guarantee computational stability in both directions. These time steps range from 2.5 s on the finest grid to 10.0 s on the coarsest grid. The total integration time for the control experiment is 240 hours. We performed a series of sensitivity tests to verify that the model physics is not sensitive to this grid configuration. Details of these sensitivity analysis will be presented in chapter 5.

4.2 Model Results

After initializing the model using the procedure discussed above., we integrate the model forward in time to simulate the future state of the tropical cyclone vortex. The evolution of the vortex is generally consistent with the results of past axisymmetric models and observational evidence. In this section, we examine this evolution beginning with the initial development of moist convection and ending with the transition to a steady state. This examination is followed by a detailed analysis of the steady-state structure and the deviations from that structure.

4.2.1 Tropical Cyclone Development

4.2.1.1 Initial Vortex

Initially, the vortex weakens and develops a low-level secondary circulation. Figure 4.3 shows the evolution of the surface vortex from 0–240 hours, in terms of the maximum

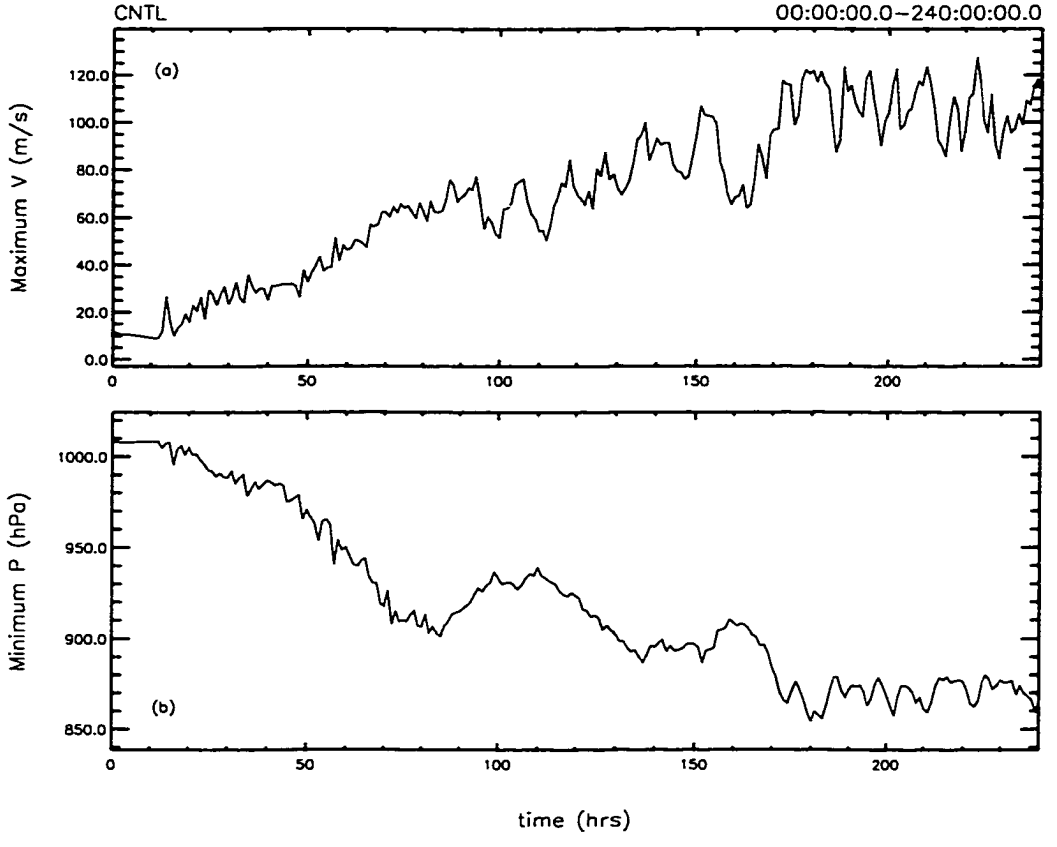

Figure 4.3: CNTL Experiment — Time series from 0–240 hours of the a) maximum tangential wind speed (m s^{-1}) and the b) central surface pressure (hPa).

tangential wind speed (v_{max}) and the minimum central pressure (p_{min}). During the first 12 hours, surface friction decelerates the vortex from $v_{max} = 12.0$ m s^{-1} to 9.2 m s^{-1}. Simultaneously, the resulting unbalanced pressure gradient accelerates a cross-isobaric radial inflow toward low pressure (not shown). Willoughby (1979) used Eliassen's (1952) balanced vortex model to demonstrate that this inflow is part of a shallow secondary circulation forced by the momentum sink, or friction, at the surface. By 12 hours, the inflow reaches a maximum of -7.3 m s^{-1} at 63.8 km.

Convection initially forms in the region of maximum radial convergence and quickly produces a short-lived intensification of the vortex. Figure 4.4 shows cross-sections of the developing convection, including the tangential wind speed, in 1-hour increments from 12–15 hours. At 12 hours, a series of four convective clouds develop between 45–70 km, with the most vigorous convection located at 63 km. Rapid ascent follows, as the moist convection consumes the ambient CAPE and penetrates the depth of the troposphere. Beneath the convection, precipitation-laden cold downdrafts diverge at the surface, spreading laterally as counter-propagating outflows. The inward-propagating outflow, conserving angular momentum, spins up the vortex to $v_{max} = 27.5$ m s^{-1}. Because of surface friction, however, the vortex rapidly weakens within two hours (see also figure 4.3).

By 14 hours, a secondary region of convection forms near the center. Internal gravity waves, generated by the initial convection, propagate laterally until impinging on the closed boundary at the center. The subsequent low-level convergence provides sufficient ascent to trigger additional moist convection.

Due to the axisymmetric geometry, the convection near the axis is structurally different from that in the interior of the domain. The divergence in cylindrical coordinates has a u/r term that is not present in rectilinear coordinates. For large r, this term is negligible, and the divergence in either coordinate is nearly identical; however, for small r, this term may be significant. For example, Murray (1970) has shown that moist convection along the axis develops an updraft vertical velocity up to five times greater in an axisymmetric model as compared to a rectilinear model. The greater ascent was forced by the increased

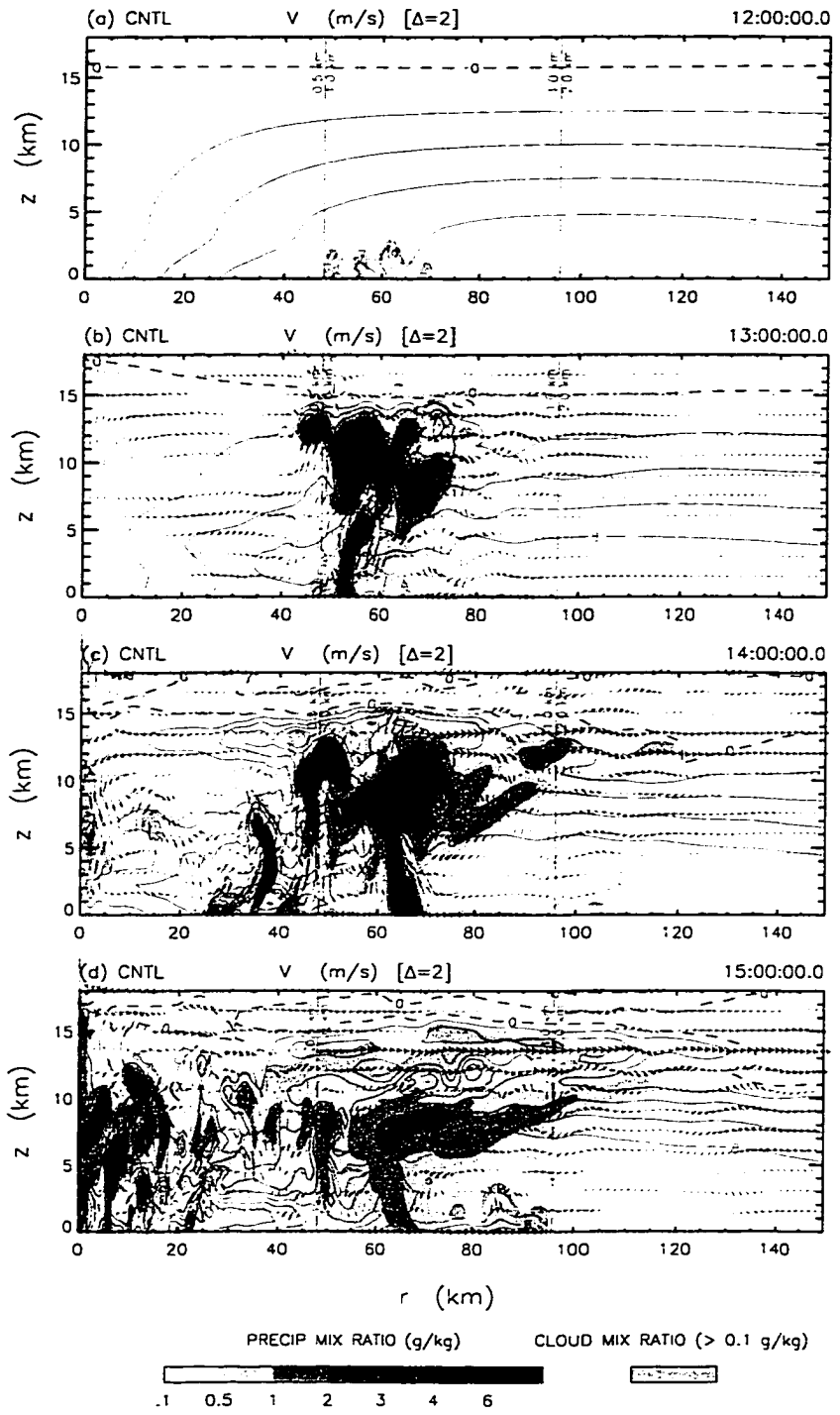

Figure 4.4: CNTL Experiment — Cross-sections depicting the initial formation of convection in terms of the tangential wind (contouring), precipitation mixing ratio (blue shading), and cloud mixing ratio (gray shading) for a) 12, b) 13, c) 14, and d) 15 hours. The wind vectors depict the relative magnitude of the winds in the plane of the cross-section. For further explanation of the figure markings, see figure 4.2.

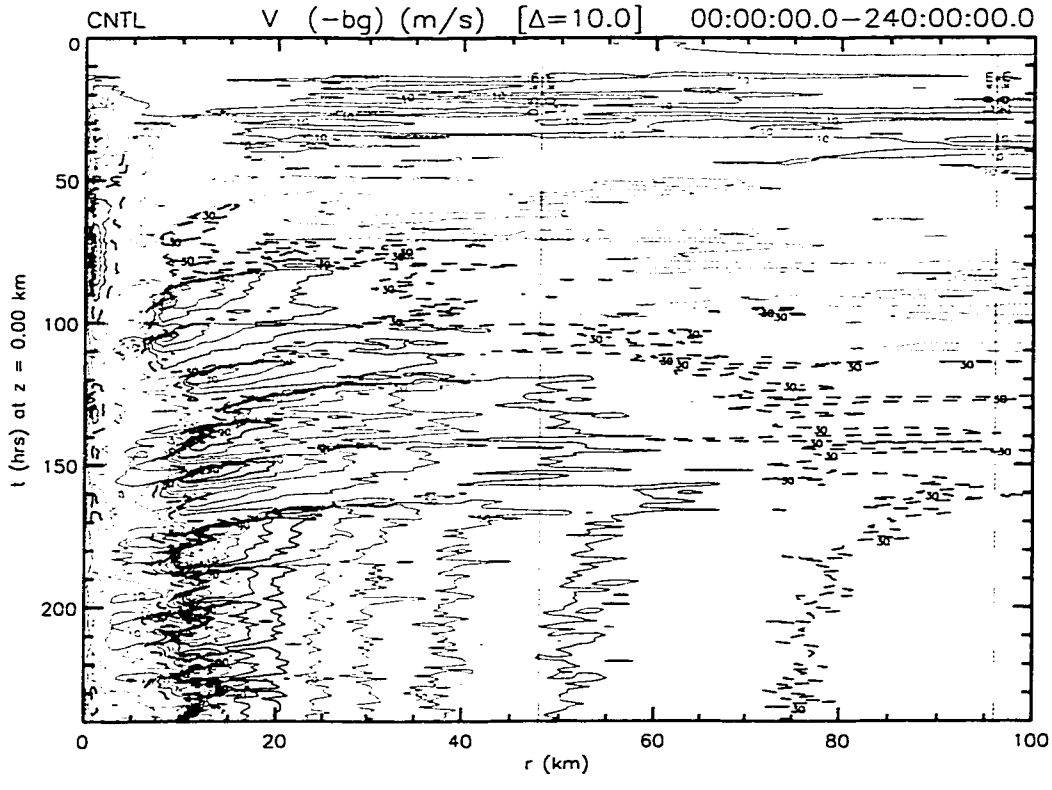

Figure 4.5: CNTL Experiment — Hovmöller diagram of the surface tangential wind speed from 0 to 100 km and 0 to 240 hours. The dashed line marks the 30 m s^{-1} contour, which is slightly less than hurricane intensity, 33 m s^{-1}.

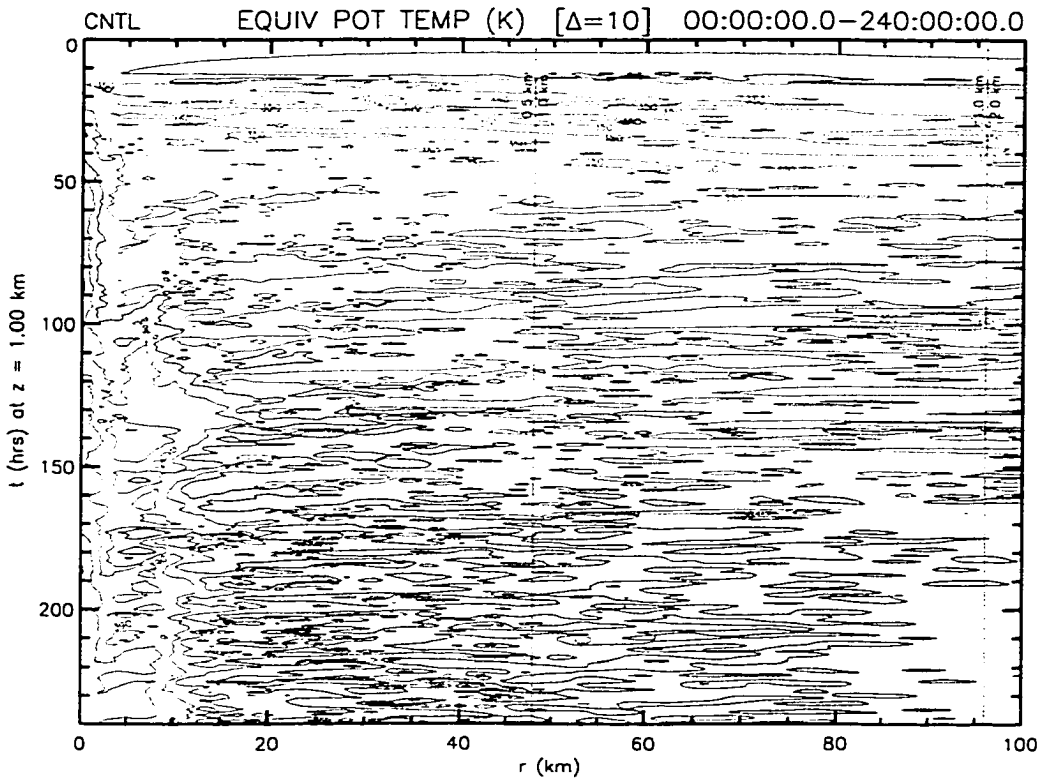

Figure 4.6: CNTL Experiment — Hovmöller diagram of θ_e at $z = 1$ km from 0 to 100 km and 0 to 240 hours.

radial convergence in the axisymmetric model. In the control experiment, the maximum updraft velocities for the initial and center convection are 18 and 26 m s^{-1}, respectively.

4.2.1.2 Central Vortex Anomaly

Such intense updrafts near the axis spin up a small self-sustaining vortex. The radial convergence of angular momentum at the base of the convection accelerates the tangential wind and increases the central relative vorticity. Maintaining gradient balance, the central pressure also decreases. To better understand the temporal and spatial evolution of the vortex, figures 4.5 and 4.6 depict the surface tangential wind speed and entropy at a height of 1 km using Hovmöller diagrams. Between 40 and 50 hours, the vortex surpasses hurricane intensity and by 72 hours reaches a maximum intensity of $v_{max} = 65$ m s^{-1}, with radius of maximum tangential wind, $r_{max} = 1.0$ km. The corresponding surface fluxes of latent and sensible energy, which average about 2400 W m^{-2} and 600 W m^{-2}, respectively,

increase θ_e at the center and are more than sufficient to sustain the moist convection. The persistent convection and corresponding convergence of entropy and angular momentum preserve the vortex against dissipation by surface friction.

Beyond 80 hours, however, the vortex weakens substantially. At this same time, as revealed in figure 4.5, a secondary tangential wind maximum forms at about 30 km and propagates inward, intensifying along the way. This wind maximum is collocated with a ring of convection, which eventually contracts to become the new tropical cyclone eyewall. According to Shapiro and Willoughby (1982) and Willoughby et al. (1982), both the convection in the eyewall and at the center produce a secondary circulation. Since the eyewall convection is more intense, the superposition of the secondary circulations results in net convergence and subsidence atop the center convection. For instance, as the primary updraft in the eyewall increases from 1 to 4 m s^{-1}, the updraft in the center decreases from 2.5 to 0.5 m s^{-1}. Furthermore, the weak surface inflow into the central convection reverses direction, becoming weak outflow, and the upper-level outflow vanishes. By 100 hours, the maximum tangential wind of the central vortex decelerates below hurricane intensity (figure 4.5) and the central pressure increases over 30 hPa (figure 4.3). However, the vortex does not completely dissipate, since a trace of it persists during the entire simulation.

Such small intense vortices, although not emphasized, seem to be a common feature of previous high-resolution axisymmetric tropical cyclone simulations. For example, Yamasaki (1983, see his fig. 2) was the first to simulate an axisymmetric tropical cyclone using a horizontal grid spacing less than 1 km. He found that a 1–3 km vortex intermittently formed prior to the development of the main eyewall. Since Yamasaki did not initialize his model with a balanced vortex but with a series of conditionally unstable warm bubbles, the vortex formation is not dependent on the pre-existence of ambient relative vorticity; however, it could be dependent on the ambient conditional instability. Willoughby et al. (1984) produced a similar feature using 2 km horizontal grid spacing.

In both of these examples, the vortex never reaches hurricane intensity and eventually dissipates. We speculate that the disparity between these results and those of the control

experiment is primarily due to differences in the use of diffusion. In the control experiment, as described in section 2.2.1.1, we use the third-order derivative constraint (i.e., $j = 3$) with a filtering scale length of $2\Delta x$ (i.e., $l_c = 2$). This is equivalent to hyperdiffusion with a sixth-degree taper in the spectral response and half-amplitude damping for the $2\Delta x$ wavelength signal (see appendix F). In contrast, both Yamasaki (1983) and Willoughby et al. (1984) used Fickian diffusion. This type of diffusion has a broader spectral response and possibly greater damping, if the eddy diffusion coefficient is relatively large. Yamasaki used constant eddy diffusion coefficients of 100 $m^2\ s^{-1}$ and 10 $m^2\ s^{-1}$ in the horizontal and vertical, respectively, whereas Willoughby et al. used a variable coefficient that was a function of the sub-grid turbulent kinetic energy. It is difficult to compare the numerical diffusion of this model to the physical forms of diffusion used by Yamasaki and Willoughby et al. In the next chapter, however, we show that if physical diffusion is included in the model, the central vortex is eliminated.

Although the central vortex is an artifact of the axisymmetric geometry, we may speculate that similar phenomena occur in nature. We can imagine a scenario in which random areas of moist convection generate internal gravity waves that may constructively interfere with one another to produce convergence, ascent, and moist convection (Emanuel, 1983; Mapes, 1993). This convection may ultimately produce the incipient vortex from which the tropical cyclone emerges.

4.2.1.3 Eyewall Replacement Cycle

From 100 to 180 hours, the tropical cyclone gradually intensifies. As shown in figure 4.3, the maximum tangential wind increases from $v_{max} = 52$ to 120 m s^{-1} while the central pressure simultaneously decreases from $p_{min} = 933$ to 854 hPa. Figure 4.3 also shows that this gradual overall increase of intensity is not steady but highly variable. For instance, during the 12-hour period following 118 hours, v_{max} oscillates over 20 m s^{-1}. The variability of the tropical cyclone intensity is apparently caused by disturbances of the boundary layer inflow and the formation of secondary rings of convection.

Since the tropical cyclone intensity is maintained by the continuous transport of angular momentum and entropy into the storm core, we examine the variability of intensity by analyzing the relative contribution of the transport terms in the tendency equations of angular momentum and entropy. To begin this analysis, we rewrite the equations for the tangential momentum per unit total mass (2.59) and for the dry-air-specific entropy of moist air (2.61) in the form

$$\frac{\partial M}{\partial t} + u\frac{\partial M}{\partial r} + \left(w + \frac{\rho_r}{\rho}W\right)\frac{\partial M}{\partial z} + \frac{\partial F_M}{\partial z} = 0, \tag{4.3}$$

$$\frac{\partial s}{\partial t} + u\frac{\partial s}{\partial r} + w\frac{\partial s}{\partial z} + \frac{1}{\rho_a}\frac{\partial}{\partial z}\left(\rho_r s_r W\right) + \frac{\partial F_s}{\partial z} = 0, \tag{4.4}$$

wherein $M = rv + \frac{1}{2}fr^2$ is the absolute angular momentum and $F_M = rF_v$. Figures 4.7–4.9 show radial profiles of each term in (4.3) and (4.4) computed at a height of 500 m and at hours a) 118, b) 121, and c) 127. For comparison and orientation, these figures also include profiles of the three wind components at 500 m, the tangential wind field, and the location of the convection and precipitation.

At 118 hours, we observe a weakening primary eyewall with a secondary eyewall beginning to form. From about 20 to 40 km, the downward and radial advection of low-entropy air by mesoscale downdrafts beneath the stratiform precipitation is greater than the upward turbulent flux of high entropy air from the surface, thus the entropy of the boundary layer decreases (figure 4.7d). This low-entropy air is then advected into the storm core, where it weakens the convection of the primary eyewall by eliminating low-level conditional instability. Any remaining convection is sustained by forced ascent due to surface convergence and buoyant ascent above the freezing level. Simultaneously, surface friction is depleting the angular momentum of the vortex more rapidly than horizontal advection can replenish it (figure 4.7c). Some acceleration of the vortex remains near 12 km radius, due to the rapid vertical advection of angular momentum from below. Without high entropy air at

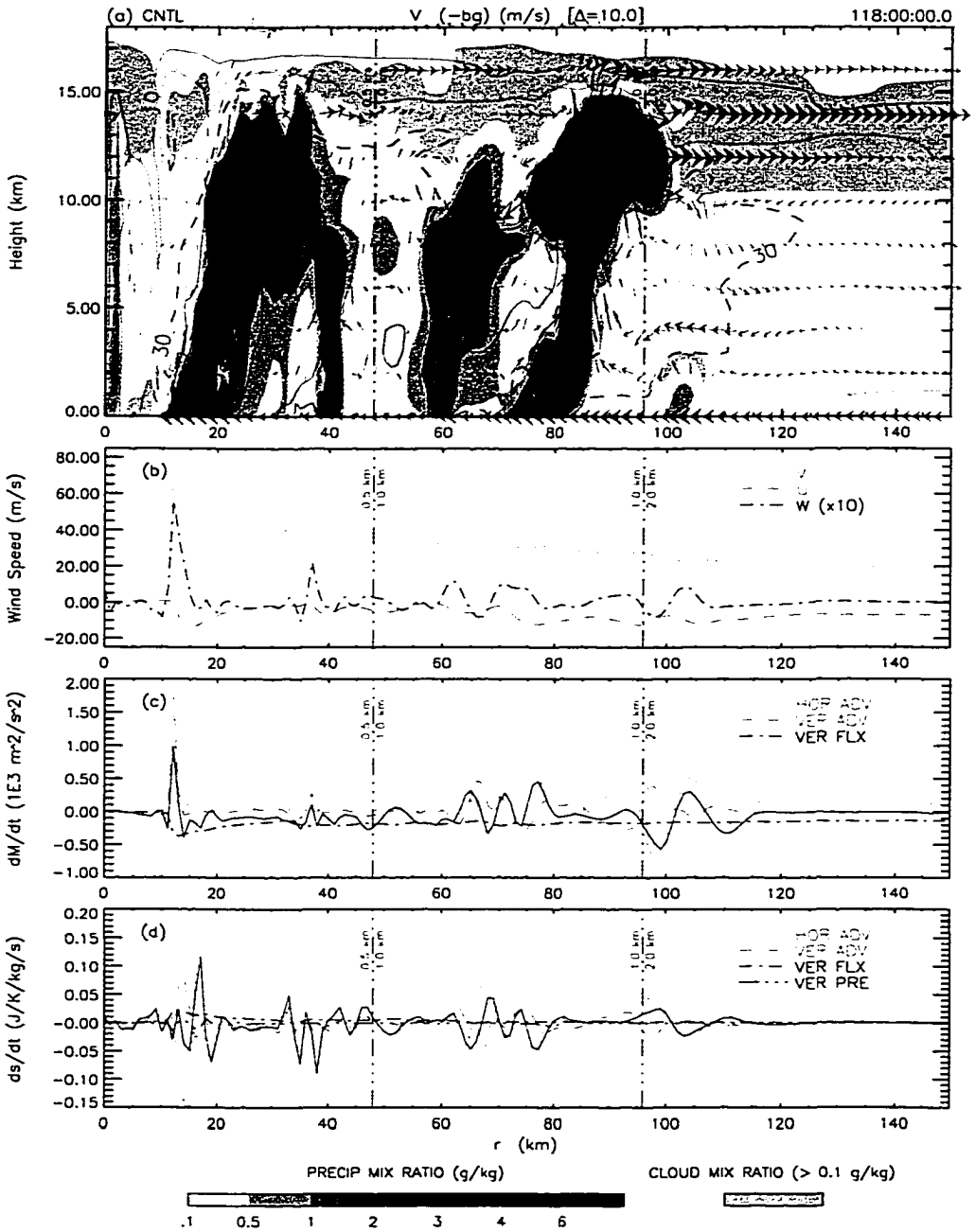

Figure 4.7: CNTL Experiment — Evolution of a concentric eyewall cycle at 118 hours. The panels contain the a) tangential wind (contour), radial and vertical winds (vectors), cloud (gray shading, 0.1 g kg^{-1}), and precipitation (blue shading, .1, .5, 1, 2, 3, 4, 6 g kg^{-1}); b) tangential (dot), radial (dash), and vertical (dash-dot, $\times 10$) wind components (radial profiles); c) equation (4.3) terms (radial profiles), and d) equation (4.4) terms (radial profiles). The terms in (4.3) and (4.4) are the local change (solid), horizontal advection (dot), vertical advection (dash), vertical turbulent flux (dash-dot), and precipitation flux (chain). All of the profiles were computed at a height of 500 m. For further explanation of the figure markings, see figures 4.2 and 4.4.

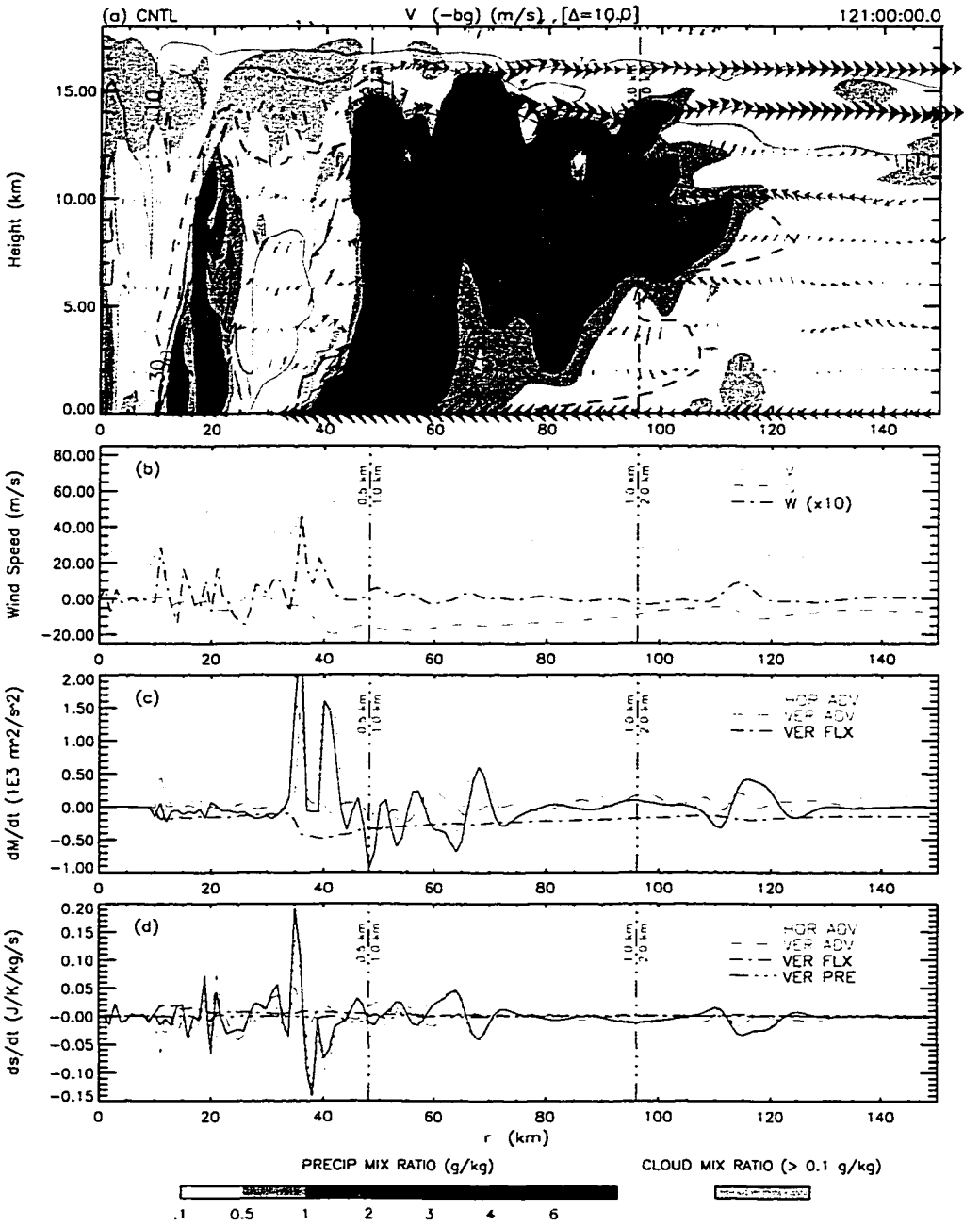

Figure 4.8: CNTL Experiment — Same as figure 4.7 except the time is 121 hours.

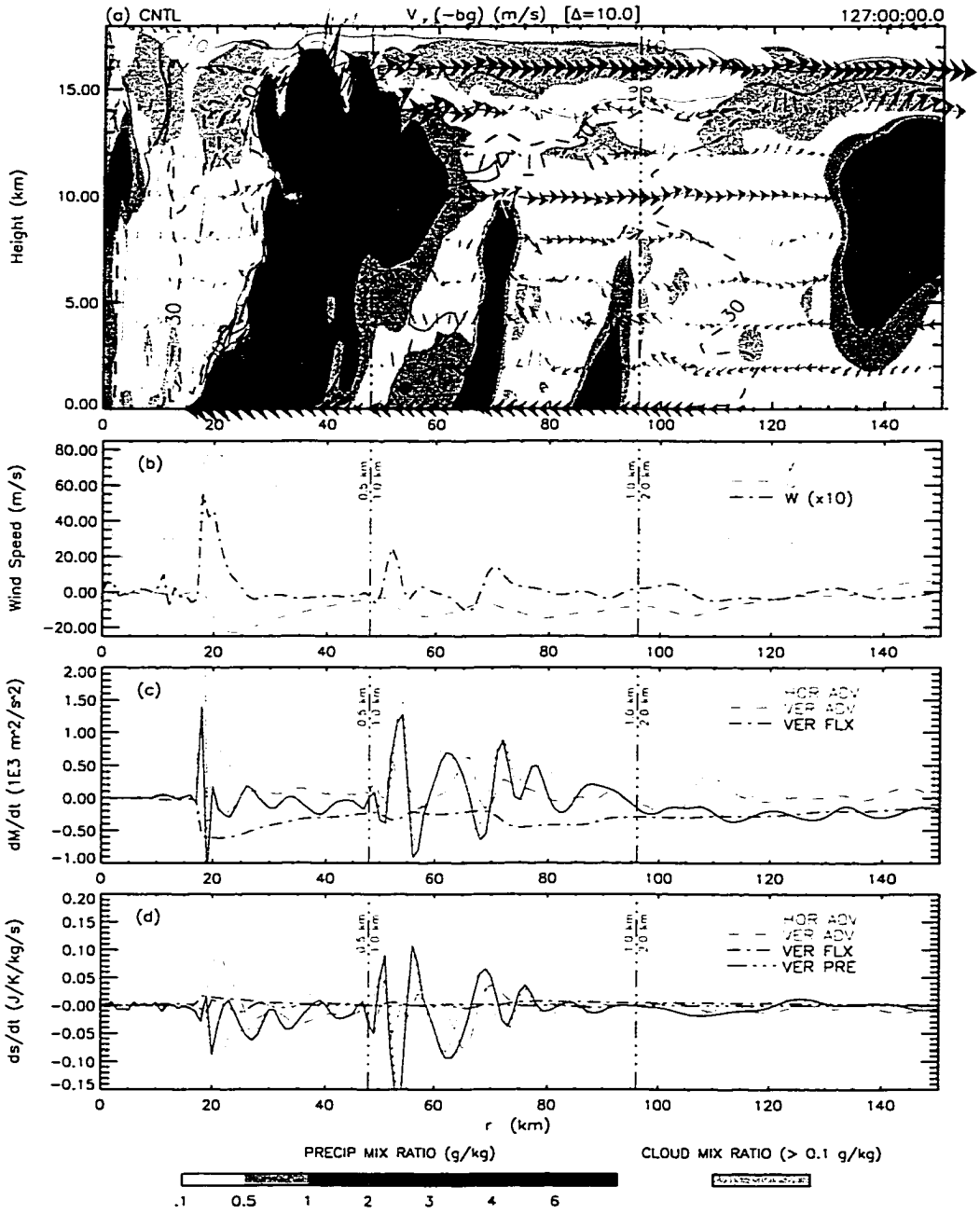

Figure 4.9: CNTL Experiment — Same as figure 4.7 except the time is 127 hours.

the surface to drive the convection and the deep upward branch of the secondary circulation, and without the import of angular momentum, both the eyewall and the vortex begin to decay. In contrast, a secondary eyewall, or ring of convection, begins to develop and intensify at a radius of about 80 km (figure 4.7a). In this case, the absence of a stratiform-precipitation-induced downdraft does not obstruct the transport of high entropy and angular momentum-rich air into this developing outer eyewall. The secondary eyewall propagates inward at a speed of -1.5 m s^{-1}, which agrees well with the observations of Willoughby et al. (1982).

By 121 hours, as seen in figure 4.8, the two eyewalls begin to interact and compete, with the outer, or secondary, eyewall dominating the competition. Inertia-gravity waves generated by the outer eyewall drive a secondary circulation, which dries the atmosphere between the two eyewalls (figure 4.8a). This dry air is entrained into the outer edge of the primary eyewall, weakening the convection. Eventually, the subsidence of the secondary circulation counteracts the ascent within the primary eyewall (Shapiro and Willoughby, 1982; Willoughby et al., 1982). In the boundary layer, the transport of entropy and angular momentum to the primary eyewall is almost completely disrupted by the presence of the secondary eyewall (figure 4.8c and d). All of these factors contribute to the eventual demise of the primary eyewall [see Camp and Montgomery (2001) for similar conclusion]. However, the demise of the secondary eyewall has also begun as low entropy air is advected into the boundary layer by the mesoscale downdrafts.

Notice the different updraft slopes of the weakening primary eyewall and the strengthening secondary eyewall at 121 hours. The slope of the primary eyewall updraft is approximately 59° from the horizontal, whereas the slope of the secondary eyewall updraft varies from 17° in the lower troposphere to 43° in the upper troposphere. In part, the slopes vary due to the baroclinicity of the vortex; however, the slope of the secondary eyewall is also modified by both the gradient and hydrostatic imbalance of the updraft. In the lower troposphere, the flow exiting the boundary layer is supergradient (Willoughby, 1990). Such supergradient flow was recently observed in Hurricane Claudette (1991) using Doppler derived winds

(Viltard and Roux, 1998). To restore gradient balance, the flow accelerates outward, decreasing the updraft slope. In contrast to this horizontal gradient imbalance, a vertical hydrostatic imbalance causes the updraft slope in the upper troposphere to increase. As condensate freezes in the updraft core above the 0°C isotherm, latent heating increases the buoyant acceleration and the updraft slope. As pointed out by Willoughby et al. (1984), the mid-level inflow of absolute angular momentum into the secondary eyewall also decreases the slope. Radar reflectivities obtained from Hurricane Bonnie (1998) during an eyewall replacement cycle showed similar structure (D. Cecil, 2000, personal communication).

As illustrated in figure 4.9, the secondary eyewall completely replaces the primary eyewall by 127 hours, and then it too begins to decay. In many respects, the new primary eyewall is identical to the original. This similarity includes the weakening processes and the possible formation of another secondary eyewall near 65 or 85 km. Ultimately, figure 4.3 shows that the new primary eyewall also decays by about 132 hours. This cycle occurs continuously and explains the periodic variations of the tropical cyclone intensity seen in figure 4.3. However, it does not explain how the cycle begins through the formation of the secondary eyewall.

4.2.1.4 Formation of Secondary Eyewalls

The secondary eyewall develops due to ascent forced by low-level convergence and the conditional instability of the atmosphere above. Figures 4.10–4.12 depict the development of the secondary eyewall prior to 118 hours using the entropy and angular momentum fields, as well as soundings through and immediately outside of the convection. The external sounding, figure 4.10b, shows that the surface fluxes of entropy and water mass warm and moisten the near surface air to 26.8°C and 100% RH, generating conditional instability. As shown in figures 4.10c and d, low-level convergence near 90 km, produced either by friction or a weak outflow boundary, triggers the initial moist convective ascent. At this time, there is no apparent disturbance above the convection to support the ascent. Over the next 30 minutes, the cloud top gradually rises from 4 km to just above 7 km. As

the condensate begins to freeze, the additional buoyancy force rapidly accelerates the updraft and causes the moist convection to quickly ascend through the remainder of the troposphere.

As the updraft ascends, it vertically advects absolute angular momentum, creating radial gradients that alter the inertial stability of the vortex. Figure 4.12d shows the development of a local minimum of absolute angular momentum in the middle troposphere (i.e., -3.5×10^5 m^2 s^{-1}) and a local maximum in the upper troposphere (i.e., 8.5×10^5 m^2 s^{-1}), as the updraft impinges on the tropopause. Radially inward of the upper-tropospheric maximum, the inertial stability of the flow increases, while the flow becomes inertially unstable outside of the maximum. As a result, the upper-level outflow rapidly accelerates outward. In contrast, radially inward of the middle-tropospheric minimum, the flow becomes inertially unstable, while the inertial stability of the flow increases outside of the minimum. The inertial stability on the outer edge of the convection restricts the radial entrainment necessary to support the accelerating updraft; however, the inertial instability on the inner edge reinforces the entrainment. The net effect of the accelerations induced by the inertial instability acts to tilt the updraft outward.

The complex interaction of the surface inflow and upper-tropospheric outflow from the secondary ring of convection results in the discrete propagation of the secondary eyewall. At the surface, the superposition of the outflow from the convective downdraft and the outflow from the secondary circulation of the vortex produces net convergence radially inward from the secondary eyewall. This convergence is enhanced radially inward of the accelerating vortex. As the downdraft descends into the boundary layer, it advects relatively high absolute angular momentum into the upper-level outflow (figure 4.12d). The inward advection of this absolute angular momentum produces a secondary maximum in the radial profile of the surface tangential wind. In the middle troposphere, the preferential entrainment inward of the secondary eyewall discussed in the previous paragraph reinforces the ascent driven by the surface convergence. The periodic formation of convection inward of the eyewall convection leads to the discrete contraction of the secondary eyewall. This discrete

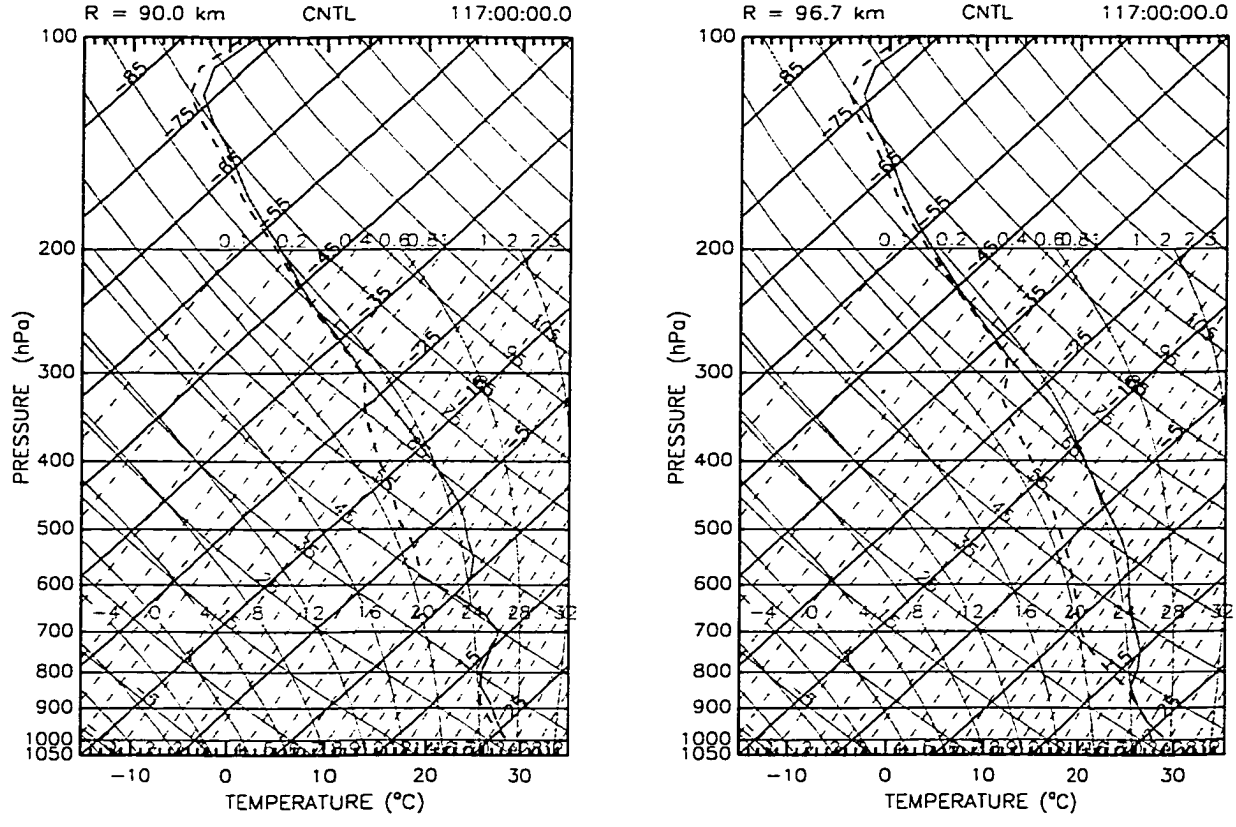

(a) (b)

Figure 4.10: CNTL Experiment — Evolution of the developing secondary eyewall at 117.0 hours. The panels contain the vertical profiles of temperature and dewpoint temperature a) through and b) outside of the secondary eyewall, and the contours of c) specific entropy and d) absolute angular momentum, the radial and vertical winds (vectors), cloud (gray shading, 0.1 g kg^{-1}), and precipitation (blue shading, .1, .5, 1, 2, 3, 4, 6 g kg^{-1}). For further explanation of the figure markings, see figures 4.2 and 4.4.

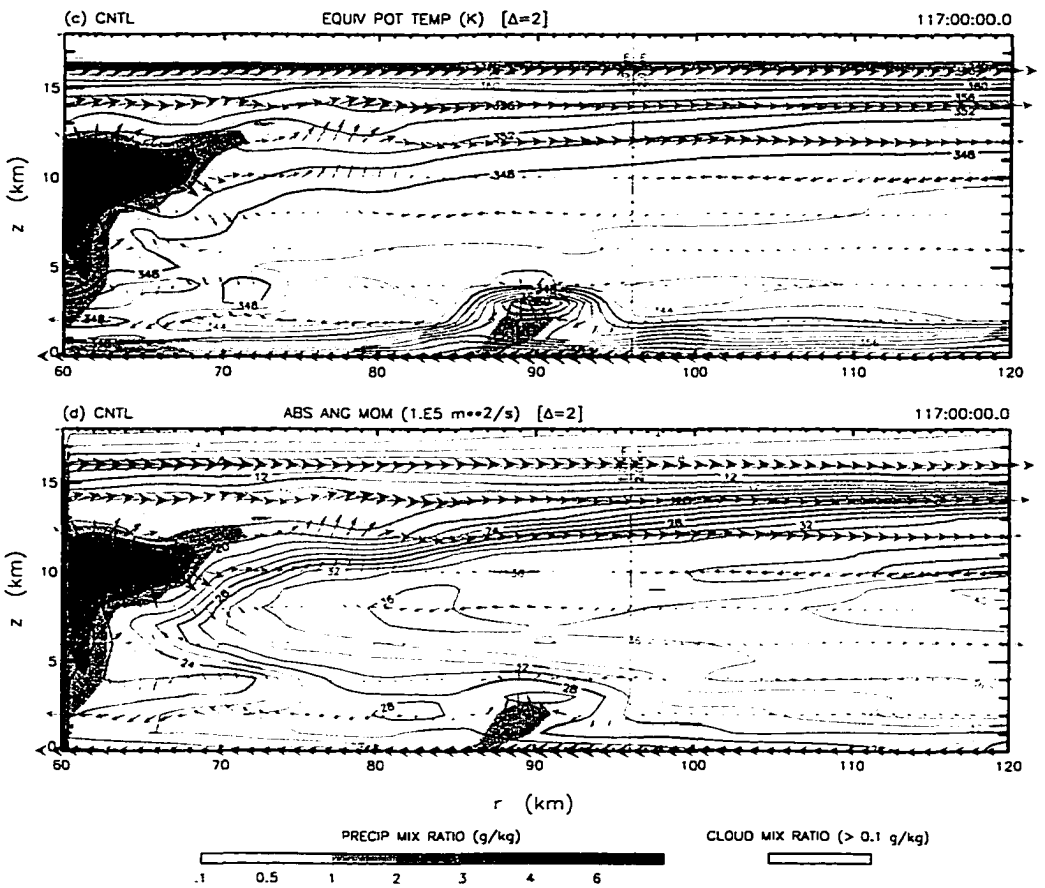

Figure 4.10: Continued.

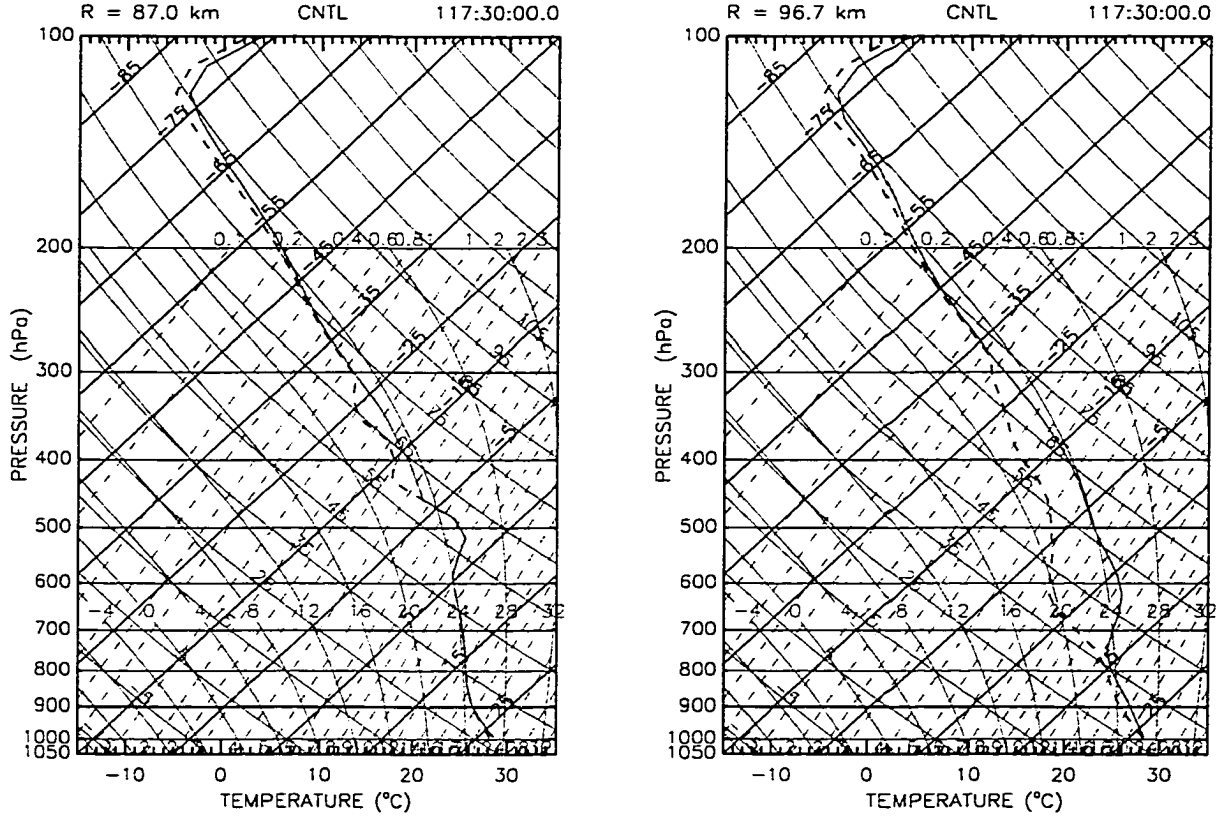

(a) (b)

Figure 4.11: CNTL Experiment — Same as figure 4.10 except the time is 117.5 hours.

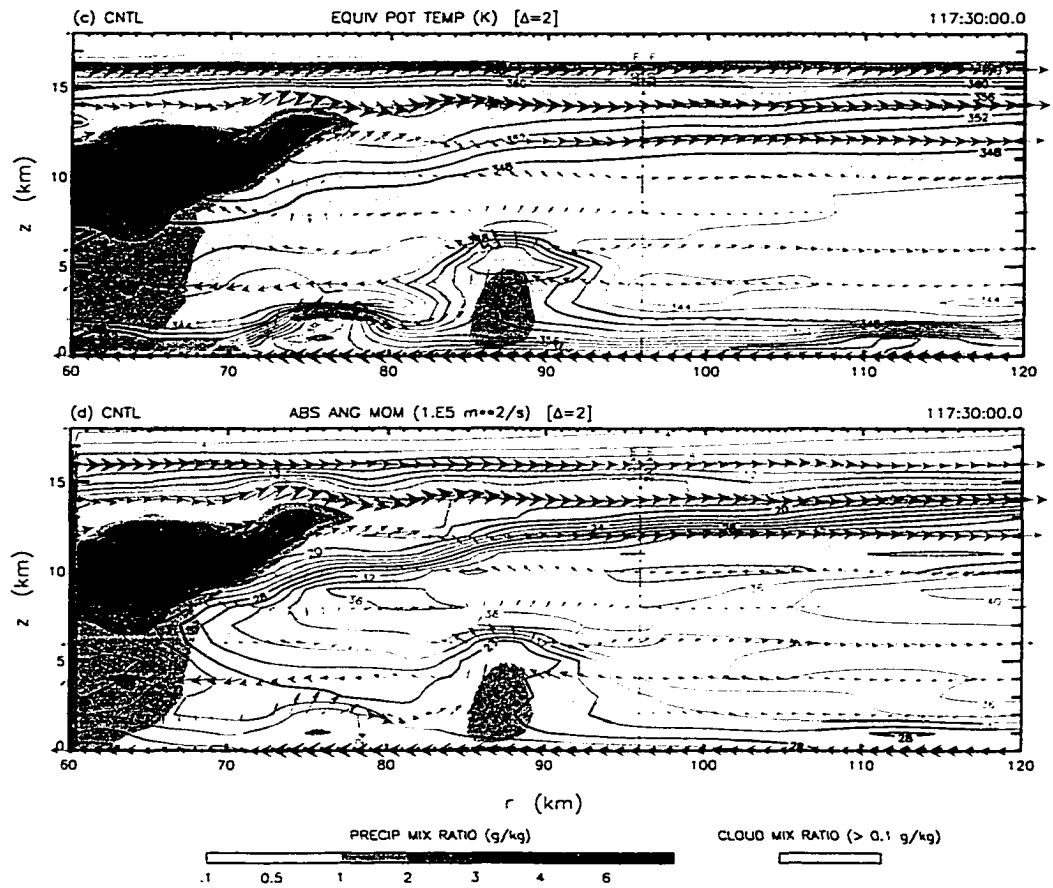

Figure 4.11: Continued.

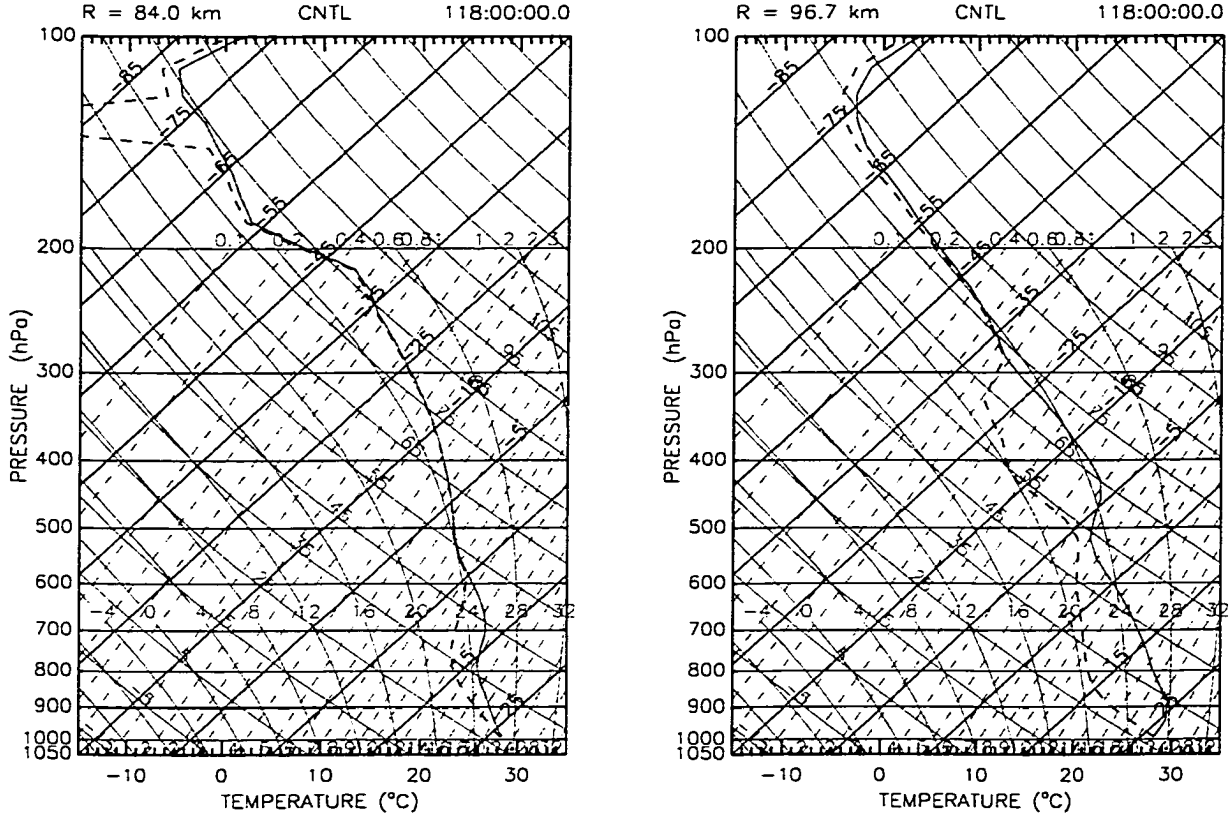

(a) (b)

Figure 4.12: CNTL Experiment — Same as figure 4.10 except the time is 118.0 hours.

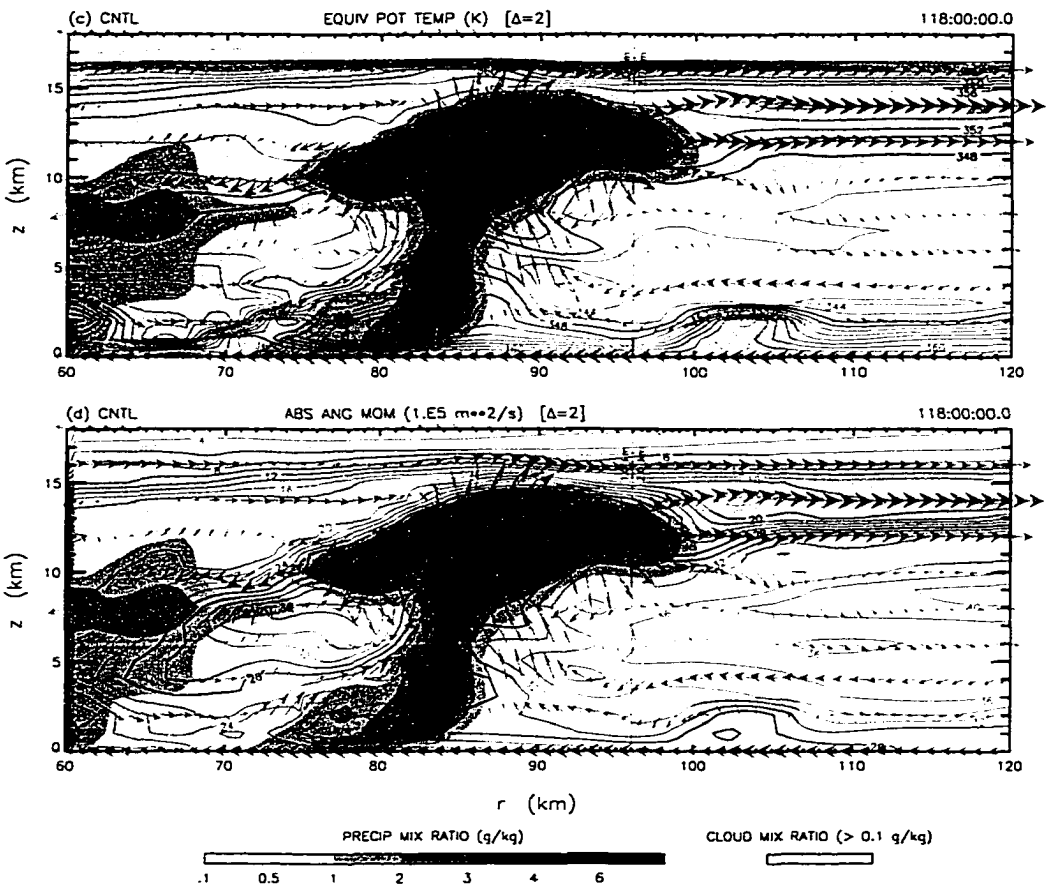

Figure 4.12: Continued.

movement ceases when the frictional convergence of the intensifying vortex dominates the production of new convection. Although the exact radius at which this occurs is unclear, the transition appears to occur within 40 km of the center.

4.2.2 Tropical Cyclone Steady State

Beyond 180 hours, the vortex settles into a quasi-steady state. We use the term quasi-steady to stress that, while the gradual intensification of the vortex ceases, there remain significant variations of the intensity resulting from the mechanism of eyewall replacement discussed previously. To understand the basic dynamics of the steady-state tropical cyclone, we next examine the 180–240 hour mean steady-state structure followed by a discussion of the variability.

4.2.2.1 Kinematic Structure

The steady-state tropical cyclone is similar in structure to observed and simulated storms but much more intense. Figures 4.13a–c depict the 180–240 hour average primary and secondary circulations. The cyclonic vortex, or primary circulation, is accelerated to a maximum mean surface wind speed of $v_{max} = 107$ m s^{-1}, with the peak located beneath the eyewall at a radius of 13.5 km. This intense vortex is produced by the advection of high angular momentum air toward the center, within the inflow branch of the secondary circulation. A fraction of this angular momentum is depleted by surface friction. This same air is later advected away from the center within the outflow branch of the secondary circulation, accelerating an anticyclonic vortex with a maximum wind speed of -30 m s^{-1} located at a radius of 1250 km and a height of 14 km (not shown). Outward from the eyewall, the rapid depletion of angular momentum near the surface also elevates the tangential wind maximum. As discussed previously, the advection of this elevated angular momentum into the boundary layer by convective downdrafts helps intensify the surface vortex. At the center, a remnant of the initial small intense vortex persists with an elevated tangential wind speed of 29 m s^{-1} at a height of 8 km.

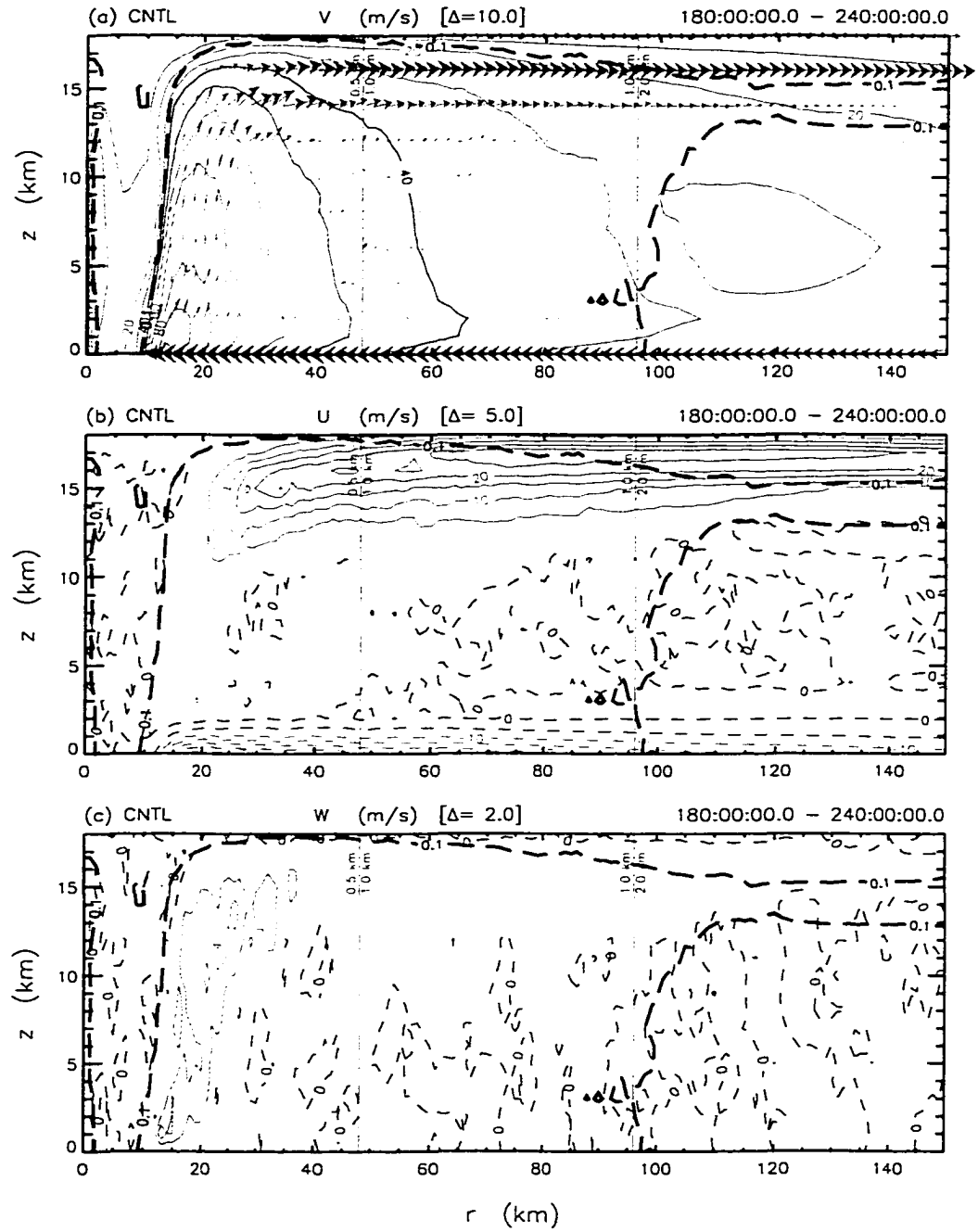

Figure 4.13: CNTL Experiment — time-averaged (180–240 hours) cross-sections of the a) tangential, b) radial and c) vertical wind speeds (ms^{-1}). The heavy dashed line denotes liquid water mixing ratios greater than 0.1 g kg^{-1}. For further explanation of the figure markings, see figure 4.2.

A weak secondary tangential wind maximum forms outside of the stratiform precipitation. This secondary maximum is similar to the mid-tropospheric vortex associated with many mesoscale convective systems (Leary and Rappaport, 1987; Gamache and Houze, 1985; Raymond and Jiang, 1990; Brandes, 1990; Houze, 1993). Although not completely evident in figures 4.13b and c, gradually ascending outflow overlies descending inflow between 40 and 120 km (Dodge et al., 1999). This solenoidal circulation is produced, in the mean, by outward-propagating convective updrafts overlying inward-propagating convective and mesoscale downdrafts (see figure 4.12 for example). Similar to the mesoscale convective systems cited above, which develop a vortex through horizontal convergence and vorticity stretching, the secondary tangential wind maximum develops from the conservation of angular momentum within the mid-tropospheric inflow.

The horizontal branches of the secondary circulation are concentrated into shallow layers at the surface and near the tropopause. According to figure 4.13b, the inflow branch is confined primarily within a layer below 2 km, with a maximum radial wind speed of -31.8 m s^{-1} located at 21 km. The maximum inflow lies just outside the radius of maximum tangential wind. Consequently, the radius of maximum convergence is then approximately collocated with the radius of maximum wind. This configuration is consistent with the steady-state structure proposed by Shapiro and Willoughby (1982) and Shapiro (1983). As noted by Montgomery (2001, personal communication), the maximum radial inflow at the surface is approximately a third of the surface maximum tangential wind speed, which is consistent with the observational evidence. Similar to the inflow, the most intense outflow is confined to a shallow layer between 12 and 18 km. The maximum outflow of 29.5 m s^{-1}, however, is located at a radius of about 75 km, which is over 50 km away from the eyewall, indicating that a broad region of divergence exists above and outside of the eyewall.

The vertical branches of the secondary circulation vary significantly in intensity and horizontal scale. Immediately above and sloping away from the region of maximum surface convergence (see figures 4.13b and c) is the ascending branch of the secondary circulation,

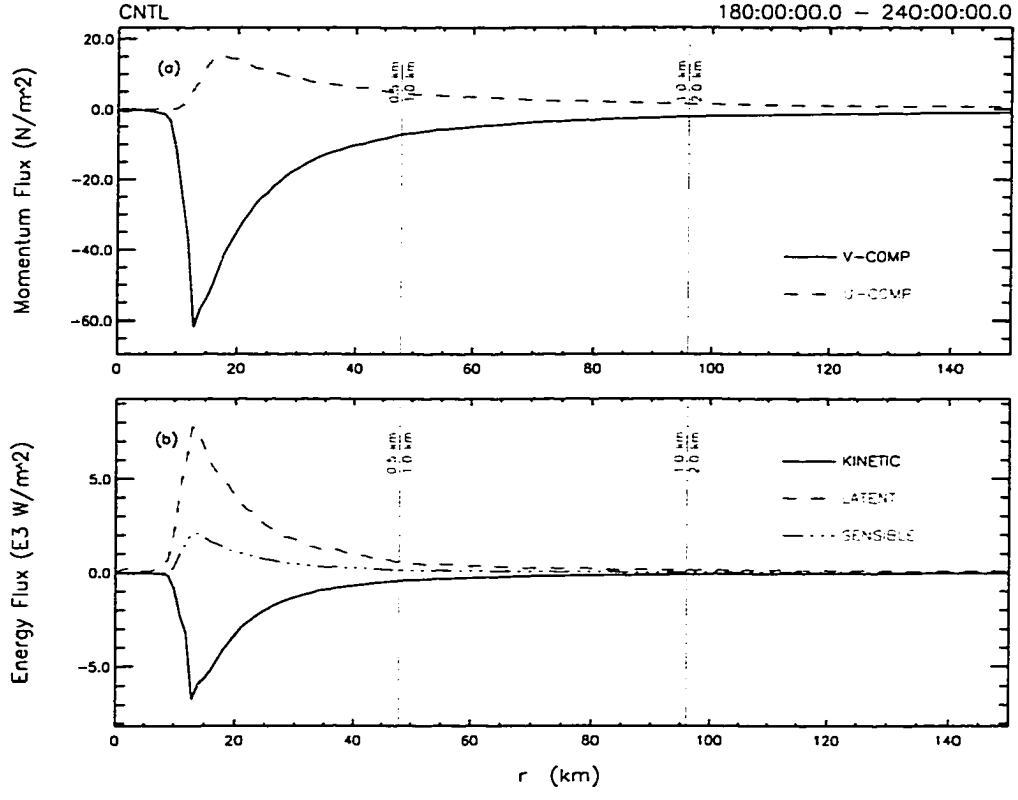

Figure 4.14: CNTL Experiment — time-averaged (180–240 hours) radial profiles of the a) u-component (solid) and v-component (dashed) surface momentum fluxes; and the b) kinetic (solid), latent (dash), and sensible (dash-dot) surface energy fluxes. For further explanation of the figure markings, see figure 4.2.

embedded within the eyewall convection. Two prominent maxima, with vertical velocities of approximately 5.5 m s^{-1}, are located within the ascending branch just above the boundary layer and in the upper troposphere. The low-level maximum is produced by the abrupt vertical redirection of the inflow near the radius of maximum tangential wind, whereas the upper-level maximum is produced by the additional buoyant acceleration resulting from the release of latent energy by freezing condensate. The width of the ascending branch also increases with height, in response to the broad region of divergence discussed previously. In contrast, the compensating subsidence in the descending branch of the secondary circulation is very weak and extends into the far field of the domain (not shown).

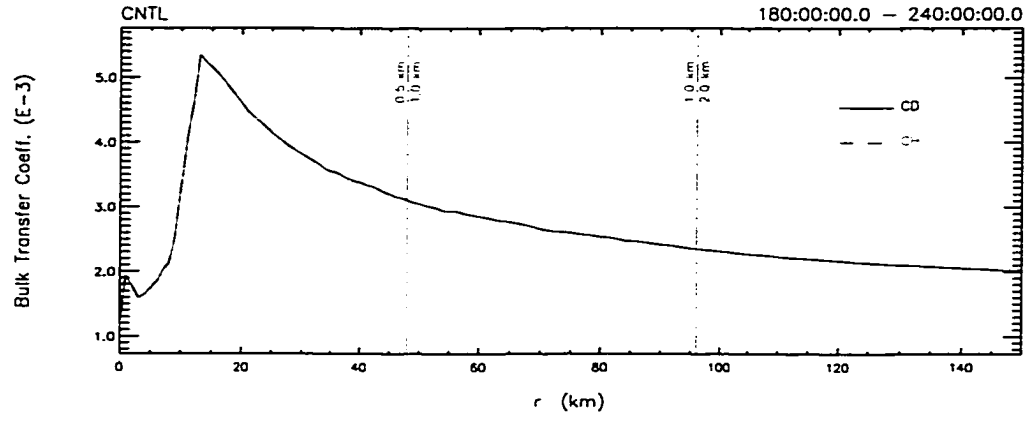

Figure 4.15: CNTL Experiment — time-averaged (180–240 hours) radial profiles of the bulk transfer coefficients for momentum (solid) and energy/mass transfers (dashed). If only a single curve is shown, then the coefficients are identical. For further explanation of the figure markings, see figure 4.2.

The extremely intense winds of the primary and secondary circulation also generate large surface fluxes of momentum and energy. Figures 4.14a and b show the radial profiles of the surface momentum and energy fluxes averaged from 180 to 240 hours. The tangential and radial momentum fluxes, or surface stresses, near the radius of maximum wind are −62 and 17 N m^{-2}, respectively. In contrast, observed surface stresses are generally less than 10–20 N m^{-2} (Hawkins and Rubsam, 1968; Hawkins and Imbembo, 1976; Shay et al., 1989; Ginis and Sutyrin, 1995). Additionally, the surface latent, sensible, and kinetic energy fluxes near the radius of maximum wind are 7800, 2200, and 6700 W m^{-2}, respectively. These values contrast with the observed surface fluxes of latent and sensible energy, which are at the extreme only 1858 and 355 W m^{-2}, respectively (Black and Holland, 1995). Finally, the Bowen ratio, or the ratio of the sensible to latent heat flux, is 0.28, which is about twice the observed value of 0.16 (Hawkins and Imbembo, 1976; Frank, 1978; Black and Holland, 1995).

The incredible surface fluxes result primarily from the large velocity-dependent mass, momentum, and energy exchange coefficients. Figure 4.15 shows the 180–240 hour average radial profiles of the drag coefficient (C_D) and the mass and energy exchange coefficient (C_H). Recall that for the control experiment, we chose $C_H = C_D$; therefore, the two profiles are identical. At the radius of maximum tangential wind, the profile of C_D has a

maximum of 5.3×10^{-3}. This large value is in agreement with the wind speed dependence of C_D as defined by equation (4.2) and with linearly extrapolated values of C_D obtained from past observational estimates, but is significantly greater than the typically observed estimates [e.g., $C_D \sim 2 \times 10^{-3}$, (Hawkins and Rubsam, 1968; Moss and Rosenthal, 1975)]. According to equation (2.26), this implies that the surface flux will also be greater than typically observed.

4.2.2.2 Thermodynamic Structure

The thermodynamic structure of the tropical cyclone is consistent with a warm-cored thermally-balanced vortex. Figure 4.16 shows the 180–240 hour mean cross-sections of T', p', and the water vapor mixing ratio (μ_v). The maximum T' produced by the secondary circulation of the primary eyewall, neglecting the effect of the central vortex, is approximately 17 K, which is centered on the axis at a height of 12 km or 197 hPa. Hydrostatically, the temperature distribution produces a minimum p' at the surface of -145 hPa or $p_{min} = 870$ hPa (see figure 4.16). In addition, the maximum pressure gradient is located near the inner edge of the eyewall, whereas there is almost no pressure gradient within the eye. This difference agrees well with the intense tangential winds beneath the eyewall and near stagnant winds inside of the eye, as shown in figure 4.13a.

The axis of maximum T' extends both outward into the stratiform precipitation and downward along the inner edge of the eyewall. Both T' anomalies result from diabatic and adiabatic warming forced by the moist convective ascent and dry descent, respectively, associated with the counter-rotating secondary circulations induced by the eyewall convection. The horizontal extent of these secondary circulations is controlled by the radius of deformation

$$\lambda = \frac{N}{\left[\left(f + \frac{\partial(rv)}{r\partial r}\right)\left(f + \frac{2v}{r}\right)\right]^{\frac{1}{2}}} H, \tag{4.5}$$

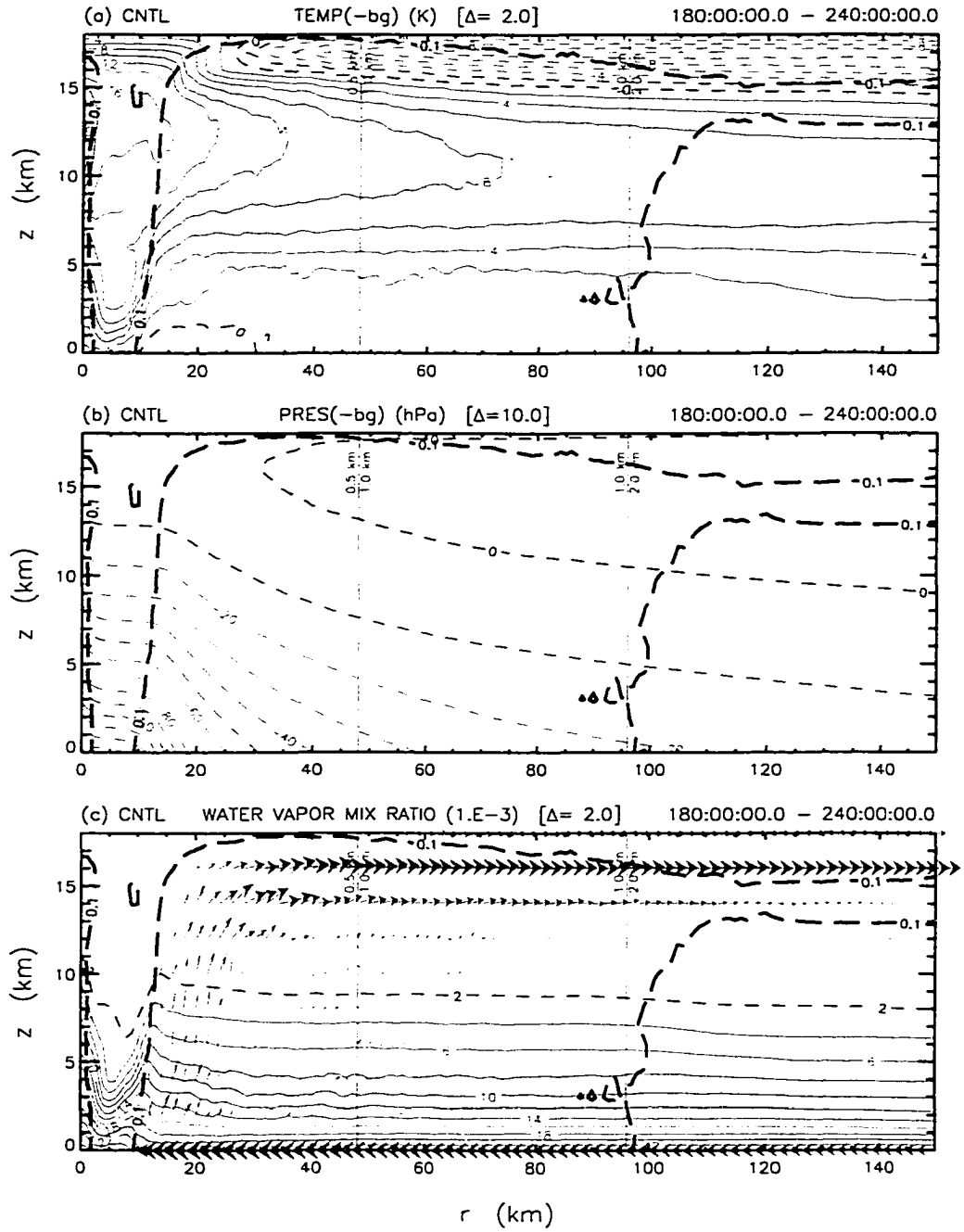

Figure 4.16: CNTL Experiment — time-averaged (180–240 hours) cross-sections of the a) perturbation temperature, b) perturbation pressure and c) water vapor mixing ratio. For further explanation of the figure markings, see figures 4.2 and 4.13.

wherein N is the Brunt-Väisälä frequency and H is the depth of the troposphere divided by π. The deformation radius is a measure of the inertial stability or "stiffness" of the vortex (Schubert and Hack, 1982). When λ is small, the vortex is stiffened such that the horizontal extent of the secondary circulation is restricted by the inertial stability of the flow. Assuming $H \approx 5$ km along the inner edge of the eyewall, λ is less than 5 km; however, within the outflow, λ is over 300 km. Therefore, we observe a narrow secondary circulation and adiabatic warming constrained to the inner edge of the eyewall, as compared to a broad secondary circulation outside of the eyewall. Note that the convection of the central vortex does produce evaporative cooling in the lower troposphere, while the predominant warming of the troposphere produces a negative surface p' over the entire domain. The latter effect results from the lack of radiative cooling discussed in section 2.1.3.2.

Minimum values of T' are found near the surface beneath the eyewall and within the outflow. Below the 0°C isotherm, both melting and evaporation cool the lower troposphere. The maximum cooling and negative T' of about 1°C are found just outside of the eyewall, where the precipitation rate is the greatest. In contrast, the negative T' in the upper troposphere is larger both in magnitude and horizontal extent. As the troposphere warms, its depth increases. The air above the tropopause adiabatically cools as it is forced upward, producing a broad temperature minimum of about -12°C. Hydrostatically, this cold anomaly induces a 1-hPa positive pressure perturbation in the outflow, which is consistent with the anticyclonic flow aloft. Rotunno and Emanuel (1987, see figure 8) produced similar temperature anomalies in an axisymmetric tropical cyclone simulation in which radiative cooling was excluded. When radiation was included, the central pressure increased and the cold temperature aloft was greatly reduced.

The dynamics of the eye and eyewall also have a distinct influence on the distribution of water vapor, as shown in figure 4.16c. Radially, μ_v is a maximum in the eyewall, due to positive vertical advection within the updraft. Inside of the eye, μ_v is a minimum along the inside of the eyewall, due to subsidence, and a maximum at the center, due to convection along the axis. At the surface, the large flux of water vapor increases μ_v outside of about

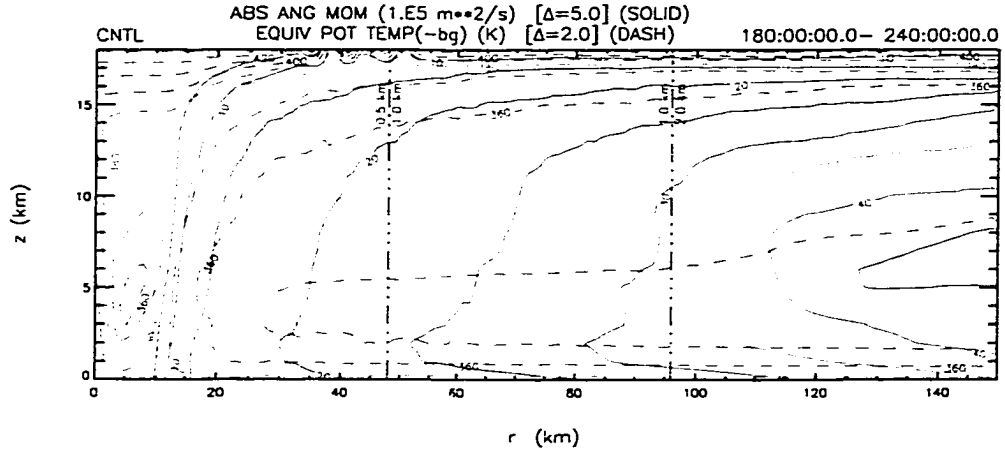

Figure 4.17: CNTL Experiment — time-averaged (180–240 hours) cross-sections of the absolute angular momentum, M (solid) and the equivalent potential temperature, θ_e (dashed). For further explanation of the figure markings, see figure 4.2.

25 km to 23.9 g kg^{-1}, which is 5.5 g kg^{-1} greater than the initial value. The corresponding surface relative humidity is nearly 100% (not shown). Beneath the eyewall, downdrafts, which have been partially dried by condensation and precipitation, produce a local surface minimum of 21.6 g kg^{-1} at a radius of 14 km.

The combined effects of temperature and water vapor on convective stability are revealed in the 180–240 average distribution of equivalent potential temperature (θ_e), as shown in figure 4.17. This figure also includes the distribution of absolute angular momentum (M). The orientation of the θ_e and M contours differs significantly across the vortex. Within the eyewall, for example, the contours are nearly aligned; however, there are subtle yet important departures. To see and understand these departures more clearly, figure 4.18a shows the 180–240 average profiles of temperature and dewpoint temperature, computed along an M contour that begins at a radius of 12 km and passes through the eyewall. Since M is materially conserved above the boundary layer, the profile represents the temperature of the ascending flow. From figure 4.18a, we observe that below the 0°C isotherm, at a height of about 5 km, θ_e is nearly conserved; however, above the 0°C isotherm, it increases due to the additional latent energy released by freezing condensate. In contrast to the eyewall, the θ_e and M contours in the surrounding environment are nearly orthogonal.

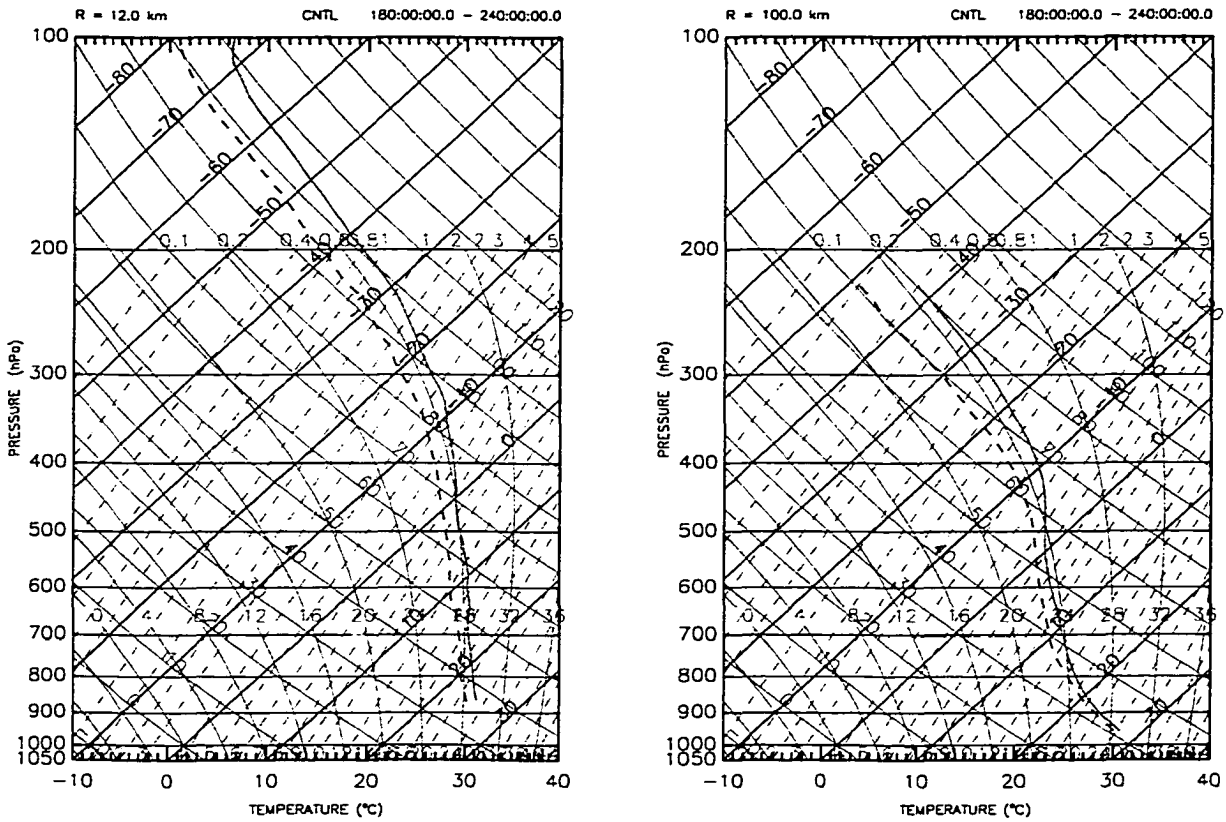

(a) (b)

Figure 4.18: CNTL Experiment — time-averaged (180–240 hours) vertical profiles of temperature and dewpoint temperature at a) $r = 12$ km and b) $r = 100$ km. Above $z = 1$ km, both profiles are computed along $R =$ constant, wherein r and R are related by $\frac{1}{2}fR^2 = rv + \frac{1}{2}fr^2$.

Figure 4.18b is identical to figure 4.18a, except that the profile begins at a radius of 100 km. Outside of the eyewall, the large surface fluxes of energy and water mass increase the surface θ_e, generating significant conditional instability in the lower troposphere. As discussed previously, this instability is a prerequisite for the formation of secondary rings of convection. Notice also that a weak stable layer develops above the 0°C isotherm. If the conditional instability were reduced (i.e., if the boundary layer was cooler and drier), the model might reproduce the multi-tiered cloud structures often observed in the tropical atmosphere (Johnson et al., 1999) and in the surrounding environment of tropical cyclones (R. Henning, 2000, personal communication).

4.2.2.3 Precipitation Structure

The distribution of precipitation is similar to the observations, but the precipitation rate is much too large. Figure 4.19 shows the 180–240 hour average cross-sections of the terminal velocity (W) and precipitation rate, overlying the cloud (μ_c) and precipitation (μ_r) mixing ratios. Above the 0°C isotherm, the terminal velocity is about 2 m s^{-1}, whereas below this level, it increases to as much as 8 m s^{-1} within the eyewall. Both values are consistent with the observations (Black and Hallett, 1996; Pruppacher and Klett, 1996). Due to the relatively small terminal velocity aloft and the intense outflow, the precipitation is advected far from the eyewall (Lord et al., 1984; Black and Hallett, 1996), resulting in surface precipitation rates of about 10–40 mm hr^{-1}. However, beneath the eyewall, W and μ_r are both large, producing a precipitation rate of over 200 mm hr^{-1}.

4.2.2.4 Moist Potential Vorticity Structure

From the kinematic and thermodynamic fields presented above, we next diagnose the moist potential vorticity of the steady state. In figure 4.20c, we see the 180–240 hour mean cross-section of the moist potential vorticity (MPV) anomaly ($P'_\rho = P_\rho - \bar{P}_\rho$). To calculate the anomaly, we derive expressions for P_ρ and $\bar{P}_\rho$ in cylindrical coordinates using equation (3.28). Assuming axisymmetry, these expressions are given by

$$P_\rho = \frac{1}{\rho}\left\{-\frac{\partial v}{\partial z}\frac{\partial \theta_\rho}{\partial r} + \left[f + \frac{\partial (rv)}{r\partial r}\right]\frac{\partial \theta_\rho}{\partial z}\right\}, \tag{4.6}$$

and

$$\bar{P}_\rho = \frac{f}{\bar{\rho}}\frac{d\bar{\theta}_\rho}{dz}. \tag{4.7}$$

Figure 4.20 also includes the vertical component of the absolute vorticity ($\zeta = f + \partial (rv) / r\partial r$), the virtual potential temperature (θ_ρ), and the eyewall cloud.

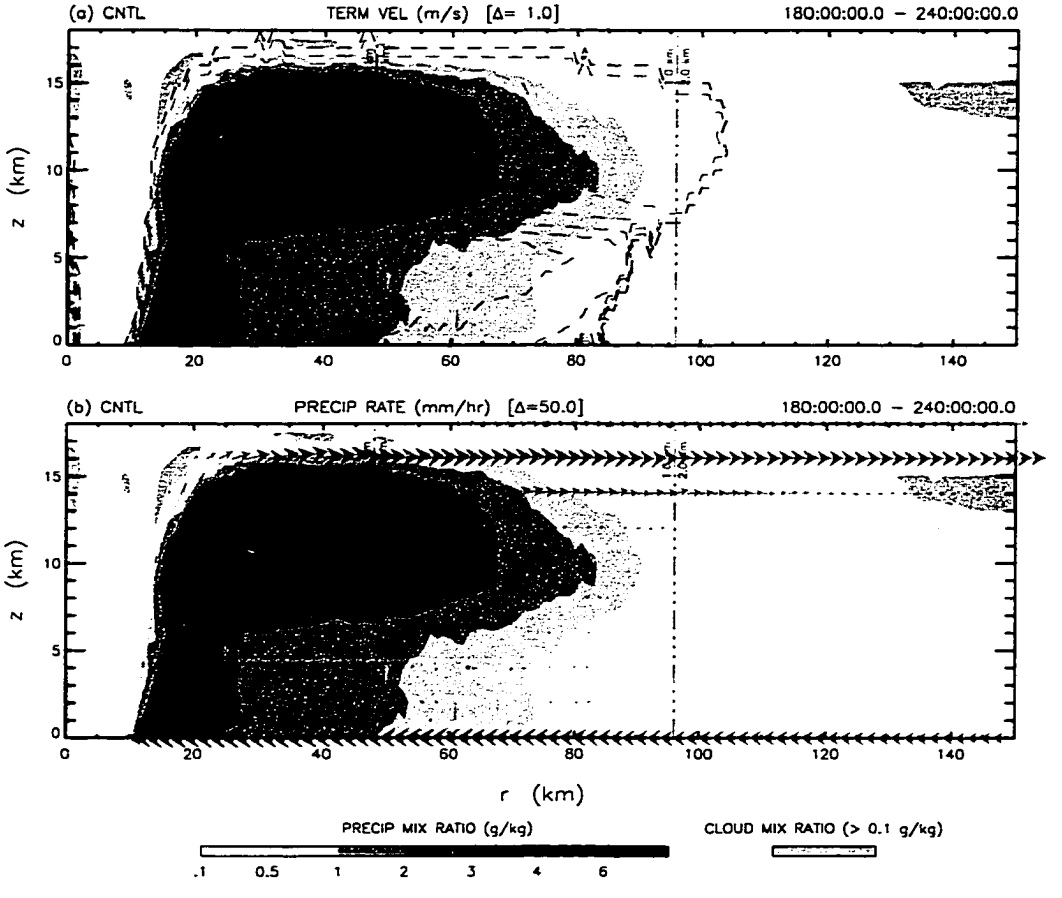

Figure 4.19: CNTL Experiment — time-averaged (180–240 hours) cross-sections of the a) terminal velocity, W and b) the precipitation rate. For further explanation of the figure markings, see figure 4.2.

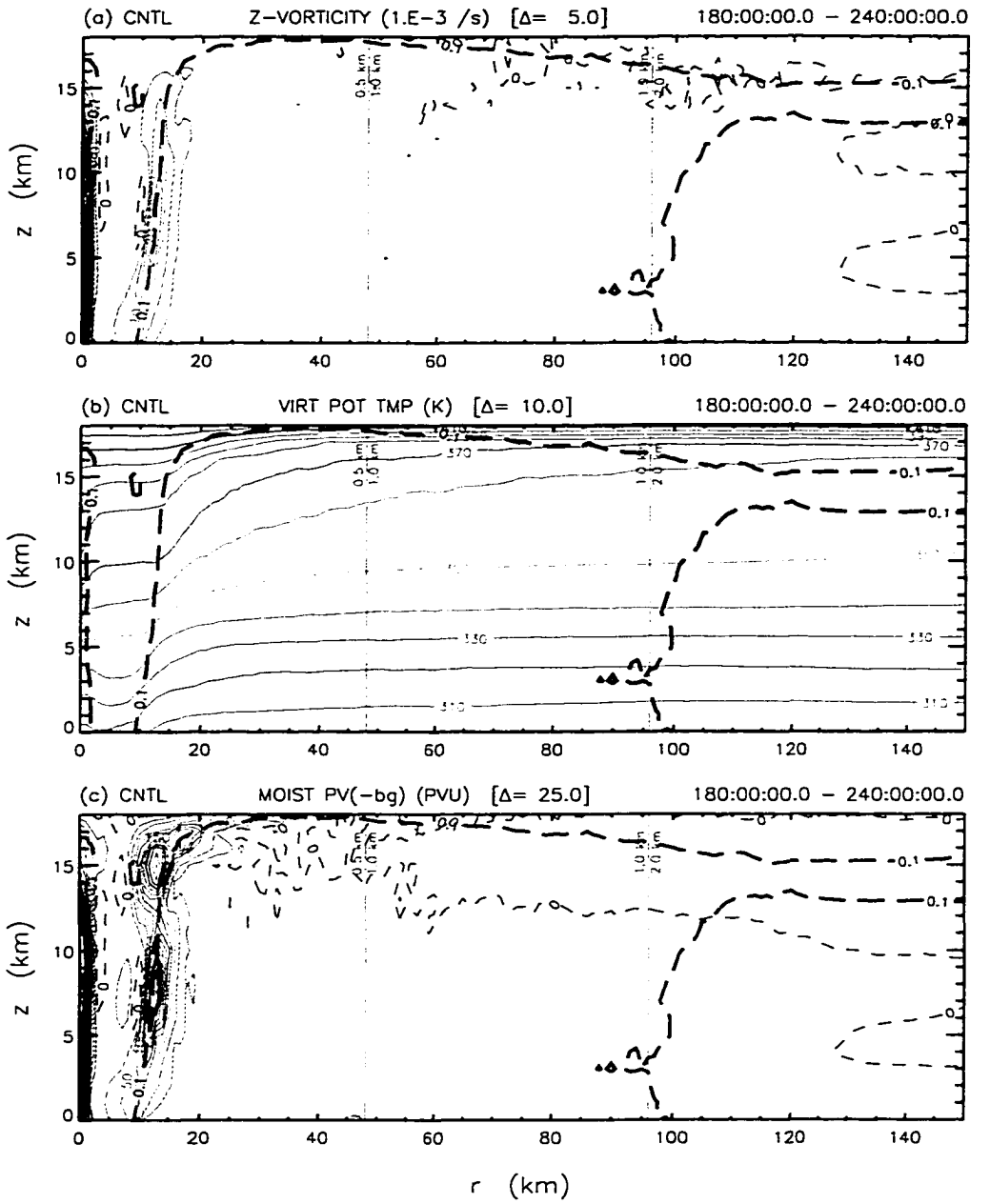

Figure 4.20: CNTL Experiment — time-averaged (180–240 hours) cross-sections of the a) vertical component of absolute vorticity, ζ; b) the virtual potential temperature, θ_ρ; and c) the moist potential vorticity, P_ρ. For further explanation of the figure markings, see figure 4.2.

The distribution of P'_ρ has three distinct maxima: one along the central axis, which is a remnant of the central vortex, and two along the inner edge of the eyewall convection. As discussed previously, the central maximum is an artifact of the axisymmetric geometry; therefore, we will not examine it in detail but concentrate instead on the other two maxima. Figure 4.13a shows that the horizontal shear across the inner edge of the eyewall is relatively large in the middle troposphere, with tangential wind speeds increasing by 60 m s^{-1} over only 5 km radius. This shear is much smaller in the upper and lower troposphere, due to the spreading of M contours, as figure 4.17 clearly indicates. In the lower troposphere, near the surface, M contours diverge as variable surface friction depletes the tangential momentum of the vortex, whereas in the upper troposphere, M contours spread within the divergent outflow of the eyewall. Obviously, as figure 4.20a confirms, such large horizontal shear translates to a maximum of ζ, and ultimately a maximum of $P'_\rho = 275$ PVU. In contrast, the upper-tropospheric maximum of $P'_\rho = 275$ PVU is a consequence of the large horizontal temperature gradient, resulting from the warm core of the vortex and the relatively large vertical shear of the tangential wind beneath the tropopause.

Other less distinct features in the distribution of P'_ρ are also of interest. Within the outflow layer, for example, $P'_\rho < 0$ and has a minimum value of $P'_\rho = -10$ PVU, which is consistent with the anticyclonic outflow. Likewise, the mid-tropospheric cyclonic inflow immediately outside of the stratiform precipitation has a maximum value of $P'_\rho = 10$ PVU. Shapiro and Franklin (1995, see figure 11) observed a similar feature with a magnitude of 4 PVU in the symmetric PV distribution of Hurricane Gloria (1985). Notice also the "notch" in the 25 PVU contour located outside of 15 km and slightly below 5 km. Beneath the 0°C isotherm, the diabatic cooling due to evaporating and melting precipitation depletes the PV, creating the vertical discontinuity.

In chapter 3, we stressed the differences between the MPV derived using θ_ρ, the equivalent PV (EPV) derived using θ_e, and the dry PV (DPV) derived using θ. These differences are revealed in the comparison of figure 4.20c with figures 4.21a and b, which show the 180–240 hour mean cross-sections of the EPV and DPV, respectively. As expected, the

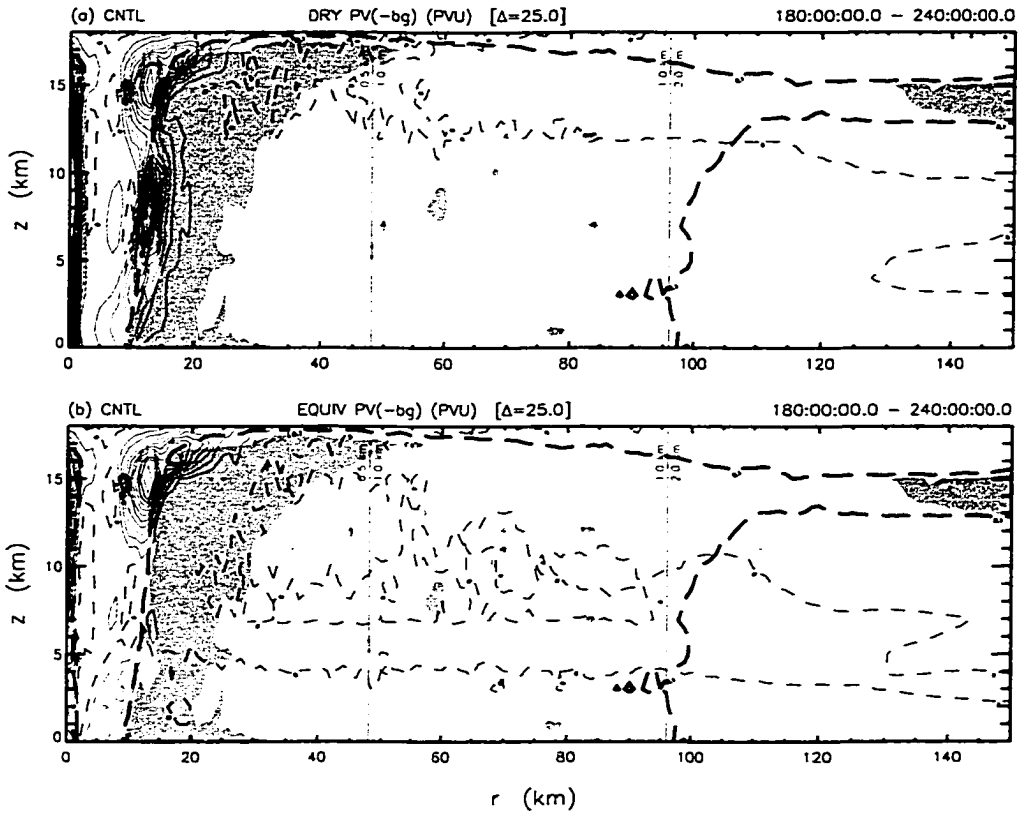

Figure 4.21: CNTL Experiment – time-averaged (180–240 hours) cross-sections of the a) dry, or Ertel, potential vorticity, P_θ and b) equivalent potential vorticity, P_e. For further explanation of the figure markings, see figure 4.2.

EPV is nearly zero in the eyewall, where the MPV and DPV are a maximum. In contrast, all three forms of PV have almost the same distribution along the inner edge of the eyewall in the upper troposphere. This similarity results because θ_e and θ_ρ reduce to θ in the upper troposphere, where the water content of the atmosphere is relatively small. Finally, comparing figures 4.20c and 4.21a, we see that the addition of vapor and condensate to the MPV apparently has little affect on the balanced dynamics, since the distribution of the MPV and DPV are nearly identical.

4.2.2.5 Deviations from Steady State

Not only the mean steady state, but the deviations from that mean, provide insight into the evolution of the tropical cyclone. Rather than calculate the statistical deviations (e.g.,

standard deviation), however, we simply consider an instantaneous example. In particular, we will examine the instantaneous state of the tropical cyclone at 180 hours.

The instantaneous kinematic fields differ significantly from the mean steady state. Figures 4.22a–c reveal that the 180-hour primary and secondary circulations are even stronger than those of the mean steady state, which were presented in figures 4.13a–c. Specifically, the maximum tangential wind speed of the primary circulation is over 120 m s^{-1} at $r = 12$ km. Similarly, the minimum and maximum radial wind speeds within the inflow and outflow layers of the secondary circulation are -34 and 47 m s^{-1}, respectively, while the maximum vertical wind speed in the ascending branch of the secondary circulation is 34 m s^{-1}. Most striking is the 25 m s^{-1} outflow atop the boundary layer within the eyewall. Similar outflows of 10–15 m s^{-1} are collocated with the convective updrafts at $r = 48$ and 60 km. In contrast, a weak secondary circulation is evident along the inner edge of the eyewall. Weak subsidence of 2–5 m s^{-1} is evident just inside of the primary eyewall. This extremely narrow secondary circulation results from the increased inertial stability along the inner edge of the eyewall, which decreases λ and restricts the radial flow (Shapiro and Willoughby, 1982).

Outside of the eyewall, the instantaneous state reveals convective updrafts and mesoscale downdrafts that are not evident in the steady state. Figure 4.22c shows two convective updrafts at $r = 48$ and 60 km, with maximum vertical velocities of 18 and 4 m s^{-1}, respectively. Freezing of condensate above the 0°C isotherm warms and buoyantly accelerates the updrafts, causing the inner deeper updraft to be more intense than the outer shallow updraft. Likewise, melting of condensate below the 0°C isotherm cools and buoyantly accelerates the downdraft. As a result, the convective updrafts are surrounded by mesoscale downdrafts of 1–2 m s^{-1} generated by the melting stratiform precipitation. According to figure 4.22b, these downdrafts disturb the inflow by transporting low radial momentum into the boundary layer. On average, the convective updrafts dominate such that the mean steady state is represented by weak ascent outside of the eyewall, as seen in figure 4.13c.

In contrast to the kinematic fields, the instantaneous thermodynamic fields are nearly identical to the steady state. For instance, the p', T', and μ_v' cross-sections at 180 hours,

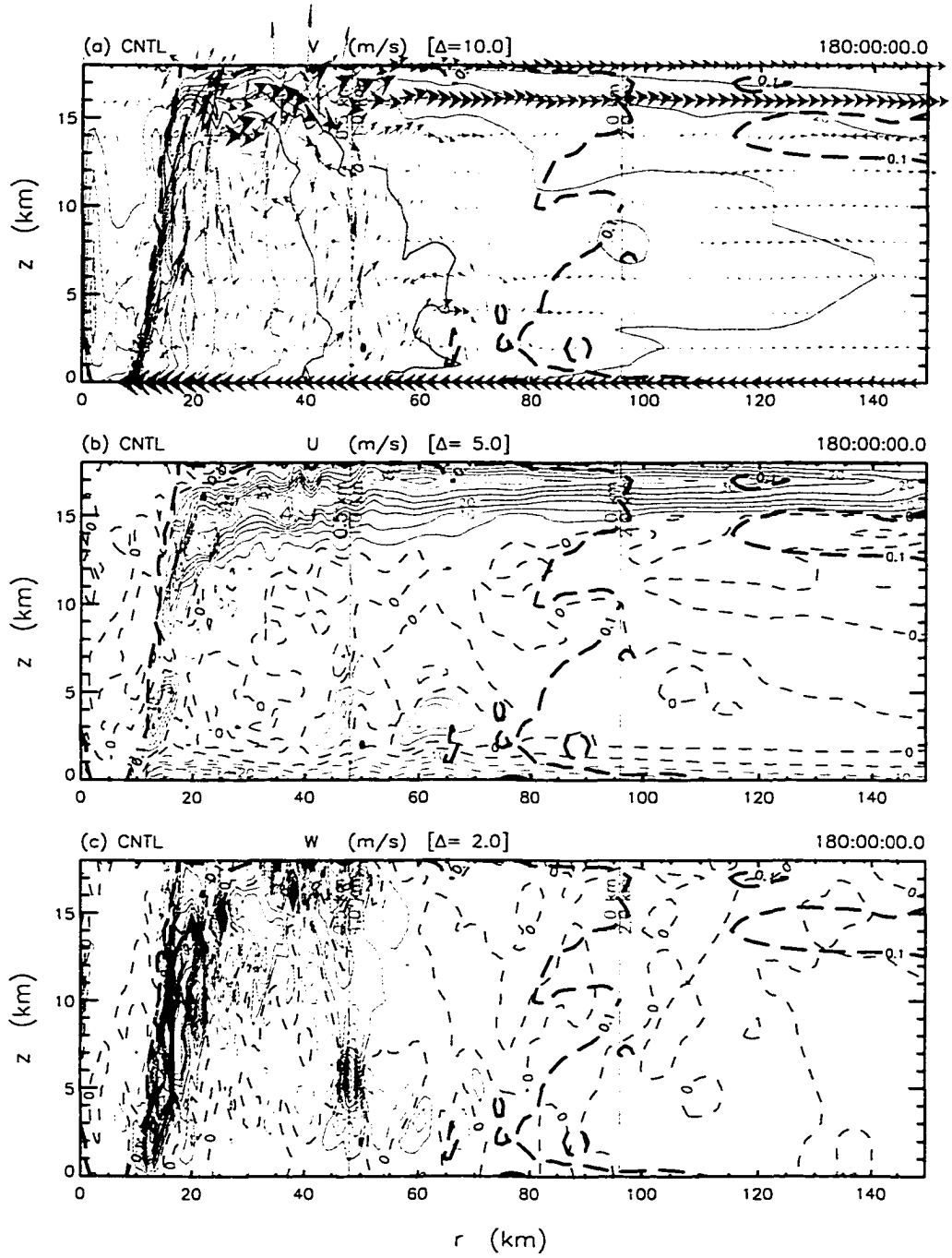

Figure 4.22: CNTL Experiment — 180-hour cross-sections of the a) tangential, b) radial and c) vertical wind speeds (ms^{-1}). For further explanation of the figure markings, see figures 4.2and 4.13.

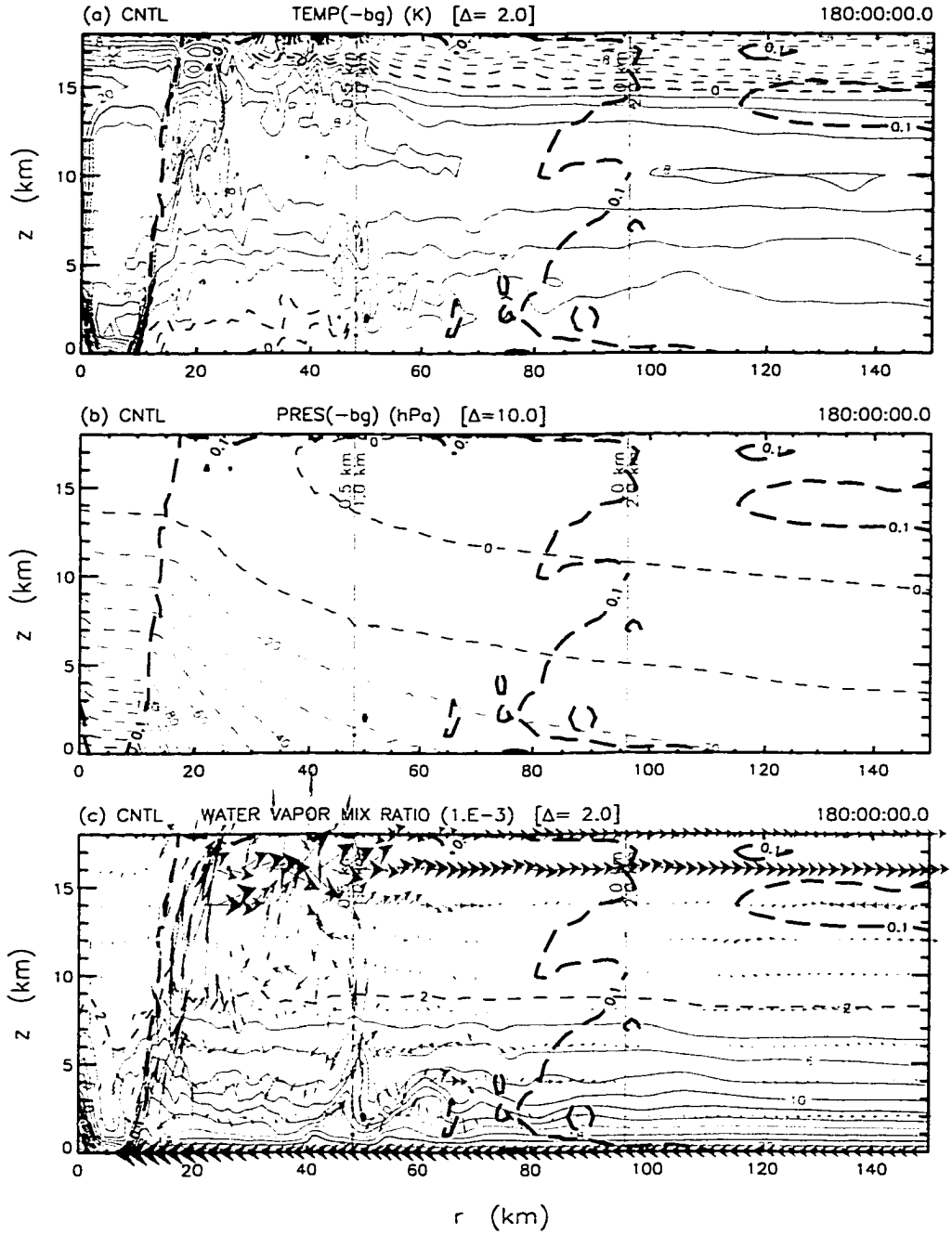

Figure 4.23: CNTL Experiment — 180-hour cross-sections of the a) perturbation temperature, b) perturbation pressure and c) water vapor mixing ratio. For further explanation of the figure markings, see figures 4.2and 4.13.

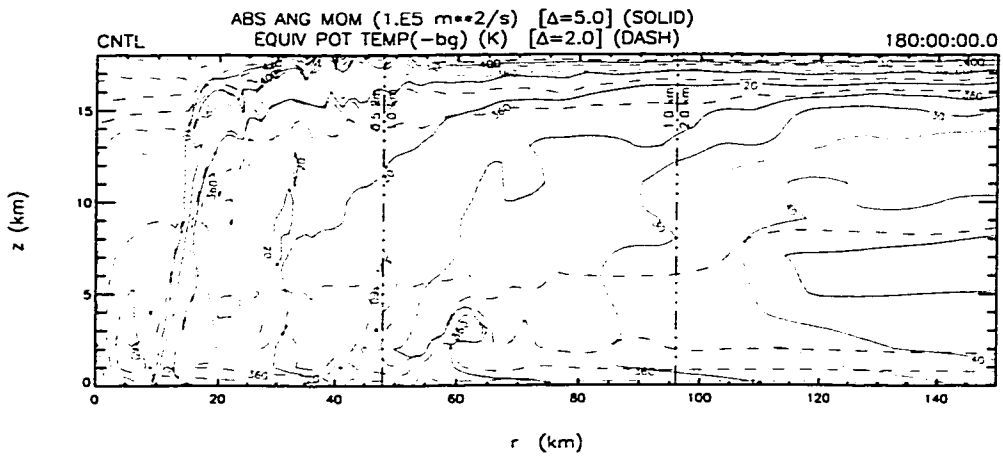

Figure 4.24: CNTL Experiment — 180-hour cross-sections of the absolute angular momentum, M (solid) and the equivalent potential temperature, θ_e (dashed). For further explanation of the figure markings, see figure 4.2.

as seen in figures 4.23a–c, are similar in overall structure to those seen in figures 4.16a–c, with the addition of small-scale perturbations produced by individual convective elements. This is especially true of the p' field. Likewise, we notice in figure 4.24 that the M and θ_e surfaces are nearly aligned within the eyewall, as in figure 4.17, except in the vicinity of the 0°C isotherm. The variability resulting from individual convective elements is eliminated in the mean.

The instantaneous PV field, which is derived from both the kinematic and thermodynamic fields, not only has a maximum in the middle troposphere, as in the steady state, but near the surface as well. Figures 4.25a–c show the 180-hour cross-sections of ζ, θ_ρ, and P'_ρ as in figures 4.20a–c. At the surface and beneath the eyewall, P'_ρ has a maximum of over 3160 PVU. The PV is generated within the eyewall near the surface and above the 0°C isotherm, where the latent heating due to condensation and freezing, respectively, are greatest. It is then advected vertically in the updraft. Simultaneously, the PV is depleted primarily by surface friction and evaporation within the boundary layer. When the eyewall weakens, the frictional and evaporative depletion dominate, and the PV anomaly decreases near the surface. As the convection of the primary eyewall dissipates, it leaves behind its signature in the PV field. This PV later merges with the PV of the replacement eyewall.

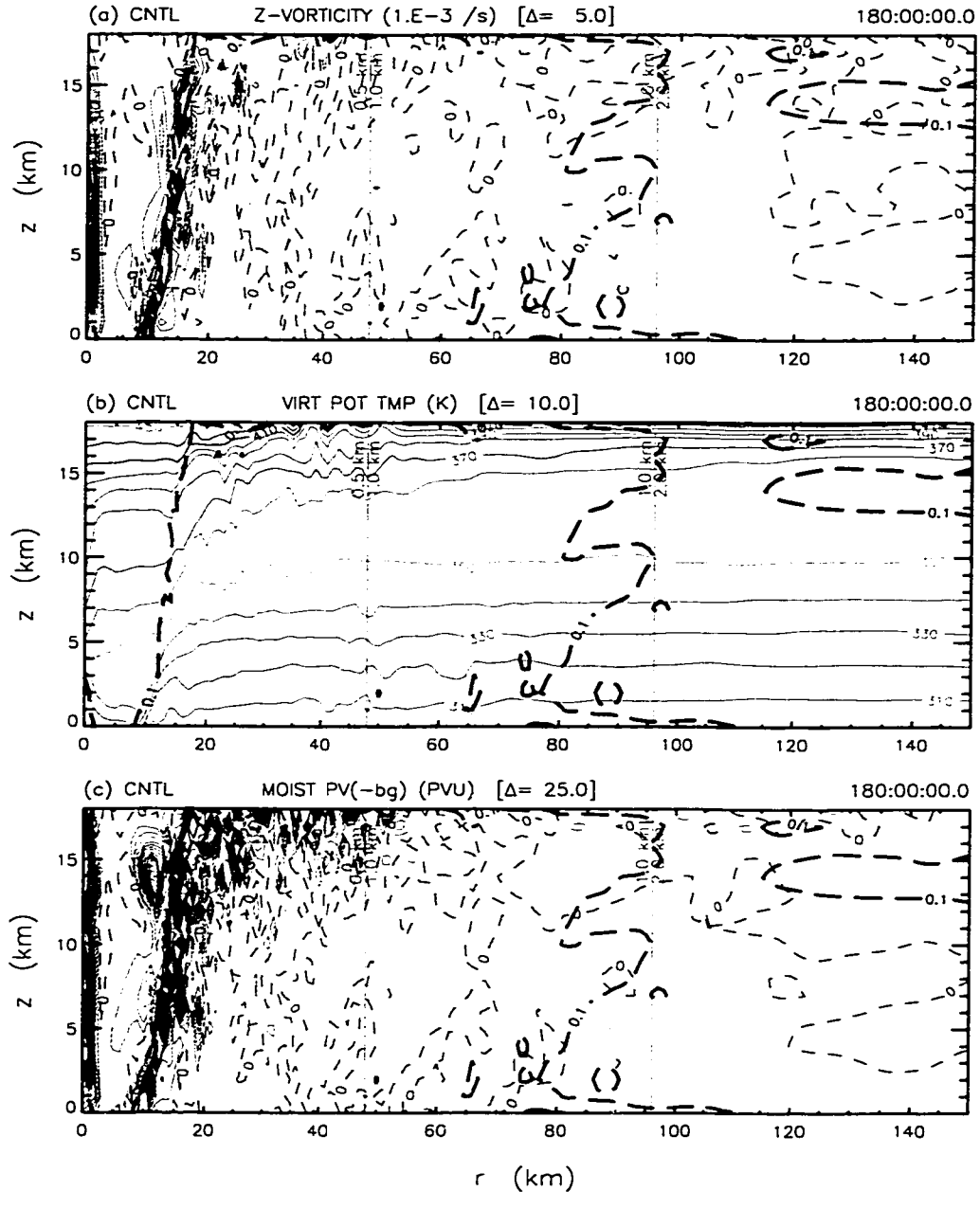

Figure 4.25: CNTL Experiment — 180-hour cross-sections of the a) vertical component of absolute vorticity, ζ; b) the virtual potential temperature, θ_ρ; and c) the moist potential vorticity, P_ρ. For further explanation of the figure markings, see figure 4.2.

One of the most interesting characteristics of the tropical cyclone depicted in figures 4.22–4.25 is the frontal-like structure of the inner eyewall. As pointed out by Emanuel (1997), the frictionally-forced radial convergence inside the radius of maximum tangential wind speed is frontogenetic. For instance, figures 4.22a and 4.23a show that the shear across the inner edge of the eyewall is 50 m s^{-1} km^{-1}, while the temperature gradient is 9 C km^{-1}. During the contraction of the eyewall, this frontal zone compresses and would eventually become a discontinuity, if not for the numerical diffusion of the model. In the next chapter, we also consider the effect of physical diffusion on the discontinuity.

Chapter 5

SENSITIVITY EXPERIMENTS

If we knew what it was we were doing, it would not be called research, would it?
Albert Einstein

In the last chapter, we conducted a control experiment to validate the simulated tropical cyclone against the observational evidence and current theory. In chapters 1 and 4, we identified several parameters affecting the intensity of a tropical cyclone. In this chapter, we test the variability of the maximum intensity, or steady state, of the simulated tropical cyclone with several of these parameters through a series of sensitivity experiments. We begin by discussing the experiments that test the sensitivity of the numerical configuration, with emphasis on the horizontal and vertical grid spacing (section 5.1). We then present several experiments that test the sensitivity of the physical configuration, including the ice and precipitation microphysics, and the diffusion (section 5.2). A list of the sensitivity experiments is presented in table 5.1.

5.1 Numerical Sensitivity Experiments

Before testing the model sensitivity to variations of the physical parameters, we verified that the control experiment was reasonably insensitive to the numerical configuration. Specifically, we tested the sensitivity to the grid resolution, the domain size, the outer boundary condition, and the depth of the damping layer. Almost all of these experiments (details not shown) indicated that the control experiment is relatively insensitive to variations of the chosen numerical configuration. The exceptions to this general conclusion were the horizontal and vertical grid spacing.

Table 5.1: Model parameters varied in each sensitivity experiment.

Experiment	Definition
HGS16KM	no ice, $\Delta r = 16$ km
HGS8KM	no ice, $\Delta r = 8, 16$ km
HGS4KM	no ice, $\Delta r = 4, 8, 16$ km
HGS2KM	no ice, $\Delta r = 2, 4, 8, 16$ km
HGS1KM	no ice, $\Delta r = 1, 2, 4, 8, 16$ km
HGSHKM	no ice, $\Delta r = 0.5, 1, 2, 4, 8, 16$ km
VGS1000M	$\Delta z = 1000$ m
VGS750M	$\Delta z = 750$ m
VGS500M	$\Delta z = 500$ m (same as CNTL)
NICE	no ice effects (same as HGSHKM)
NOTV	no temperature dependent W
NILE	no ice latent effects
NWMO	no conservation of precipitation momentum
PSAD	pseudoadiabatc
CDIF	constant horizontal diffusion
SDIF	Smagorinsky horizontal diffusion

5.1.1 Horizontal Grid Spacing (HGS[H–16]KM)

To determine the optimal resolution in the horizontal, we performed a series of experiments that tested the model sensitivity to changes in the horizontal grid spacing (Δr). Each experiment was identical to the control, except that the number of grids and Δr on each grid were varied. In addition, to decrease the time required to reach a steady state, ice was neglected. The first experiment used a single grid with $\Delta r = 16$ km (i.e., grid number 6 as defined in table 4.2). In successive experiments, a grid with $\frac{1}{2}\Delta r$ of the finest grid from the previous experiment was added. The final experiment then used six grids with $\Delta r = 0.5$,1.0,2.0,4.0,8.0 and 16.0 km (i.e., grid numbers 1–6).

From these experiments, we discovered that the model steady state is extremely sensitive to Δr within a range of values commonly used in previous axisymmetric tropical cyclone models. Figure 5.1 shows the results of the six sensitivity experiments, expressed using the maximum tangential wind speed (v_{max}), the minimum surface pressure (p_{min}) and the center surface equivalent potential temperature (θ_e). From figure 5.1a, we see that, as Δr of the finest grid decreases below 16 km, v_{max} increases from 63 m s^{-1} to an approximate

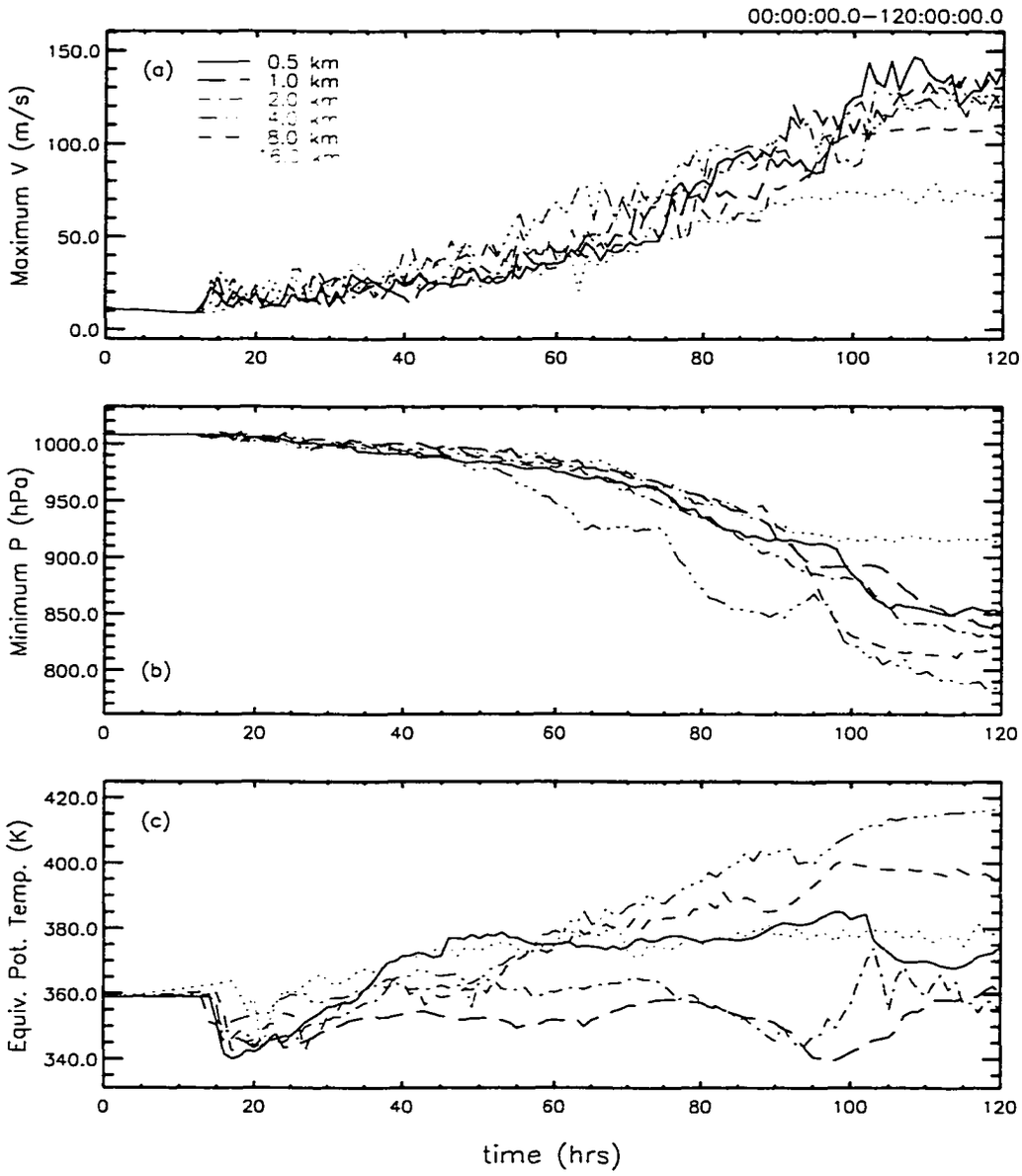

Figure 5.1: HGS[H–16]KM Experiments — Same as figure 4.3, including the c) central surface equivalent potential temperature (K).

maximum of 130 m s^{-1}. Convergence to this maximum value occurs when $\Delta r \leq 4$ km. According to figures 5.1b and c, unlike v_{max}, the values of p_{min} and θ_e do not change linearly with Δr. As Δr decreases below 16 km, p_{min} decreases from 913 to 784 hPa and θ_e increases from 379 to 417 K; however, when Δr decreases below 4 km, the changes in p_{min} and θ_e reverse. As Δr reduces to 0.5 km, p_{min} increases to 850 hPa and θ_e decreases to 375 K. Most importantly, these results demonstrate that the model physics is extremely sensitive to Δr, which arguably has long been understood (Rosenthal, 1970a; Lord and Lord, 1988) but seldom emphasized when interpreting results.

To understand this sensitivity, we examine the variability of the tropical cyclone dynamics to changes in Δr through the radius of maximum tangential wind speed (r_{max}) at the surface and the length scale of the horizontal diffusion (i.e., the cutoff wavelength, l_c, discussed in section 2.2.1.1). Figures 5.2 and 5.3 show the cross-sections of tangential wind speed and temperature for $\Delta r = 1$, 4, and 16 km of the finest grid. As we reduce Δr, the value of r_{max} decreases from 23 to 9 km, whereas v_{max} increases from 73 to 112 m s^{-1}. The value of r_{max} decreases because the model resolves a smaller eye; and the value of v_{max} increases because the inflow, which is limited by r_{max}, advects angular momentum closer to the center. Since the angular momentum is not advected beyond r_{max} into the eye, the acceleration of the tangential wind inside of r_{max}, which is necessary to maintain the rotation of the eye against dissipation by surface friction, must be produced by the diffusion of angular momentum into the center. The radial extent of this diffusion is greatest from 2–4 Δr (i.e., $l_c = 2$). Thus, for $\Delta r \geq 4$ km, the diffusion extends to the center and the tangential wind inside of r_{max} approaches solid body rotation Conversely, for $\Delta r < 4$ km, the diffusion does not extend to the center and the tangential wind speed inside of the eye is relatively stagnant, with a sharp gradient just inside of r_{max}. Not surprisingly, this sharp gradient has an approximate width of 2–4Δr; thus, in the limit of infinitesimally small Δr, the sharp gradient would become a discontinuity. Furthermore, it appears that r_{max} would converge to a value somewhere between 7 and 10 km.

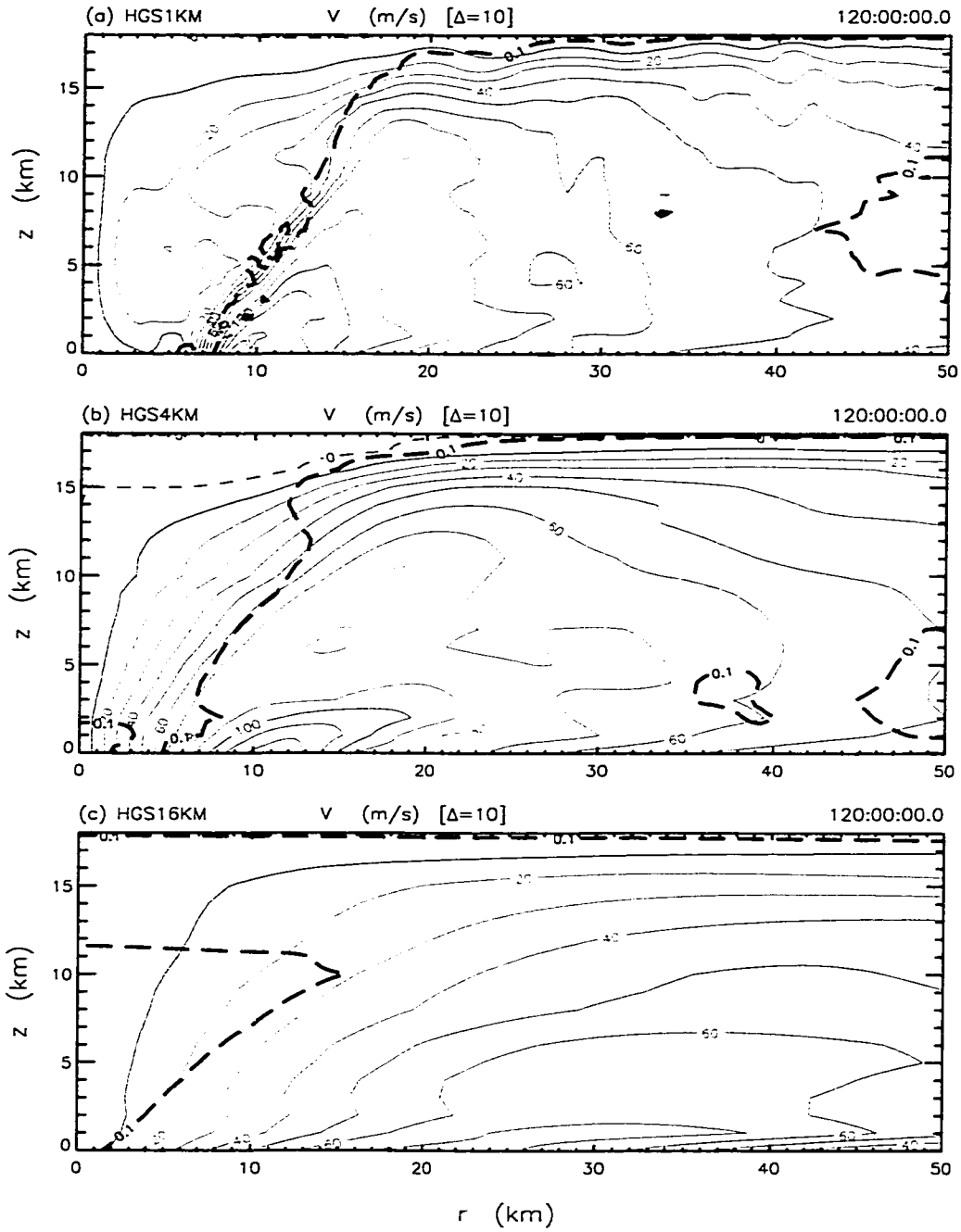

Figure 5.2: HGS[1, 4, 16]KM Experiments — 120-hour (near steady state) cross-sections of the tangential wind speed for a) $\Delta r = 1$ km, b) $\Delta r = 4$ km, and c) $\Delta r = 16$ km. For further explanation of the figure markings, see figures 4.2 and 4.13.

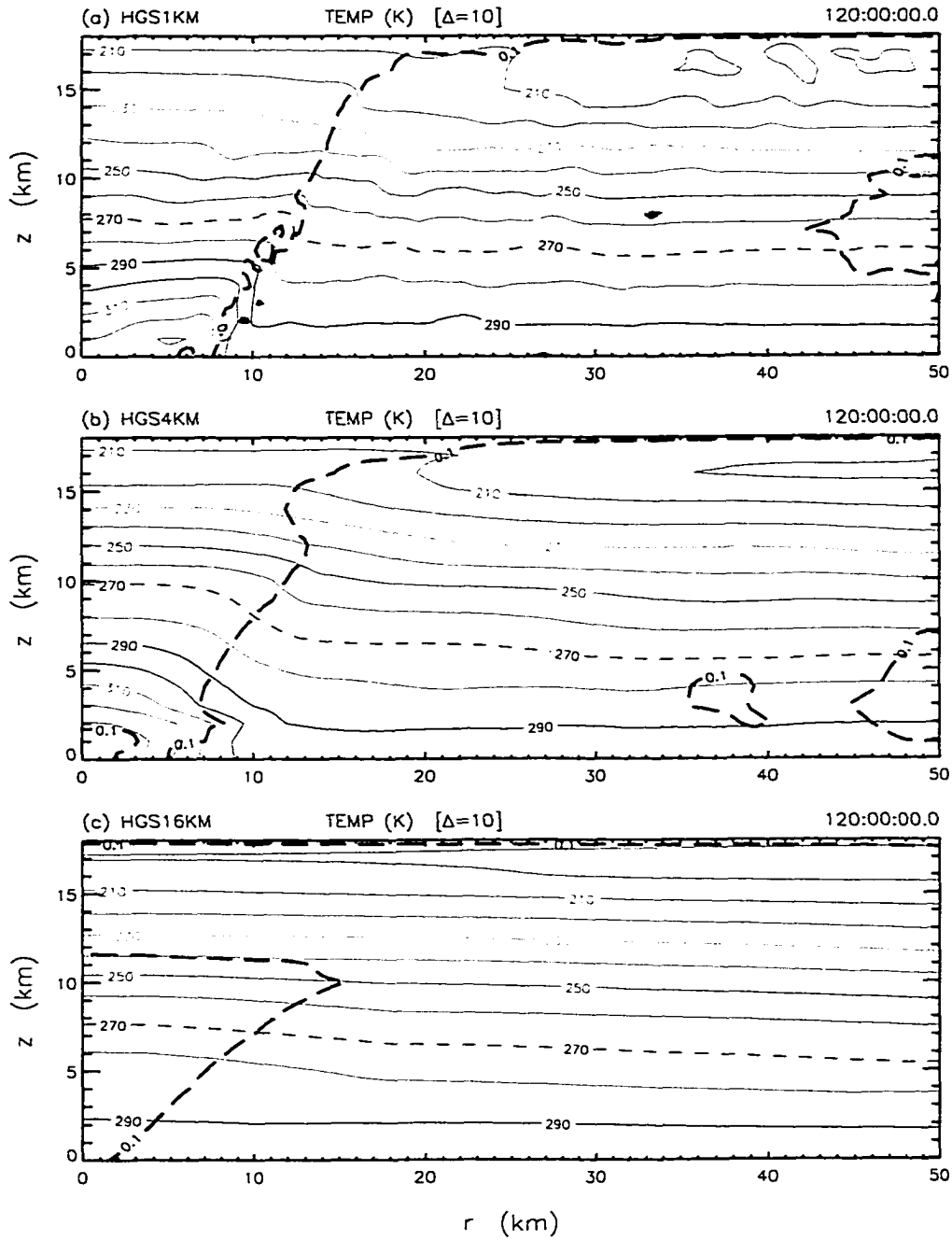

Figure 5.3: HGS[1, 4, 16]KM Experiments — 120-hour (near steady state) cross-sections of the temperature for a) $\Delta r = 1$ km, b) $\Delta r = 4$ km, and c) $\Delta r = 16$ km. For further explanation of the figure markings, see figures 4.2 and 4.13.

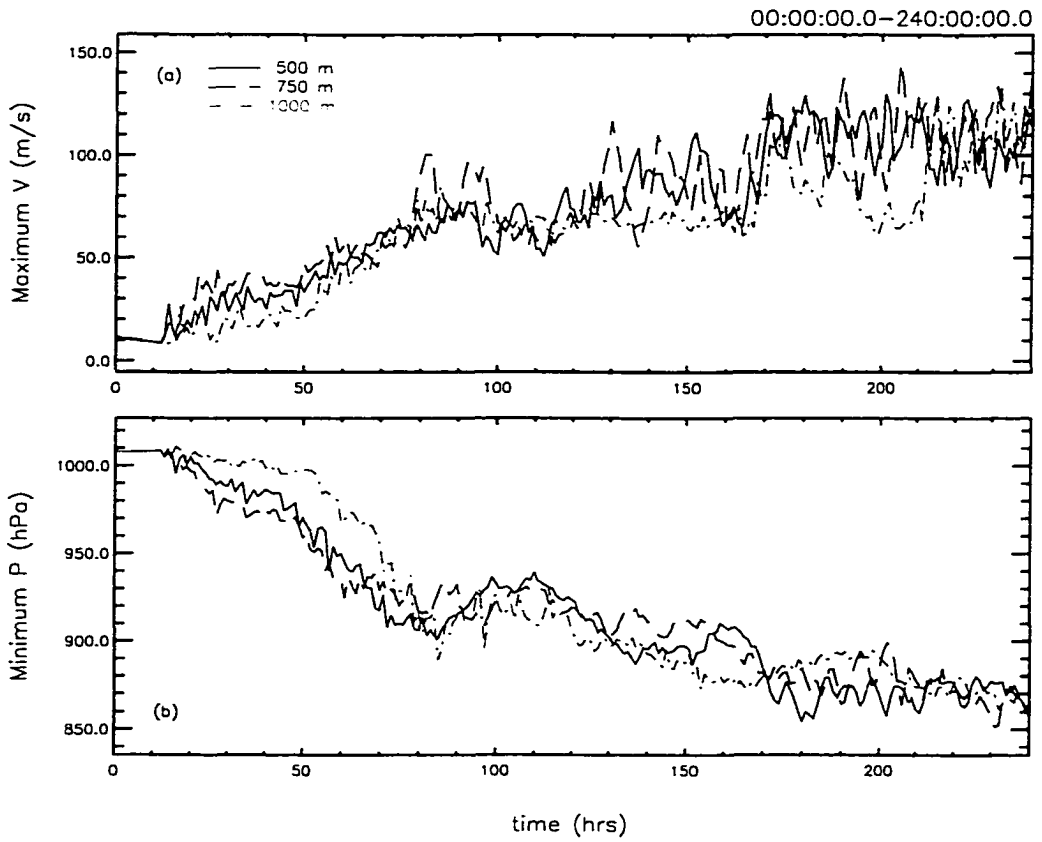

Figure 5.4: VGS[500,750,1000]M Experiments — Same as figure 4.3.

5.1.2 Vertical Grid Spacing (VGS[500,750,1000]M)

We also performed a series of experiments to test the model sensitivity to changes in the vertical grid spacing (Δz). Specifically, we conducted three tests with Δz = 500, 750, and 1000 m. In addition, we included ice in these experiments to verify that the model resolves convective and stratiform outflows within the boundary layer, which are enhanced by the latent cooling produced by melting precipitation. Figure 5.4 shows the results of the three sensitivity experiments, expressed using v_{max} and p_{min}. From these results, it appears that the model is less sensitive to Δz than to Δr; however, it is not apparent that this result will hold for even smaller Δz. Unfortunately, our ability to further resolve the vertical is restricted by computational limitations.

5.2 Physical Sensitivity Experiments

Previous axisymmetric models have been used to test the sensitivity of tropical cyclone development to various parameters, including the surface exchange coefficients (Ooyama, 1969; Rosenthal, 1971), Coriolis parameter (Khain, 1984; DeMaria and Pickle, 1988; Bister, 1997), and sea surface temperature (Ooyama, 1969; Rotunno and Emanuel, 1987; Zeng, 1996). To be consistent, we performed similar tests and verified that the model has the same sensitives. Rather than focus on these results, however, we focus instead on other sensitivities that remain unsolved or unexplored, including the ice and precipitation microphysics, and turbulent diffusion. From these sensitivity tests, we gain new insights into the parameters limiting tropical cyclone intensity.

5.2.1 Ice (NICE/NOTV/NILE)

From the introduction, we recall that Willoughby et al. (1984), Lord et al. (1984), and Lord and Lord (1988) numerically studied tropical cyclone intensity changes resulting from variations to the ice microphysics (see figure 1.1). From their results, we discover that the simulated tropical cyclone intensifies more slowly when ice is included, and attains a peak

Table 5.2: Matrix illustrating the relationship between the ice microphysics experiments.

Experiment	latent effects	temperature-dependent terminal velocity
CNTL	Y	Y
NOTV	Y	N
NILE	N	Y
NICE	N	N

intensity that is slightly less and more variable than when ice is not included. According to Willoughby et al., the differences develop because the primary eyewall in the simulation with ice is disturbed by the formation of numerous secondary rings of convection. This formation was apparently sensitive to the distribution of ice outside of the eyewall and the mesoscale downdrafts that melting ice produces. The secondary rings, or eyewalls, in conjunction with the mesoscale downdraft, inhibit the convection of the primary eyewall, and disturb the necessary inflow of mass, momentum, and energy into the storm core. However, in all of their experiments, the latent effects alone are somewhat obscured by the complexity of the ice microphysics.

We next test the sensitivity of our model to variations in the ice microphysics using the simple representation of ice formulated in section 2.1.3.2. The latent effects of ice are incorporated into the model not through various species of frozen condensate and numerous conversion processes, but through a single combined condensate, represented by an interpolation of the saturation vapor pressures over a plane surface of water and ice. Furthermore, the reduced settling speed of geometrically complex ice particles is included in the model through a temperature-dependent terminal velocity, which decreases for temperatures below freezing. Remembering that our CNTL experiment presented in chapter 4 included ice, we now perform sensitivity experiments with no ice dependencies (i.e., experiment NICE), with the latent effects of ice but no temperature-dependent terminal velocity (i.e., experiment NOTV), and with the temperature-dependent terminal velocity but no latent effects of ice (i.e., experiment NILE). Table 5.2 illustrates the relationship between the various ice microphysics experiments.

It is clear from these experiments that the ice microphysics systematically affects the tropical cyclone steady-state intensity. Figure 5.5 shows the evolution of the simulated tropical

cyclone in terms of v_{max} and p_{min} for the CNTL, NICE, NOTV, and NILE experiments. Notice that the CNTL, NICE, and NOTV experiments are relatively similar during the first 80 hours. This similarity is primarily due to the anomalous central vortex discussed in section 4.2.1.2 and not the developing tropical cyclone vortex. Beyond 180 hours, however, all four experiments settle into a near steady state. The NICE and NOTV experiments have a steady-state intensity that is significantly greater than the CNTL and NILE experiments. To understand the physics behind these differences, we next consider each ice microphysics experiment independently.

In the NICE experiment, the simulated tropical cyclone develops more rapidly and attains a steady-state intensity that is greater than the CNTL experiment. Figure 5.5 shows that the intensities of the CNTL and NICE experiments diverge substantially at about 93 hours. During the next 30 hours, the NICE tropical cyclone rapidly intensifies and reaches a near steady state, with $v_{max} \approx 135$ m s^{-1} and $p_{min} \approx 830$ hPa. In contrast, the CNTL tropical cyclone requires an additional 60 hours to reach a steady state, with $v_{max} \approx 101$ m s^{-1} and $p_{min} \approx 870$ hPa. Not only is the steady-state intensity of the CNTL experiment distinctly less than the NICE experiment, but it is noticeably more variable as well. Specifically, the periodic variations of v_{max} in the CNTL experiment are 10–20 m s^{-1} greater than in the NICE experiment.

As evidenced in section 4.2.1.4, the differences between the CNTL and NICE experiments are caused by the development and contraction of secondary eyewalls in the CNTL experiment that do not develop in the NICE experiment. To illustrate the point, figure 5.6 shows the Hovmöller diagram of the surface tangential wind speed for the NICE experiment. Comparing this figure with figure 4.5, we see that the initial contraction of the primary eyewall in the CNTL experiment (i.e., ≈ -0.75 m s^{-1}) is more rapid than in the NICE experiment (i.e., ≈ -0.25 m s^{-1}), assuming that a maximum in the tangential wind field is coincident with the convection of the eyewall. The rate of contraction in the CNTL experiment is enhanced by the additional buoyant decent induced by melting precipitation. By about 123 hours, in the NICE experiment, the eyewall contraction decelerates to a near

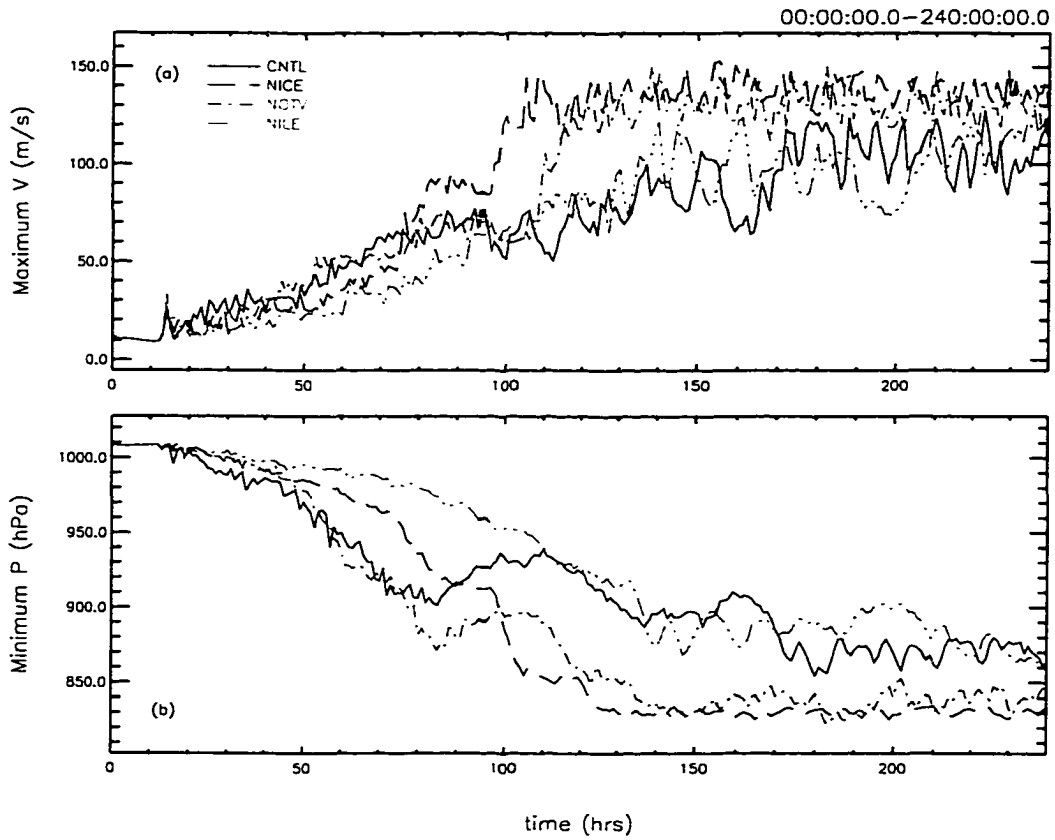

Figure 5.5: NICE, NOTV, and NILE Experiments — Same as figure 4.3.

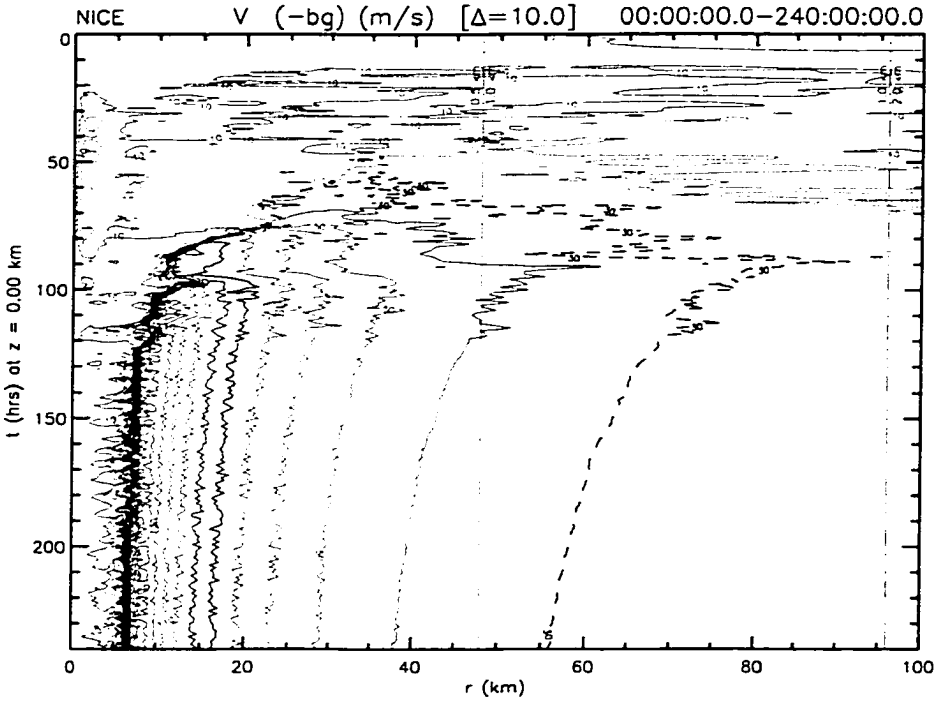

Figure 5.6: NICE Experiment — Same as figure 4.5.

steady state, with a radius of maximum tangential wind speed of 8.5 km. In the CNTL experiment, however, the primary eyewall dissipates as a secondary eyewall develops, contracts, and replaces the primary eyewall. Several of these eyewall replacement cycles occur during the tropical cyclone development. Beyond 180 hours, the CNTL tropical cyclone attains a quasi-steady state with a radius of maximum tangential wind speed of approximately 13.5 km. With no secondary eyewalls to disturb the development of the primary eyewall, the NICE experiment rapidly develops a relatively intense steady tropical cyclone with a relatively small eye.

The reason that secondary eyewalls do not form in the NICE experiment is that the necessary stratiform precipitation, discussed in section 4.2.1.4, does not develop. Figures 5.7–5.10, which are identical to figures 4.13–4.20, except that the fields are averaged from 120–240 hours, show the structure of the NICE tropical cyclone. Comparing the figures, we see that above 5 km the minimum terminal velocity is -10 m s^{-1} in the NICE experiment and -2 m s^{-1} in the CNTL experiment. In contrast to this relatively large difference, the instantaneous secondary circulations are relatively similar in magnitude,

with the NICE experiment being slightly stronger by 5–10 m s^{-1}. Thus, in the CNTL experiment, the precipitation is lofted into the outflow and advected far from the eyewall; however, in the NICE experiment, much of the precipitation falls from the sloping updraft without being ejected into the outflow. As a result, the surface precipitation extends to almost 100 km in the CNTL experiment but only about 45 km in the NICE experiment. Furthermore, since the precipitation is distributed over a smaller area in the NICE experiment, the precipitation rate is a factor of four greater than the CNTL experiment. Without the stratiform precipitation to precondition the atmosphere for moist convection, and to provide the mesoscale downdrafts that induce surface convergence and ascent, secondary eyewalls do not form in the NICE experiment.

Two additional comments must be made regarding the NICE experiment. First, notice that figures 5.7–5.10 more closely resemble the instantaneous state of the CNTL experiment depicted in figures 4.22–4.23 than the mean steady state shown in figures 4.13–4.16. This resemblance exists because the NICE experiment is steadier than the CNTL experiment; therefore, important details are not lost when time-averaging. We stress the similarity between these figures to highlight the frontal structure of the eyewall discussed in section 4.2.2.5. As shown in figures 5.7a and 5.8a, the shear across the inner edge of the eyewall is 45 m s^{-1} km^{-1}, while the temperature gradient is 10 C km^{-1}. Dynamically, this structure translates to a large moist potential vorticity (MPV) anomaly of 400 PVU, as shown in figure 5.10c. Second, notice in figure 5.7c that the updraft appears to accelerate above the melting level. This acceleration is not due to the buoyancy produced by freezing condensate, as in the CNTL experiment, but is an artifact of the time-averaging. While the upper-level portion of the eyewall updraft is extremely steady, the position of the low-level updraft oscillates radially with the variations of the supergradient outflow shown in in figure 5.7a. The time-averaging then damps the magnitude of the low-level updraft but preserves the magnitude of the upper-level updraft, causing an apparent acceleration of the updraft above about 5 km.

The NOTV experiment indirectly verifies that the stratiform precipitation and embedded secondary eyewalls limit tropical cyclone intensity. Returning to figure 5.5, we see that

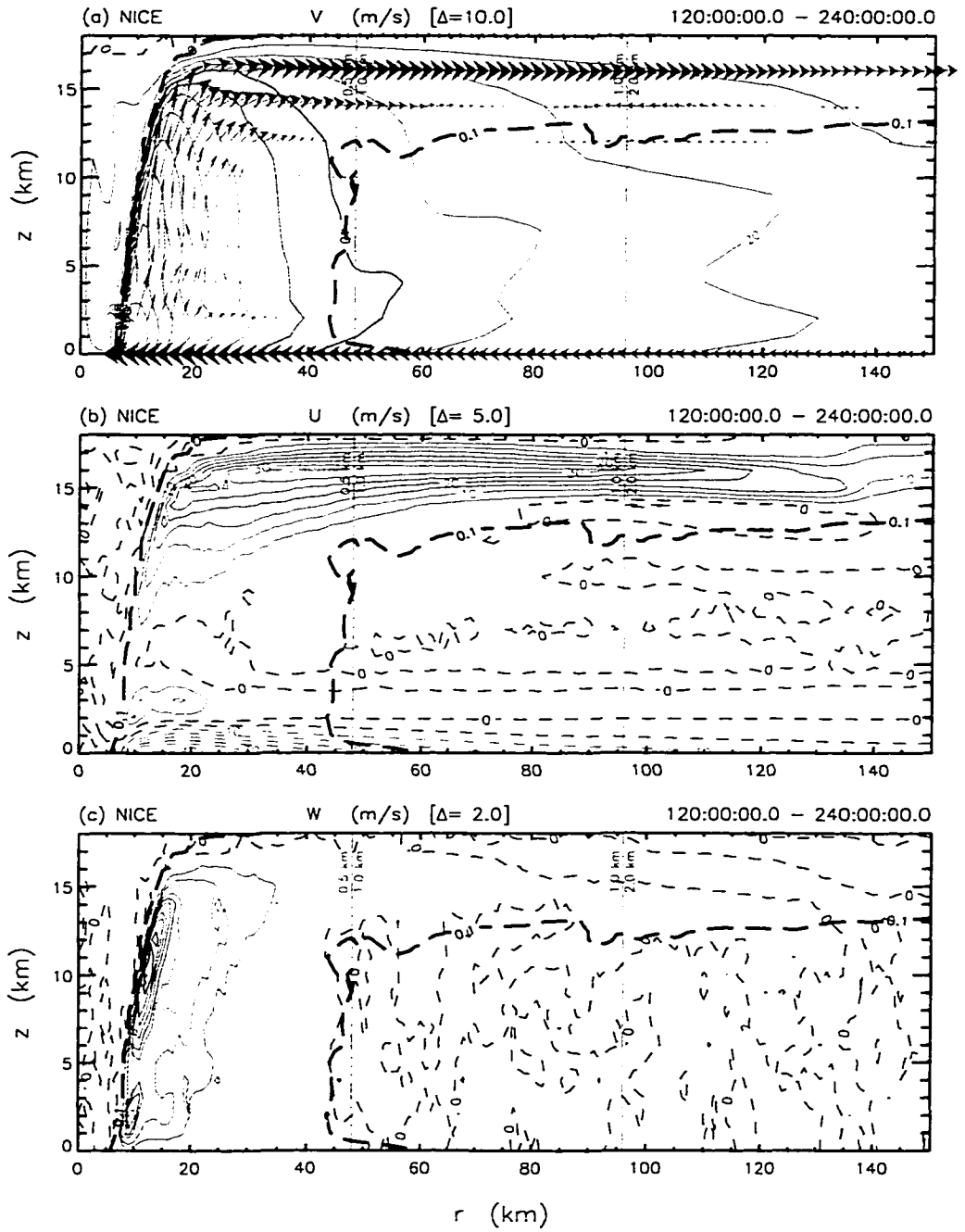

Figure 5.7: NICE Experiment — Same as figure 4.13 but for 120–240 hour time-average.

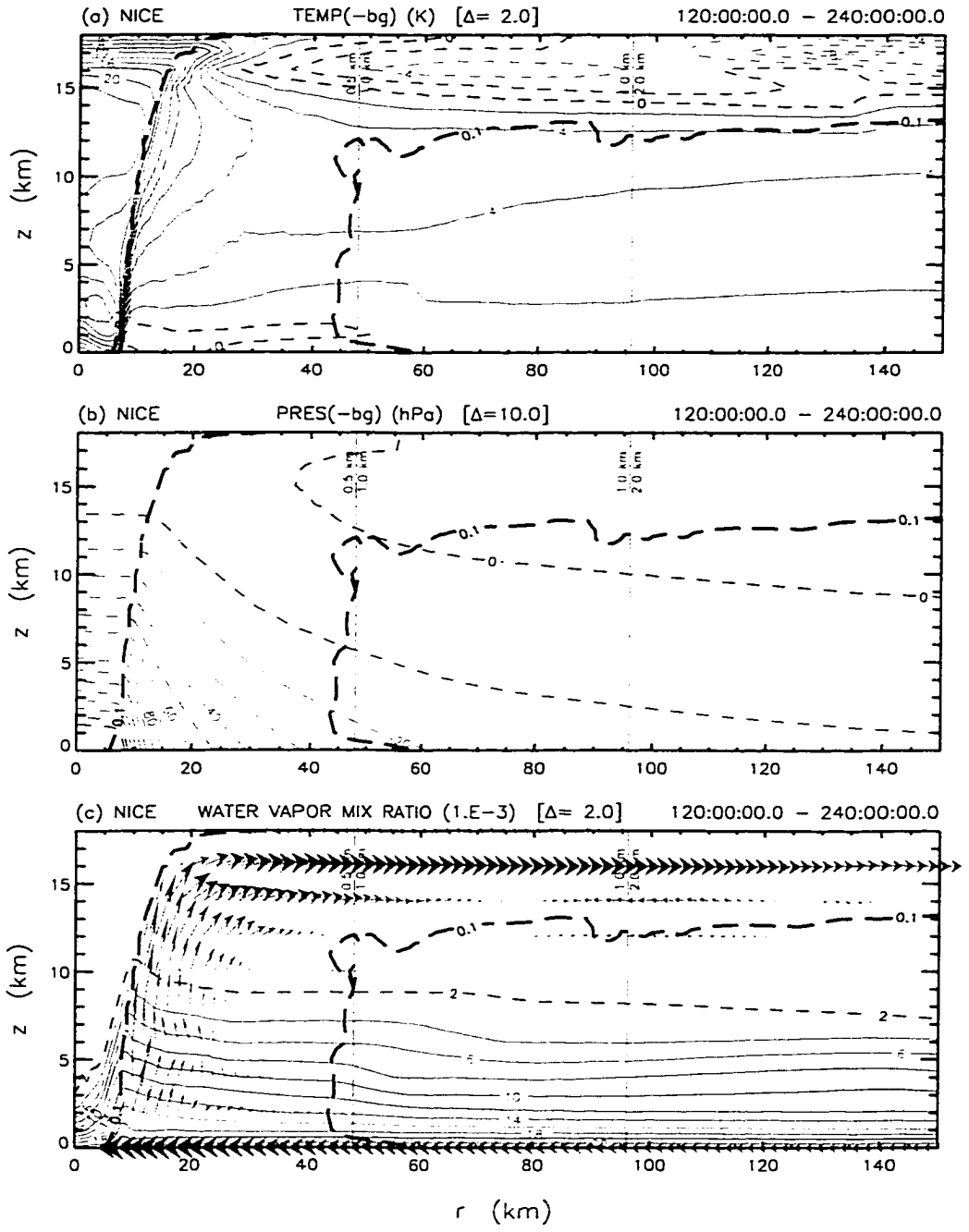

Figure 5.8: NICE Experiment — Same as figure 4.16 but for 120–240 hour time-average.

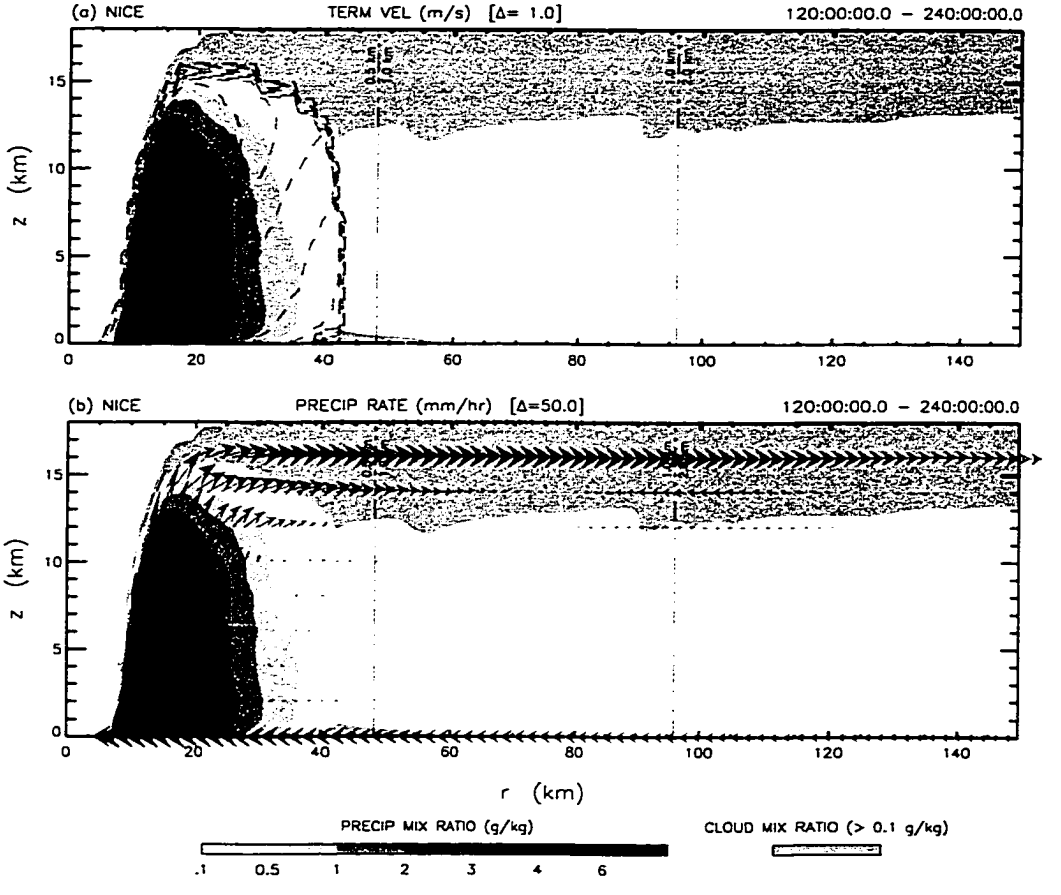

Figure 5.9: NICE Experiment — Same as figure 4.19 but for 120–240 hour time-average.

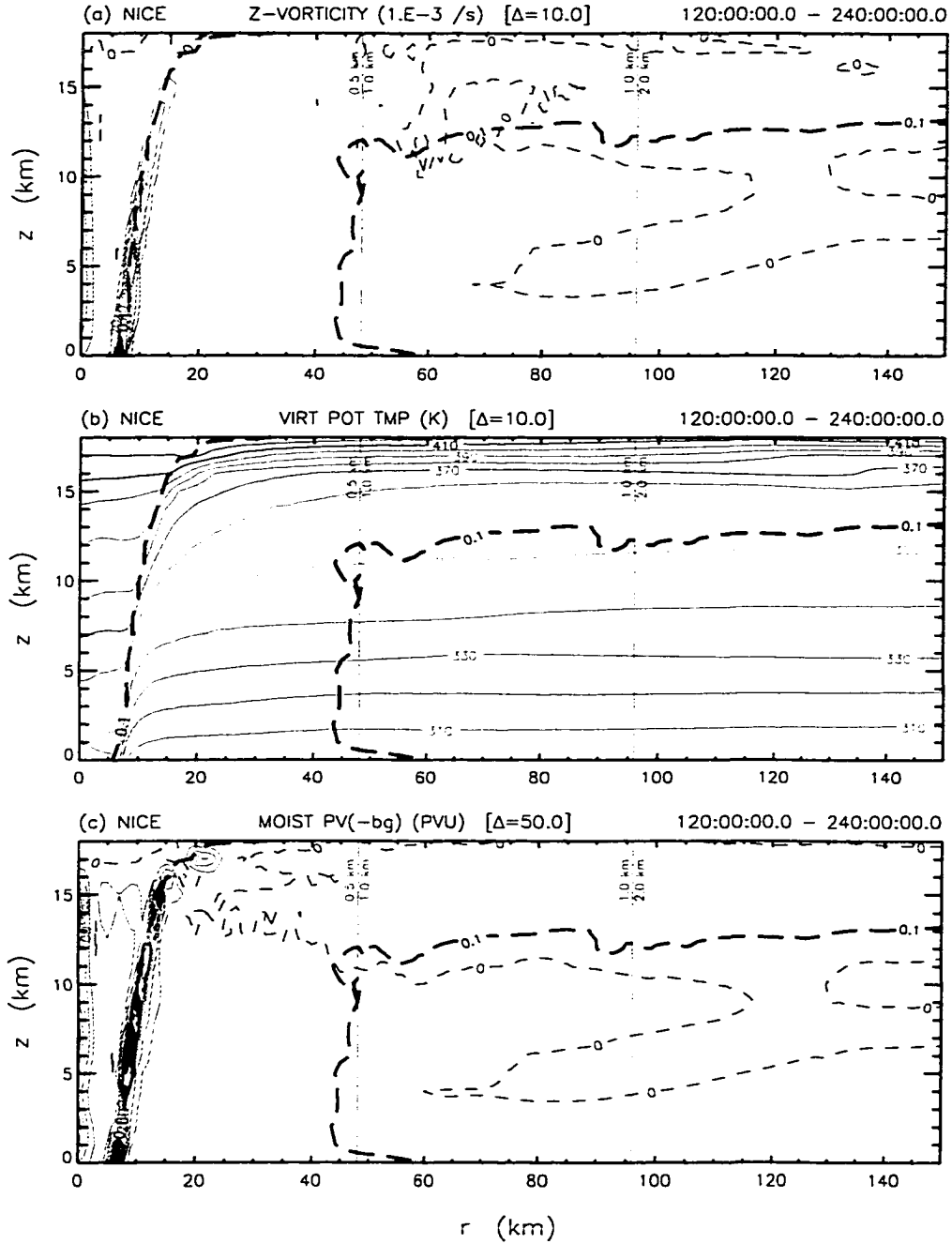

Figure 5.10: NICE Experiment — Same as figure 4.20 but for 120–240 hour time-average.

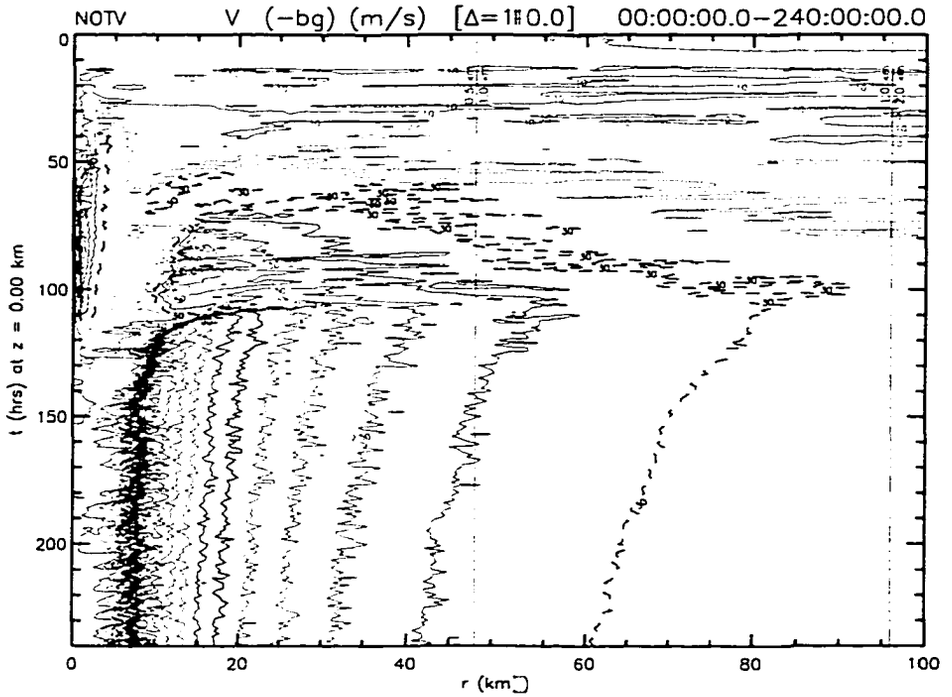

Figure 5.11: NOTV Experiment — Same as figure 4.5.

the NICE and NOTV experiments are notably similar, except that the NOTV experiment requires an additional 18 hours to attain its steady-state intensity, and is slightly weaker by 10–15 m s^{-1} and 5–10 hPa. In both of these experiments, the precipitation is not advected away from the eyewall but rapidly falls from the sloping updraft. Without the stratiform precipitation, it is impossible for secondary eyewalls to form; thus, the latent effects of ice alone cannot explain the significant differences between the NICE and CNTL experiments. As further proof, we compare figures 4.5 and 5.6 to figure 5.11, the Hovmöller diagram of the surface tangential wind speed for the NOTV experiment. Initially, the NOTV experiment develops like the CNTL experiment, with unsteady contraction of the initial primary eyewall and the formation of an intense center vortex. Eventually, however, the NOTV experiment develops like the NICE experiment, with a relatively steady primary eyewall and no secondary eyewalls. Thus, we determine that the ice microphysics has almost no effect on intensity, unless the ice is ejected outward away from the eyewall to form a broad region of stratiform precipitation.

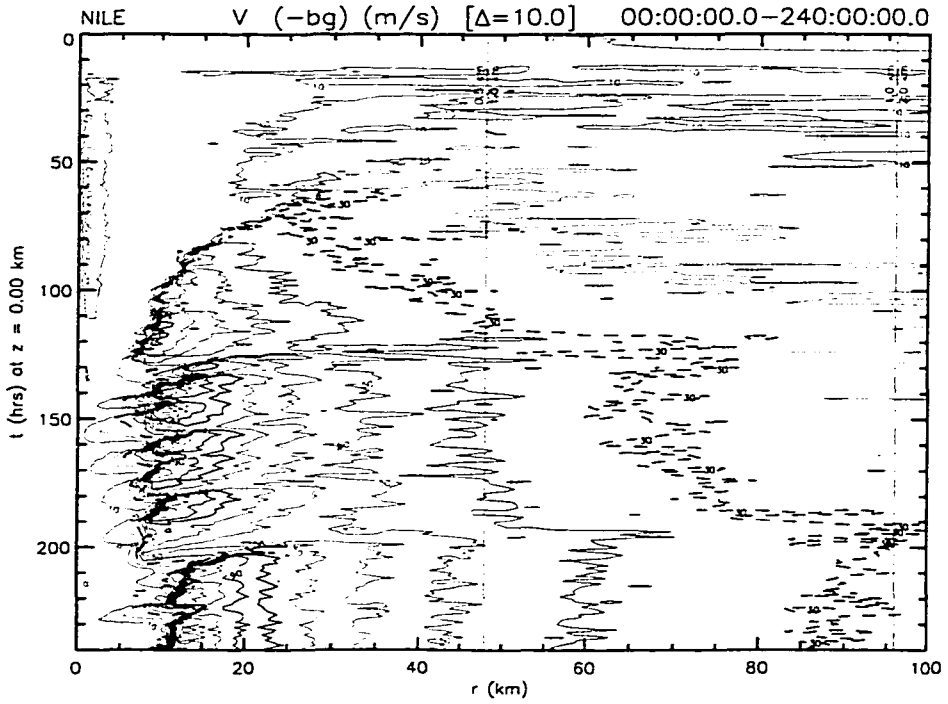

Figure 5.12: NILE Experiment — Same as figure 4.5.

The NILE experiment completes the ice sensitivity experiments and demonstrates that, even without ice latent effects, the mesoscale downdrafts driven by the stratiform precipitation continue to generate secondary eyewalls, which limit the tropical cyclone intensity. Figure 5.5 shows that the steady-state intensity of the NILE experiment, which does not include ice, is nearly identical to the CNTL experiment, which does include ice. Figures 4.5 and 5.12, the Hovmöller diagram of the surface tangential wind speed for the NILE experiment, further show the similarity between the two experiments. Initially, the inclusion of ice in the CNTL experiment produces more rapid intensification and the formation of the central vortex; however, beyond 120 hours, the two experiments attain nearly identical steady-state intensities. Precipitation drag and evaporative cooling are sufficient to drive the mesoscale downdrafts, indirectly limiting the intensity of the tropical cyclone. Ice then merely enhances the downdraft, as seen in the NOTV experiment.

In conclusion, there are several distinct differences between our sensitivity experiments on ice microphysics and those of Willoughby et al. (1984) and Lord and Lord (1988). Comparing figures 1.1 and 5.5, we see that our simulated tropical cyclone develops more

slowly and becomes much more intense. For instance, the NICE experiment in figure 5.5, which is comparable to the W experiment in figure 1.1, reaches a steady state 75 hours later, with v_{max} nearly 100 m s^{-1} greater and p_{min} approximately 110 hPa lower. Furthermore, there is almost no difference in the mean steady-state v_{max} of the FR, W, and I experiments in figure 1.1, whereas v_{max} varies by as much as 50 m s^{-1} or more between the CNTL, NICE, NOTV, and NILE experiments in figure 5.5. Finally, and most importantly, our results show that the stratiform precipitation is the primary factor modifying the intensity between the CNTL and NICE experiments. The latent effects of ice are a secondary effect, unlike that proposed by Willoughby et al. (1984) and Lord and Lord (1988).

5.2.2 Precipitation Physics (NWMO/PSAD)

One distinctive attribute of our model is its thorough bulk formulation of the precipitation dynamics and thermodynamics. Specifically, the model equations (2.5)–(2.6) conserve the total momentum and entropy, and contain terms representing the vertical fluxes of momentum and entropy by precipitation. In contrast, virtually all previous axisymmetric tropical cyclone models conserve only the dry or moist air momentum and entropy, and neglect the vertical fluxes of precipitation momentum and entropy (i.e., pseudoadiabatc). The additional precipitation microphysics in our model may significantly affect the development of the simulated tropical cyclone.

We can easily evaluate the sensitivity of the simulated tropical cyclone to the complete bulk precipitation microphysics by neglecting the unique precipitation-related terms in the model predictive equations (2.58)–(2.61). First, in the NWMO experiment, we neglect the terms involving W in (2.58)–(2.60). The resulting momentum equations are then nearly identical to those used in past models (Willoughby et al., 1984; Rotunno and Emanuel, 1987; Zeng, 1996). Recall from section 2.3, however, that (2.58)–(2.60) are the components of the approximate form of (2.5). Despite the intermediate level of approximation, we may still learn something from the experiment. Second, in the PSAD experiment, we again neglect the terms involving W in (2.6). The resulting entropy equation is then pseudoadiabatc, in the absence of other sources or sinks of entropy.

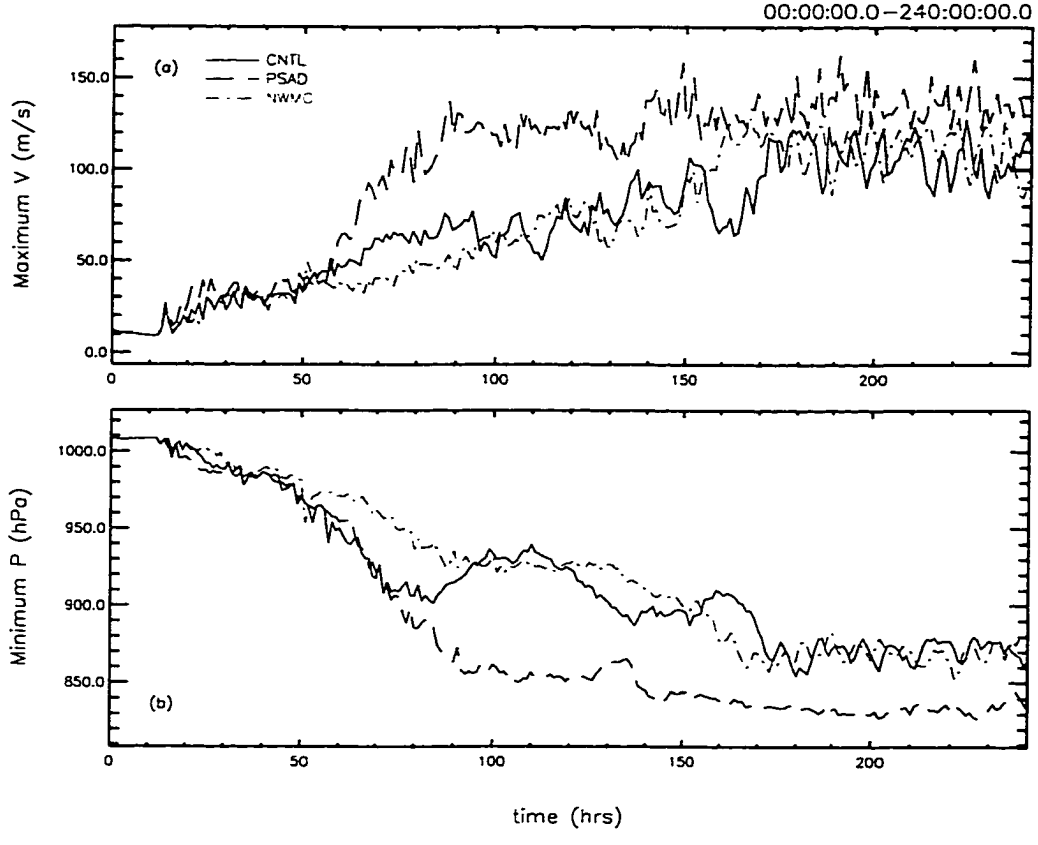

Figure 5.13: PSAD and NWMO Experiments — Same as figure 4.3.

The results of the NWMO and PSAD experiments demonstrate that the additional terms in the momentum equations have relatively little impact on tropical cyclone development, whereas the additional terms in the entropy equation significantly alter both the intensification and steady-state intensity. Figure 5.13 shows the evolution of the simulated tropical cyclone in terms of v_{max} and p_{min} for the CNTL, NWMO, and PSAD experiments. Immediately, we see that the NWMO and CNTL experiments are nearly identical, except that the NWMO experiment intensifies more slowly. This result is not unexpected considering that the relative momentum of the precipitation (i.e., $\rho_r W$) is three orders of magnitude smaller than the total momentum of the mass moving with the parcel (i.e., ρw), as discussed in section 2.3; therefore, variations of the precipitation momentum have little affect on the total momentum. In contrast, the PSAD and CNTL experiments differ substantially, suggesting that the precipitation entropy significantly affects the total entropy. For instance, the PSAD tropical cyclone rapidly intensifies from 60 to 90 hours, attaining a near steady state 70 hours earlier than in the CNTL experiment. Furthermore, the steady-state intensity in the PSAD experiment is approximately 25 m s^{-1} greater and 35 hPa lower as compared to the CNTL experiment. Recall that early rapid intensification occurred in the simulations of Willoughby et al. (1984) and Lord and Lord (1988), as shown in figure 1.1.

The differences between the PSAD and CNTL experiments result from changes in the boundary layer entropy, or equivalent potential temperature (θ_e). Figures 5.14 and 5.15 show the Hovmöller diagrams of the surface tangential wind speed and θ_e at a height of 1 km for the PSAD experiment. Comparing figures 4.6 and 5.15, we see that the θ_e of inflowing air is 10 K warmer beneath the eyewall in the PSAD experiment than in the CNTL experiment. Furthermore, comparing figures 4.5 and 5.14, we find that the PSAD experiment does not develop secondary eyewalls. In the PSAD experiment, precipitation does not transport entropy from the boundary layer through the lower boundary; therefore, the total entropy of downdraft air is greater than in the CNTL experiment, which from equation (2.10) requires a higher temperature. As a result, the negative buoyancy of the downdrafts is reduced, inhibiting development of the secondary eyewall. Given this result, it is unclear why other pseudoadiabatc models are able to produce secondary eyewalls (Willoughby et al., 1984, e.g.,).

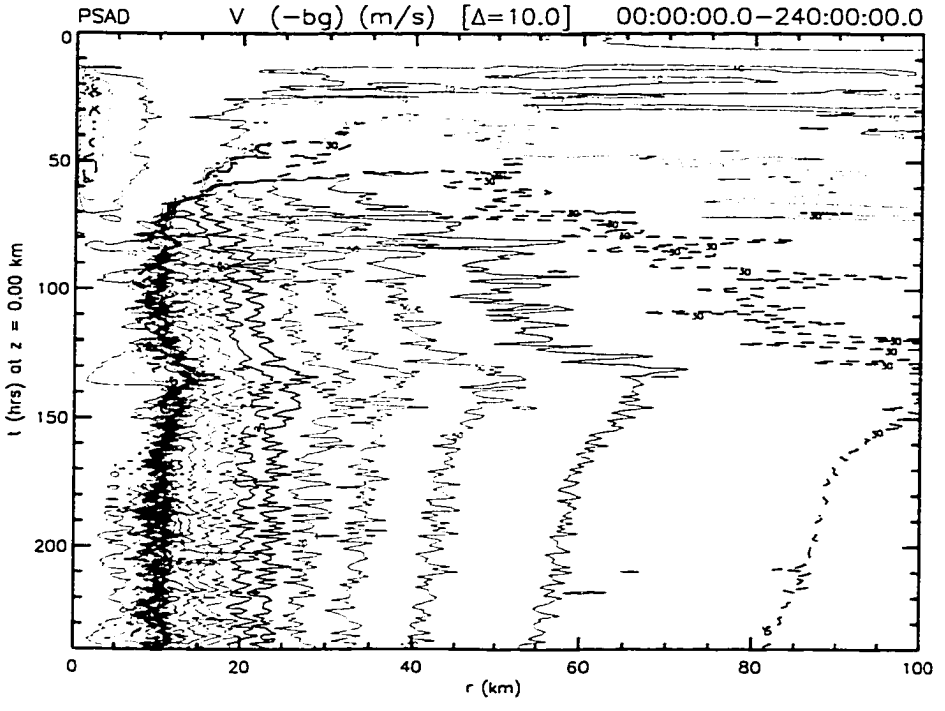

Figure 5.14: PSAD Experiment — Same as figure 4.5.

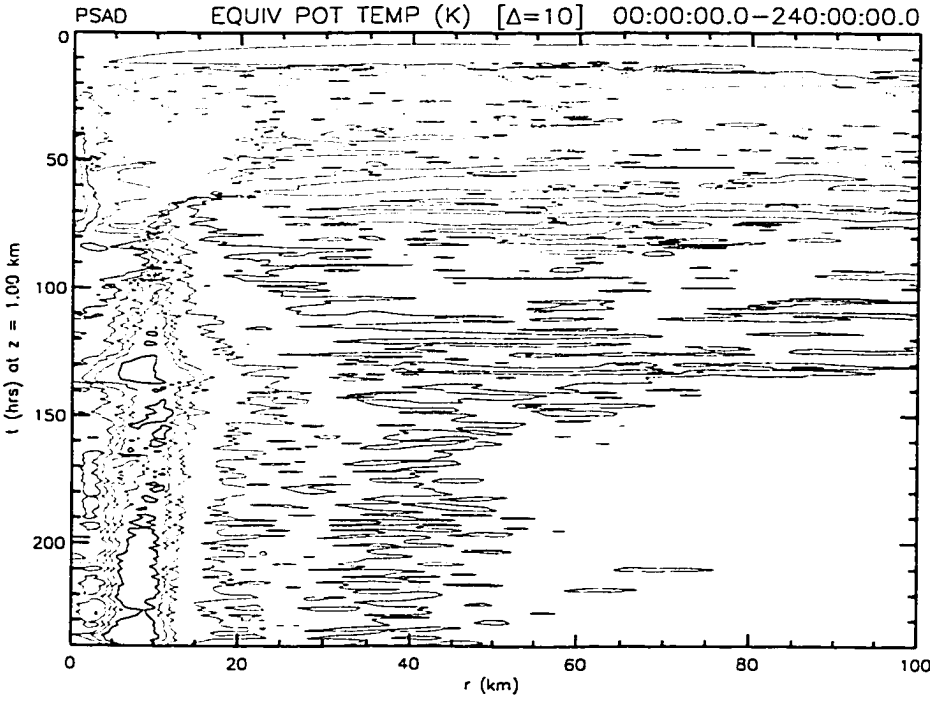

Figure 5.15: PSAD Experiment — Same as figure 4.6.

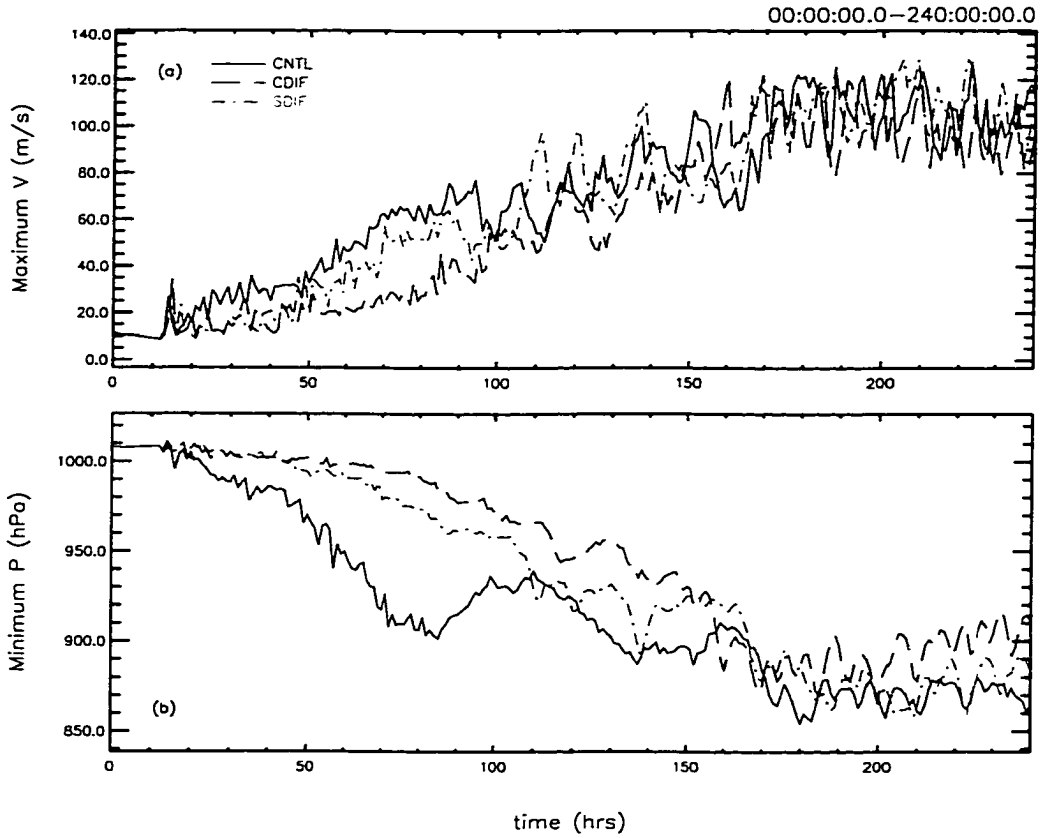

Figure 5.16: CDIF and SDIF Experiments — Same as figure 4.3.

5.2.3 Diffusion (SDIF/CDIF)

As discussed in section 2.1.3.2, other axisymmetric tropical cyclone models have used diffusion to parameterize the asymmetric mixing by horizontal, two-dimensional turbulence. In contrast, our model does not parameterize any turbulent mixing but applies a numerical filter to control the accumulation of signal at the resolution limit. To better understand the impact of horizontal diffusion on the tropical cyclone development, we performed two experiments. First, in the CDIF experiment, we use simple ∇^2 diffusion with a constant diffusion coefficient of $\nu = 10^3$ m^2 s^{-1}. Second, in the SDIF experiment, we use the Smagorinsky diffusion defined by equation (2.22). The deformation ($\mathbf{D}$) is that defined by Rotunno and Emanuel (1987). According to Ooyama (2001), both types of physical diffusion dominate over the numerical diffusion.

Both the CDIF and SDIF experiments demonstrate that diffusion only slightly modifies tropical cyclone development. Figure 5.16 shows the evolution of the simulated tropical cyclone in terms of v_{max} and p_{min} for the CNTL, CDIF, and SDIF experiments. In addition, figures 5.17 and 5.18 show the Hovmöller diagrams of the surface tangential wind speed for the CDIF and SDIF experiments, respectively. In both experiments, notice that the central vortex is almost completely eliminated by the diffusion. Furthermore, the development of the SDIF experiment is closer to the CNTL experiment than the CDIF experiment. As expected, the constant diffusion of the CDIF experiment disperses the tangential momentum uniformly across the domain. Conversely, the focused diffusion of the SDIF experiment, which is greatest across areas of large shear, disperses the tangential momentum primarily along the inner edge of the eyewall. Also, the CDIF tropical cyclone does not maintain a steady state but gradually weakens. Specifically, from 180 to 240 hours, the average v_{max} in the CDIF experiment weakens by 10-20 m s^{-1}. Most importantly, in neither experiment does the diffusion of tangential momentum accelerate the tangential wind field inside of the eye to near solid body rotation. Instead, a u-shaped wind profile exists inside of the eye. The implications of this result will be discussed in the next chapter.

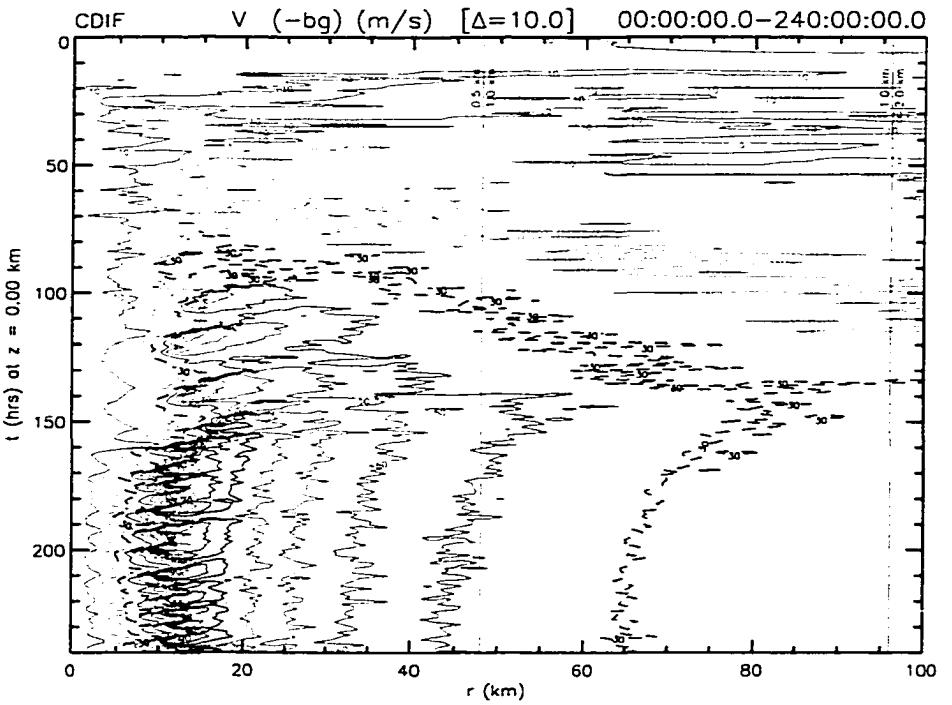

Figure 5.17: CDIF Experiment — Same as figure 4.5.

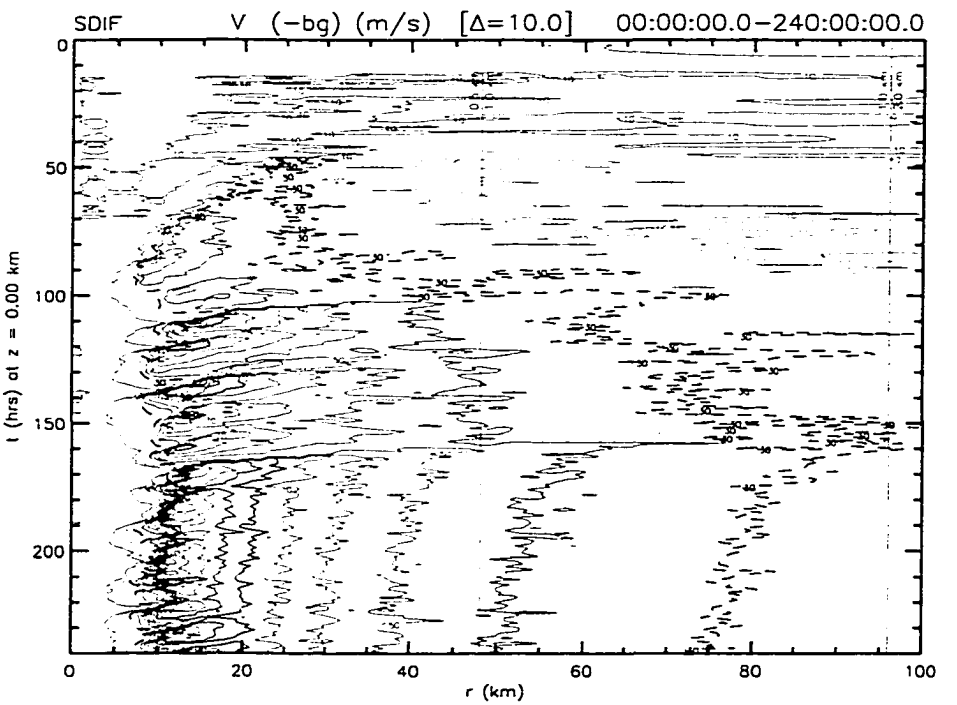

Figure 5.18: SDIF Experiment — Same as figure 4.5.

Chapter 6

DISCUSSION

> The most exciting phrase to hear in science, the one that heralds new discoveries, is not "Eureka!" (I found it) but "That's funny ..."
>
> Isaac Asimov

In the last two chapters, we performed a control experiment and a series of sensitivity experiments to better understand the processes that regulate the intensity of a symmetric tropical cyclone. From these experiments, we discovered that our model produces a more intense tropical cyclone than the current empirical and theoretical evidence might support. For instance, the most intense tropical cyclone on record was Typhoon Tip (1979) (Dunnavan and Diercks, 1980), with estimated sustained winds of 85 m s^{-1}. By comparison, our control simulation develops a near steady-state tropical cyclone with maximum tangential wind speeds of about 107 m s^{-1}. Because tropical cyclones with similar intensity have developed in past axisymmetric models (Yamasaki, 1977a, 1983; Bister, 1996; Zeng, 1996), we conclude that the intensity of our simulated tropical cyclone is not erroneous but is consistent with the approximate physics of the model. By approximating the physics, however, we have clearly omitted essential processes that limit tropical cyclone intensification.

In this chapter, we discuss in greater detail several of the limiting processes that are either included or excluded from the model. To begin, we compare our explanation for the formation of secondary eyewalls and the evolution of eyewall replacement cycles to past theories involving conditional and symmetric instability (section 6.1). Next, we examine the frontal structure of the eyewall, and consider the implications of this structure to barotropic instability and horizontal mixing (section 6.2). Finally, we briefly discuss the critical sensitivity of the tropical cyclone intensity to the boundary layer moisture (section 6.3).

6.1 Secondary Eyewalls and Eyewall Replacement Cycles

6.1.1 Observational Evidence and Current Theory

Both composite radar images and aircraft observations have clearly revealed the existence of multiple eyewalls encircling intense tropical cyclones (Willoughby et al., 1982). For instance, during an aerial weather reconnaissance flight through Typhoon Sarah (1956), Fortner (1958) was the first to observe, as he put it, an "eye within an eye". This intriguing feature has since been detected in many tropical cyclones (Jordan and Schatzle, 1961; Black et al., 1972; Holliday, 1974; Black and Willoughby, 1992). In fact, after analyzing flight-level data from aircraft traverses through Hurricanes Anita (1977), David (1979), and Allen (1980), Willoughby et al. (1982) suggested that secondary eyewalls may be "common" to intense symmetric tropical cyclones.

More importantly, the observational evidence also suggests that intensification of the tropical cyclone often ceases, following the formation of a secondary eyewall. For example, from observations of Hurricane David (1979), Willoughby et al. (1982) discovered that the formation and contraction of the secondary eyewall around the primary eyewall, or eyewall replacement cycle, marked the end of a period of deepening. In addition, they noted that each eyewall coincided with a maximum in the tangential wind profile and that this maximum increased as the eyewall contracted. In particular, the digital radar composite of David between 1045 and 1131 GMT on 30 August showed two distinct symmetric eyewalls (see figure 5, Willoughby et al). The corresponding maximum tangential wind speeds of the inner and outer eyewall were approximately 48 m s^{-1} at 19 km and 43 m s^{-1} at 39 km, respectively. Within 24 hours, however, only one eyewall remained, with a maximum tangential wind speed of 61 m s^{-1} at 19 km (see figure 8, Willoughby et al). During this same time period, the deepening of the minimum surface pressure ceased. Later observational studies further verified that eyewall replacement cycles modulate the intensity of tropical cyclones (Willoughby, 1990; Black and Willoughby, 1992).

Presently, we do not completely understand why secondary eyewalls form nor why eyewall replacement cycles occur. Willoughby et al. (1982) speculated that they may form due to internal gravity waves, surface convergence along the leading edge of outflow boundaries, or symmetric instability of the upper-level vortex. Several numerical studies have since attempted to confirm these and other mechanisms (Willoughby, 1979; Shapiro and Willoughby, 1982; Willoughby et al., 1984; Zeng, 1996).

To determine the physical mechanism of eyewall contraction, Willoughby (1979), and Shapiro and Willoughby (1982) used Eliassen's (1952) transverse circulation equation to investigate the response of a balanced vortex to point sources of heat and momentum. They found that the heat source produced two counter-rotating secondary circulations. The horizontal extent of these circulations differed in response to the local Rossby number (see figure 9, Shapiro and Willoughby), which is a function of the inertial stability. For instance, radially inward from the eyewall heat source, the inertial stability was relatively large due to the cyclonic shear of the vortex. As a result, the secondary circulation inside the eye was horizontally constrained to lie along the inner edge of the eyewall. The corresponding subsident warming and hydrostatic surface pressure decrease were similarly constrained, causing the maximum height and tangential wind tendencies to form immediately inside the radius of maximum tangential wind. In response to this configuration, the tangential wind maximum and eyewall contracted (see figure 10, Shapiro and Willoughby). Similar tendencies were identified in the observational data of Willoughby et al. (1982). While Shapiro and Willoughby also theorize that the superposition of secondary circulations associated with concentric eyewalls may explain why the outer eyewall replaces the inner, they do not propose a mechanism for the formation of secondary eyewalls.

Using an axisymmetric nonhydrostatic tropical cyclone model with sophisticated precipitation microphysics, Willoughby et al. (1984) verified the eyewall contraction mechanism proposed by Shapiro and Willoughby (1982) and investigated the formation mechanism of secondary eyewalls. Sensitivity experiments with and without the ice microphysics demonstrated that the inclusion of ice caused numerous secondary eyewalls to develop, contract,

and occasionally replace the primary eyewall. From these experiments, Willoughby et al. proposed a possible mechanism for secondary eyewall formation involving the combination of low-level convective instability and upper-level symmetric instability. Specifically, low-level convective instability is generated as the latent cooling from melting condensate overlies warming from the surface fluxes. In general, this instability does not produce moist convective ascent, because it is capped by the subsidence of the secondary circulation extending outward from the eyewall. However, if the gradual low-level ascent resulting from symmetric instability of the upper-level outflow overcomes the descent of the secondary circulation, deep moist convection develops and forms the secondary eyewall. Using the discriminant of Eliassen's (1952) transverse circulation equation, Willoughby et al. demonstrated that the outflow is dry-symmetrically unstable (see figures 11 and 12, Willoughby et al.); however, they did not provide sufficient evidence to prove that this symmetric instability represents a mechanism leading to the formation of secondary eyewalls.

Motivated by Willoughby et al.'s (1984) conjecture, Zeng (1996) sought to prove, at least within the framework of another axisymmetric nonhydrostatic model, that symmetric instability is a necessary precursor to the formation of secondary eyewalls. For simplicity, Zeng approximately evaluated the symmetric instability of the vortex in terms of the inertial instability. According to his simulations, the initial shallow convection is driven by low-level convective instability (see figure 7, Zeng). As this convection ascends, it advects absolute angular momentum upward, producing a local maximum of angular momentum. Radially inside of the maximum, the inertial stability of the flow increases, whereas outside of the maximum, the flow becomes inertially unstable. Deep moist convection is then driven upward in response to the upper-level divergence forced by the inertial instability. Zeng concludes that the deep convection of secondary eyewalls cannot develop without inertial, or symmetric, instability. However, his model does not include ice; therefore, the simulated moist convection does not experience the additional buoyant acceleration forced by the release of latent heat during the freezing of condensate (Willoughby et al., 1984).

6.1.2 Comparison of Current Theory with Our Results

Our results indicate that symmetric instability is not necessary for the initial development of the secondary eyewall. Both Willoughby et al. (1984) and Zeng (1996) argue that, given sufficient low-level convective instability, secondary eyewalls form when upper-level symmetric instability induces low-level ascent. The results presented in section 4.2.1.4 show that the initial convection of the secondary eyewall was not forced by symmetric instability, but by low-level convergence and the additional buoyancy generated by freezing condensate. This does not imply, however, that symmetric instability does not exist or is not important.

Although symmetric instability is not responsible for the initial development of the secondary eyewall, it does force subsequent convection, which results in the discrete inward propagation of the existing secondary eyewall (see figures 4.10–4.12). As the updraft of the secondary eyewall vertically advects lower-tropospheric air with high angular momentum, the middle and upper troposphere become inertially unstable, resulting in localized overturning (Ooyama, 1966). Simultaneously, the superposition of the inflow from the secondary circulation of the primary eyewall and the convective outflow from the secondary eyewall produce net radial convergence and new moist convection inward of the secondary eyewall. Additional ascent, forced by the middle- and upper-level inertially unstable flow, reinforces the new convection. Similar periodic developments lead to the discrete inward propagation of the secondary eyewall. Eventually, the discrete contraction ceases as the convergence associated with the tangential wind maximum overcomes that produced by the convective outflow. Following this transition, the contraction follows a model similar to that proposed by Shapiro and Willoughby (1982).

The disparity between our results and those of Zeng (1996) may be due, at least in part, to poor spatial resolution. If the model grid spacing is too coarse, the Reynolds number of the simulated flow will be too small; thus, the simulated moist convection will develop very slowly. In this context, we define the Reynolds number by

$$\mathrm{Re} = \frac{U\,(\Delta x)^{2j-1}}{\nu_j}, \tag{6.1}$$

wherein U is a representative wind speed of the simulated flow (e.g., $U \sim 50$ m s^{-1}), Δx is the grid spacing, j is the order of the numerical or physical diffusion (e.g., $j = 1$ for Fickian diffusion or $j = 3$ for hyper-diffusion), and ν_j is the effective viscosity (see appendix F). For example, Zeng uses an expandable grid with a relatively fine grid spacing of 1.3 km near the central axis; however, his grid spacing expands to 11 km at the radius where the secondary eyewall forms. Because the Reynolds number is relatively small at this radius (i.e., Re $\sim 10^2$–10^3 with $\nu_1 = 10^3$ m^2 s^{-1}), the moist convection of the secondary eyewall requires 24 hours to ascend through the depth of the troposphere. Compare this to the 1-km horizontal grid spacing and 1-hour ascent illustrated in figures 4.10–4.12. In this model, the Reynolds number is an order of magnitude larger (i.e., Re $\sim 10^3$–10^4 with $\nu_3 = 5 \times 10^{12}$ m^6 s^{-1}). According to Ooyama (2001), the horizontal grid spacing must be 2 km or less for the moist convection to develop "realistically". When the grid spacing is larger than 2 km, the slowly evolving convection is strongly influenced by the weak ascent produced by the symmetric instability. In contrast, when the grid spacing is less than 2 km, the rapidly evolving convection is influenced more by the conditional instability of the lower and middle troposphere than by symmetric instability of the upper troposphere.

Our results not only suggest that secondary eyewalls form in the absence of symmetric instability but in the absence of ice latent effects as well. Willoughby et al. (1984), and Lord and Lord (1988) performed two ice experiments similar to our NICE and NOTV experiments, as presented in section 5.2.1. From these, they concluded that the "thermodynamic input [of ice] by itself is a noticeable, but secondary effect." However, this conclusion was based on two experiments that did not produce a broad region of stratiform precipitation. In both experiments, the secondary eyewalls formed unrealistically close to the primary eyewall. Our NILE experiment extends the results of Willoughby et al. (1984), and Lord and Lord (1988) by excluding the latent effects of ice, while including the temperature-dependent terminal velocity. The results of this experiment show that secondary eyewalls

form within a broad region of stratiform precipitation in the absence of ice latent effects. When ice latent effects were included, the development of secondary eyewalls was enhanced by the additional negatively-buoyant descent and subsequent low-level convergence driven by the melting condensate.

Although the theories discussed in the last section address the destructive effects of the secondary eyewall on the primary eyewall, none of them consider the self-destructive effects of the primary eyewall on itself. Shapiro and Willoughby (1982) proposed that the superposition of the secondary circulations induced by the primary and secondary eyewalls is dominated by that of the latter; thus, the primary eyewall is eventually eliminated and replaced by the secondary eyewall. Willoughby et al. (1984), and Samsury and Zipser (1995) further suggest that the outflow from a secondary eyewall or from the surrounding rainbands, disturbs the boundary layer inflow into the primary eyewall. Our results, as presented in figures 4.7–4.9, indicate that the mesoscale downdraft induced by the precipitation beneath the stratiform region of the primary eyewall also disturbs the boundary layer inflow by advecting air with low entropy and angular momentum from the mid-troposphere into the boundary layer. As a result, the primary eyewall is partially the instrument of its own demise. During brief periods, for instance, the primary eyewall is observed to weaken and often reintensify, while the secondary eyewall is absent or far removed. A similar oscillation of the primary eyewall was recently observed during Hurricane Bonnie (D. Cecil, 2000, personal communication).

The formation of secondary eyewalls is also sensitive to the entropy flux by precipitation. If we assume that the precipitation process is pseudoadiabatic [i.e., neglecting the precipitation flux term in equation (2.6) as in experiment PSAD], secondary eyewalls do not form. When the precipitation does not materially conserve its entropy, no entropy passes through the lower boundary; therefore, the entropy of the downdrafts must increase. As a result, the negative buoyancy and low-level convergence is dramatically reduced, precluding the formation of secondary eyewalls.

Finally, in direct contradiction to our results, one might argue that including ice latent effects should produce a more intense tropical cyclone, due to the additional release of latent

heat. However, one must consider not only the magnitude of the latent heating but its vertical location as well. Using Eliassen's (1952) transverse circulation equation, Shapiro and Willoughby (1982) diagnosed the secondary circulation resulting from a point source of heat. From their results (see figure 9, Shapiro and Willoughby), we see that a low-level source of latent heating (e.g., condensation) produces a shallow layer of inflow near the surface, with a deep layer of outflow above. Furthermore, the magnitude of the inflow and outflow decrease rapidly away from the source. Thus, if the heat source is elevated (e.g., freezing), it produces very little surface inflow. Keep in mind that the tropical cyclone will only intensify if the low-level inflow advects entropy and angular momentum into the storm core. Therefore, while freezing may significantly enhance the mid-level inflow, it will have little effect on the surface inflow that maintains or intensifies the tropical cyclone.

6.2 Asymmetries

6.2.1 Sensitivity to the Horizontal Grid Spacing and Physical Diffusion

Ideally, the solution to any computer model should be largely independent of the numerics. Yet, in chapter 5, we discovered that our model is extremely sensitive to the horizontal grid spacing. In particular, as the grid spacing decreased from 16 km to 0.5 km, we found that the simulated tropical cyclone became smaller and more intense, with convergence of the solution for grid spacings less than 2 km (see figure 5.1). A similar sensitivity appears to exist in the cumulative results of past axisymmetric tropical cyclone simulations. For instance, figures 6.1a and b show the magnitude and radius, respectively, of the steady-state maximum tangential wind speed of the solutions to 13 different axisymmetric tropical cyclone models (see appendix A for details). Similar to our model, those models with finer grid spacing tend to produce smaller, more intense tropical cyclones.

One might argue that the trends depicted in figure 6.1 are trivially obvious. In other words, as the grid spacing decreases, we certainly can expect to resolve finer details, including a smaller eye. Nevertheless, if our intent is to understand the fundamental dynamics of

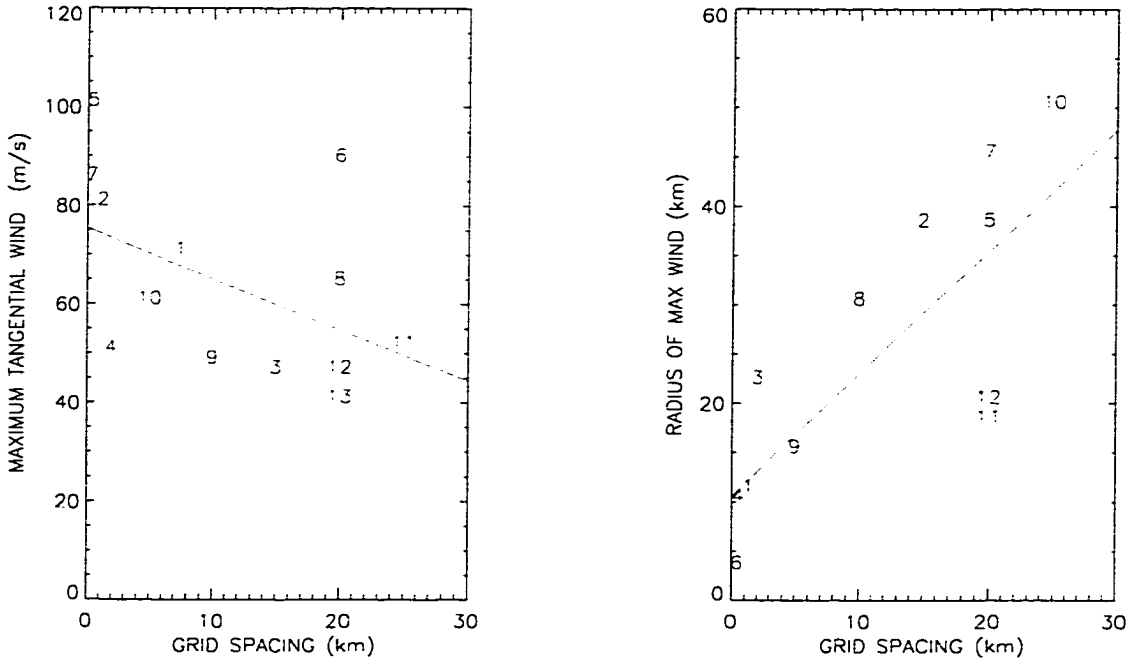

(a) (b)

1. Bister and Emanuel (1998)
2. Zeng (1996)
3. Rotunno and Emanuel (1987)
4. Willoughby et al. (1984)
5. Yamasaki (1983)
6. Rosenthal (1978)
7. Yamasaki (1977a)
8. Kurihara (1975)
9. Anthes (1971b)
10. Ooyama (1968, 1969)
11. Sundqvist (1970a)
12. Rosenthal (1970a)
13. Yamasaki (1968a)

Figure 6.1: Comparison of past axisymmetric tropical cyclone simulations in terms of the reported a) magnitude and b) radius of the maximum tangential wind speed as a function of the horizontal grid spacing. Each number in the figures matches the corresponding reference in the list below the figures. The line represents a linear fit to the data points.

the tropical cyclone eye, we must prevent the numerics from contaminating the essential physics, otherwise the conclusions drawn from the results will be questionable. For example, Rotunno and Emanuel (1987) used an axisymmetric nonhydrostatic primitive equation model, with 15 km horizontal grid spacing, to validate the steady-state intensity model of Emanuel (1986). They concluded that the steady-state solutions of the two models were in excellent agreement. In apparent contradiction to this conclusion, however, Bister and Emanuel (1998) used a slightly modified version of the same primitive equation model with 7.5 km horizontal grid spacing, and simulated a tropical cyclone that was nearly a third more intense than that simulated by Rotunno and Emanuel. More recently, Persing and Montgomery (2001, personal communication) have verified the sensitivity of Rotunno and Emanuel's model to horizontal grid spacing.

The problem of inadequate horizontal resolution is only aggravated by the physical diffusion used to control numerical noise. All of the models illustrated in figure 6.1 use some form of physical diffusion [e.g., see equation (2.22)] to control the numerical noise that develops at the resolution limit. As shown in section 5.2.3, this diffusion is obviously most effective at the smallest resolved scales (i.e., 2–4 Δr). Therefore, if the grid spacing is too coarse, important fine details of the eye and eyewall will be eliminated. Even with fine grid spacing, the CDIF and SDIF experiments verify that relatively small scale details are either diffused or eliminated.

We belabor this point to emphasize that important dynamic processes of the tropical cyclone eye and eyewall are obscured if the horizontal grid spacing is too coarse and the physical diffusion is too large. In particular, we used relatively fine horizontal grid spacing and minimal numerical diffusion to reproduce the isolation and conservation of mass within the eye, as observed by Willoughby (1998), and the frontal collapse of the eyewall, as theorized by Emanuel (1997). Ultimately, this structure has distinct implications to the barotropic stability of the vortex that no axisymmetric tropical cyclone model can properly simulate.

6.2.2 The Eye as a Containment Vessel

Conflicting observations of the tropical cyclone eye have stimulated an interesting debate concerning the existence of mixing between the eye and eyewall. Using eye soundings from Hurricanes Jimena (1991) and Olivia (1994), Willoughby (1998) shows that the airmass entrapped by the developing eye "has a long lifetime inside the eye, experiences only a few kilometers total subsidence, and mixes only weakly with the moist air from the eyewall." In contrast, Kossin and Eastin (2000) used radial profiles of tangential wind speed and vorticity across Hurricanes Diana (1984), Elena (1985), Andrew (1992), and Hortense (1996), to show that mixing between the eyewall and eye is relatively common and often occurs as the tropical cyclone approaches its peak intensity.

In agreement with Willoughby's (1998) observations, the evolving eye in our control experiments is comparable to a semi-permeable containment vessel. When the eyewall forms, the troposphere is divided into two airmasses (see figures 4.7 and 4.9). The airmass outside of the eyewall is theoretically infinite, due to the open outer boundary condition, whereas the airmass inside of the eyewall is isolated, due to the symmetric boundary condition of the center. To conserve mass, the contracting eyewall entrains air from the shrinking volume of the eye and exports it to the outer airmass. In contrast, there is almost no transfer of mass from the eyewall into the eye.

The thermodynamic structure of the eye adjusts to the intensifying vortex through the inward propagation of inertia-gravity waves. These waves produce convergence and net subsidence inside the eye. The resulting adiabatic warming restores the thermal balance of the evolving vortex. Eventually, the tropical cyclone transitions to a near steady state. After this point in time, the inertia-gravity wave activity virtually ceases and the eye airmass is relatively stagnant, as the vortex remains in approximate thermal wind balance. Note that this result is also consistent with Willoughby's (1979) observation that the eye subsidence is better correlated with the rate of change of intensity than with the intensity itself. Even though our results generally support Willoughby's (1998) conclusion that the eye is a containment vessel, we still have not explained the disparity with the observational evidence presented above.

6.2.3 Frontal Structure of the Eyewall

Emanuel's (1997) theory describing the frontal collapse of the eyewall may explain why the observed structure of the eye varies during the lifetime of a tropical cyclone (Kossin and Eastin, 2000). Using three idealized models, each characterized by their amount of horizontal diffusion, Emanuel demonstrated that the tropical cyclone eyewall is frontogenetic and that the maximum intensity is unattainable without diffusive mixing between the eye and eyewall. Specifically, with the zero-diffusion model, he showed that a tropical cyclone intensifies in the absence of any mixing between the eye and eyewall. To maintain gradient balance, the thermally-indirect secondary circulation of the eyewall warms the eye. This warming uniformly raises the temperature profile of the eye to that of the eyewall, creating a uniform hydrostatic pressure decrease and a stagnant tangential wind field in the eye. A frontal discontinuity thus develops between the eyewall and the surrounding environment. Empirically, however, such discontinuities are unobserved and naturally prevented by diffusive processes (e.g., turbulent mixing). With the other two models that include diffusion, Emanuel further showed that horizontal diffusion of momentum inward from the eyewall accelerates the tangential wind speed of the eye. To maintain gradient balance, the secondary circulation then intensifies to further warm the column and decrease the pressure, which also increases the surface entropy. In these models, the maximum tangential wind speed increases more rapidly and has a greater magnitude than in the zero-diffusion model. Emanuel argues that the greater magnitude results from the diffusion of momentum inside the radius of maximum wind, which increases the tangential wind speed and the surface entropy flux. With increased surface entropy in the storm core, the moist convection of the eyewall increases and the tropical cyclone intensifies.

Our results verify the frontal collapse theorized by Emanuel (1997) but not the greater intensity resulting from horizontal diffusion. To demonstrate this, we refer back to the horizontal grid spacing experiments of section 5.1.1. When the grid spacing is fine (i.e., 0.5–2 km), the numerical diffusion is horizontally restricted and the frictional convergence inside the radius of maximum wind compresses the structure of the eyewall, as shown

in figures 5.2a and 5.3a. This compression, in combination with the adiabatic warming of the eye by the secondary circulation, gives the eyewall its frontal appearance. Notice that, in agreement with Emanuel's theory, the eye temperature is equal to that in the eyewall at each level. As a result, there is almost no horizontal pressure gradient and the tangential wind speeds are nearly zero in comparison to the eyewall. In contrast, when the grid spacing is coarse (i.e., 4–16 km), the numerical diffusion obscures the eyewall structure. This diffusion mixes momentum into the eye, accelerating the tangential wind profile to near solid body rotation, as seen in figure 5.2b. The resulting gradient imbalance drives a thermally-indirect secondary circulation, in addition to that produced by the eyewall convection, that warms the eye above the temperature of the eyewall, as shown in figures 5.2b. Hydrostatically, the additional warming further decreases the surface pressure. In summary, while the extreme value of v_{max} develops independent of the eye, the extreme value of p_{min} depends on the acceleration of the eye tangential wind field to near solid body rotation by the diffusion of angular momentum from the eyewall into the eye. However, in contrast to Emanuel's theory, figure 5.1 shows that v_{max} actually decreases as the grid spacing and corresponding diffusion increase.

One possible explanation for the conflicting observations may be that the eye passes through two different stages during its lifecycle. Initially, the convection of the eyewall isolates the airmass of the eye, and clears and warms it through the inward propagation of inertia-gravity waves. Simultaneously, frontogenesis collapses the structure of the eyewall toward a discontinuity. Eventually, an instability must develop to mix away this discontinuity. Some have argued that this mixing must be due to the three-dimensional turbulent eddies along the inner edge of the eyewall; however, the horizontal scale of these eddies is relatively small in comparison to the size of the eye. Instead, we theorize that the mixing is due to two-dimensional turbulence resulting from the barotropic instability of the vortex.

6.2.4 Barotropic Instability and Horizontal Mixing

Of all the assumptions discussed in chapter 2, axisymmetry is the most restrictive and problematic. Recent observational and theoretical studies suggest that asymmetries modify

the tropical cyclone intensity and eye structure. For example, Kossin and Eastin (2000) identified a close correlation between changes in the intensity of Hurricanes Diana (1984) and Olivia (1994) to rapid changes in the kinematic and thermodynamic structure of each hurricane's eye. They speculate that these rapid changes were due to mixing between the eye and eyewall, triggered by barotropic instability during intensification. Schubert et al. (1999) theoretically demonstrated this same mixing process using an unforced barotropic nondivergent model. They found that enhanced rings of vorticity, similar to those observed by Kossin and Easton, are barotropically unstable. The instability subsequently mixes vorticity into the vortex center, accelerating the flow in the eye and decelerating the flow in the eyewall, which weakens the vortex [see Schubert et al. (1999) fig. 4]. These mixing processes are excluded from the axisymmetric dynamics and therefore have no influence on intensity or eye structure.

To simulate mixing due to asymmetries, previous axisymmetric tropical cyclone models used diffusion to crudely parameterized the physics of horizontal mixing. Riehl and Malkus (1961) observed that the horizontal diffusion coefficient in Hurricane Daisy (1958) was three orders of magnitude larger than the vertical diffusion coefficient. This difference implied that horizontal mixing was larger than vertical mixing; however, according to Rosenthal (1970a), "a valid formulation for the lateral mixing [was] not at all clear." As a result of these observations, the earliest models applied a parameterization with constant diffusion coefficients, in which the horizontal coefficient was greater than the vertical. Later, lacking any additional physical insight, Rosenthal, Anthes and others assumed that the mixing was due to shear instability inside the radius of maximum wind and applied a diffusion parameterization based on Smagorinsky's (1963) approach (see chapter 2 for details). Even the most recent models use this type of diffusion (Rotunno and Emanuel, 1987; Zeng, 1996).

Diffusion, however, does not accurately simulate the mixing due to barotropic instability. Kossin (2000a) compared the analytical solution of a one-dimensional axisymmetric model of vorticity diffusion to the numerical solution of a two-dimensional barotropic model of vorticity mixing. He discovered that the peak vorticity in the eyewall is strongly damped

when vorticity diffuses into the eye, whereas the peak is nearly conserved when vorticity is mixed. This conservation results from the formation and advection of coherent vortices that preserve the peak vorticity against dissipation. Furthermore, the amount of diffusion is greatest at the smallest resolved scales; therefore, as shown in our CDIF and SDIF experiments, diffusion is incapable of efficiently mixing entropy and momentum into the center of the eye when the horizonal grid spacing is small relative to the scale of the eye and eyewall.

Whether by diffusion or mixing, vorticity is transfered from the eyewall to the center, weakening the vortex. We naturally wonder if vorticity mixing might limit the intensity of the control experiment. Since Kossin's (2000a) results indicate that diffusion inaccurately captures this process, we chose not to include any diffusion in our control experiment, other than that absolutely necessary for numerical stability. Instead, as a first step, we indirectly investigate the effects of mixing on our steady-state tropical cyclone using the Schubert et al. (1999) barotropic model, initialized with a vorticity (i.e., PV) profile obtained from the mean steady-state data of the control experiment.

Of course, there are significant differences between the two models. Using an axisymmetric primitive equation model with moist thermodynamics, we can investigate the generation of PV by non-conservative boundary layer and moist convective processes; however, as noted above, we cannot accurately simulate horizontal mixing. In contrast, using a barotropic model, we can investigate the horizontal mixing that results from an initially unstable PV (i.e., vorticity) distribution; however, we cannot simulate the non-conservative processes. Despite these differences and limitations, Schubert et al. (1999) have demonstrated that, given an initially symmetric but unstable vorticity distribution, the barotropic model reproduces the elementary geometric structures observed in many tropical cyclones.

As mentioned previously, the Schubert et al. (1999) model simulates the mixing, or nonlinear advection, resulting from the disturbance of a barotropically unstable vortex. The future structure of the vortex is predicted by solving the two-dimensional nondivergent vorticity equation

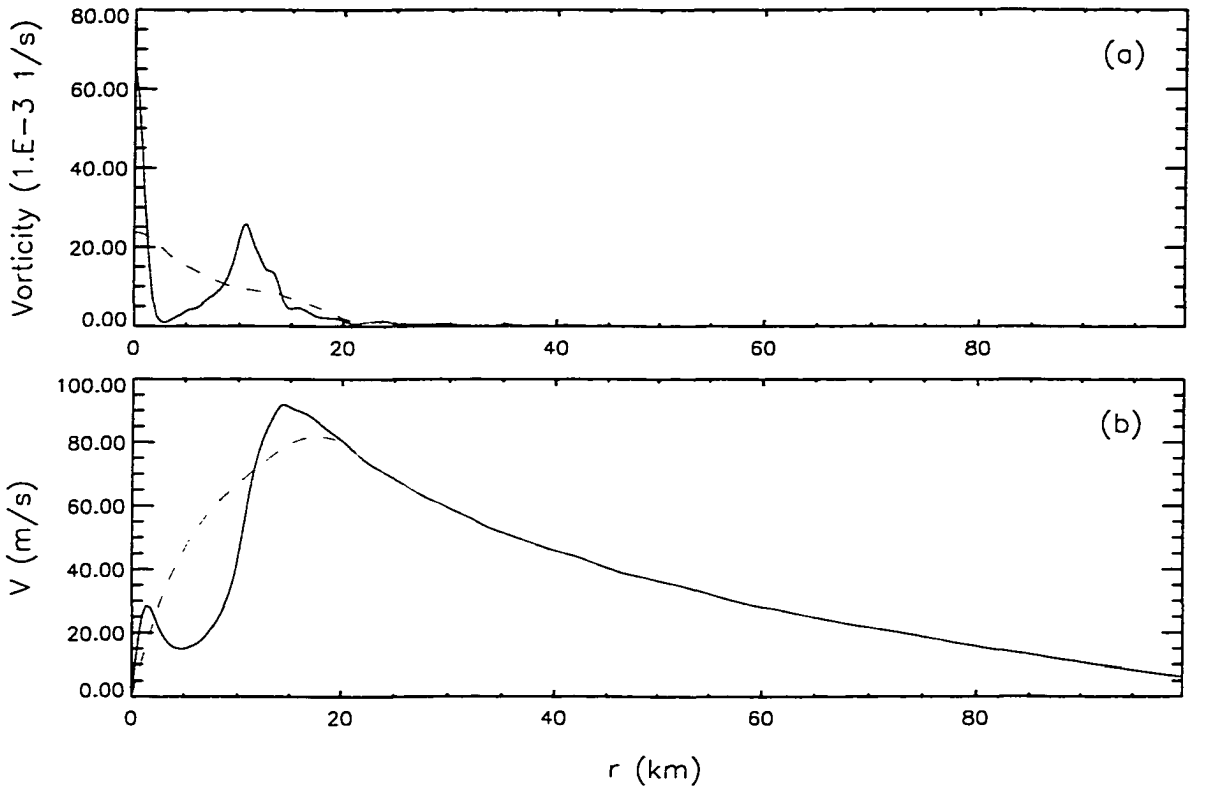

Figure 6.2: Azimuthally-averaged a) vorticity and b) tangential wind profiles for the initial (solid) and final (dashed) states.

$$\frac{\partial \zeta}{\partial t} = -u\frac{\partial \zeta}{\partial x} - v\frac{\partial \zeta}{\partial y} + \nu \nabla^2 \zeta. \tag{6.2}$$

The ordinary (∇^2) diffusion, with $\nu = 15$ m^2 s^{-1}, is required to damp the cascade of enstrophy at the resolution limit. Spatially, (6.2) is solved using the double-Fourier pseudospectral method on a 200 × 200 km doubly-periodic domain with 512 × 512 equally spaced collocation points. After dealiasing, the domain resolves 170 × 170 Fourier modes. Temporally, (6.2) is integrated over 10 hours using the fourth-order Runge-Kutta method with a 3 s timestep. See the paper by Schubert et al. (1999) for more details.

To investigate the stability of the control experiment vortex, we initialize the barotropic model using the steady-state vorticity obtained from the axisymmetric primitive equation model. Figures 6.2a and b show the initial symmetric (solid) and final azimuthally-averaged (dashed) vorticity and tangential wind profiles, respectively. From figure 4.20, we see that

the maximum MPV anomaly is located in the mid-troposphere. In the barotropic model, this MPV is represented by the vorticity profile at a given level; therefore, we initialize the model with a symmetric vortex derived from the 180–240 hour average vorticity profile at a height of 5 km. This vortex is then perturbed with proportional random noise confined to an annulus extending from $r = 5$ km to $r = 15$ km. The magnitude of the perturbation is one percent or less than the local basic state vorticity.

The results of the simulation reveal that the vorticity profile obtained from the steady-state vortex is barotropically unstable. Figure 6.3 shows the evolution of the vorticity field at 0, 0.5, 1, 2, 4, and 8 hours. By 0.5 hours, we see that the initially symmetric vortex develops a finite amplitude wavenumber five perturbation. After another 0.5 hours, the maximum vorticity in the eyewall has been gathered into five coherent vortices, with vorticity filaments forming along the outer edge. Within another hour, the vorticity within the coherent vortices mixes into the eye and the peak vorticity initially at the eye center is severely deformed. By eight hours, the mixing process has essentially ceased. In the final state, the initial maximum vorticity of the center has been eliminated by diffusion and the eyewall vorticity is now found in the center.

The results also demonstrate that mixing vorticity from the eyewall into the eye weakens the vortex (Schubert et al., 1999). Comparing figures 6.2 and 6.3, we see that the peak vorticity at the center is eliminated and that the vorticity in the eyewall is mixed to the center, with only a slight decrease in the peak value from 2.6×10^{-3} to 2.4×10^{-3} s^{-1}. As the vorticity is mixed inward, v inside the eye increases, whereas in the eyewall, it decreases. For example, at $r = 5$ km, v increases from 15.0 to 45.0 m s^{-1}. In contrast, v_{max} in the eyewall decreases and expands outward from 93 m s^{-1} at $r_{max} = 14$ km to 83 m s^{-1} at $r_{max} = 17$ km.

We must address two caveats to the conclusions drawn from this experiment. First, as mentioned previously, moist convection continuously generates PV in a tropical cyclone, even as it is being mixed into the eye, whereas in the barotropic model, the PV is imposed initially with no additional forcing. Only a three-dimensional primitive equation model,

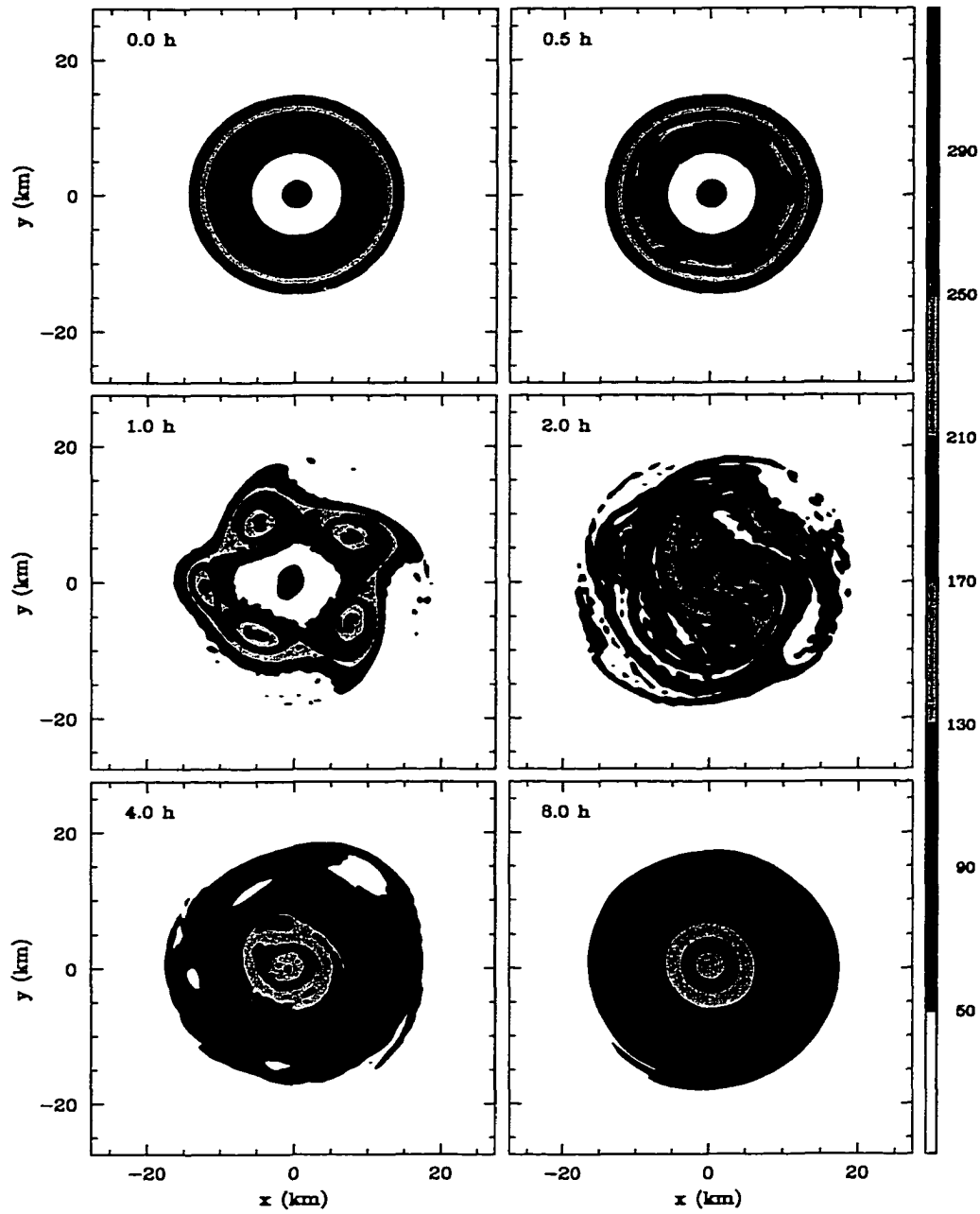

Figure 6.3: Evolution of a barotropically-unstable vortex illustrated using vorticity (10^{-5} s^{-1}) at 0, 0.5, 2.0, 4.0, and 8.0 hours.

with explicit moist thermodynamics will reproduce the complete PV dynamics. Second, the central vortex, with its relatively large vorticity, alters the instability and the mixing (Schubert et al., 1999). According to Kossin (2000b), the peak vorticity in the eye partially stabilizes the unstable vorticity annulus of the eyewall; therefore, in the absence of the center vorticity, the eyewall is unstable to higher wavenumber perturbations with even larger growth rates.

6.3 Boundary Layer Moisture

The excessive moisture content of the boundary layer inflow may explain much of the unrealistic intensity of our simulated tropical cyclone. The inflow advects nearly saturated moist air with 23.9 g kg^{-1} of water vapor into the storm core. This moisture eventually condenses in the eyewall and precipitates at a maximum rate of 200 mm hr^{-1}. Such an incredible precipitation rate equates to tremendous latent heating, which ultimately governs the intensity of the vortex (Eliassen, 1952; Shapiro and Willoughby, 1982; Schubert and Hack, 1982). Since the ocean surface in the model represents an infinite reservoir of latent energy, the intensification of the vortex continues unabated until surface friction and internal dissipation overcome the energy input. Thus, in order to limit the intensification, we must incorporate additional microphysics into the model to more accurately reproduce the moisture content of the boundary layer.

In the sub-tropical atmosphere, the moisture profile of the steady-state boundary layer is maintained by a subtle balance between the upward flux of moist air from the surface and the net downward flux of dry air through the trade-wind inversion (Nitta and Esbensen, 1974; Betts, 1975). Specifically, below the inversion, turbulent eddies transport moist air from the surface upward, while above the inversion, large-scale subsidence transports dry air downward. Shallow cumulus clouds detrain the moist air into the free atmosphere above and entrain the dry air down into the boundary layer below. The steady relative humidity (RH) profile of the boundary layer is then maintained by a balance between the upward turbulent flux of moist air and the downward turbulent flux of dry air.

In a simple model of the boundary layer that neglects such details as the trade inversion and shallow cumulus clouds, the balance between the upward and downward turbulent fluxes is achieved indirectly between the downward advection of dry air by large-scale subsidence and the upward flux of moist air by diffusion. In our model, at least initially, there is no such balance. To understand why, consider the model predictive equation for the total water mass, (2.56), as expressed within the boundary layer, i.e.,

$$\frac{\partial \nu'}{\partial t} = -u\frac{\partial \nu'}{\partial r} - w\frac{\partial \nu}{\partial z} - F_\nu \left(\frac{d\phi_a}{dz} + \phi_a \frac{\partial \xi}{\partial z} \right), \tag{6.3}$$

wherein we have also neglected the precipitation flux. According to this expression, the change of water mass at a point within the boundary layer is governed by the horizontal advection, vertical advection, and vertical diffusion. Initially, however, the horizontal and vertical advection are zero, because there is no secondary circulation or large-scale subsidence (i.e., $u = w = 0$). In contrast, the vertical diffusion is not zero, due to the surface flux produced by the initial vortex (i.e. $v \neq 0$, $F_\nu \neq 0$). The change of water mass is then governed by the vertical diffusion alone. As a result, the RH increases rapidly to near 100%. Observationally, the RH should be no greater than 84% in the surrounding environment or 95% in the tropical cyclone core (Hawkins and Imbembo, 1976). Even after the secondary circulation of the tropical cyclone develops, the boundary layer RH remains near saturation. With such large values of RH in the boundary layer inflow, the tropical cyclone has a rich supply of latent energy from which to intensify.

Even analytical models like that from Emanuel (1986) demonstrate a marked sensitivity of the steady-state tropical cyclone to the RH, or moist entropy, of the boundary layer inflow. As a simple thought experiment, Emanuel derived the boundary layer closure for his model, assuming that the vertical turbulent, or diffusive, flux vanishes at the top of the boundary layer. The steady-state solution then required a balance between the vertical turbulent flux convergence and horizontal advection by the inflow. However, the horizontal moisture gradient necessary to achieve this balance was unrealistic; thus, according to Emanuel, the solution to the modified model produced an "absurd" distribution of entropy and angular

momentum. As a result of this unrealistic solution, the final model was derived assuming instead that horizontal advection was negligible, and that the vertical turbulent fluxes at the top and bottom of the boundary layer approximately balanced to produce a near constant value of RH. However, even if the vertical turbulent flux at the top of the boundary layer were properly incorporated into our model, the moist entropy would still increase, because there is no initial large-scale subsidence to continuously replenish the dry air.

Large-scale subsidence in the subtropical atmosphere is driven by radiational cooling. For example, radiative cooling of 2°C day^{-1} would produce a gradual descent of about 0.4 km day^{-1} or 4.6 mm s^{-1}. As noted in chapter 2, such cooling is absent from most axisymmetric tropical cyclone models. Recently, however, Rotunno and Emanuel (1987), and Zeng (1996) incorporated a crude representation of radiative cooling using a simple Newtonian scheme, which relaxes the temperature profile toward a fixed-background profile. This scheme apparently achieves the desired result in the surrounding environment; unfortunately, it also subtly yet unrealistically alters the evolution of the tropical cyclone core. As stressed in chapter 2, we have chosen not to contaminate the essential physics with an efficient yet crude representation of the radiation. We will save this test for a future version of the model that contains a physically-consistent radiation parameterization.

Chapter 7

CONCLUSION

> There are no foolish questions and no man becomes a fool until he has stopped asking questions.
>
> Charles Proteus Steinmetz (1865–1923)
> German-American electrical engineer who
> pioneered the use of alternating current.

In the introduction, we posed the fundamental question: What regulates the intensity of tropical cyclones? To answer this question, we developed a two-dimensional nonhydrostatic primitive equation model to simulate a symmetric tropical cyclone-like vortex. Certainly, this type of model cannot answer the posed question definitively; however, the simulations presented here do verify and even extend many existing theories, and provide new insight into the parameters and processes governing tropical cyclone intensity.

7.1 Summary

The model physics are based on the unique set of nonhydrostatic, primitive equations and bulk microphysics formulated by Ooyama (1990, 1997, 1999, 2001). Dynamically, these equations contain the complete bulk physics of a precipitating atmosphere, because they materially conserve not only the precipitation mass, but the precipitation momentum and entropy as well. In other words, the equations are not pseudoadiabatic, as in many other models. Thermodynamically, the reversible processes are computed exactly; therefore, any empiricism is isolated in the irreversible processes, which are represented by the microphysical parameterizations. Finally, the ice bulk microphysics scheme is simple yet physically

consistent. Instead of representing each ice species independently, we represent water and ice collectively as a single synthesized condensate, which we define using a temperature interpolation of the saturation vapor pressures over a plane surface of water and ice. The phase change of water to ice is then manifest as a large positive anomaly in the synthesized specific heat.

The model spatial numerics are also unique and based on the Spectral Application of Finite Element Representation (SAFER) method developed by Ooyama (1984, 1987) and DeMaria et al. (1992). As the name implies, the SAFER method is a spectral approach that uses the cubic B-spline finite element as the basis function. This method incorporates favorable characteristics from both the Fourier spectral and grid point methods. Because the first two derivatives of the B-spline are continuous, the SAFER method has smaller dispersion errors, similar to the Fourier spectral method. Yet, because the B-spline is locally defined, the SAFER method has flexible boundary conditions, similar to a grid point method. With reduced dispersion errors and flexible boundary conditions, the SAFER method provides for noise-free nest and lateral boundary conditions. Finally, unlike other spectral methods that use nonorthogonal basis functions, the SAFER method is computationally efficient, considering the expense per degree of freedom.

To better understand the dynamics of a precipitating atmosphere, we further derived a generalized form of the moist potential vorticity (MPV) principle from the model equations. Specifically, we generalized Ertel's (1942b) dry PV (DPV) principle using a virtual potential temperature (θ_ρ) that is a function of the total pressure and total density, including condensate. This form of the MPV has several advantages over other forms. First and foremost, θ_ρ exactly eliminates the solenoidal term from the PV conservation equation; therefore, the MPV is exactly invertible. Second, the MPV satisfies the impermeability theorem of Haynes and McIntyre (1987, 1990). Third, the MPV contains all of the moist physics, including precipitation. Last, since θ_ρ is a virtual temperature, the MPV distribution is similar to that of the DPV. In contrast, the more commonly used equivalent potential vorticity (EPV), defined using the equivalent potential temperature, does not

share these advantages. For instance, the EPV is not exactly invertible and is not comparable to the DPV (i.e., the EPV is zero in the eyewall where the DPV and MPV are a maximum).

To test and validate the model against current observations and theory, we performed a control experiment and a series of sensitivity experiments. The control experiment was defined using relatively standard microphysical parameterizations, and initial and boundary conditions. This approach facilitated the comparison of the control experiment with past axisymmetric tropical cyclone simulations. Several additional experiments were then performed to test the sensitivity of the model physics and numerics. In particular, we tested the sensitivity to the horizontal and vertical grid spacing, the ice and precipitation microphysics, and the horizontal diffusion.

7.2 Conclusions

From our analysis of the control and sensitivity experiments, we have gained new insight into the intensification of symmetric tropical cyclones, including the following conclusions:

- Most importantly, to our knowledge, this is the first primitive equation model to simulate the frontal collapse of the tropical cyclone eyewall, as theorized by Emanuel (1997). During the collapse and frontogenesis, a large MPV anomaly develops in the mid-troposphere of the eyewall. Supplemental experiments using a barotropic nondivergent model (Schubert et al., 1999) suggest that this MPV distribution is unstable. However, the axisymmetric model is incapable of simulating the ensuing turbulent mixing; instead, it nearly conserves the airmass inside the eye. These results may help explain the conflicting observations of mixing (Kossin and Eastin, 2000) and non-mixing (Willoughby, 1998) between the eye and eyewall.

- Axisymmetric tropical cyclone models are extremely sensitive to the horizontal grid spacing. It is clear from these results, and implied in the past results of other axisymmetric tropical cyclone models, that the intensity of the vortex increases and

the size decreases as the horizontal grid spacing is reduced. Furthermore, these experiments indicate that independence from the numerics does not occur until the horizontal grid spacing is less than 2 km.

- In contrast to the results of Willoughby et al. (1984) and Zeng (1996), secondary eyewalls do not form due to symmetric instability, but due to low-level conditional instability and the additional buoyant ascent resulting from the freezing of condensate. Nevertheless, symmetric instability does sustain the secondary eyewall and supports its discrete inward propagation.

- The primary eyewall and vortex weakens not only due to the secondary circulation and convective outflow from a secondary eyewall, as proposed by Shapiro and Willoughby (1982) and Willoughby et al. (1982), but also due to the stratiform outflow of the primary eyewall itself. The mesoscale downdraft from the stratiform precipitation transports low entropy and angular momentum from the mid-troposphere into the boundary layer, and eventually into the storm core, which weakens the eyewall convection and the vortex.

- The intensity of the simulated tropical cyclone exceeds observed values in the absence of large-scale subsidence. If this subsidence is not present, the upward turbulent flux of moisture from the surface is not balanced by the downward advection of dry air from the mid-troposphere. As a result, the boundary layer moisture increases to near saturation. This moisture then provides an excessive source of latent energy to the tropical cyclone, allowing it to intensify beyond realistic bounds. In the subtropical atmosphere, the subsidence is driven by radiational cooling; however, in virtually all axisymmetric tropical cyclone models, radiative cooling is either neglected or crudely parameterized (Rotunno and Emanuel, 1987; Zeng, 1996). We speculate that those models neglecting radiative cooling apparently avoid the excessive intensity. This is accomplished in one of two ways: indirectly, through coarse horizontal grid spacing, which restricts the size and intensity of the vortex, or directly, through excessive vertical diffusion, which transports the moisture through a greater depth.

7.3 Future Work

The most serious disparity between our results and the observational evidence is the extreme intensity of the steady-state tropical cyclone. As discussed above, this shortcoming can be corrected by including radiative cooling. Most importantly, we do not think that limiting the intensity will invalidate our qualitative conclusions but will certainly change the quantitative results. To determine the magnitude of the change, a physically consistent yet computationally efficient radiation parameterization must be incorporated into the next version of the model.

In this version of the model, we also chose to use simple microphysical parameterizations that incorporate only the fundamental physics necessary to simulate a tropical cyclone. In the future, we will include more complex microphysics to understand the more subtle effects of ice, precipitation, and diffusion. For instance, we could incorporate a relatively elaborate precipitation scheme (Lin et al., 1983, e.g.,) to investigate the sensitivity of various ice species, similar to Willoughby et al. (1984), Lord et al. (1984), and Lord and Lord (1988). A more detailed surface flux parameterization, based on Monin-Obukhov similarity theory, has already been incorporated and is being tested. This parameterization includes Charnock's (1955) factor, which integrates the influence of wave height on the roughness length, but still does not contain the latent effects of sea spray (Bao et al., 2000).

A significant accomplishment of this work is the derivation of the MPV principle; however, we have only partially assessed its utility. We have diagnosed the MPV, but we have not inverted it. Since the power of PV is in its invertibility, we must next invert the MPV and diagnose the balanced flow.

The diagnosed MPV was also indirectly used to evaluate the potential barotropic instability of our symmetric vortex. To directly evaluate the instability requires a three-dimensional version of the model numerics. Although such a version is theoretically possible, it would

be computationally expensive as well. According to Ooyama (2000, personal communication), the numerics can be approximated to decrease the computational cost; however, the spectral filter is then no longer isotropic. As a result, our symmetric tropical cyclone would eventually have a square appearance. Until a three-dimensional version of the numerics can be perfected, we will continue to investigate two-dimensional problems. For instance, the model has been used extensively to study squall lines (Ooyama, 1995, 1997, 1999; Garcia, 2000). In the near future, we plan to use it to investigate the dynamics of the Hadley circulation.

REFERENCES

Anthes, R. A., 1971a: Numerical experiments with a slowly varying model of the tropical cyclone. *Mon. Wea. Rev.*, **99**, 636–643.

Anthes, R. A., 1971b: A numerical model of the slowly varying tropical cyclone in isentropic coordinates. *Mon. Wea. Rev.*, **99**, 617–635.

Anthes, R. A., 1972: Development of asymmetries in a three–dimensional numerical model of the tropical cyclone. *Mon. Wea. Rev.*, **100**, 461–476.

Anthes, R. A., S. L. Rosenthal, and J. W. Trout, 1971a: Preliminary results from an asymmetric model for the tropical cyclone. *Mon. Wea. Rev.*, **99**, 744–758.

Anthes, R. A., J. W. Trout, and S. L. Rosenthal, 1971b: Comparisons of tropical cyclone simulations with and without the assumption of circular symmetry. *Mon. Wea. Rev.*, **99**, 759–766.

Asselin, R., 1972: Frequency filter for time integrations. *Mon. Wea. Rev.*, **100**, 487–490.

Bao, J.-W., J. M. Wilczak, J.-K. Choi, and L. H. Kantha, 2000: Numerical simulation of air-sea interaction under high wind conditions using a coupled model: A study of hurricane development. *Mon. Wea. Rev.*, **128**, 2190–2210.

Bénard, P., J.-P. Lafore, and J.-L. Redelsperger, 1992: Nonhydrostatic simulation of frontogenesis in a moist atmosphere. Part II: Moist potential vorticity budget and wide rainbands. *J. Atmos. Sci.*, **49**, 2218–2235.

Bennetts, D. A., and B. J. Hoskins, 1979: Conditional symmetric instability–A possible explanation for frontal rainbands. *Quart. J. Roy. Meteor. Soc.*, **105**, 945–962.

Betts, A. K., 1975: Parametric interpretation of trade-wind cumulus budget studies. *J. Atmos. Sci.*, **32**, 1934–1945.

Bister, M., 1996: Development of tropical cyclones from mesoscale convective systems. Ph.D. dissertation, Massachusetts Institute of Technology, 112 pp.

Bister, M., 1997: Effect of the coriolis parameter on tropical cyclogenesis: The dominant role of outer convection. *Proc. 22th Tech. Conf. on Hur. and Trop. Meteor.*, Fort Collins, CO, Amer. Meteor. Soc., 553–554.

Bister, M., and K. A. Emanuel, 1998: Dissipative heating and hurricane intensity. *Meteorol. Atmos. Phys.*, **65**, 233–240.

Black, M. L., R. W. Burpee, and F. D. Marks, Jr., 1996: Vertical motion characteristics of tropical cyclones determined with airborne Doppler radial velocities. *J. Atmos. Sci.*, **53**, 1887–1909.

Black, M. L., and H. E. Willoughby, 1992: The concentric eyewall cycle of Hurricane Gilbert. *Mon. Wea. Rev.*, **120**, 947–957.

Black, P. G., and G. J. Holland, 1995: The boundary layer of Tropical Cyclone Kerry (1979). *Mon. Wea. Rev.*, **123**, 2007–2028.

Black, P. G., H. V. Senn, and C. L. Courtright, 1972: Airborne radar observations of eye configuration changes, bright band distribution, and precipitation tilt during the 1969 multiple seeding experiments in Hurricane Debbie. *Mon. Wea. Rev.*, **100**, 208–217.

Black, R. A., H. B. Bluestein, and M. L. Black, 1994: Unusually strong vertical motions in a Caribbean hurricane. *Mon. Wea. Rev.*, **122**, 2722–2739.

Black, R. A., and J. Hallett, 1996: Observations of the distribution of ice in hurricanes. *J. Atmos. Sci.*, **43**, 802–822.

Bluestein, H. B., 1992: *Synoptic-Dynamic Meteorology in Midlatitudes.* Vol. 1. Oxford Univ. Press, 431 pp.

Böhm, J. P., 1992: A general hydrodynamic theory for mixed-phase microphysics. Part I: Drag and fall speed of hydrometeors. *Atmos. Res.*, **27**, 253–274.

Brandes, E. A., 1990: Evolution and structure of the 6-7 may 1985 mesoscale convective system and associated vortex. *Mon. Wea. Rev.*, **118**, 109–128.

Browning, G., H.-O. Kreiss, and J. Oliger, 1973: Mesh refinements. *Mathematics of Computation*, **27**, 29–39.

Camp, J. P., 1999: Hurricane maximum intensity: Past and present. M.S. thesis, Colorado State University, 147 pp.

Camp, J. P., and M. T. Montgomery, 2001: Hurricane maximum intensity: Past and present. *Mon. Wea. Rev.*, submitted.

Cao, Z., and H. Cho, 1995: Generation of moist potential vorticity in extratropical cyclones. *J. Atmos. Sci.*, **52**, 3263–3281.

Charnock, H., 1955: Wind stress on the water surface. *Quart. J. Roy. Meteor. Soc.*, **98**, 639–640.

DeBoor, C., 1972: On calculating with B–splines. *J. Approximation Theory*, **6**, 50–62.

DeMaria, M., S. D. Aberson, K. V. Ooyama, and S. J. Lord, 1992: A nested spectral model for hurricane track forecasting. *Mon. Wea. Rev.*, **120**, 1628–1643.

DeMaria, M., and J. D. Pickle, 1988: A simplified system of equations for simulation of tropical cyclones. *J. Atmos. Sci.*, **45**, 1542–1554.

Dodge, P., R. W. Burpee, and F. D. Marks, Jr., 1999: The kinematic structure of a hurricane with sea level pressure less than 900 mb. *Mon. Wea. Rev.*, **127**, 987–1004.

Dunnavan, G. M., and J. W. Diercks, 1980: An analysis of Supertyphoon Tip (October 1979). *Mon. Wea. Rev.*, **180**, 1915–1923.

Dutton, J. A., 1995: *Dynamics of Atmospheric Motions.* Dover Publications, 617 pp. Formerly titled The Ceaseless Wind.

Dvorak, V. F., 1975: Tropical cyclone intensity analysis and forecasting from satellite imagery. *Mon. Wea. Rev.*, **103**, 420–430.

Eliassen, A., 1952: Slow thermally or frictionally controlled meridional circulation in a circular vortex. *Astrophys. Norv.*, **5**, 19–60.

Elsberry, R. L., G. G. Coltrane, and P. L. Krueger, 1975: Statistical forecasts of 24, 48 and 72 h typhoon and tropical storm intensity change. *J. Appl. Meteor.*, **14**, 445–451.

Emanuel, K. A., 1983: Elementary aspects of the interaction between cumulus convection and the large-scale environment. *Mesoscale Meteorology: Theories, Observation and Models*, D. K. Lilly and T. Gal-Chen, Eds., D. Reidel, 551–575.

Emanuel, K. A., 1986: An air-sea interaction theory for tropical cyclones Part I: Steady-state maintenance. *J. Atmos. Sci.*, **43**, 585–604.

Emanuel, K. A., 1988: The maximum intensity of hurricanes. *J. Atmos. Sci.*, **45**, 1143–1155.

Emanuel, K. A., 1989: The finite-amplitude nature of tropical cyclogenesis. *J. Atmos. Sci.*, **46**, 3431–3456.

Emanuel, K. A., 1995a: The behavior of a simple hurricane model using a convective scheme based on subcloud-layer entropy equilibrium. *J. Atmos. Sci.*, **52**, 3960–3968.

Emanuel, K. A., 1995b: Sensitivity of tropical cyclones to surface exchange coefficients and a revised steady-state model incorporating eye dynamics. *J. Atmos. Sci.*, **52**, 3969–3976.

Emanuel, K. A., 1997: Some aspects of hurricane inner-core dynamics and energetics. *J. Atmos. Sci.*, **54**, 1014–1026.

Enagonio, J., and M. T. Montgomery, 1998: Tropical cyclogenesis via convectively forced vortex rossby waves in a three-dimensional quasigeostrophic model. Paper 656, Dept. of Atmospheric Science, Colorado State University, 115 pp.

Ertel, H., 1942a: Ein neuer hydrodinamischer Wirbelsatz. *Meteor. Z.*, **59**, 271–281.

Ertel, H., 1942b: Ein neuer hydrodynamischer Erhaltungssatz. *Naturwiss.*, **30**, 543–544.

Estoque, M. A., 1966: Heating due to penetrative convection. *Studies on the Hurricane Boundary Layer and Penetrative Convection. Part IV*, University of Hawaii, 97–113.

Estoque, M. A., and J. J. Fernandez-Partagas, 1968: Hurricane studies, Part I – Cumulus and small-scale exchange processes in hurricanes; Part II – Preliminary report on modeling the mature hurricane. Paper no. 2, Grant ESSA E-19-67(G), 65 pp.

Fortner, Jr., L. E., 1958: Typhoon Sarah, 1956. *Bull. Amer. Meteor. Soc.*, **39**, 633–639.

Frank, W. M., 1978: The life cycles of GATE convective systems. *J. Atmos. Sci.*, **35**, 1256–1264.

Frank, W. M., and E. A. Ritchie, 1999: Effects of environmental flow upon tropical cyclone structure. *Mon. Wea. Rev.*, **127**, 2044–2061.

Gamache, J. F., and R. A. Houze, Jr., 1985: Further analysis of the composite wind and thermodynamic structure of the 12 September GATE squall line. *Mon. Wea. Rev.*, **113**, 1241–1259.

Garcia, M., 2000: Simulated tropical convection. Atmospheric Science Report No. 690, Colorado State University, 273 pp.

Ginis, I., and G. Sutyrin, 1995: Hurricane-generated depth-averaged currents and sea surface elevation. *J. Phys. Oceanogr.*, **25**, 1218–1242.

Gray, W. M., 1968: Global view of the origin of tropical disturbances and storms. *Mon. Wea. Rev.*, **96**, 669–700.

Gray, W. M., 1979: Hurricanes: Their formation, structure, and likely role in the tropical circulation. *Meteorology Over the Tropical Oceans*, D. B. Shaw, Ed., Roy. Meteor. Soc., 155–218.

Gray, W. M., 1998: The formation of tropical cyclones. *Meteorol. Atmos. Phys.*, **67**, 37–69.

Guinn, T. A., and W. H. Schubert, 1993: Hurricane spiral bands. *J. Atmos. Sci.*, **50**, 3380–3403.

Guoxiong, W., C. Yaping, and T. Xiaojing, 1996: Conservation of moist potential vorticity and down-sliding slantwise vorticity development. *Acta Meteorologica Sinica*, **10**, 399–418.

Haltiner, G. J., and R. T. Williams, 1980: *Numerical Prediction and Dynamic Meteorology*. 2nd edition. John Wiley & Sons, 477 pp.

Hauf, T., and H. Höller, 1987: Entropy and potential temperature. *J. Atmos. Sci.*, **44**, 2887–2001.

Hawkins, H. F., and S. M. Imbembo, 1976: The structure of a small, intense hurricane – Inez 1966. *Mon. Wea. Rev.*, **104**, 418–442.

Hawkins, H. F., and D. T. Rubsam, 1968: Hurricane Hilda, 1964 II. Structure and budgets of the hurricane on October 1, 1964. *Mon. Wea. Rev.*, **96**, 617–636.

Haynes, P. H., and M. E. McIntyre, 1987: On the evolution of vorticity and potential vorticity in the presence of diabatic heating and frictional or other forces. *J. Atmos. Sci.*, **44**, 828–841.

Haynes, P. H., and M. E. McIntyre, 1990: On the conservation and impermeability theorems for potential vorticity. *J. Atmos. Sci.*, **47**, 2021–2031.

Hebert, P. J., and B. R. Jarvinen, 1977: National Hurricane Center (NHC) diagnostic calculations on tropical cyclones. *Proc. 11th Tech. Conf. on Hur. and Trop. Meteor.*, Miami Beach, FL, Amer. Meteor. Soc., 247–252.

Holland, G. J., 1997: The maximum potential intensity of tropical cyclones. *J. Atmos. Sci.*, **54**, 2519–2541.

Holliday, C. R., 1974: Double intensification of Typhoon Gloria. *Mon. Wea. Rev.*, **105**, 523–528.

Hoskins, B. J., M. E. McIntyre, and A. W. Robertson, 1985: On the use and significance of isentropic potential-vorticity maps. *Quart. J. Roy. Meteor. Soc.*, **111**, 877–946.

Houze, Jr., R. A., 1977: Structure and dynamics of a tropical squall-line system. *Mon. Wea. Rev.*, **105**, 1540–1567.

Houze, Jr., R. A., 1993: *Cloud Dynamics*. Academic Press, 573 pp.

Houze, Jr., R. A., F. D. Marks, Jr., and R. A. Black, 1992: Dual-aircraft investigation of the inner core of Hurricane Norbert. Part II: Mesoscale distribution of ice particles. *J. Atmos. Sci.*, **49**, 943–962.

Jarvinen, B. R., and C. J. Neumann, 1979: Statistical forecasts of tropical cyclone intensity for the North Atlantic Basin. NOAA Tech. Memo., NWS NHC 10, 22 pp.

Johnson, R. H., T. M. Rickenback, S. A. Rutledge, P. E. Ciesielski, and W. H. Schubert, 1999: Trimodal characteristics of tropical convection. *J. Climate*, **12**, 2397–2418.

Jones, R. W., 1977: A nested grid for a three-dimensional model of a tropical cyclone. *J. Atmos. Sci.*, **34**, 1528–1553.

Jordan, C. L., 1958: Mean soundings for the west indies area. *J. Meteor.*, **15**, 91–97.

Jordan, C. L., and F. J. Schatzle, 1961: The 'double eye' of Hurricane Donna. *Mon. Wea. Rev.*, **89**, 354–356.

Jorgensen, D. P., E. J. Zipser, and M. A. LeMone, 1983: Vertical motions in intense hurricanes. *J. Atmos. Sci.*, **42**, 839–856.

Kasahara, A., 1961: A numerical experiment on the development of a tropical cyclone. *J. Meteor.*, **18**, 259–282.

Keenan, T. D., 1982: Diagnostic study of tropical cyclone forecasting in Australia. *Austral. Meteor. Mag.*, **30**, 69–80.

Kessler, E., 1969: On the distribution and continuity of water substance in atmospheric circulation. Meteor. Monogr. No. 32, 84 pp.

Khain, A. P., 1984: Modeling tropical cyclone development at different latitudes. *Soviet Meteorology and Hydrology*, **3**, 29–32.

Kinzer, G. D., and R. Gunn, 1951: The evaporation, temperature and thermal relaxation-time of freely falling waterdrops. *J. Meteor.*, **8**, 71–83.

Kleinschmidt, E., 1951: Grundlagen einer theorie der tropischen zyklonen. *Arch. Meteorol. Geophys. Bioklimatol.*, **A4**, 53–72.

Klemp, J. B., and R. B. Wilhelmson, 1978: The simulation of three-dimensional convective storm dynamics. *J. Atmos. Sci.*, **35**, 1070–1096.

Kossin, J. P., 2000a: Barotropic instability and asymmetric mixing in hurricanes with primary and secondary eyewalls. Ph.D. dissertation, Colorado State University, 174 pp.

Kossin, J. P., 2000b: Unstable interactions between a hurricane's primary eyewall and a secondary ring of enhanced vorticity. *J. Atmos. Sci.*, 3893–3917, 57.

Kossin, J. P., and M. D. Eastin, 2000: Two distinct regimes in the kinematic and thermodynamic structure of the hurricane eye and eyewall. *J. Atmos. Sci.*, in press.

Kossin, J. P., and W. H. Schubert, 2000: Mesovortices, polygonal flow patterns, and rapid pressure falls in hurricane-like vortices. *J. Atmos. Sci.*, submitted.

Kuo, H. L., 1958: Dynamics of convective vortices and eye formation. *The Atmosphere and the Sea in Motion*, B. Bolin, Ed., Rockefeller Institute Press, 413–424.

Kuo, H. L., 1965: On formation and intensification of tropical cyclones through latent heat release by cumulus convection. *J. Atmos. Sci.*, **22**, 40–63.

Kurihara, Y., 1975: Budget analysis of a tropical cyclone model simulated in an axisymmetric numerical model. *J. Atmos. Sci.*, **32**, 25–59.

Leary, C. A., and R. A. Houze, Jr., 1979: The structure and evolution of convection in a tropical cloud cluster. *J. Atmos. Sci.*, **36**, 437–457.

Leary, C. A., and E. N. Rappaport, 1987: The life cycle and internal structure of a mesoscale convective complex. *J. Atmos. Sci.*, **115**, 1503–1527.

Lin, Y.-L., R. D. Farley, and H. D. Orville, 1983: Bulk parameterization of the snow field in a cloud model. *J. Climate Appl. Meteor.*, **22**, 1065–1092.

List, R. J., 1949: *Smithsonian Meteorological Tables*. Smithsonian Institution Press, 527 pp.

Liu, Y., D.-L. Zhang, and M. K. Yau, 1997: A multiscale numerical study of Hurricane Andrew (1992). Part I: Explicit simulation and verification. *Mon. Wea. Rev.*, **125**, 3073–3093.

Lord, S. J., and J. M. Lord, 1988: Vertical velocity in an axisymmetric, nonhydrostatic tropical cyclone model. *J. Atmos. Sci.*, **45**, 1453–1461.

Lord, S. J., H. E. Willoughby, and J. M. Piotrowicz, 1984: Role of a parameterized ice phase microphysics in an axisymmetric, nonhydrostatic tropical cyclone model. *J. Atmos. Sci.*, **41**, 2836–2848.

Lyche, T., and L. L. Schumaker, 1973: Computation of smoothing and interpolating natural splines via local bases. *SIAM J. Numer. Anal.*, **10**, 1027–1038.

Malkus, J. S., and H. Riehl, 1960: On the dynamics and energy transformations in steady-state hurricanes. *Tellus*, **12**, 1–20.

Mapes, B. E., 1993: Gregarious tropical convection. *J. Atmos. Sci.*, **50**, 2026–2037.

Marks, Jr., F. D., and R. A. Houze, Jr., 1987: Inner core structure of Hurricane Alicia from airborne doppler radar observations. *J. Atmos. Sci.*, **44**, 1296–1317.

Merrill, R. T., 1988: Environmental influences on hurricane intensification. *J. Atmos. Sci.*, **45**, 1665–1677.

Miller, B. I., 1958: On the maximum intensity of hurricanes. *J. Meteor.*, **15**, 184–195.

Molinari, J., S. Skubis, and D. Vollaro, 1995: External influences on hurricane intensity: Part III: Potential vorticity structure. *J. Atmos. Sci.*, **52**, 3593–3606.

Molinari, J., S. Skubis, D. Vollaro, F. Alsheimer, and H. E. Willoughby, 1998: Potential vorticity analysis of tropical cyclone intensification. *J. Atmos. Sci.*, **55**, 2632–2644.

Möller, J. D., and M. T. Montgomery, 1999: Tropical cyclone evolution via potential vorticity anomalies in a three-dimensional balance model. *J. Atmos. Sci.*, submitted.

Möller, J. D., and R. K. Smith, 1994: The development of potential vorticity in a hurricane-like vortex. *Quart. J. Roy. Meteor. Soc.*, **120**, 1255–1265.

Montgomery, M. T., and J. Enagonio, 1998: Tropical cyclogenesis via convectively forced vortex rossby waves in a three-dimensional quasigeostrophic model. *J. Atmos. Sci.*, 3176–3207, 55.

Montgomery, M. T., J. M. Hidalgo, and P. D. Reasor, 2000: A semi-spectral numerical method for modeling the vorticity dynamics of the near-core of hurricane-like vortices. Atmospheric Science Paper, Dept. of Atmospheric Science, Colorado State University, 115 pp., [In preparation for availability from Dept. of Atmospheric Science, Colorado State University, Fort Collins, CO 80523].

Moss, M. S., and S. L. Rosenthal, 1975: On the estimation of planetary boundary layer variables in mature hurricanes. *Mon. Wea. Rev.*, 980–988, 103.

Murray, F. W., 1970: Numerical models of a tropical cumulus cloud with bilateral and axial symmetry. *Mon. Wea. Rev.*, **98**, 14–28.

Nguyen, C. M., H. Zhu, R. Smith, and M. J. Reeder, 2000: A minimal axisymmetric tropical cyclone model. Preprints, *24th Conf. on Hur. and Trop. Meteor.*, Fort Lauderdale, FL, Amer. Meteor. Soc., 39–40.

Nitta, T., and S. Esbensen, 1974: Heat and moisture budget analysis using BOMEX data. *Mon. Wea. Rev.*, **102**, 17–28.

Nolan, D. S., and M. T. Montgomery, 2000a: The algebraic growth of wavenumber one disturbances in hurricane-like vortices. *J. Atmos. Sci.*, **57**, 3514–3538.

Nolan, D. S., and M. T. Montgomery, 2000b: Three-dimensional, asymmetric, nonhydrostatic, unstable eigenmodes in initially balanced, hurricane-like vortices. Preprints, *24th Conf. on Hur. and Trop. Meteor.*, Fort Lauderdale, FL, 163–164.

Ooyama, K. V., 1966: On the stability of the baroclinic circular vortex: A sufficient criterion for instability. *J. Atmos. Sci.*, **23**, 43–53.

Ooyama, K. V., 1968: Numerical simulation of tropical cyclones with an axi-symmetric model. *Proc. WMO/IUGG Sympos. Numer. Wea. Pred.*, Tokyo, Japan, Japan Meteor. Agency, 81–88.

Ooyama, K. V., 1969: Numerical simulation of the life cycle of tropical cyclones. *J. Atmos. Sci.*, **26**, 3–40.

Ooyama, K. V., 1984: A model for hurricane prediction. Postprints, *15th Conf. on Hur. and Trop. Meteor*, Miami, FL, Amer. Meteor. Soc., 344–349.

Ooyama, K. V., 1987: Scale-controlled objective analysis. *Mon. Wea. Rev.*, **115**, 2479–2506.

Ooyama, K. V., 1990: A thermodynamic foundation for modeling the moist atmosphere. *J. Atmos. Sci.*, **47**, 2580–2593.

Ooyama, K. V., 1995: A thermodynamic foundation for modeling the moist atmosphere. Part II: Test of microphysics in the formation of squall lines. Preprints, *21st Conf. on Hur. and Trop. Meteor.*, Miami, FL, Amer. Meteor. Soc., 219–221.

Ooyama, K. V., 1997: The semi-implicit integration of a nested spectral model and the result of tests in squall-line simulation. Preprints, *22nd Conf. on Hur. and Trop. Meteor.*, Fort Collins, CO, Amer. Meteor. Soc., 531–532.

Ooyama, K. V., 1999: Boundary-layer parameterization in a cloud-resolving model using the radical thermodynamic formulation. Preprints, *23rd Conf. on Hur. and Trop. Meteor.*, Dallas, TX, Amer. Meteor. Soc., 150–152.

Ooyama, K. V., 2001: A dynamic and thermodynamic foundation for modeling the moist atmosphere with parameterized microphysics. *J. Atmos. Sci.*, accepted.

Orville, H. D., and F. J. Kopp, 1977: Numerical simulation of the history of a hailstorm. *J. Atmos. Sci.*, **34**, 1596–1618.

Palmén, E., 1948: On the formation and structure of tropical hurricane. *Geophysica*, **3**, 26–38.

Persson, O., 1995: Simulations of the potential vorticity structure and budget of FRONTS 87 IOP8. *Quart. J. Roy. Meteor. Soc.*, **121**, 1041–1081.

Pike, A. C., 1985: Geopotential heights and thicknesses as predictors of Atlantic tropical cyclone motion and intensity. *Mon. Wea. Rev.*, **113**, 931–939.

Pruppacher, H. R., and J. D. Klett, 1996: *Microphysics of Clouds and Precipitation.* Kluwer Acad. Publ., 954 pp.

Pueschel, R. F., D. A. Allen, C. Black, S. Faisan, G. V. Ferry, S. D. Howard, J. Livingstone, J. Redemann, C. E. Sorenson, and S. Verma, 1995: Condensed water in tropical cyclone oliver, 8 February 1993. *Atmos. Res.*, **38**, 297–313.

Raymond, D. J., and H. Jiang, 1990: A theory for long-lived mesoscale convective systems. *J. Atmos. Sci.*, **47**, 3067–3077.

Riehl, H., and J. S. Malkus, 1961: Some aspects of Hurricane Daisy, 1958. *Tellus*, **13**, 181–213.

Robert, A. J., 1969: The integration of a spectral model of the atmosphere by the implicit method. *Proc. WMO/IUGG Sympos. Numer. Wea. Pred.*, Tokyo, Japan, Japan Meteor. Agency, VII 19–24.

Rosenthal, S. L., 1964: Some attempts to simulate the development of tropical cyclones by numerical methods. *Mon. Wea. Rev.*, **92**, 1–21.

Rosenthal, S. L., 1969: Numerical experiments with a multilevel primitive model designed to simulate the development of tropical cyclone: Experiment I. ESSA Tech. Memo., ERLTM–NHRL 82, 36 pp.

Rosenthal, S. L., 1970a: A circularly symmetric primitive equation model of tropical cyclone development containing and explicit water vapor cycle. *Mon. Wea. Rev.*, **98**, 643–663.

Rosenthal, S. L., 1970b: A survey of experimental results obtained from a numerical model designed to simulate tropical cyclone development. ESSA Tech. Memo., ERLTM–NHRL 88, 78 pp.

Rosenthal, S. L., 1971: The response of a tropical cyclone model to variations in boundary layer parameters, initial conditions, lateral boundary conditions, and domain size. *Mon. Wea. Rev.*, **99**, 767–777.

Rosenthal, S. L., 1978: Numerical simulation of tropical cyclone development with latent heat release by resolvable scales. I: Model description and preliminary results. *J. Atmos. Sci.*, **35**, 258–271.

Rosenthal, S. L., 1979: The sensitivity of simulated hurricane development to cumulus parameterization details. *Mon. Wea. Rev.*, **107**, 193–197.

Rotunno, R., and K. A. Emanuel, 1987: An air-sea interaction theory for tropical cyclones. Part II: Evolutionary study using a nonhydrostatic axisymmetric numerical model. *J. Atmos. Sci.*, **44**, 542–561.

Rotunno, R., and J. Klemp, 1985: On the rotation and propagation of simulated supercell thunderstorms. *J. Atmos. Sci.*, **42**, 271–292.

Salmon, R., 1992: What is potential vorticity? *Dynamics of the Outer Planets: 1992 Summer Study Program in Geophysical Fluid Dynamics*, G. Flierl, A. Ingersoll, J.-I. Yano and B. Ewing-DeRemer, Eds., Woods Hole Oceanog. Inst. Tech. Rept., WHOI–93–24, 181–189.

Samsury, C. E., and E. J. Zipser, 1995: Secondary wind maxima in hurricanes: Airflow and relationship to rainbands. *Mon. Wea. Rev.*, **123**, 3502–3517.

Sasamori, T., 1968: The radiative cooling calculation for application to general circulation experiments. *J. Appl. Meteor.*, **7**, 721–729.

Schade, L. R., and K. A. Emanuel, 1999: The ocean's effect on the intensity of tropical cyclones: Results from a simple coupled atmosphere-ocean model. *J. Atmos. Sci.*, **56**, 642–651.

Schoenberg Ferrier, B., W.-K. Tao, and J. Simpson, 1995: A double-moment multiple-phase four-class bulk ice scheme. Part II: Simulation of convective storms in different large-scale environments and comparisons with other bulk parameterizations. *J. Atmos. Sci.*, **52**, 1001–1033.

Schubert, W. H., and B. T. Alworth, 1987: Evolution of potential vorticity in tropical cyclones. *Quart. J. Roy. Meteor. Soc.*, **113**, 147–162.

Schubert, W. H., and J. J. Hack, 1982: Inertial stability and tropical cyclone development. *J. Atmos. Sci.*, **39**, 1687–1697.

Schubert, W. H., M. T. Montgomery, R. K. Taft, T. A. Guinn, S. R. Fulton, J. P. Kossin, and J. P. Edwards, 1999: Polygonal eyewalls, asymmetric eye contraction, and potential vorticity mixing in hurricanes. *J. Atmos. Sci.*, **56**, 1197–1223.

Shapiro, L. J., 1983: The asymmetric boundary layer flow under a translating hurricane. *J. Atmos. Sci.*, **40**, 1984–1998.

Shapiro, L. J., 1996: The motion of Hurricane Gloria: A potential vorticity diagnosis. *Mon. Wea. Rev.*, **124**, 2497–2508.

Shapiro, L. J., and J. L. Franklin, 1995: Potential vorticity in Hurricane Gloria. *Mon. Wea. Rev.*, **123**, 1465–1475.

Shapiro, L. J., and H. E. Willoughby, 1982: The response of balanced hurricanes to local sources of heat and momentum. *J. Atmos. Sci.*, **39**, 378–394.

Shay, L. K., R. L. Elsberry, and P. G. Black, 1989: Vertical structure of the ocean current response to a hurricane. *J. Phys. Oceanogr.*, **19**, 649–669.

Skamarock, W. C., and J. B. Klemp, 1992: The stability of time-split numerical methods for the hydrostatic and the nonhydrostatic elastic equations. *Mon. Wea. Rev.*, **120**, 2109–2127.

Smagorinsky, J., 1963: General circulation experiments with the primitive equations: I. The basic experiment. *Mon. Wea. Rev.*, **91**, 99–164.

Smolarkiewicz, P. K., 1991: Nonoscillatory advection scheme. *Proc. Proc. of the Seminar on Numerical Methods in Atmos. Models*, ECMWF, November 1991.

Sundqvist, H., 1970a: Numerical simulation of the development of tropical cyclones with a ten-level model: Part I. *Tellus*, **22**, 359–390.

Sundqvist, H., 1970b: Numerical simulation of the development of tropical cyclones with a ten-level model: Part II. *Tellus*, **22**, 504–510.

Syono, S., 1962: A numerical experiment of the formation of tropical cyclones. *Proc. Int. Symp. Numer. Wea. Pred.*, Tokyo, Japan, Meteor. Soc. Japan, 405–418.

Viltard, N., and F. Roux, 1998: Structure and evolution of Hurricane Claudette on 7 September 1991 from airborne Doppler radar observations. Part II: Thermodynamics. *Mon. Wea. Rev.*, **126**, 281–302.

Walko, R. L., W. R. Cotton, M. P. Meyers, and J. Y. Harrington, 1995: New rams cloud microphysics parameterization, Part I: The single-moment scheme. *Atmos. Res.*, **38**, 29–62.

Wilhelmson, R. B., 1977: On the thermodynamic equation for deep convection. *Mon. Wea. Rev.*, **105**, 545–549.

Willoughby, H. E., 1979: Forced secondary circulations in hurricanes. *J. Geophys. Res.*, **84**, 3173–3183.

Willoughby, H. E., 1990: Temporal changes of the primary circulation in tropical cyclones. *J. Atmos. Sci.*, **47**, 242–264.

Willoughby, H. E., 1998: Tropical cyclone eye thermodynamics. *Mon. Wea. Rev.*, **126**, 3053–3067.

Willoughby, H. E., J. A. Clos, and M. G. Shoreibah, 1982: Concentric eye walls, secondary wind maxima and the evolution of the hurricane vortex. *J. Atmos. Sci.*, **39**, 395–411.

Willoughby, H. E., H.-L. Jin, S. J. Lord, and J. M. Piotrowicz, 1984: Hurricane structure and evolution as simulated by an axisymmetric nonhydrostatic numerical model. *J. Atmos. Sci.*, **41**, 1169–1186.

Wu, C.-C., and K. A. Emanuel, 1995a: Potential vorticity diagnostics of hurricane movement. Part I: A case study of Hurricane Bob (1991). *Mon. Wea. Rev.*, **123**, 69–92.

Wu, C.-C., and K. A. Emanuel, 1995b: Potential vorticity diagnostics of hurricane movement. Part II: Tropical Storm Ana (1991) and Hurricane Andrew (1992). *Mon. Wea. Rev.*, **123**, 93–109.

Yamasaki, M., 1968a: Numerical simulation of tropical cyclone development with the use of primitive equations. *J. Meteor. Soc. Japan*, **46**, 178–201.

Yamasaki, M., 1968b: A tropical cyclone model with parameterized vertical partition of released latent heat. *J. Meteor. Soc. Japan*, **46**, 202–214.

Yamasaki, M., 1977a: A preliminary experiment of the tropical cyclone without parameterizing the effects of cumulus convection. *J. Meteor. Soc. Japan*, **55**, 11–30.

Yamasaki, M., 1977b: The role of surface friction in tropical cyclones. *J. Meteor. Soc. Japan*, **55**, 559–572.

Yamasaki, M., 1983: A further study of the tropical cyclone without parameterizing the effects of cumulus convection. *Papers Meteor. Geophys.*, **34**, 221–260.

Zeng, X., 1996: Numerical simulation of tropical cyclones by an axisymmetric nonhydrostatic model. *Meteorol. Atmos. Phys.*, **60**, 207–224.

Appendix A

SUMMARY OF PAST AXISYMMETRIC TROPICAL CYCLONE MODELS

This appendix contains a tabular summary of past axisymmetric models developed by the following authors:

1. Kasahara (1961)
2. Syono (1962)
3. Rosenthal (1964)
4. Kuo (1965)
5. Estoque and Fernandez-Partagas (1968)
6. Yamasaki (1968a,b)
7. Ooyama (1968, 1969)
8. Rosenthal (1970a,b)
9. Sundqvist (1970a,b)
10. Anthes et al. (1971a,b)
11. Kurihara (1975)
12. Rosenthal (1978)
13. Yamasaki (1977a,b)
14. Yamasaki (1983)
15. Willoughby et al. (1984)
16. Rotunno and Emanuel (1987)
17. Zeng (1996)

In the tables that follow, a dash indicates that the information was not included in the paper.

Table A.1: Model physics. In reference to the precipitation microphysics, warm and cold denote with or without ice microphysics, respectively.

Model	Balanced	Convection	Precipitation	Radiation	Remarks
1	Hydr.	warming $\propto w$	Cold	No	no surf. sens. energy flux
2	Hydr.	warming $\propto w$	Warm	No	
3	Hydr.	warming $\propto w$	Warm	No	
4	Hydr./Grad.	Kuo (1965) param.	Warm	No	
5	Hydr.	Estoque (1966)	Warm	No	
6	Hydr.	warming $\propto w$	Warm	No	no surf. sens. energy flux
7	Hydr./Grad.	warming $\propto w$	Warm	No	
8	Hydr.	Kuo (1965) type param.	Warm	No	simple surf. energy flux
9	Hydr./Grad.	Kuo (1965) type param.	Warm	Yes	no conv. trans.
10	Hydr.	prescribed	Dry	Yes	
11	Hydr.	moist conv. adj.	Warm	No	no conv. trans.
12	Hydr.	implicit	Warm	No	dry conv. adj.
13	Nonhydr.	explicit	Warm	No	no surf. energy flux
14	Nonhydr.	explicit	Warm	No	
15	Nonhydr.	explicit	Cold	No	
16	Nonhydr.	explicit	Warm	Relaxation	
17	Nonhydr.	implicit	Warm	Relaxation	anelastic

Table A.2: Model diffusion, wherein K_V and K_H are the vertical and horizontal diffusion coefficients, respectively; l is the scale length of the horizontal diffusion; and C_D is the surface drag coefficient.

Model	$K_V\,(\mathrm{m^2 s^{-1}})$	$K_H\,(\mathrm{m^2 s^{-1}})$	l	C_D	Remarks
1	-	1.6×10^4	50 km	3×10^{-3}	
2	-	-	-	-	
3	10	$5 \times 10^{4-5}$	-	2.5×10^{-1}	hor. diff. decreases cloud-scale growth rate, slows the secondary circulations
4	10^{1-2}	10^4	33 km	2.5×10^{-3}	
5	var.	10^{0-4}	var.	-	similarity theory used in ABL
6	10	10^3	-	2.5×10^{-3}	
7	5×10^{-4}	10^3	6 km	$\left[0.5 + 0.06\left(u^2+v^2\right)^{1/2}\right] \times 10^{-3}$	
8	10	10^4	-	3×10^{-3}	
9	10	5×10^3	-	1.5×10^{-3}	
10	5×10^2	5×10^4	-	3×10^{-3}	
11	≤ 10	var. ~ 5×10^3	-	Monin-Obukhov	
12	var.	5×10^3–2.5×10^4	var.	5×10^{-3}	shear/stability dependent K_v Smagorinsky type K_H
13	10	3×10^2	-	2.5×10^{-3}	
14	10	10^2	-	1.5×10^{-3}	
15	$K_{V_{min}} \approx 5$	var.	-	3×10^{-3}	K_H is a prognostic variable
16	var.	$\sim 10^4$	3 km	$1.1 \times 10^{-3} + 4 \times 10^{-5}\left(u^2+v^2\right)^{1/2}$	
17	$K_{V_{min}} \approx 5$	$K_{H_{min}} \approx 50$	-	$\alpha + \beta\left(u^2+v^2\right)^{\gamma/2}$	α, β, γ are functions of the surface wind

Table A.3: Model numerics, wherein Δr is the radial grid interval; Δz or Δp is the vertical grid interval in height or pressure coordinates, respectively; and Δt is the time step.

Model	Hor. Dom.	Vert. Dom.	Grid (vert. × hor.)	Δr	Δz or Δp	Duration	Δt	Remarks
1	810 nm	1000-100 mb	19 × 81	10 nm	50 mb	176 min	1 min	
2	1593 km	1000-100 mb	10 × 24	$6 + 3(i-1)^2$ km, $1 < i \leq 24$ 0, $i = 1$	100 mb	60 min	4.5-9 min	
3	1000 km	1000-100 mb	31 × 26	40 km	550 m	9 hrs	2 min	
4	1170 km	1000-100 mb	3 × 45	$i(0.5i + 3.5)$ km, $i = 0, 1, 2, \ldots, 44$	-	36 hrs	-	
5	500 km	0-20 km	11 × 20	var.	var.	3.5	-	
6	2410 km	1000-0 mb	4 × 22	20-364 km	300 mb	10 days	2-4 min	
7	1000 km	3 layer	4 × 200	5 km	5 km	10 days	0.12-1 hrs	$\Delta z = h$
8	440 km	1015-100 mb	7 × 22	20	100-200 mb		120 sec	
9	600 km	1000-100 mb	10 × 24	25 km	10 mb	210 hrs	229-413 sec	
10	1000 km	310-370 K	6 × 51	20 km	10 K	-	-	isentropic coordinate
11	2000 km	1000-30 mb	12 × (10c + 15v + 10c)	20-100 km	var.	10 days	45 sec	
12	3400 km	1000-100 mb	12 × (20c + 18v)	$\geq$ 20 km	35-100 mb	120 hrs	30 sec	
13	1350	0-20 km	25 × (150c + 47v + 22c)	0.4 km, $r \leq 60$ km 0.4 – 40 km, 60 km $\leq r \leq$ 470 km 40 km, 470 km $\leq r \leq$ 1350 km	600 m, $z \leq 9$ km var., $z > 9$ km	80 hrs	20 sec, $t \leq 30$ hrs 10 sec, $t > 30$ hrs	
14	2500	0-22.6 km	30 × (600c + 120v)	0.5 km, $r \leq 300$ km	600 m, $z \leq 12$ km var., $z > 12$ km	160 hrs	var.	
15	1500 km	20 km	20 × (50c + n × v)	20 (out to 100 km)-55 km	1 km	110 hrs	2,20 sec	time-splitting
16	1500 km	25 km	20 × 100	15 km	1.25 km	180 hrs	20 sec	
17	1002 km	19.2 km	32 × 60	15 km × $\ln\left(\frac{r+20\text{ km}}{20\text{ km}}\right)$ +1 km 1.3 - 65.9 km	0.6 km	10 days	30 sec	

Table A.4: Model initial conditions, wherein v_{max} is the maximum tangential wind speed, r_{max} is the radius of v_{max}, f is the Coriolis parameter, T_s is the sea surface temperature, and p_s is the surface pressure of the surrounding background environment.

Model	v_{max} (ms^{-1})	r_{max} (km)	f (s^{-1})	T_s (deg C)	p_s (r_b) (mb)	Remarks
1	0	0	-	-	1000	Jordan (1958) sounding, 99% RH, secondary circulation
2	0	0	3.775×10^{-5}	27.0	1013.25	conditionally unstable to 200 mb, secondary circulation
3	≈ 16.0	≈ 225.0	5×10^{-5}	26.3	1010	exp. VII, initial 2.4 K warm temp. anomaly at 11 km
4	10.0	141.42	-	28.0	-	exp. IIa
5	≈ 37.0	≈ 50.0	-	-	-	exp. 1E, initial 14 K pot. temp. pert. of mean hur.
6	4.7	100.0	5×10^{-5}	27.0	1000	exp. IIa
7	10.0	50.0	5×10^{-5}	27.5	1015	case A
8	7.0	250.0	5×10^{-5}	28.2	1015	Exp I, initial 0.16 K temp anomaly
9	15.0	200.0	5×10^{-5}	27.5	1010	Jordan (1958) sounding, uniform RH, balanced vortex
10	37.0	80.0	5×10^{-5}	-	1011	
11	8.6	190.0	5×10^{-5}	29.0	1010	conditionally unstable basic state
12	7.2	220.0	5×10^{-5}	-	1015	Jordan (1958) sounding, balanced vortex
13	-	-	5×10^{-5}	-	1010	warm bubbles
14	-	-	5×10^{-5}	29.0	1010	9, 1K warm bubbles at intervals of 10 km
15	8.0	75.0	-	28.0	-	Exp I7A,Jordan (1958) sounding, balanced vortex
16	12.0	82.5	5×10^{-5}	26.3	-	Exp A,Jordan (1958) sounding
17	10.0	80.0	5×10^{-5}	29.0	≈ 1015	Jordan (1958) sounding, humidity profile of, 4 K warm bubble

Table A.5: Model results, wherein, v_{max} is the maximum tangential wind speed, r_{max} is the radius of v_{max}, t_{max} is the time at which v_{max} is attained, p_{min} is the minimum surface pressure, and t_{min} is the time at which p_{min} is attained.

Model	v_{max} (ms^{-1})	r_{max} (km)	t_{max} (hrs)	p_{min} (hPa)	t_{min} (hrs)	Remarks
1	1	130 nm	128 min	-	-	most unstable at cumulus scale; exp. growth
2	0.4	5	1	980	1	most unstable at cumulus scale
3	≈ 42	≈ 180	9	≈ 976	9	exp. VII
4	36.7	≈ 40	10	-	-	exp. IIa
5	≈ 42	≈ 50	3.5	-	-	exp 1E, no eye circ.
6	40	20	192	≈ 970	210	exp. IIa, no eye
7	≈ 61	≈ 10	≈ 120	≈ 945	≈ 146	case A
8	46	≈ 50	192	974	195	Exp 1
9	51	50	84	951	92	
10	34	60	-	-	-	exp. 6
11	64	45	90	931	115	extensive budget analysis
12	70	38	120	890	120	hor. diff. unimportant
13	85	3.2	58–80 hr avg	925	≈ 70	very small eye
14	≈ 120	≈ 10 km	160	900	153	
15	50	20	60	950	100	Exp I7A, pressure continues to fall
16	46	38	≈ 120	973	-	Exp A
17	80	≈ 11	120	≈ 950	240	ME01, pressure continues to fall

Appendix B

DERIVATION OF THE MOMENTUM EQUATION

In Chapter 2, section 2.1.2 we use a single equation (2.5) to represent the total momentum of a parcel. Although separate momentum conservation equations could represent the momentum of each constituent and phase of matter within a parcel of moist air, a single equation for the total mass is more mathematically convenient and computationally efficient. This appendix provides a detailed derivation of equation (2.5).

Let us begin our derivation with the momentum conservation equations for the dry air, water vapor, cloud, and precipitation mass, separately

$$\rho_a \frac{D_a \mathbf{u}_a}{Dt} + 2\boldsymbol{\Omega} \times (\rho_a \mathbf{u}_a) + \rho_a \nabla \Phi + \nabla p_a = \mathbf{I}_a^j + \rho_a \mathbf{D}_{\mathbf{u}_a}, \tag{B.1}$$

$$\rho_v \frac{D_v \mathbf{u}_v}{Dt} + 2\boldsymbol{\Omega} \times (\rho_v \mathbf{u}_v) + \rho_v \nabla \Phi + \nabla p_v = \mathbf{I}_v^j + \rho_v \mathbf{D}_{\mathbf{u}_v}, \tag{B.2}$$

$$\rho_c \frac{D_c \mathbf{u}_c}{Dt} + 2\boldsymbol{\Omega} \times (\rho_c \mathbf{u}_c) + \rho_c \nabla \Phi = \mathbf{I}_c^j + \rho_c \mathbf{D}_{\mathbf{u}_c}, \tag{B.3}$$

$$\rho_r \frac{D_r \mathbf{u}_r}{Dt} + 2\boldsymbol{\Omega} \times (\rho_r \mathbf{u}_r) + \rho_r \nabla \Phi = \mathbf{I}_r^j + \rho_r \mathbf{D}_{\mathbf{u}_r}, \tag{B.4}$$

where for $i = a, v, c, r$; $\mathbf{u}_i$ is the velocity; ρ_i is the density; p_a and p_v are the partial pressures of dry air and water vapor, respectively; $\mathbf{I}_i^j$ is the internal frictional force between different

forms of matter with $j = a, v, c, r$ for $j \neq i$; $\mathbf{D}_{\mathbf{u}_i}$ is the external frictional force per unit mass; $\mathbf{\Omega}$ is the Earth's angular velocity; $\Phi \equiv \phi - \frac{1}{2}|\mathbf{\Omega} \times \mathbf{r}|^2$ is the potential of the Earth's gravitational and centrifugal forces; and $D_i/Dt = \partial/\partial t + \mathbf{u}_i \cdot \nabla$ is the material derivative. By making several simplifying assumptions, we will combine equations (B.1)–(B.4) into a single expression.

First, we combine equations (B.1)–(B.3). Letting the dry air and water vapor represent a mixture of ideal gases, the total pressure, according to Dalton's law, is given by $p = p_a + p_v$. In addition, we assume that the dry air and water vapor constitute moist air and move together with the same velocity (i.e., $\mathbf{u}_a = \mathbf{u}_v = \mathbf{u}$). We further assume that the cloud has zero inertia and negligible settling velocity such that it also moves with the moist air (i.e., $\mathbf{u}_c = \mathbf{u}_a = \mathbf{u}$). These assumptions allow us to combine (B.1)–(B.3), leaving

$$\rho_{am}\frac{D\mathbf{u}}{Dt} + 2\mathbf{\Omega} \times (\rho_{am}\mathbf{u}) + \rho_{am}\nabla\Phi + \nabla p = \mathbf{I}^r_{am} + \rho_{am}\mathbf{D}_\mathbf{u}, \tag{B.5}$$

where $\rho_m = \rho_v + \rho_c$ is the mass density of airborne water; $\rho_{am} = \rho_a + \rho_m$ is the mass density of the dry air and airborne water; $\mathbf{I}^j_i = -\mathbf{I}^i_j$ with $i, j = a, v, c$ for $i \neq j$; $\mathbf{I}^r_{am} \equiv \mathbf{I}^r_a + \mathbf{I}^r_v + \mathbf{I}^r_c$; and $\rho_{am}\mathbf{D}_\mathbf{u} \equiv \rho_a\mathbf{D}_{\mathbf{u}_a} + \rho_v\mathbf{D}_{\mathbf{u}_v} + \rho_c\mathbf{D}_{\mathbf{u}_c}$.

At first glance, it may seem unnatural that the pressure gradient force results in an acceleration of cloud mass. This apparent violation of hydrodynamical principles is eliminated by considering the acceleration as a two–stage process. First, the unbalanced pressure gradient force accelerates the dry air and water vapor, resulting in a velocity difference between the mixture of gases and the cloud. Second, the frictional exchange of momentum rapidly removes the velocity difference, decelerating the mixture of gases and accelerating the cloud. The net effect is that the total mass, including the mixture of gases and cloud, is accelerated by the pressure gradient force.

Finally, we combine (B.4) and (B.5). First, both equations are converted to flux form using the mass continuity equations for ρ_{am} and ρ_r given by

$$\frac{\partial \rho_{am}}{\partial t} + \nabla \cdot (\rho_{am}\mathbf{u}) = -Q_r + D_{\rho_{am}}, \tag{B.6}$$

$$\frac{\partial \rho_r}{\partial t} + \nabla \cdot (\rho_r \mathbf{u}_r) = Q_r + D_{\rho_r}. \tag{B.7}$$

wherein Q_r represents sources/sinks of precipitation, and $D_{\rho_{am}}$ and D_{ρ_r} represent the turbulent diffusion of ρ_{am} and ρ_r. Combining (B.5) with (B.6) and (B.4) with (B.7), we obtain

$$\frac{\partial}{\partial t}(\rho_{am}\mathbf{u}) + \nabla \cdot (\rho_{am}\mathbf{u}\mathbf{u}) + 2\boldsymbol{\Omega} \times (\rho_{am}\mathbf{u}) + \rho_{am}\nabla\Phi + \nabla p = \mathbf{I}^r_{am} + \mathbf{D}_{\rho_{am}\mathbf{u}} - Q_r\mathbf{u}, \tag{B.8}$$

$$\frac{\partial}{\partial t}(\rho_r \mathbf{u}_r) + \nabla \cdot (\rho_r \mathbf{u}_r \mathbf{u}_r) + 2\boldsymbol{\Omega} \times (\rho_r \mathbf{u}_r) + \rho_r \nabla\Phi = \mathbf{I}^{am}_r + \mathbf{D}_{\rho_r \mathbf{u}_r} + Q_r \mathbf{u}_r. \tag{B.9}$$

wherein $\mathbf{D}_{\rho_{am}\mathbf{u}} = \rho_{am}\mathbf{D}_{\mathbf{u}} + \mathbf{u}D_{\rho_{am}}$ and $\mathbf{D}_{\rho_r \mathbf{u}_r} = \rho_r \mathbf{D}_{\mathbf{u}_r} + \mathbf{u}_r D_{\rho_r}$. Let the precipitation velocity, $\mathbf{u}_r = \mathbf{u} + \mathbf{U}$, be composed of the velocity of the moist, cloudy air, $\mathbf{u}$, and a terminal velocity, $\mathbf{U}$. Substituting this definition into (B.9), with $\mathbf{I}^r_{am} = -\mathbf{I}^{am}_r$, and summing the result with (B.8), we obtain

$$\frac{\partial}{\partial t}(\rho\bar{\mathbf{u}}) + \nabla \cdot (\rho\bar{\mathbf{u}}\mathbf{u} + \rho_r \mathbf{u}_r \mathbf{U}) + 2\boldsymbol{\Omega} \times (\rho\bar{\mathbf{u}}) + \rho\nabla\Phi + \nabla p = \mathbf{D}_{\rho\bar{\mathbf{u}}} + Q_r \mathbf{U}, \tag{B.10}$$

where $\rho = \rho_a + \rho_m + \rho_r$ is the total mass density,

$$\bar{\mathbf{u}} \equiv \frac{\rho_{am}\mathbf{u} + \rho_r \mathbf{u}_r}{\rho} = \mathbf{u} + \frac{\rho_r}{\rho}\mathbf{U} \tag{B.11}$$

is a density-weighted mean velocity or the velocity of the center of mass, and $\mathbf{D}_{\rho\bar{\mathbf{u}}} \equiv \mathbf{D}_{\rho_{am}\mathbf{u}} + \mathbf{D}_{\rho_r \mathbf{u}_r}$.

Equations (B.10) and (B.11) are significantly different from those used to represent momentum conservation in other models (e.g., MM5, RAMS, ARPS) and thus require additional explanation. Notice that the flux has two terms. The first term represents the flux of total momentum along the motion of the parcel, while the second represents the flux of precipitation momentum into or out of the parcel. Also, the final term in (B.10) represents the addition of momentum as cloud mass converts to precipitation mass. Inside real clouds, growing cloud particles slowly become precipitation particles as gravity accelerates them to some appreciable $\mathbf{U}$. Inside model clouds, this acceleration occurs instantaneously as cloud mass with $\mathbf{U} = 0$ becomes precipitation mass with $\mathbf{U} \neq 0$ for $Q_r > 0$.

We next rewrite (B.10) in advective form. Combining (B.6) with (B.7) and using (B.11), we write the mass continuity equation for ρ in terms of $\bar{\mathbf{u}}$, i.e.,

$$\frac{\partial \rho}{\partial t} + \nabla \cdot (\rho \bar{\mathbf{u}}) = D_\rho, \tag{B.12}$$

wherein D_ρ is the turbulent diffusion of ρ. We then use (B.12) to rewrite (B.10) in the advective form

$$\frac{D\bar{\mathbf{u}}}{Dt} + 2\boldsymbol{\Omega} \times \bar{\mathbf{u}} + \nabla\Phi + \frac{1}{\rho}\nabla p = \frac{\bar{\mathbf{u}}}{\rho}\nabla \cdot (\rho_r \mathbf{U}) - \frac{1}{\rho}\nabla \cdot (\rho_r \mathbf{u}_r \mathbf{U}) + \frac{Q_r}{\rho}\mathbf{U} + \mathbf{D}_{\bar{\mathbf{u}}}. \tag{B.13}$$

Note that this expression may also be written in the form

$$\frac{\bar{D}\bar{\mathbf{u}}}{Dt} + 2\boldsymbol{\Omega} \times \bar{\mathbf{u}} + \nabla\Phi + \frac{1}{\rho}\nabla p = -\frac{1}{\rho}\nabla \cdot [\rho_r (\mathbf{u}_r - \bar{\mathbf{u}})\, \mathbf{U}] + \frac{Q_r}{\rho}\mathbf{U} + \mathbf{D}_{\bar{\mathbf{u}}}, \tag{B.14}$$

where $\bar{D}/Dt = \partial/\partial t + \bar{\mathbf{u}} \cdot \nabla$ is the material derivative following a parcel moving with velocity $\bar{\mathbf{u}}$. When deriving the potential vorticity principle in Chapter 3, it will also be useful to know the rotational form of (B.14). Substituting the vector identity $(\bar{\mathbf{u}} \cdot \nabla)\,\bar{\mathbf{u}} = \nabla\left(\frac{1}{2}\bar{\mathbf{u}} \cdot \bar{\mathbf{u}}\right) + (\nabla \times \bar{\mathbf{u}}) \times \bar{\mathbf{u}}$, we rewrite (B.14) as

$$\frac{\partial \bar{\mathbf{u}}}{\partial t} + \bar{\boldsymbol{\zeta}} \times \bar{\mathbf{u}} = -\nabla \left(\frac{1}{2} \bar{\mathbf{u}} \cdot \bar{\mathbf{u}} + \Phi \right) - \frac{1}{\rho} \nabla p + \bar{\mathbf{F}}, \tag{B.15}$$

wherein $\bar{\boldsymbol{\zeta}} = 2\boldsymbol{\Omega} + \nabla \times \bar{\mathbf{u}}$ is the density-weighted absolute vorticity and

$$\bar{\mathbf{F}} \equiv -\frac{1}{\rho} \nabla \cdot \left[\rho_r \left(\mathbf{u}_r - \bar{\mathbf{u}} \right) \mathbf{U} \right] + \frac{Q_r}{\rho} \mathbf{U} + \mathbf{D}_{\bar{\mathbf{u}}}. \tag{B.16}$$

Notice that, in the dry limit (i.e., $\rho_v = \rho_c = \rho_r = 0$, $\rho = \rho_a$, $p = p_a$, $\bar{\mathbf{u}} = \mathbf{u}$), equation (B.15) reduces to

$$\frac{\partial \mathbf{u}}{\partial t} + \boldsymbol{\zeta} \times \mathbf{u} = -\nabla \left(\frac{1}{2} \mathbf{u} \cdot \mathbf{u} + \Phi \right) - \frac{1}{\rho_a} \nabla p_a + \mathbf{F}, \tag{B.17}$$

wherein $\mathbf{F} = \mathbf{D}_{\mathbf{u}}$.

Finally, in Chapter 2, due to a numerical restriction on the lower boundary condition of $\bar{w}$, we approximated the momentum equation by letting $D_r W / Dt = 0$. Applying this approximation to (B.10) and neglecting $2\boldsymbol{\Omega} \times (\rho_r \mathbf{U})$ for consistency, we obtain

$$\frac{\partial}{\partial t} (\rho \mathbf{u}) + \nabla \cdot (\rho \bar{\mathbf{u}} \mathbf{u}) + 2\boldsymbol{\Omega} \times (\rho \mathbf{u}) + \rho \nabla \Phi + \nabla p = \mathbf{D}_{\rho \mathbf{u}} + \rho_r \mathbf{D}_{\mathbf{U}}, \tag{B.18}$$

which in advective form is given by

$$\frac{\bar{D}\mathbf{u}}{Dt} + 2\boldsymbol{\Omega} \times \mathbf{u} + \nabla \Phi + \frac{1}{\rho} \nabla p = \mathbf{D}_{\mathbf{u}} + \frac{\rho_r}{\rho} \mathbf{D}_{\mathbf{U}}. \tag{B.19}$$

The rotational form of (B.19) is similar to both (B.15) and (B.17). Separating out the advection of momentum by the precipitation, we rewrite (B.19) as

$$\frac{D\mathbf{u}}{Dt} + 2\boldsymbol{\Omega} \times \mathbf{u} + \nabla\Phi + \frac{1}{\rho}\nabla p = \mathbf{D}_{\mathbf{u}} + \frac{\rho_r}{\rho}\mathbf{D}_{\mathbf{U}} - \frac{\rho_r}{\rho}\mathbf{U} \cdot \nabla\mathbf{u}. \tag{B.20}$$

Next, we substitute the vector identity $(\mathbf{u} \cdot \nabla)\,\mathbf{u} = \nabla\left(\frac{1}{2}\mathbf{u} \cdot \mathbf{u}\right) + (\nabla \times \mathbf{u}) \times \mathbf{u}$ to obtain the rotational form of the approximate momentum equation

$$\frac{\partial\mathbf{u}}{\partial t} + \boldsymbol{\zeta} \times \mathbf{u} = -\nabla\left(\frac{1}{2}\mathbf{u} \cdot \mathbf{u} + \Phi\right) - \frac{1}{\rho}\nabla p + \tilde{\mathbf{F}}, \tag{B.21}$$

wherein

$$\tilde{\mathbf{F}} \equiv \mathbf{D}_{\mathbf{u}} + \frac{\rho_r}{\rho}\mathbf{D}_{\mathbf{U}} - \frac{\rho_r}{\rho}\mathbf{U} \cdot \nabla\mathbf{u}. \tag{B.22}$$

Equation (B.21) is nearly identical to (B.17), except that $\tilde{F}$ contains terms involving precipitation similar to $\bar{F}$ in (B.15).

Appendix C

PRECIPITATION MICROPHYSICS

Precipitation microphysics in atmospheric models may be represented using various levels of complexity. One of the least complex and most widely used representations is the bulk parameterization scheme developed by Kessler (1969). The model reviewed in Chapter 2 uses a variant of Kessler's parameterization developed by Klemp and Wilhelmson (1978) and further modified by Ooyama (1995, 2001). We present the details of this parameterization in this appendix.

The mass conservation equations contain two terms involving precipitation that must be parameterized: the precipitation generation rate (Q_r) and the precipitation settling speed (W). Equations (2.3) and (2.4) show that airborne water is converted to and from precipitation through the precipitation generation rate (kg m^{-3} s^{-1}),

$$Q_r = Q_{auto} + Q_{accr} - Q_{evap}, \tag{C.1}$$

which is composed of the autoconversion of cloud to precipitation (Q_{auto}), the accretion of cloud by precipitation (Q_{accr}), and the evaporation of precipitation (Q_{evap}). We have neglected the generation of precipitation by condensation, and the generation of cloud by the breakup or evaporation of precipitation (assuming the cloud evaporates before precipitation). The retained generation terms comprising Q_r are then given by

$$Q_{auto} = \left(0.001 \text{ s}^{-1}\right)\left(\rho_c - 0.001\rho_a\right), \tag{C.2}$$

$$Q_{accr} = f_{ice}\left(2.20\ \mathrm{s}^{-1}\right)\rho_c\left(\frac{\rho_r}{\rho_a}\right)^{0.875} \tag{C.3}$$

$$Q_{evap} = \frac{f_{vent}\left(10^{-4}\ \mathrm{s}^{-1}\right)\left[\rho_v^*(T) - \rho_v\right]}{\left(2.03\ \mathrm{m^3kg^{-1}}\right)\rho_v^*(T) + \left(3.337\ \mathrm{K}/T\right)}\left(\frac{\rho_r}{1.0\ \mathrm{kgm^{-3}}}\right)^{0.525}, \tag{C.4}$$

where

$$f_{vent} = 1.6 + 30.39 f_{ice}^{1.5}\left(\frac{\rho_r}{1.0\ \mathrm{kg\ m^{-3}}}\right)^{0.2046}, \tag{C.5}$$

is the ventilation factor and

$$f_{ice} = \begin{cases} 0.2 + 0.8\ \mathrm{sech}\left[\left(T_0 - T\right)/5.0\ \mathrm{K}\right], & \text{if } T < T_0, \\ 1.0, & \text{if } T \geq T_0, \end{cases} \tag{C.6}$$

is the ice factor. All other variables are defined in the List of Symbols. Note that if the generation rates become negative they are set to zero.

The prognostic equations also contain a term involving the settling velocity (W), which we parameterize using

$$W = -f_{ice}\left(14.164\ \mathrm{m\ s^{-1}}\right)\left(\frac{\rho_r}{1.0\ \mathrm{kg\ m^{-3}}}\right)^{0.1364}\left(\frac{\rho_{a0}}{\rho_a}\right)^{0.5}. \tag{C.7}$$

Klemp and Wilhelmson (1978) neglected ice in their formulation. To correct for this approximation, Ooyama (2001) added the ice factor (f_{ice}) to account for the observed variation of the settling speed across the melting level (Böhm, 1992). Since the accretion of cloud by precipitation (Q_{accr}) and the ventilation (f_{vent}) are also functions of the settling speed, Ooyama (2001) includes f_{ice} in these definitions as well.

Appendix D

NUMERICAL BOUNDARY CONDITIONS

In this appendix, we use the cubic B–spline to derive the numerical boundary conditions needed to solve the transformation from physical to spectral space. We first derive a general form of boundary condition. The general boundary condition is then used to derive specific boundary conditions for the lateral boundaries and the interface between grids. This derivation is compiled from material found in Ooyama (1984, 1987, personal notes) and DeMaria et al. (1992).

D.1 General Boundary Condition

To begin, let us derive a general form of the boundary condition by defining a second–order, linear, differential operator of the form

$$G\left[u\left(x,t\right)\right] = g_0 u + g_1 u_x + g_2 u_{xx}, \tag{D.1}$$

where g_0, g_1, and g_2 are constant coefficients that may or may not be zero, and the subscripts x and xx denote the first and second partial derivatives with respect to x. The boundary conditions at a given point x_j are then given by $G_i\left[u\left(x_j,t\right)\right] = \hat{g}_i\left(t\right)$, where $\hat{g}_i$ is the condition and $i = 1, 2,$ or 3 is the number of the condition. If $\hat{g}_i = 0$, the boundary condition is homogeneous; otherwise, it is inhomogeneous.

We may impose many different ranks and types of boundary conditions. The number of mathematical conditions determines the rank, which for the cubic B–spline basis function

ranges from 0 to 3. For example, if the rank is 2, there are 2 boundary conditions: $G_1 = \hat{g}_1$ and $G_2 = \hat{g}_2$. If the rank is 0, there are no boundary conditions. In addition to the rank, there are different types of boundary condition. The type indicates whether the boundary condition constrains the function (type 0), its first derivative (type 1), its second derivative (type 2), or some combination. For instance, if the rank is 1 and the type is 0, then $g_0 \neq 0$ and $g_1 = g_2 = 0$ such that $g_0 u = \hat{g}_1$, or if the rank is 1 and the type is 10, then $g_0 \neq 0$, $g_1 \neq 0$, and $g_2 = 0$ such that $g_0 u + g_1 u_x = \hat{g}_1$. If the rank is 3, the type is always 3. We symbolize the rank and type of boundary condition using the notation RrTtt, where r is the rank and tt is the type. For example, R2T20 is a rank 2 type 20 boundary condition with $g_0 u = \hat{g}_1$ and $g_2 u_{xx} = \hat{g}_2$.

D.2 Lateral or Outer Boundary Conditions

The transform to spectral space requires lateral boundary conditions. These boundary conditions convert the basis functions from open, $\psi_m(x)$, to closed, $\phi_m(x)$, form. A specific example of this conversion is presented here.

Consider a R1, homogeneous boundary condition of arbitrary type along the left boundary of the domain at $x = x_0$, i.e.,

$$g_0 u(x_0) + g_1 u_x(x_0) + g_2 u_{xx}(x_0) = 0, \tag{D.2}$$

Substituting (2.29) for $u(x)$ into (D.2), noting that $\psi_m(x)$ for $m \geq 2$ is zero at x_0, we obtain

$$g_0 \sum_{m=-1}^{1} a_m \psi_m(x_0) + g_1 \sum_{m=-1}^{1} a_m \psi_m'(x_0) + g_2 \sum_{m=-1}^{1} a_m \psi''(x_0) = 0, \tag{D.3}$$

which, if rearranged, yields the amplitude at the auxiliary node

$$a_{-1} = -a_0 \frac{g_0\psi_0(x_0) + g_1\psi_0'(x_0) + g_2\psi_0''(x_0)}{g_0\psi_{-1}(x_0) + g_1\psi_{-1}'(x_0) + g_2\psi_{-1}''(x_0)} - a_1 \frac{g_0\psi_1(x_0) + g_1\psi_1'(x_0) + g_2\psi_1''(x_0)}{g_0\psi_{-1}(x_0) + g_1\psi_{-1}'(x_0) + g_2\psi_{-1}''(x_0)}. \quad \text{(D.4)}$$

Thus, given the boundary condition, the amplitude at the auxiliary node is expressed as a linear combination of the first two amplitudes inside the domain. Letting

$$\beta_m \equiv \frac{\sum_{k=0}^{2} g_k \psi_m^{(k)}(x_0)}{\sum_{k=0}^{2} g_k \psi_{-1}^{(k)}(x_0)}, \quad \text{(D.5)}$$

and assuming that the denominator is nonzero, (D.4) condenses to

$$a_{-1} = \beta_0 a_0 + \beta_1 a_1. \quad \text{(D.6)}$$

Similarly, along the right boundary of the domain at $x = x_M$, the amplitude of the auxiliary node is given by

$$a_{M+1} = \beta_M a_M + \beta_{M-1} a_{M-1}. \quad \text{(D.7)}$$

For reference, table D.1 lists values of β_m for various types of the R1, homogeneous boundary condition.

Finally, to obtain $\phi_m(x)$, we substitute (D.6) and (D.7), using (D.5), into (D.3) to eliminate a_{-1} and a_{M+1} such that

$$\phi_m(x) = \begin{cases} \psi_m(x) + \beta_m\psi_{-1}(x), & m = 0, 1, \\ \psi_m(x) & m = 2, 3, \ldots, M-2, \\ \psi_m(x) + \beta_m\psi_{M+1}(x), & m = M-1, M. \end{cases} \quad \text{(D.8)}$$

Examples of $\phi_m(x)$ for R1T0, R1T1, and R1T2 are illustrated in figure D.1. The shape of the two closed splines intersecting the outer boundary changes from the open form to accommodate the rank and type of the boundary condition.

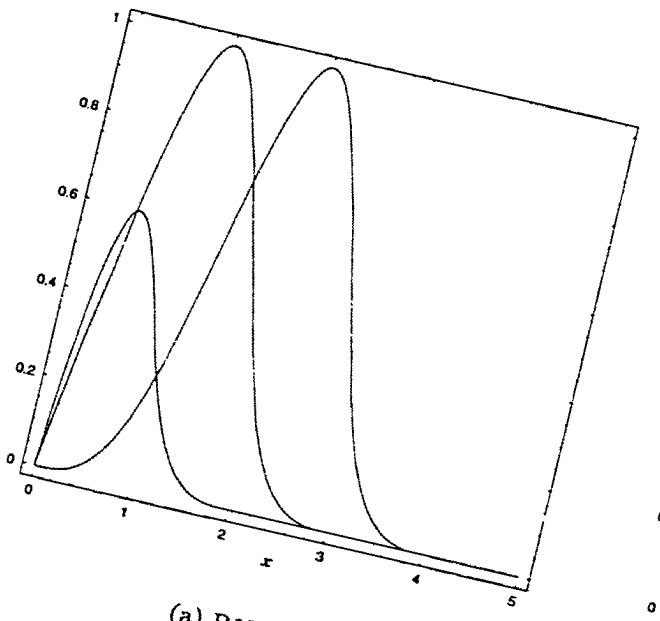

(a) R1T0

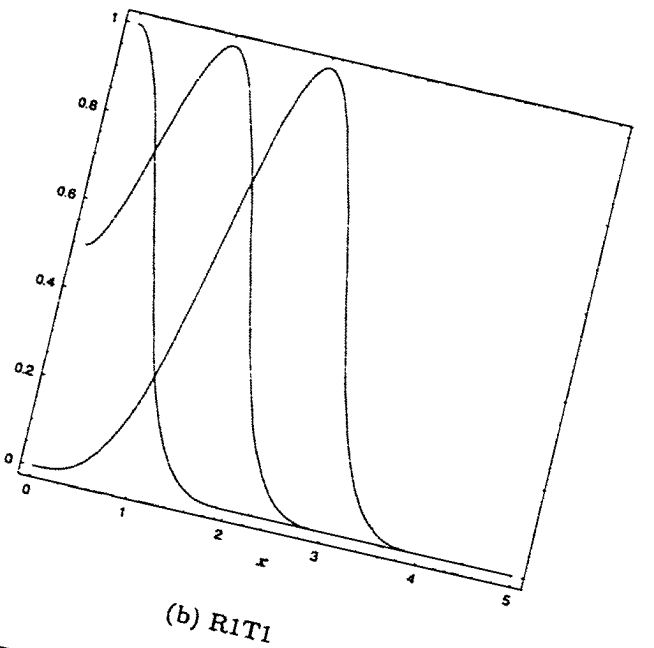

(b) R1T1

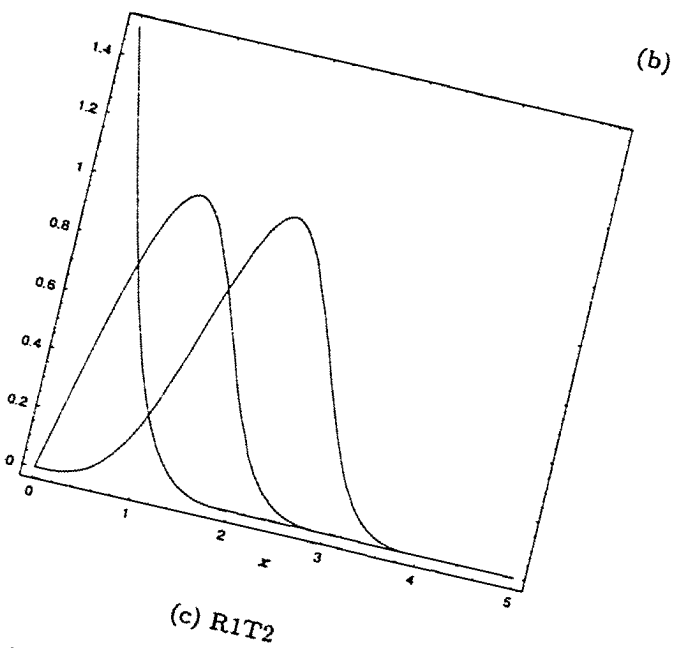

(c) R1T2

Figure D.1: Examples of the closed cubic B–spline basis function, $\phi_m(x)$, for the homogeneous boundary conditions a) R1T0, b) R1T1, and c) R1T2.

Table D.1: Values of β_m for various R1, homogeneous boundary conditions. The constant λ is a scale length for the outward exponential decay of u or u_x beyond the boundary, and Δx is the constant nodal spacing.

Type	B.C. at x_0 or x_M	β_0, β_M	β_1, β_{M-1}
0	$u = 0$	-4	-1
1	$u_x = 0$	0	1
2	$u_{xx} = 0$	2	-1
10	$u = \pm\lambda u_x$	$\frac{-4\Delta x}{2\lambda+\Delta x}$	$\frac{2\lambda-\Delta x}{2\lambda+\Delta x}$
21	$u_x = \pm\lambda u_{xx}$	$\frac{6\lambda}{3\lambda+\Delta x}$	$\frac{2\lambda-\Delta x}{2\lambda+\Delta x}$

D.3 Nesting or Interface Conditions

One distinct advantage of the SAFER method over finite–difference methods is the simple yet accurate condition that exists at the interface between nested grids. To show this advantage, let us derive the inhomogeneous boundary condition at this interface.

Imagine two grids that are nested as shown in figure 2.5. The function $u(x)$ is represented on the two grids by

$$u(x,t) = \sum_{m=-1}^{M+1} a_m(t)\,\psi_m(x) \qquad \text{(fine mesh)}, \tag{D.9}$$

$$U(x,t) = \sum_{n=-1}^{N+1} A_n(t)\,\psi_n(x) \qquad \text{(coarse mesh)}, \tag{D.10}$$

where a_m and A_n, $\psi_m(x)$ and $\psi_n(x)$, m and n, and M and N are the amplitudes, spline basis functions, node numbers and number of nodal intervals for the fine and coarse grid, respectively.

Let us consider the boundary conditions at the left interface of the fine grid, which is symbolized by the subscript L. At this interface, we use a rank-3 inhomogeneous boundary condition satisfying

$$u(x,t) = U(x,t), \tag{D.11}$$

$$u_x(x,t) = U_x(x,t), \tag{D.12}$$

$$u_{xx}(x,t) = U_{xx}(x,t). \tag{D.13}$$

Substituting (D.9) and (D.10) into (D.11)–(D.13), using the definition of the cubic B–spline, and assuming for simplicity that $\Delta x = 1$, we obtain

$$\begin{bmatrix} a_{-1} \\ a_0 \\ a_1 \end{bmatrix} = \begin{bmatrix} \frac{1}{2} & \frac{1}{2} & 0 \\ \frac{1}{8} & \frac{3}{4} & \frac{1}{8} \\ 0 & \frac{1}{2} & \frac{1}{2} \end{bmatrix} \begin{bmatrix} A_{L+1} \\ A_L \\ A_{L-1} \end{bmatrix}. \tag{D.14}$$

A similar matrix solution is obtained at the right boundary of the fine mesh.

Appendix E

DISPERSION ERRORS

In Chapter 2, section 2.2.1.5, we compared the dispersion errors of the centered, finite–difference method and the SAFER method, as applied to the linear advection equation

$$\frac{\partial u}{\partial t} + c_s \frac{\partial u}{\partial x} = 0, \tag{E.1}$$

with constant advective phase speed, c_s. The dispersion equations used to make this comparison are derived in this appendix.

E.1 Exact Solution

To calculate the dispersion errors associated with each method, we must know the analytic solution to (E.1). Let us assume that this solution is periodic in x with wavelength $l\Delta x$, and is propagating with computational phase speed c such that

$$u(x,t) = \exp\left[\frac{i2\pi(x-ct)}{l\Delta x}\right]. \tag{E.2}$$

Substituting this expression into (E.1) and solving for c yields the dispersion relation for the analytic solution

$$c = c_s. \tag{E.3}$$

This result shows that c has no wavenumber or wavelength dependence. All of the waves propagate with the same phase speed; therefore, the analytic or exact solution is nondispersive. In contrast, the numerical or approximate solutions are dispersive, as demonstrated below.

E.2 Centered, Finite–Difference Method

Next, we derive the dispersion equation for the finite–difference method. To derive this equation, we approximate the temporal and spatial derivatives in (E.1) using centered, finite–differences, i.e.,

$$\frac{u_j^{n+1} - u_j^{n-1}}{2\Delta t} + c_s \frac{u_{j+1}^n - u_{j-1}^n}{2\Delta x} = 0, \tag{E.4}$$

wherein $u_j^n = u(j\Delta x, n\Delta t)$; $j-1$, j, $j+1$ are integers identifying the location of three successive grid points centered on the point $j\Delta x$; $\Delta x = x_{j+1} - x_j = x_j - x_{j-1}$ is the constant grid interval; $n-1$, n, $n+1$ are integers identifying the location of three successive time levels centered on the current time $n\Delta t$; and Δt is the constant time step. To solve (E.4), we assume a solution similar to (E.2), except that it is not continuous but discretely defined at the grid points and time levels, i.e.,

$$u_j^n = \exp\left[\frac{i2\pi\,(j\Delta x - cn\Delta t)}{l\Delta x}\right], \tag{E.5}$$

Substituting (E.5) into (E.4) and solving for c, we obtain the dispersion relationship

$$c = c_s \frac{\sin^{-1}\left[\mu \sin\left(2\pi/l\right)\right]}{\mu 2\pi/l}, \tag{E.6}$$

where $\mu = c_s\Delta t/\Delta x$ is the Courant number. If we represent time continuously, this expression simplifies to

$$c = c_s \frac{\sin(2\pi/l)}{2\pi/l}, \tag{E.7}$$

In contrast to the analytic solution, we see that the finite–difference solution has wavenumber dependent phase speed, resulting in computational dispersion.

E.3 SAFER Method

Finally, we derive the dispersion equation for the SAFER method. In this case, we approximate the temporal derivative in (E.1) using a centered finite–difference method and the spatial derivative using the SAFER method, i.e.,

$$\frac{u_j^{n+1} - u_j^{n-1}}{2\Delta t} + c_s \frac{\partial u}{\partial x} = 0, \tag{E.8}$$

As shown in section 2.2.1.5, the spline representation of a single wave is given by the sum of two waves, i.e.,

$$u(x,t) = r_o(l) \exp\left[\frac{i2\pi(x - cn\Delta t)}{l\Delta x}\right] + r_p(l') \exp\left[-\frac{i2\pi(x - cn\Delta t)}{l'\Delta x}\right], \tag{E.9}$$

wherein $l\Delta x$ and $r_o(l)$ are the wavelength and reduced amplitude of the input wave, and $l'\Delta x$ and $r_p(l')$ are the wavelength and amplitude of the representational error or parasite wave (see figure 2.8). Substituting (E.9) into (E.8) and solving for c, we obtain the dispersion relationship

$$c = c_s \frac{\sin^{-1}[(\mu 2\pi/l) f(l,l')]}{\mu 2\pi/l}, \tag{E.10}$$

where

$$f\left(l,l'\right)=\frac{1-\frac{l}{l'}\frac{r_p(l')}{r_o(l)}}{1+\frac{r_x(l')}{r_o(l)}}. \tag{E.11}$$

Again, if we represent time continuously, this expression simplifies to

$$c=c_s f\left(l,l'\right). \tag{E.12}$$

Clearly, whenever there is representational error (i.e., if the parasite wave is present such that $r_p\left(l'\right)\neq 0$), the SAFER solution is also dispersive.

Appendix F

SPECTRAL CHARACTERISTICS OF THE DERIVATIVE CONSTRAINT

In Chapter 2, section 2.2, we derived an expression for the reverse transformation from physical to spectral space. Included in this transformation was a derivative constraint, which serves as a low–pass filter. To better understand and quantify the effects of this filter, we analyze the spectral characteristics of the derivative constraint.

F.1 Response Function

To begin this analysis, we examine the effect of the derivative constraint on a single harmonic mode, excluding the spline representation of the mode. The total error between $\bar{u}(x)$ and $u(x)$, including the derivative constraint or penalty term given by (2.33), may be rewritten as

$$\int_{\mathcal{D}} \left[[u(x) - \bar{u}(x)]^2 + \alpha \left(\frac{d^j u}{dx^j} \right)^2 \right] dx \;=\; \min, \tag{F.1}$$

where j is the order of the derivative constraint and α is a yet undetermined parameter used to control the length scale of the filter. By minimizing this error, using the least–squares approximation, we obtained the transformation from physical to spectral space.

Another minimization technique involves variational calculus. Taking the variation, δ, of (F.1) and recognizing that δu may be chosen arbitrarily, we obtain the following Euler–Lagrange equation for u in terms of $\bar{u}$

$$(-1)^j \alpha \left(\frac{d^{2j} u}{dx^{2j}} \right) + u(x) = \bar{u}(x) . \tag{F.2}$$

Thus, given $\bar{u}$, the solution of this equation yields the filtered version of u that also minimizes the total error.

To understand how the filter alters the amplitude of u as compared to $\bar{u}$, consider the case when $\bar{u}(x) = \exp(i2\pi x / l\Delta x)$ over the domain $x \in [0, l]$ with periodic boundary conditions, where $l\Delta x$ is the wavelength and Δx is the nodal spacing. Assuming a solution of the form $u(x) = r_\alpha(l) \exp(i2\pi x / l\Delta x)$, (F.2) reduces to

$$(-1)^j \alpha r_\alpha(l) \left(i \frac{2\pi}{l\Delta x} \right)^{2j} + r_\alpha(l) = 1. \tag{F.3}$$

Recognizing that $(-1)^j \left[(i)^2 \right]^j = (-1)^j (-1)^j = \left[(-1)^2 \right]^j = 1$ and letting $\alpha \equiv (l_c \Delta x / 2\pi)^{2j}$, the amplitude of u or the Fourier spectral response function is then given by

$$r_\alpha(l) = \left[\frac{1}{1 + \left(\frac{l_c}{l} \right)^{2j}} \right], \tag{F.4}$$

where l_c is the cutoff wavelength. Figures F.1a–c illustrate (F.4) for $j = 1-3$, respectively, each with $l_c = 2,\ 4,$ and 8 . As l increases, $r_\alpha(l)$ approaches 1; conversely, for vanishingly small l, $r_\alpha(l)$ reduces to 0. Notice that when $l = l_c$, $r_\alpha(l_c) = \frac{1}{2}$; therefore, l_c is the wavelength for which the filter reduces the input amplitude by half. Also, as j increases, the slope of $r_\alpha(l)$ increases, which sharpens the cutoff between filtered and unfiltered waves. Of course, if the spectral cutoff is too sharp, the solution in physical space may "ring with side lobes" due to the Gibbs effect (Ooyama, 1984). In summary, the derivative constraint acts as a low-pass filter with a $(2j)^{th}$ degree taper in the spectral response.

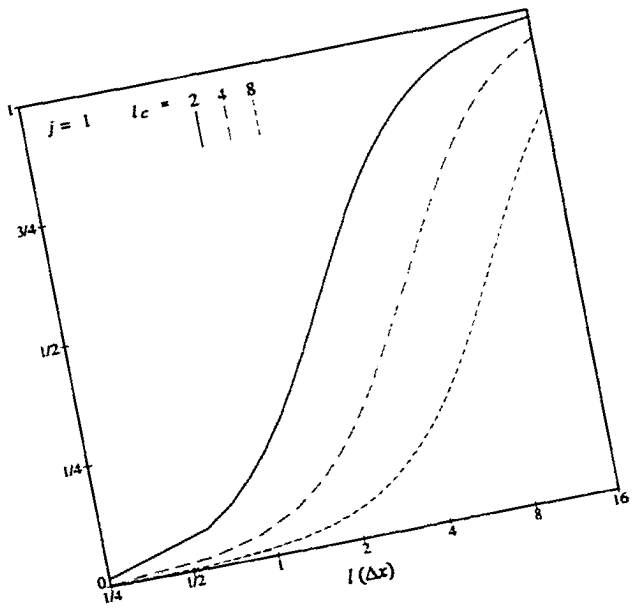

(a)

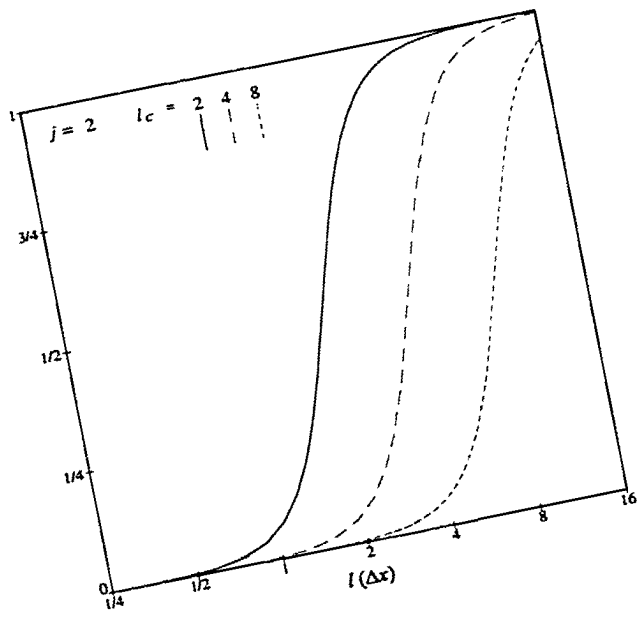

(b)

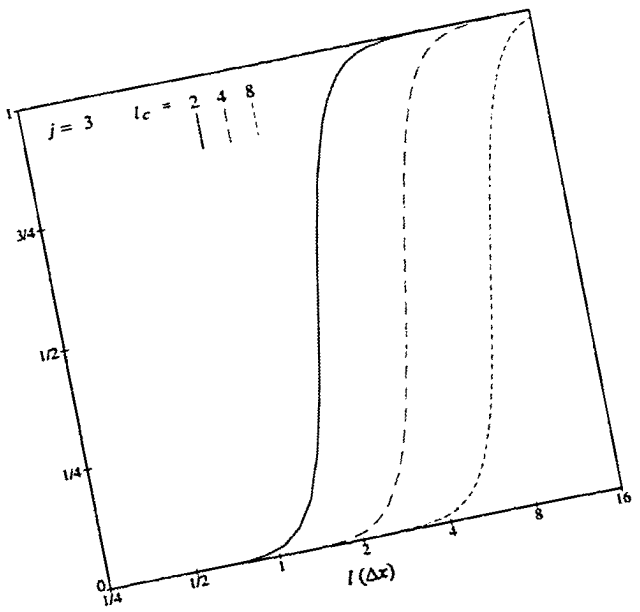

(c)

Figure F.1: Response function $r_\alpha(l)$ for derivative constraints a) $j = 1$, b) $j = 2$, and c) $j = 3$ and cutoff wavelengths, $l_c = 2, 4, 8$.

F.2 Effective Viscocity

We can easily show that the derivative constraint acts as numerical diffusion. By comparing this numerical diffusion with a form of physical diffusion, we can calculate an effective viscosity. The diffusion (or hyperdiffusion) equation for u, with no other forcing, is given by

$$\frac{\partial u}{\partial t} = -\nu \frac{\partial^{2j} u}{\partial x^{2j}}, \tag{F.5}$$

where ν is the viscosity coefficient. Using a backward finite–difference to approximate the time derivative, we obtain

$$\nu \Delta t \frac{\partial^{2j} u_{n+1}}{\partial x^{2j}} + u_{n+1} = u_n, \tag{F.6}$$

where n indicates the time level and u_{n+1} represents the diffused form of the input u_n.

Notice the similarity between (F.2) and (F.6). Based on this similarity, we infer that the derivative constraint acts as a numerical form of diffusion. Equating the coefficients of the derivatives in (F.2) and (F.6), we find that the effective viscosity coefficient is given by

$$\nu = \frac{(-1)^{j-1}}{\Delta t} \left(\frac{l_c \Delta x}{2\pi} \right)^{2j}. \tag{F.7}$$

Thus, the larger the filter scale (i.e., l_c) or the more often the derivative constraint is applied (i.e., the smaller Δt), the greater the diffusion. As an example, given $j = 3$, $l_c = 2$, $\Delta x = 500$ m, and $\Delta t = 2.5$ s, the effective hyperviscosity coefficient is $\nu = 6.5 \times 10^{12} \mathrm{m}^6 \mathrm{s}^{-1}$. Although this hyperdiffusion may seem large, it is spectrally focused due to the sixth-degree taper in the spectral response (see figure F.1c).